UAB

Universitat Autònoma de Barcelona

Doctoral Thesis

Unveiling Nanomedicine Using Correlative Super-Resolution and Electron Microscopy

Teodora Andrian

UAB
Universitat Autònoma
de Barcelona

IBEC
Institute for Bioengineering of Catalonia

Unveiling Nanomedicine Using Correlative Super-Resolution and Electron Microscopy

Facultat de Medicina

Departament de Bioquímica i Biologia Molecular

Programa de Doctorat de Bioquímica, Biologia Molecular i Biomedicina

Thesis presented by **Teodora Andrian** for the degree of Doctor of Philosophy (PhD) in Biochemistry, Molecular Biology and Biomedicine by Universitat Autonoma de Barcelona

Research affiliation: Institute for Bioengineering of Catalonia

Barcelona, 2022

Directors: Dr Lorenzo Albertazzi & Dra Silvia Pujals

Tutor: Dr Simo Schwartz Navarro

PhD candidate: Teodora Andrian

Happiness can be found in even the darkest of times if one only remembers to turn on the light.

Albus Dumbledore

Success is a mixture of preparation and luck.

House of Cards

Contents

Abstract in English

Current cancer treatments beyond surgery include chemotherapies that have limited success. They typically demonstrate low effectiveness and serious toxicity profiles leading to a reduced quality of life due to their non-specific targeting of cancerous cells. Delivery of anticancer therapeutics using nanocarriers (nanomedicine) offers the promise of increasing the selective delivery of these drugs to specific target sites, improving their efficacy, and lowering their side effect profiles. Nanomaterials used for this purpose possess specific and unique physicochemical properties that have a crucial impact on their biological behavior. Importantly, these properties vary greatly in comparison to small-molecular drug entities. This means that they require extra and more complex characterization, particularly at the nanoscale and at a single-particle level. However, there is currently a lack of suitable state-of-the-art techniques that are optimized to assess physicochemical properties and biological fates of nanomaterials, which is one of the main causes for their poor translation to the clinic.

In this Thesis, we propose the development, optimization, and application of advanced imaging techniques such as super-resolution microscopy (SRM), transmission electron microscopy (TEM) and correlative light and electron microscopy (CLEM) to characterize nanocarriers *in vitro* and to study their biological behavior in cells. Using these studies, we aim to delve deeper into our understanding of nanocarriers.

Chapter 1 demonstrates the application of DNA-PAINT and qPAINT in quantifying surface ligand functionalization and heterogeneity in nanomaterials. First, various PLGA-PEG NP formulations were manually prepared and functionalized with oligonucleotides as model ligands. Using these techniques, the number of accessible ligands was quantified and compared between each formulation. DNA-PAINT also permitted the study of heterogeneity in ligand functionalization by applying information at a single particle and molecule level. The consequent results prompted the redesign and reformulation of the PLGA-PEG NPs by modifying the surface PEG architecture, as to expose more surface functional ligands.

Chapter 2 follows the development of a CLEM technique to study the interplay between different physicochemical properties in PLGA-PEG NPs *in vitro*, namely ligand functionalization and size. To do this, the ligand quantification ability of DNA-PAINT was correlated with the excellent morphological ability of TEM on the same field-of-view (FOV) and the information was extracted at a single particle level. Sub-populations with different ligand functionalization were identified, that could lead to different and unpredictable biological behaviors. It was also demonstrated that as opposed to our correlative protocol, characterization by a one-method-at-a-time approach could limit the information obtained.

Chapter 3 introduces the rational selection and optimization of a *d*STORM-TEM correlative protocol for the intracellular trafficking of PLGA-PEG NPs. The optimized protocol allowed us to directly visualize fluorescently labelled NPs by *d*STORM, in the complex intracellular milieu offered by TEM. As such, the distribution of NPs in different endo-lysosomal compartments at different time points was quantified, getting a better understanding of their trafficking route. Finally, the change in NP distribution upon

incubation with the lysomotropic agent chloroquine was studied, demonstrating quantitatively that it promotes endosomal escape.

Chapter 4 follows on from the previous Chapter, through the application of the *d*STORM-TEM protocol to study the intracellular behavior of pBAE polyplexes. Using two color *d*STORM both carrier (pBAE polymer) and cargo (pDNA) molecules were tracked and quantified and using TEM they were localized in different locations in the cellular milieu. Using this information, the endosomal escape properties of two different polyplexes were compared, demonstrating the power of correlative imaging in the rational design and selection of nanomedicines. Lastly, the CLEM images offered useful information regarding the cellular uptake mechanisms for the two formulations.

Resumen en Castellano

Los tratamientos actuales contra el cáncer más allá de la cirugía incluyen quimioterapias que tienen un éxito limitado. La quimioterapia es inespecífica al cáncer, y por lo tanto puede causar efectos secundarios graves que conducen a una calidad de vida reducida. La administración de terapia contra el cáncer mediante nanotransportadores promete aumentar la selectividad de estos medicamentos. Los nanomateriales poseen propiedades fisicoquímicas específicas y únicas que tienen un impacto crucial en su comportamiento, y por eso las propiedades y las dianas biológicas de estos nanotransportadores deben estudiarse. Sin embargo, las herramientas utilizadas para caracterizar estas entidades siguen siendo similares a las que se utilizan para los fármacos de bajo peso molecular. Los nanomateriales tienen propiedades fisicoquímicas que varían mucho en comparación con los fármacos clásicos. Esto significa que requieren una caracterización adicional y más compleja. Actualmente, existe una falta de técnicas adecuadas que estén optimizadas para evaluar las propiedades fisicoquímicas y las dianas biológicas de los nanomateriales, que es una de las principales causas de su mala translación en la clínica.

En esta tesis, proponemos el desarrollo y la aplicación de técnicas de imagen avanzadas como la microscopía de super-resolución (SRM), la microscopía electrónica de transmisión (TEM) y la microscopía correlativa óptica y electrónica (CLEM) para caracterizar y mejorar nuestra comprensión de los nanotransportadores.

El **Capítulo 1** demuestra la aplicación de DNA-PAINT y qPAINT en la cuantificación de la funcionalización de los ligandos de superficie y la heterogeneidad en las propiedades de los nanomateriales. Así, formulamos varias formulaciones de nanopartículas (NPs) PLGA-PEG funcionalizadas con oligonucleótidos como ligandos modelo y cuantificamos y comparamos el número de ligandos accesibles en cada formulación. Usando información obtenida partícula a partícula y molécula a molécula, DNA-PAINT permitió el estudio de la heterogeneidad en la funcionalización de los ligandos. Los resultados nos llevaron a rediseñar y reformular nuestras PLGA-PEG NPs modificando la arquitectura del PEG en superficie, para exponer más ligandos funcionales en superficie.

El **Capítulo 2** sigue el desarrollo de una técnica CLEM para estudiar la interacción entre diferentes propiedades fisicoquímicas en PLGA-PEG NPs, como el número de ligandos y el tamaño de la NP. Para hacer esto, correlacionamos la capacidad de cuantificación de ligandos de DNA-PAINT, con la excelente resolución de TEM para visualizar la morfología de las NPs. Eso se hizo en el mismo campo de visión y extrajimos así la información partícula a partícula. Identificamos subpoblaciones de NPS con diferentes números de ligandos, que conferirán diferentes comportamientos biológicos. Demostramos que, a diferencia de nuestro protocolo correlativo, la caracterización los dos métodos por separado puede limitar la información.

El **Capítulo 3** presenta la selección racional y la optimización de un protocolo *d*STORM-TEM CLEM para el tráfico intracelular de PLGA-PEG NPs. El protocolo optimizado nos permitió visualizar directamente las NPs fluorescentes en *d*STORM, y posicionarlas con gran resolución en la ultraestructura celular que ofrece TEM. Con

esta información, cuantificamos la distribución de NPs en diferentes compartimentos endo-lisosomales en diferentes tiempos. Finalmente, cuantificamos el cambio en la distribución intracelular de las NP tras la incubación con el agente lisomotrópico cloroquina, lo que demuestra que promueve el escape de los endosomas.

El **Capítulo 4** incluye la aplicación del protocolo *d*STORM-TEM optimizado para estudiar el comportamiento intracelular de los complejos poliméricos de pBAE. Usando *d*STORM con dos colores, pudimos localizar y cuantificar las moléculas transportadoras (polímeros de pBAE) y su cargo (pDNA). Usando TEM localizamos los complejos con precisión dentro del medio intracelular. Con esta información, comparamos la capacidad de escapar de los endosomas entre dos complejos poliméricos diferentes. Por último, pudimos sugerir una diferencia en los mecanismos de internalización celular entre las dos formulaciones.

Resum en Català

Els tractaments actuals contra el càncer més enllà de la cirurgia inclouen teràpies que tenen un èxit limitat. Això és degut a efectes secundaris greus, que condueixen a una qualitat de vida reduïda i una baixa efectivitat. L'administració de quimioteràpia mitjançant nanotransportadors promet augmentar la selectivitat d'aquests medicaments. Els nanomaterials tenen propietats fisicoquímiques específiques i úniques que tenen un impacte crucial en el seu comportament biològic. Per tant, les propietats i les dianes biològiques s'han d'estudiar. Encara que l'arsenal de nanomaterials complexos està en constant maduració, les eines utilitzades per caracteritzar amb precisió aquestes entitats continuen sent similars a les que s'utilitzen per als fàrmacs de baix pes molecular. Éls nanomaterials tenen propietats fisicoquímiques que varien molt en comparació dels fàrmacs clàssics. Això significa que requereixen una caracterització més complexa, particularment a la nanoescala i al nivell d'una sola partícula. Actualment, hi ha una manca de tècniques adequades que estiguin optimitzades per avaluar les propietats fisicoquímiques i les dianes biològiques dels nanomaterials, que és una de les principals causes de la seva mala translació a la clínica.

En aquesta tesi, proposem el desenvolupament, l'optimització i l'aplicació de tècniques d'imatge avançades com ara la microscòpia de super-resolució (SRM), la microscòpia electrònica de transmissió (TEM) i la microscòpia correlativa òptica i electrònica (CLEM) per caracteritzar i millorar la nostra comprensió dels nanotransportadors.

El **Capítol 1** demostra l'aplicació de DNA-PAINT i qPAINT a la quantificació de la funcionalització dels lligands de superfície i l'heterogeneïtat a les propietats dels nanomaterials. Així, formulem manualment diverses formulacions de nanopartícules (NPs) PLGA-PEG funcionalitzades amb oligonucleòtids com a lligands model i quantifiquem i comparem el nombre de lligands accessibles a cada formulació. Usant informació obtinguda partícula a partícula i molècula a molècula, DNA-PAINT va permetre l'estudi de l'heterogeneïtat en la funcionalització dels lligands. Els resultats ens van portar a redissenyar i reformular les PLGA-PEG NPs modificant l'arquitectura del PEG en superfície per exposar més lligands funcionals.

El **Capítol 2** segueix el desenvolupament d'una modalitat de CLEM per a estudiar la interacció entre diferents propietats fisicoquímiques en NPs de PLGA-PEG, com el nombre de lligands i la mida de la NP. Correlacionem la capacitat de quantificació de lligands de DNA-PAINT, amb l'excel·lent resolució de TEM per visualitzar la morfologia de les NPs. Això es va fer en el mateix camp de visió i vam extreure així la informació partícula a partícula. Vam identificar subpoblacions de NPs amb diferents números de lligands, que conferiran diferents comportaments biològics. Vam demostrar que, a diferència del nostre protocol correlatiu, la caracterització dels dos mètodes per separat pot limitar la informació.

El **Capítol 3** presenta la selecció racional i optimització d'un protocol dSTORM-TEM CLEM per al trànsit intracel·lular de PLGA-PEG NP. El protocol optimitzat ens va permetre visualitzar directament les NP fluorescents a dSTORM, i posicionar-les amb gran resolució a la ultraestructura cel·lular que ofereix TEM. Amb aquesta informació, quantifiquem la distribució de NP en diferents compartiments endo-lisosomals en

diferents temps, obtenint una millor comprensió de trànsit intracel·lular. Finalment, quantifiquem el canvi en la distribució intracel·lular de les NP després de la incubació amb l'agent lisomotròpic cloroquina, fet que demostra que promou l'escapament dels endosomes.

El **Capítol 4** és l'aplicació del protocol dSTORM-TEM optimitzat per estudiar el comportament intracel·lular dels complexos polimèrics de pBAE. Usant dSTORM amb dos colors, vam poder localitzar i quantificar les molècules transportadores (polímers de pBAE) i el seu cargo (pDNA). D'altra banda, usant TEM podem localitzar els complexos amb precisió dins del medi intracel·lular. Comparem la capacitat d'escapar dels endosomes entre dos complexos polimèrics diferents. Per acabar, vam poder suggerir una diferència en els mecanismes d'internalització cel·lular entre les dues formulacions.

Introduction

Nanomaterials for medical applications and their characterization using advanced imaging techniques.

This chapter provides a brief introduction to nanomedicine and its role in treating disease in oncology. It focuses on different nanoformulations with specific examples, and the impact of their physicochemical properties on their biological behavior. Finally, it introduces the crucial roles of advanced microscopy techniques such as super-resolution microscopy, electron microscopy, and correlative light and electron microscopy on nanoparticle characterization and intracellular studies.

This Introduction contains parts of the following published Review and Book Chapters:

*Andrian T., Riera R., Pujals S., Albertazzi L. **Nanoscopy for endosomal escape quantification**. Nanoscale Adv. 2021;3(1):10–23. As an author in this paper, I contributed to the overall organization, literature research, figure preparation and manuscript writing, together with Riera R. Pujals S and Albertazzi L contributed with providing periodic feedback and review for the manuscript.*

*Andrian T., Bakkum T., van Elsland D.M., Bos E., Koster A.J., Albertazzi L., van Kasteren S.I., Pujals S. **Super-resolution correlative light-electron microscopy using a click-chemistry approach for studying intracellular trafficking**. In: Methods in Cell Biology. Elsevier; 2021. As an author in this paper, I contributed to the overall organization, literature research, figure preparation and manuscript writing, together with Bakkum T. The rest of the authors contributed with providing periodic feedback and review for the manuscript.*

1. From nanotechnology to nanomedicine

Nanotechnology has become a foundation for remarkable applications in the pharmaceutical, cosmetic and food industries, among others. It now encompasses areas of science and engineering whereby events at the nanoscale are used in the design, characterization, production and application of materials, structures, devices, and systems[1,2]. The convergence of nanotechnology with the biomedical and pharmaceutical sciences has given rise to the field of nanomedicine, incorporating drug delivery, nanoimaging and theragnostics[1,3,4]. Nanocarriers are nanoparticles (NPs) typically between 1-100 nm in diameter used for the encapsulation and delivery of therapeutics, due to their unique advantages over conventional medicines. The main distinctive features of nanocarriers include i) enhanced pharmaceutical properties (e.g. improved solubility and stability, increased half-life of drug and tumor accumulation)[3,5–8], ii) improvement of the drug therapeutic index by improving efficacy and/or reducing their toxicity profile[4,9–11], iii) co-delivery of multiple therapeutics to improve efficacy and/or overcome drug resistance and[12] iv) targeted delivery of drugs to specific cells or tissues[13].

These unique and appealing features make NPs particularly useful as drug delivery systems for different therapeutics: i) small molecular drugs that are poorly soluble, easily degradable and/or cytotoxic[14], ii) proteins that are prone to degradation and toxicity[15] and iii) nucleic acids such as mRNA, DNA and CRISPR/Cas9 that are easily degradable and require mediated delivery into the target cell[16]. Therefore, their clinical applications as drug delivery systems span from oncology[14] and cardiology[17], to their role as vaccine delivery platforms in infectious diseases[18]. For these engineered NPs to successfully achieve site-specific delivery, their design must be carefully tailored to ensure they overcome various challenges upon entering systemic circulation, such as the presence of plasma proteins and detection by the immune system[3], as well as various intracellular barriers, as will be later explained.

1.1. The nanomedicine landscape

Research on nanomaterials within the pharmaceutical field has started as early as the 1960's, with first clinical authorization of a nanocarrier received in 1995, when the FDA granted Doxil – a liposomal formulation of doxorubicin – approval for AIDS-related Kaposi sarcoma[19] (Figure 1). Since then, the landscape has steadily evolved, with the number of new nanomedicine products entering the market considerably increasing in the past years, with the majority approved as anticancer therapies[20]. Most of the formulations on the market are nanocarriers of already-approved drugs, as this tactic reduces the time of the approval process by regulatory agencies. Notably, the main clinical value of these nanocarriers has been a reduction in the toxicity profile compared to the free drug (such as in the case of Doxil and Abraxane), rather than an enhancement in the efficacy. However, several formulations currently in clinical trials are showing promising results with improved efficacy, that are expected to receive regulatory approval[21]. Currently, most approved nanomedicines are anticancer therapies, but recently more and more formulations in clinical trials are aimed at different therapeutic applications, that could allow us to see an expansion in the scope of nanomedicine. For example, the first nanocarrier for RNA delivery was approved in 2018 for the treatment of transthyretin amyloidosis (Onpattro)[22], and the recent

emergency use authorization for the mRNA-based liposomal vaccines such as Pfizer-BioNTech has demonstrated the versatile therapeutic potential of nanomedicine at a global level[20]. The accelerated translation of nanocarriers and the trust placed on nanomedicine by regulatory agencies is a big push in ensuring that more applications will soon arrive[23].
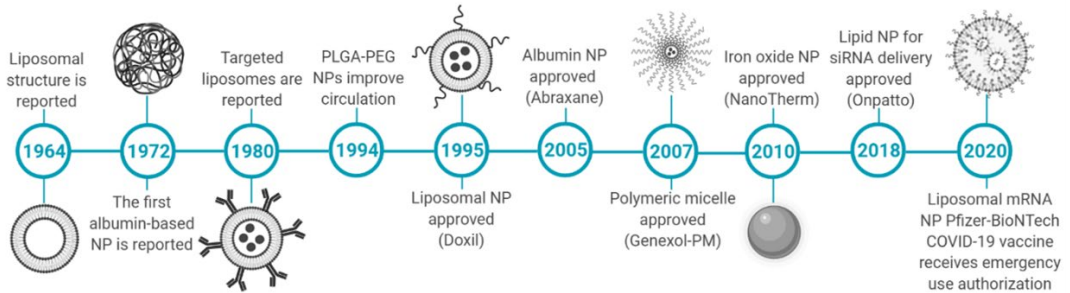
Figure 1 Historical timeline of nanomedicine development. This timeline highlights some of the most relevant discoveries in nanomedicine including the introduction and clinical approval of various nanoformulations. Created with Biorender.com.

1.2. An arsenal of nanomaterials for nanomedicine

A wide range of nanomaterials have been employed as drug carriers with different physicochemical characteristics. These can be divided into five main groups depending on the main material used for the formulation: lipid-based, polymer-based, inorganic, drug conjugates and viral nanoparticles (Figure 2), although combinations of nanomaterials have also been developed.
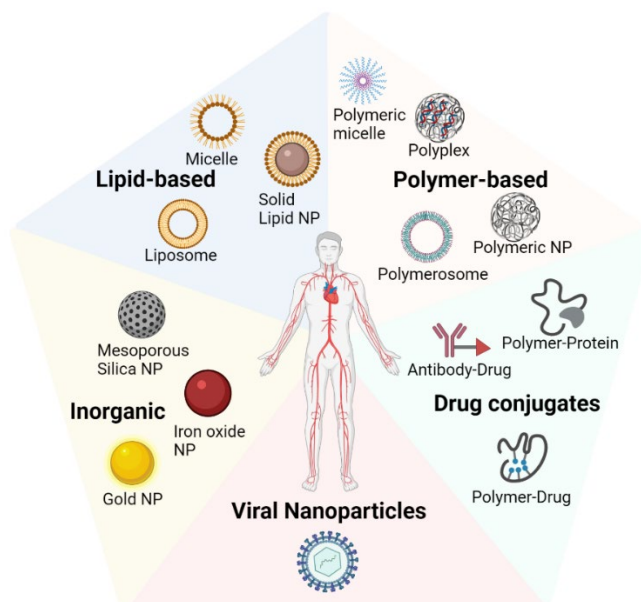
Figure 2 Main types of nanocarriers used in nanomedicine. Created with Biorender.com.

1.2.1 Lipid-based

These include liposomes, micelles, and solid lipid NPs (Figure 2), and are typically spherical and comprise of at least one internal aqueous environment and at least one surrounding lipid bilayer. Because their structure mimics that of the cell membrane, they offer biocompatibility and biodegradability, making them almost ideal nanocarriers, and the most common class of FDA-approved nanomaterials[24]. They have payload flexibility since both hydrophobic and hydrophilic drugs can be encapsulated. Their clinical indications include cancer, bacterial, fungal and viral infections and cardiovascular problems, amongst others[25]. However, this class can be limited by low drug encapsulation efficiency and biodistribution that can lead to high uptake in the liver and spleen[26].

Liposomes, a subset of lipid-based drug carriers, are nearly-spherical vesicles composed of an amphiphilic lipid bilayer membrane that allow the encapsulation of hydrophilic drugs in their aqueous core, or of hydrophobic drugs in their lipophilic membrane[27]. They were the first lipid-based nanocarriers to receive regulatory approval for human use - PEGylated liposomal formulation of doxorubicin (Doxil) in 1995 for HIV-related Kaposi's sarcoma - and hence a flagship in the development of new formulations. Doxil is now routinely used also in cancers of the breast and the ovary, thanks to the reduction in the side effects profile of the chemotherapeutic drug doxorubicin (particularly acute cardiac toxicity) and prolonged circulation time[28]. Notably, no clear improvement in the antitumor efficacy has been seen in clinical trials as compared to free drug[29,30].

Micelles are formed through the aggregation of amphiphilic molecules at a specific concentration (above critical micelle concentration/CMC), pressure and temperature. They solubilize hydrophobic molecules in their core, while polar molecules can be adsorbed on the surface. Depending on the material of the amphiphile, these can be classified as lipid or polymeric micelles. Up to date, the only approved lipid micelle nanocarrier is Estrasorb (Novavax), a topical lotion of estradiol in micellar form for the reduction of vasomotor symptoms in menopausal women[1]. Transdermal delivery reduces the side effect profile and avoids first pass metabolism, achieving stable serum levels for a prolonged time[3].

1.2.2. Drug conjugates

This class of nanomaterials is formed through the conjugation of an active drug to a polymer, peptide, or targeted antibody. Antibody-drug conjugates (ADCs) have shown the most significant translational progress among the various drug delivery strategies. They contain a highly selective monoclonal antibody (mAb) that specifically recognizes tumor-associated antigens, and a potent cytotoxic drug via a chemical linker that is stable in circulation but able to release the cytotoxic agent at the tumor site, reducing the risk of off-target toxicity[31]. Mylotarg (gemtuzumab ozogamicin) was the first ADC to receive FDA approval for treatment of acute myeloid leukemia (AML). It comprises of an anti-CD33 mAb and a specific acid-liable linker that is cleaved within the acidic environment of lysosomes, releasing the cytotoxic drug calicheamicin[32]. With the number of clinical trials having more than tripled in the past years, promising new treatments are being envisioned[31].

1.2.3. Viral nanoparticles

Viruses provide an ideal basis as drug delivery systems, owing to their ability to infect specific cells with excellent efficiency and to deliver their genetic payload directly into the cell. It is thus of no surprise that scientists have explored viral nanoparticles (VNPs) and virus-like particles (VLPs) in nanomedicine. VLPs consist of protein structures that resemble viruses but that are genome-free, providing in principle a safer alternative to their VNP counterparts[33]. Viral immunotherapy is attractive in various medical fields such as targeted drug-delivery, biomedical imaging, and vaccines. In oncology, viruses are particularly attractive, as they offer a combination of selective tumor cell killing properties (e.g. through specific cellular entry and heightened viral replication in tumor cells) and antitumor immunity (e.g. through the release of cell waste and viral antigens in the tumor microenvironment)[34]. As such, in 2015 the first oncolytic virotherapy talimogene laherparepvec (Imlygic) was approved by the FDA for advanced melanoma. It is composed of an attenuated herpes simplex virus type 1 (HSV-1) engineered to express human granulocyte-macrophage colony-stimulating factor (GM-CSF)[35]. Although there is an increasing array of oncolytic viruses in clinical trials, no new formulations have yet reached the market, probably since thorough biosafety and cytocompatibility studies must be taken into account[36,37]. Nonetheless, VNPs offer us smart and versatile machinery for applications in medicine, and optimized combinations with other immune therapies may lead to exciting advances in patient outcomes.

1.2.4. Inorganic nanoparticles

These nanomaterials are promising platforms in the clinical trial pipeline for a wide range of indications, from therapeutics and imaging applications to dental caries in dentistry and UV-protection in cosmetics. Various materials are being investigated including iron, gold, silica, calcium, zinc, titanium and hafnium[38].

Iron-based nanoparticles (IONPs) have found far-ranging applications in therapeutics and bioimaging. When coated in low-molecular-weight sugars (e.g. dextran/sucrose), iron oxide colloids play an important role in iron-deficiency anemia, as they reduce immunogenicity issues linked to free iron by mouth or IV. A hallmark in this category is CosmoFer, the first inorganic nanomedicine to be approved by the FDA in 1974; since then, seven more similar formulations have been authorized[24]. Magnetic iron oxide NPs have an important role as contrasting agents for MRI, due to their large surface area and intrinsic magnetic responsiveness that produces efficient contrast for imaging of tumors and other pathologies[38,39]. Superparamagnetic iron oxide NPs (SPIONs), have a valuable application as magnetic hyperthermia agents. Nanotherm (aminosilane-coated SPIONs) is a clinically approved formulation for treatment of glioblastoma; it is locally injected in the tumor, where a magnetic field is applied to reach an increase in the local temperature (40-45ºC), leading to tumor cell death and avoiding damage to healthy tissues[38,40].

Gold-based NPs confer several advantages such as optical and thermal and malleable physicochemical properties, rendering them suitable for various biomedical applications including diagnostics, site-specific drug delivery and photothermal/dynamic therapy[41]. CYT-6091 (Cytimmune Sciences) is an

investigational gold NP formulation for solid tumor treatment, whereby human tumor necrosis factor (rhTNF) is bound to colloidal gold via a PEG linker for antifouling properties and improved accumulation in tumors. Immobilization to gold NPs allowed the dosage of rhTNF to be three times greater than free rhTNF without displaying toxic effects and showed effective targeting of tumors[42]. Gold NPs are also endowed with surface plasmon resonance (SPR) properties, and for this reason they have acquired great interest in the field of mediated tumor photothermal ablation[43]. As an example, AuroLase is a silica-gold NP formulation coated with PEG, showing positive results in clinical trials for ablation of various solid tumors by near-infrared (NIR) irradiation[38,44]. However, they face significant challenges in clinical translation, with few formulations in clinical trials (6 in 2020), and none with regulatory approval[38]. One of the main reasons are inconclusive results at the pre-clinical level on their biological fate and safety due to differences in NP properties and experimental conditions, highlighting the need for systematic research.

1.2.5. Polymer-based

Polymeric NPs are widely applicable due to their simple synthesis and extensive data regarding their efficacy and safety[1,3]. These can be either natural (e.g. proteins and glycans) or synthetic materials (e.g. poly(lactide) and polyesters) and can be formulated as polymeric NPs, polymeric micelles, polyplexes, polymersomes or polymer drug conjugates. Drug delivery is possible via different mechanisms, for example encapsulated in the core, in the polymer matrix or conjugated to the surface of the nanoparticle, allowing both hydrophobic and hydrophilic payloads to be used[13]. Polymeric NPs make model drug-delivery candidates due to their biodegradability, solubility, biocompatibility and malleable surface chemistries allowing for additional targeting[45].

The encapsulation of small molecular drugs in protein-based nanocarriers can improve their solubility and prolong their circulation time whilst circumventing the requirement for toxic solvents, as seen for albumin-bound paclitaxel (Abraxane)[46]. Meanwhile, polymers such as poly(ethylene glycol) (PEG), a well-studied synthetic material, are commonly applied as surface coatings on NPs (PEGylation) to increase circulation times by reducing nonspecific protein adsorption, opsonization and consequent clearance, as seen in the case of Doxil and the recent mRNA COVID-19 vaccines.

Polymeric micelles are amphiphilic molecules which self-assemble as previously described. They are attractive delivery vesicles due to their ability to entrap hydrophobic drugs in their core and allow a controlled cellular release over time. Genexol-PM® is a polyethylene glycol-poly(D,L-lactide) (mPEG-PLA) polymeric micelle of paclitaxel, approved for various cancers in South Korea[48,49], whilst other promising formulations are currently in clinical trials[50].

Despite the fact that polymeric NPs have been regarded as the gold standard of drug delivery carriers due to their excellent pharmacokinetic properties[51,52], this class of NPs has not yet moved past clinical trials. However, the future seems bright since several promising formulations are currently under clinical trials[53]. The first polymeric targeted NP has reached advanced clinical trials (BIND-014) for anticancer therapy[54]. This polylactide-polyethylene glycol (PLA-PEG) nanoformulation encapsulates the drug

docetaxel and is conjugated to an active ligand, which specifically targets the prostate specific membrane antigen (PSMA); it has shown an increase in efficacy as compared to the free drug in phase 1 clinical trials and positive outcomes in phase 2 trials[54]. PICN® is a polylactide-polyethylene glycol formulation of paclitaxel that has already been approved in India[55] for metastatic breast cancer and currently in clinical trials in USA, that circumvents the use of toxic surfactants and solvents.

Polyplexes are complexes which are spontaneously formed between nucleic acids (e.g. DNA/RNA) and cationic polymers (e.g. poly(lysine) and poly(ethylenimine)). They have been studied as carriers for gene delivery, whereby they condense their cargo to a high density and protect it from various physiological barriers including degradation in systemic circulation and endo-lysosomal pathways[56]. Although they have not reached the clinic yet, due to their chemical diversity and potential for functionalization, these nanomaterials show promise as gene delivery carriers[56].

1.3. *Nanomaterials for drug delivery in oncology*

Cancer is the second main cause of death worldwide, after cardiovascular diseases, with the number of cases expected to gradually grow as a result of increased life expectancy[57,58]. For local and regional (non-metastatic) cancers, the mainline treatments are surgery and radiography, whilst for metastasized cancers therapies such as chemotherapy, biological molecules and immunotherapies offer the best efficacy, as they are able to reach target organs via the blood stream[59]. Chemotherapeutics are toxic drugs that generally inhibit the excessive proliferation of cancer cells, but by doing so and since they have a lack of specificity for cancerous tissues, they collaterally hinder the necessary growth of healthy cells needed for the maintenance of the bone marrow, gastrointestinal tract, and hair follicles. This causes distressing and potentially fatal side-effects such as suppression of the bone marrow, infertility, mucositis and nausea[60–62]. Furthermore, most drugs in this class exhibit disadvantageous properties such as poor solubility and bioavailability, and thus require high and toxic doses to achieve a therapeutic effect.

Nanocarriers, as already described, have a clear role to play in the delivery of anticancer therapeutics. As of 2019, there are at approximately 15 cancer NP formulations on the market, and 75 in clinical trials[63]. Due to their tunable properties, they can encapsulate both hydrophobic and hydrophilic drugs, including small molecular weight drugs and macromolecules such as genes or proteins. In principle they are expected to achieve targeted delivery, to improve drug accumulation at the tumor site and to avoid healthy tissues during their biological journey[61,64]. By encapsulating the drugs, they can improve their solubility, protect them from degradation, reduce their clearance, enhance their half-life in the circulation, and even offer controlled release properties[3,21,36]. In terms of tumor targeting capabilities of nanocarriers, two crucial processes are involved, namely "passive targeting" and "active targeting"[65], that promote the delivery of nanocarriers directly to the tumor site and even inside cancerous cells. Thereafter, the intracellular trafficking of these nanocarriers plays a significant role in how the cargo is processed and transported (Figure 3).
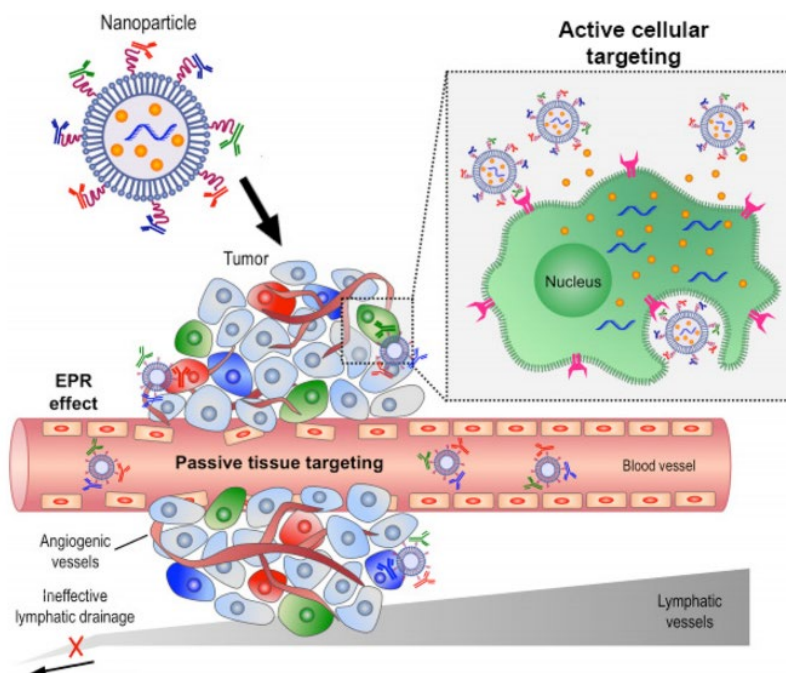
Figure 3 *Passive and active targeting processes as promising transporters of anticancer drugs to tumors. Passive targeting makes use of the leaky vasculature and poor lymphatic drainage of tumors via the Enhanced Permeation and Retention (EPR) effect to allow the permeation of nanocarriers in the tumor environment. Active targeting refers to the conjugation of functional ligands on the surface of nanocarriers typically encapsulated with chemotherapy drugs, that allow the selective recognition of receptors or antigens overexpressed on the surface of cancer cells. Reprinted with permission from reference 65. © 2014 Peer; licensee BioMed Central Ltd.*

1.3.1. Passive targeting – size matters

A possible explanation to how nanocarriers achieve specific accumulation at the tumor site is via a process called Enhanced Permeability and Retention (EPR) effect[66]. This process can be described by analyzing the pathophysiological differences between healthy and tumor tissues. As opposed to healthy tissues, tumors have a damaged vasculature and microenvironment; in particular they show large fenestrations between endothelial cells (mainly between 1-100 nm[67]) that allow the extravasation of nanocarriers within that specific size range into tumor tissues, and a reduced lymphatic drainage which promotes nanocarrier accumulation and penetration[64] (Figure 3). However, although the aim of this thesis is not to elucidate passive targeting, it is necessary to point out that recent literature has revealed rather controversial results regarding the EPR effect as a "gold standard" in nanomedicine. Notably, it is greatly heterogenous, with NP showing differences in accumulation depending on the tumor type[63,68], but even in patients with the same kind of cancer[69]. In a recent article, Warren Chan and colleagues found that up to 97% of NPs are in fact transported into solid tumors via a transcytosis process by endothelial cells - rather than through inter-endothelial gaps, and that the frequency of fenestrations between cells is too low to allow NP accumulation[70,71]. These findings may lead to active transcytosis being studied further to boost delivery of nanocarriers to tumors, for example using tumor-penetrating peptides[70,72].

1.3.2. Active targeting – affinity matters

An approach that shows greater promise in improving specific cellular uptake of nanocarriers is active targeting. This referes to the conjugation of functional groups/ligands on the surface of NPs that interact with antigens or receptors exclusively found or overexpressed on the surface of cancer cells. There are various types of ligands that have been explored such as proteins and oligopeptides, small targeting molecules, vitamins, antibodies and aptamers[73–77], depending on the characteristics of the target receptor. Conjugation can be achieved through various approaches such as covalent binding of lingands to target groups present on the NP surface (e.g. via maleimide-thiol chemistry) or to surface-coating polymers such as PEG[78,79], as was achieved for the BIND-014 polymeric formulation (Figure 4).

As of 2019, thirteen targeted nanomedicines are found in clinical trials[80]. Trastuzumab is a standard immunotherapy agent in HER2-positive breast cancer patients and is generally combined with chemotherapy for this purpose. Despite the initial positive response, cancers generally progress and acquire resistance over time. Doxorubicin is a well-established and effective chemoterapeutic, but with life-threatening side-effects limiting its use in the clinic. MM-302 is a HER2-targeted PEGylated liposome currently in phase 3 clinical trials – the liposome is conjugated via a PEG spacer to anti-HER2 antibodies on its surface and encapsulates doxorubicin crystals in its core (Figure 4). Pre-clinical and clinical trial data combining trastuzumab and MM-302 have shown promising results in terms of efficacy and improved safety profile.[81,82]
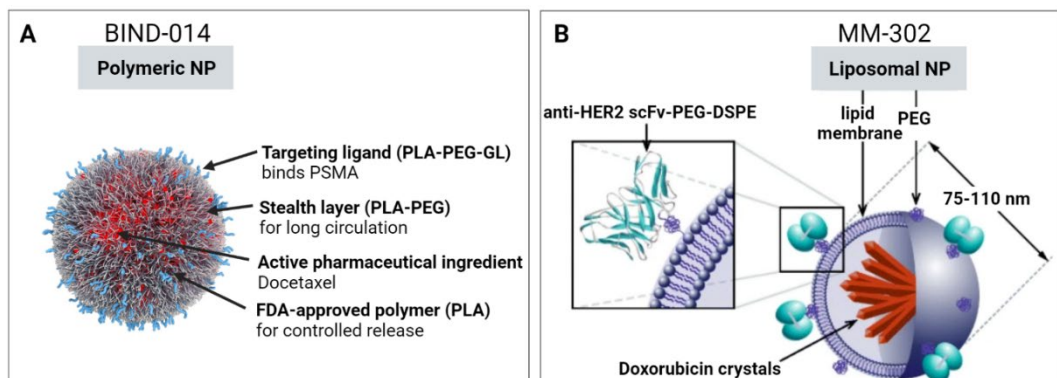
Figure 4 *Schematic representations of A) BIND-014 and B) MM-302 nanoparticle formulations. BIND-014 is a polymeric NP formulation encapsulating docetaxel, consisting of PLA-PEG together with the targeting polymer PLA-PEG-GL that is functionalized with a small molecule that selectively targets PSMA, a cell-surface protein expressed on prostate cancer cells[83]. Figure adapted from reference 83 with permission from Dove Medical Press Limited, Copyright © 2014. B) MM-302 is a HER2-targeted antibody-liposomal doxorubicin conjugate consisting of doxorubicin encapsulated in a liposomal nanocarrier that is conjugated to anti-HER2 scFv antibody via PEGspacer, currently in clinical trials for HER2-positive breast cancer[84]. Figure adapted from reference 84 with permission from BioMedCentral, copyright © 2016.*

It is important to point out however, that the concept of active targeting has first been envisoned more than four decades ago with targeted-liposomes[85]; still, since then no targeted nanomedicine has moved past the clinic. There are clearly many complex questions that must be answered to ensure the benefits of active targeting are

translated to patient care, many of them regarding the optimal physicochemical properties required and their biological effects.

1.4. The impact of nanomaterial properties on drug delivery to tumors

To ensure quality, safety and efficacy of nanomaterials, a comprehensive characterization of their physicochemical properties is of utmost importance. This may not be particularly relevant for small-molecular drugs, whereby information on their chemical identity and molecular structure is generally sufficient to identify and characterize the drug. Due to the complexity and variety between nanocarriers, small changes in physicochemical properties such as size, shape, surface charge and surface composition including targeting ligands can have a significant impact on their systemic delivery to tumors[80,86,87]. These can influence their targeted delivery properties, interaction with blood proteins, circulation lifetime, biodistribution, cell targeting and intracellular trafficking and their drug release profile (Figure 5)[86–90].
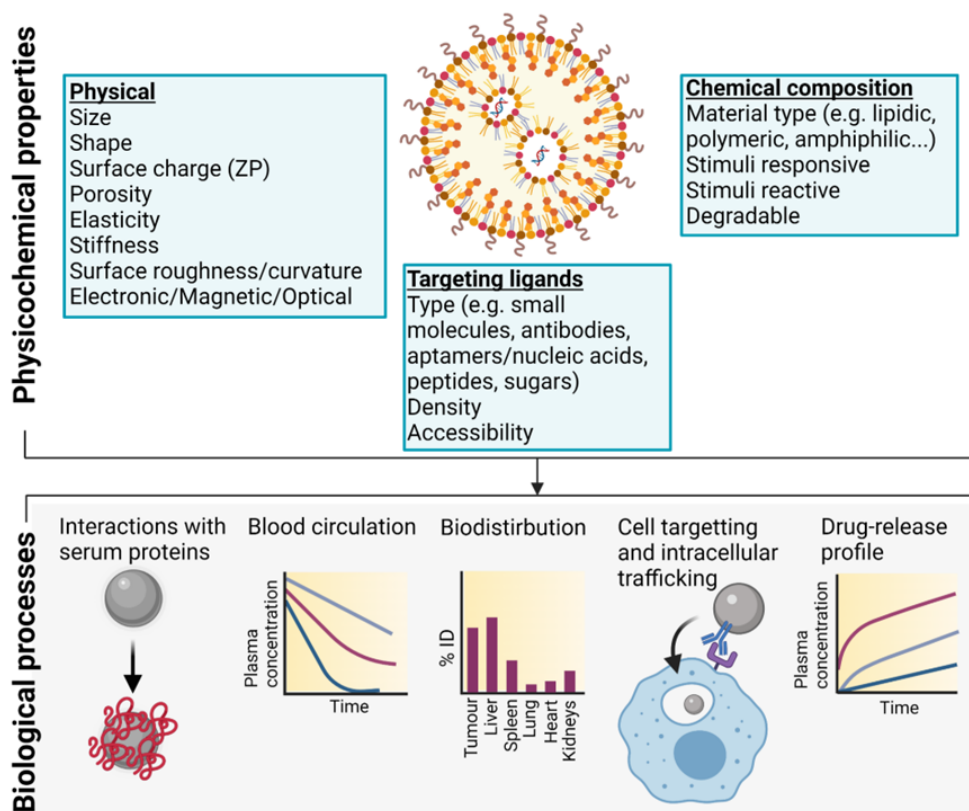
Figure 5 *The impact of NP physicochemical properties (e.g. size, surface charge, material type and functionalization with targeting ligands) on biological processes. Inspired from reference 88 and created with Biorender.com*

1.4.1. Size and size distribution

Size is a major contributing factor of a nanocarrier's *in vivo* fate: it determines the cellular uptake[80,91,92], half-life in the blood circulation[93,94], biodistribution[87,95,96], tumor permeability[97], and immune response[98] (Figure 6). For example, a nanocarrier should

be greater in diameter than approx. 5 nm (as tested on quantum dots using the hydrodynamic radius[99]) to avoid renal filtration but no larger than 150-200 nm to avoid excessive liver and spleen accumulation[100,101]. Large spherical particles with diameters >2000 nm display preferential accumulation in the spleen, liver and lung capillaries. NPs smaller than 100 nm display reduced protein attachment and hence extended blood half-lives *in vivo*[102,103].
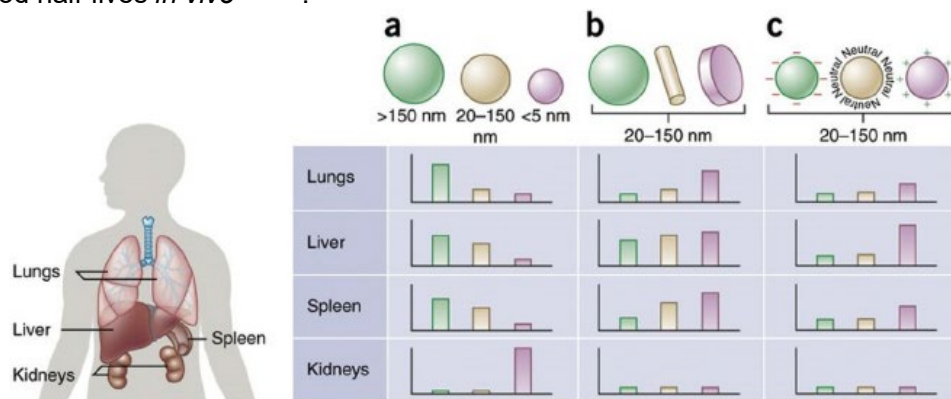
Figure 6 The effect of various physicochemical properties such as a) size, b) shape and 3) surface charge on the biodistribution of nanocarriers to different organs including the lungs, liver, spleen, and kidneys. Reprinted from reference 87 with permission from Nature Publishing Group, a division of Macmillan Publishers Limited, copyright © 2015.

For this reason, reliable size analysis is essential in nanomaterial science. Size analysis at the nanoscale can be achieved via different techniques depending on the material evaluated, including Dynamic Light Scattering (DLS), Laser Diffraction spectroscopy (LD), Atomic Force Microscopy (AFM), Electron Microscopy (EM) and size exclusion chromatography. For example, DLS allows analysis of the hydrodynamic radius of NPs in suspension and is probably the most used method for NP size determination due to its ease of use and cheap cost. Contrary to DLS and LD, AFM and EM allow NP analysis at a single particle level and with nanoscale morphological detail (Figure 7). It must be noted that it is recommended to use multiple methods to characterize the size and size distribution of nanomaterials, to ensure the most reliable description is given[104]. For instance, inorganic metal NPs tend to have the same size in both wet and dry conditions, and therefore quantification using only one method may be appropriate. In contrast, organic NPs may display different sizes depending on their state (e.g. dry vs wet), such that results measured by TEM (size in dry form) and DLS (hydrodynamic radius in solution) will give substantially distinct values[105].
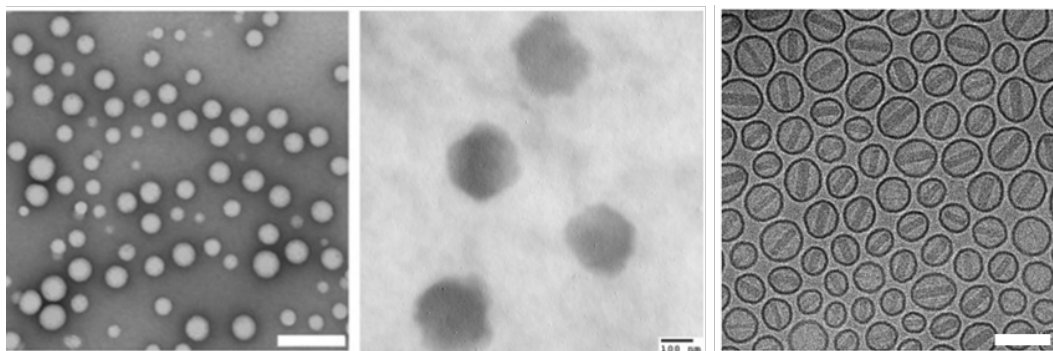
Figure 7 *Nanomaterial characterization by electron microscopy. A) PLGA-PEG NPs by TEM; adapted from reference 106 with permission, copyright © 2021 PLOS ONE; scale bar 200 nm. B) Albumin-bound paclitaxel NPs (Abraxane) by TEM; adapted from reference 107 with permission, copyright © 2021 PLOS ONE; scale bar = 100 nm. C) Doxorubicin loaded liposomal NPs (Doxil/Caelyx) by cryo-TEM; adapted from reference 108 with permission, copyright © 2014 New York Academy of Sciences; scale bar = 100 nm.*

1.4.2. Shape

Shape also heavily influences the *in vivo* fate and cellular uptake. Different NP shapes display specific flow characteristics that can alter their circulation lifetimes and target cell interactions, leading to variable biodistributions to organs (Figure 6)[87]. Rod and filamentous-shaped NPs have been shown to have longer circulation times as opposed to spherical NPs, due to a greater difficulty in removing non-spherical NPs from the reticuloendothelial system (RES)[109] but also due to a generally lower RES uptake[110]. For example, filamentous polymer micelles displayed a much longer circulation half-life post-administration (> 1 week) compared to spherical NPs (2-3 days)[111]. Shape can also influence cellular uptake, for example nanorods had a lower uptake in HeLa cells as opposed to the same spherical nanomaterial, since greater aspect ratios can affect the contact area between NPs and cellular receptors, reducing cellular uptake[112]. Like size characterization, EM techniques are also used for the morphological characterization of nanoparticles due to their excellent resolutions.

1.4.3. Surface charge

This is an important factor for the stability of NPs in suspension and is a critical factor in biodistribution[87] (Figure 6) and the adsorption of NPs on the cell membrane[113]. Surface charge is customized via different surface chemistries to prolong the circulation half-life and to improve accumulation of NPs at the tumor site. Specifically, neutral and negatively charged NPs show longer circulation lifetimes through a reduction in serum protein adsorption to their surface[114], and exhibit lower accumulation in liver and spleen[115]. Positively charged NPs also display attractive properties; for example, better uptake in non-phagocytic cells due to less electrostatic repulsion with the negatively charged cell membranes[116–118], a preferential uptake in angiogenic tumors compared to normal vasculature[119,120] and can achieve endosomal escape via processes such as the 'proton sponge effect' (e.g. cationic polymers)[121,122]. With this said, zwitterionic nanoparticles with a tunable charge depending on environmental factors can be used to improve tumor accumulation and cellular uptake[123].

Zeta potential analysis is typically used to determine the surface charge of NPs in solution. It is also predictive (but not an absolute measurement) of NP stability, as it describes the degree of repulsion between charged particles in the solution. It is measured using electrophoretic light scattering and electroacoustic determination techniques[124]. Atomic Force Microscopy (AFM) could also be potentially used for this purpose; using the relationship in the forces acting between a nanoparticle surface and the tip of the microscope, one can derive the surface charge density and show charge variation over heterogeneous surfaces[125].

1.4.4. Ligand functionalization

Ligand type, number and density, conjugation strategy and orientation are also of critical importance in nanomedicine, as NP functionalization with target ligands governs the active targeting mechanisms required for cancer cell specificity. Generally, an increase in the ligand density leads to an increase in the cellular attachment, up to a specific threshold, after which it either remains constant or it decreases[126]. In several studies, the highest degree of receptor targeting was achieved by NPs that had an intermediate number of ligands per NP[90,126,127]. Higher targeting ligand densities can in fact cause steric hinderance and a higher consumption of cellular receptors per binding event, leading to decrease in cell binding[126]. Furthermore, surface ligands are not useful unless they are orientated correctly as to bind their target receptors. In a recent study it was found that only 3.5% of proteins on the surface of a NP formulation had the correct orientation for target receptor recognition[128].

1.4.5. Heterogeneity in physicochemical properties

It is important to mention that all synthesis methods yield mixed populations of NPs leading to variations (heterogeneity) in their physicochemical properties, such as in size and functional ligand numbers. In an extensive review, Rabanel et al. explained that particle heterogeneity can be divided into two separate groups: i) at suspension level, whereby heterogeneity is displayed in subpopulations within the same batch and thus these different NP subpopulations can have different efficacies, and ii) at a NP level, whereby heterogeneity is found within the core or surface of individual NPs[129].

As previously discussed, physicochemical properties govern the biological fate of NPs, and hence their safety and efficacy. Thus, small changes can have a great impact on the formulation's biological performance, and in hindsight can lead to poorly predicted effective doses. Particularly, reporting only average values of physicochemical properties is insufficient, as these mask the whole NP population within the formulation. For example, polyamidoamine (PAMAM) dendrimers are generally considered to have narrow distributions, but even so, upon quantification at a single particle level using HPLC it was demonstrated that the average ligand number per NP was very different from the median or mode values (Figure 8)[130,131].
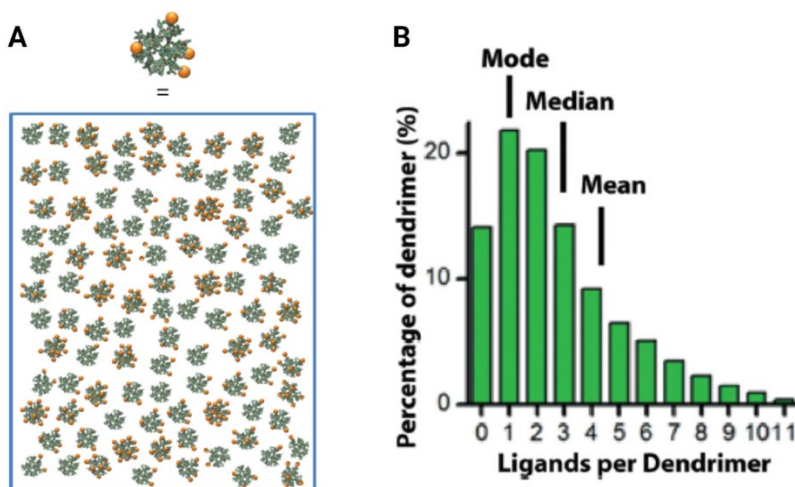
Figure 8 *The importance of ligand quantification at a single particle level[129,130]. A) Average results can mask the true heterogeneity of a population. B) Dendrimer-ligand distributions highlighting differences in mode, median and mean numbers of ligands per NP. Figure A adapted from reference 130 with permission, copyright © 2011 American Chemical Society. Figure B adapted from reference 129 with permission, copyright © 2019 The Royal Society of Chemistry.*

It is therefore expected that when a functionalized nanocarrier is reported, a quantitative assessment of the system should be given, particularly at a single particle level, in terms of size, and ligand number and density of functional ligands on the NP surface. However, as opposed to studying size, quantification of ligand numbers and distribution is a more challenging task, and in fact is still generally carried out based on average values from ensemble techniques that mask the heterogeneity of formulations[129]. This is in large part due to a lack of analytical techniques that allow quantification at a single particle level[130]. This poses a serious challenge for the development of functionalized nanomaterials, and the absence of rigorous protocols may hamper large-scale manufacturing of such formulations and slow down their translation to the clinic[130,132,133]. With this said, it is envisioned that with the development of more meaningful characterization tools – that allow quantification of biologically functional ligand number and density – the smart engineering of nanoparticles will also improve[134].

1.4.5. The interplay between ligand density and other parameters

Despite recent efforts in elucidating the effect of ligand density on the biological outcome of NPs, not much information is available on the interplay between ligand density and other properties such as size and shape. It is highly envisaged that the effects of ligand density are entangled with other parameters, and that the *in vivo* distributions will undeniably vary depending on the relationship between these various physicochemical properties. A multiparametric understanding of such physicochemical properties would shine light on fundamental information to improve the design and formulation of smarter nanocarriers[126].

For example, the effect of ligand density on NP internalization and tumor targeting was studied for similar rod-shaped NPs (80 x 320 nm) and spherical NPs (55 x 60 nm nm)[126,135]. An increase in the ligand density on the surface of rod-shaped NPs led to a

rise in the number of NP bound to the target cell membrane receptors. However, this result did not reflect an increase in cellular uptake, and in fact, after a 'maximum ligand density', the number of NPs entering cells decreased. This reduction in cell uptake was assumingly due to more rigid ligands at higher densities and thus less favorable interactions with receptors, and large contact area of the rod-shaped NPs that leads to receptor-depletion and restricted receptor-mediated endocytosis[135]. In contrast, the internalization of targeted spherical NPs (50 nm) was not affected by an increase of ligand density. This highlights the importance of considering the dependence and relationship between different parameters, however current characterization techniques lack in the ability to characterize different properties at a single particle level.

1.5.   Intracellular fate of nanomaterials

The aim of nanocarriers is to deliver their therapeutic cargos directly to the target site. For example, a pre-requisite for RNA and DNA delivery is for these molecules to reach the cytoplasm or nucleus, respectively[122]. However, the cellular journey of nanocarriers to their final destination is riddled with biological barriers. With a focus on cellular barriers, these NPs must be taken up by their target cells, and depending on their shape, size, surface charge and functionalization the cell uptake mechanism will differ[96,116,120,136]. Generally, NPs get taken up in cancer cells by endocytosis (clathrin dependent and independent, and caveolae-mediated), macropinocytosis and pinocytosis[137]. Notably, following uptake, intracellular trafficking determines the final destination within cellular compartments of the nanocarrier, which is in fact one of the most limiting bottlenecks in drug delivery using nanocarriers[138–142]. Once NP are taken up via endocytosis, they are generally distributed to endocytic vesicles[122,143–146]. Within these acidic vesicles, the carrier-drug ensemble can be degraded, and its bioavailability within the intracellular milieu reduced[147]. Within these organelles, the pH gradually drops from neutral to acidic, owing to membrane-incorporated vacuolar-type ATPases. The cargo is first transported into the early endosome (pH ~ 5.5), followed by the late endosome and lysosomes; in the latter, the cargo is degraded by hydrolytic enzymes present in the low pH environment (pH 5-4.5) (Figure 9). Whilst the recycling endosome may direct some cargo back to the outer cellular space, the majority remains entrapped in the endo-lysosomal pathway where it gets degraded[145,146,148].
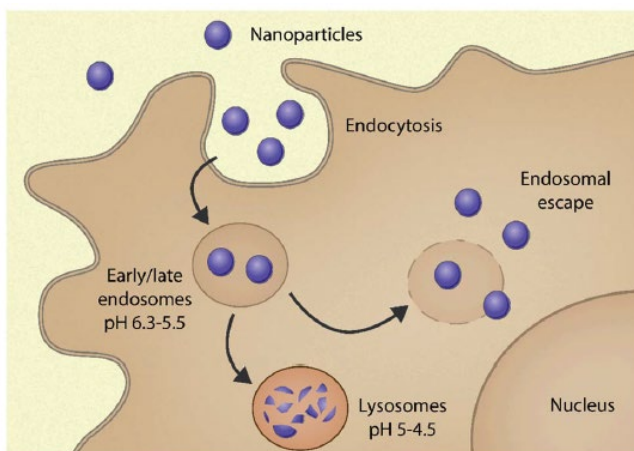
Figure 9 *Typical route of NP entry and trafficking within the cell. NP are generally first internalized by endocytosis into early endosomes, where they are trafficked through the endo-lysosomal pathway and ultimately degraded into the lysosomes. Some NP formulations can escape endosomes to avoid degeneraiton and deliver their therapeutic cargo into the cytoplasm[146]. Reprinted from reference 146, with permission from The Royal Society of Chemistry, copyright © 2021.*

Therefore, although cellular entry is necessary for the cargo to exert its effect, the subsequent endosomal entrapement represents a significant bottleneck in using NP systems for gene delivery[138,139,149], where cargo is normally delivered to the nucleus or cytoplasm, and proteins or small moleclar drugs that exert their therapeutic effect outside of the endo-lysosomal system, for the treatment of a variety of diseases[140–142].

It thus comes as no surpirse that research is focusing on NP formulations that can achieve endosomal escape. Various mechanisms have been proposed and reviewed thoroughly in literature, such as the "proton sponge" effect, membrane fusion, pore formation, membrane disruption and vesicle budding and collapse[122,145,150]. For example, cationic polyplexes are believed to achieve endosomal escape through several mechanisms (Figure 10). The first is the "proton sponge" effect: the polymer amino groups become protonated in the acidic compartments, leading to an enhanced chloride ion influx. This osmotic balance causes swelling of the endo-lysosomal compartment through water influx, followed by its rupture. Another mechanism is that after protonation of their amino groups, they are able to interact with the endo-lysosomal membrane, and consequently cause disintegration and local hole formation, allowing polyplex escape[122].
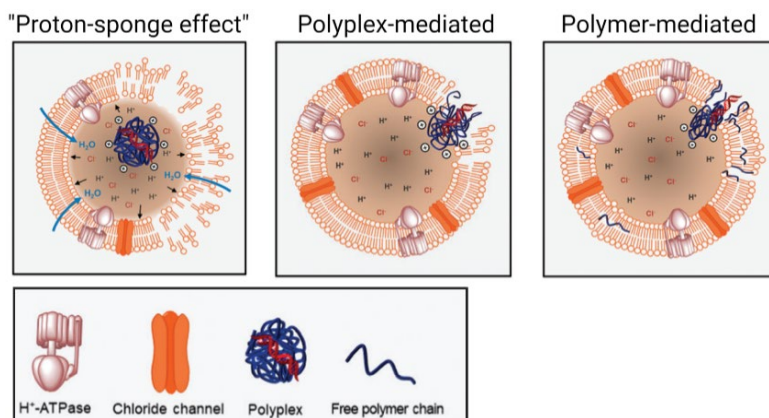
Figure 10 *Overview of endosomal escape strategies of cationic polymers and polyplexes*[122]. *The "proton-sponge effect" states that the presence of weakly basic molecules can lead to bursting of endosomes by an osmotic effect. The polyplex-mediated mechanism wrorks by a time-dependent protonation of amino groups present in the polyplex whilst inside the endosome, leading to an interaction with the endosomal membrane and permeability/local hole formation. Polymers can mediate membrane permeability and hole formation by intercalation with the plasma membrane of the endosome. Adapted from reference 122 with permission from The Royal Society of Chemistry, copyright © 2018.*

Thus, it is critical to be able to localize nanomaterials within the cellular milieu, whether they are membrane-bound, endosome-entrapped or in the cytosol/nucleus, as this will allow the identification of intracellular barriers that prevent the successful delivery of therapeutic cargo. However, techniques to study the uptake and intracellular fate of nanomaterials rely greatly on ensemble methods such flow cytometry and assays using fluorescence microscopy[147,151–153]. Notably, flow cytometry is an appropriate option for cellular uptake assays as it measures relative fluorescence intensity per cell, particularly when used in conjugation with fluorescence microscopy (FM) since it is unable to distinguish between internalized vs membrane-bound NPs. However, it cannot discriminate the intracellular location of NPs. Traditionally, fluorescence microscopy (FM) has been used to determine the uptake mechanism and intracellular localization of NPs, as it allows specific labelling of different structures of interest[151,154,155]. Notably, its spatial resolution is limited by light diffraction to a few hundreds of nanometers, hampering its use in the field of nanomedicine, whereby resolutions of 100 nm and less are required to reliably identify, track, and quantify nanomaterials at a single particle level. Furthermore, co-localization may be falsely assigned when sub-resolution objects that are found closer to each other than the resolution limit of the microscope[152]. Recent advances in the field of super-resolution microscopy (SRM) have overcome this limitation, enabling unique imaging of nanomaterials at the nanoscale.

The next sections will focus in more detail on the advantages and drawbacks of advanced microscopy techniques such as super-resolution microscopy (SRM), transmission electron microscopy (TEM) and correlative light and electron microscopy (CLEM) for the *in vitro* characterization and intracellular trafficking of nanomaterials.

2. Super-Resolution Microscopy

Fluorescence microscopy (FM) offers multicolor imaging properties in native conditions and enables the study of dynamics in real-time, but unfortunately is diffraction-limited, such that two fluorescent structures that are closer than 250 nm cannot be individually distinguished (Figure 11), as described by Abbe in 1873 and later by Lord Rayleigh[156]. This poses a problem in nanomedicine since nanomaterials cannot be resolved nor reliably quantified.
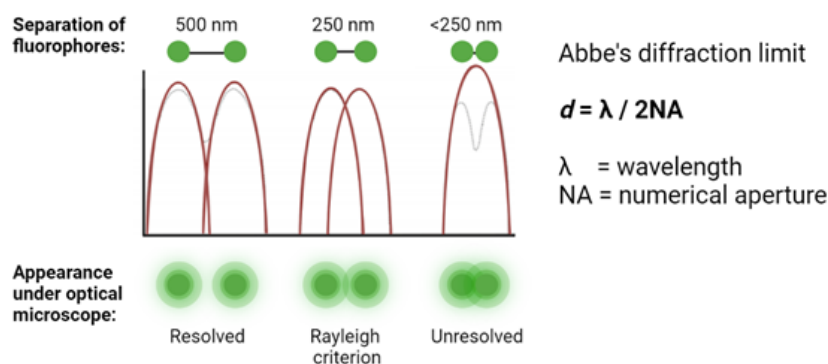
Figure 11 Resolution and its limits in light microscopy[156]. Rayleigh's criterion states that an optical microscope can resolve two objects if they are separated by a minimum separation distance of 250 nm or more but will not be resolved if they are closer than this distance (<250 nm). Abbe's diffraction limit explains that the minimum resolved angle between two fluorescent dyes (d) is determined by the wavelength of the light excitation (λ) and the numerical aperture (NA) of the microscope's objective (1.4-1.6). Inspired from reference 156 and created with Biorender.com.

An advancement in FM is super-resolution microscopy (SRM), or nanoscopy, a group of far-field optical techniques that bypass the diffraction limit and are able to reach nanoscale resolutions (1-100 nm)[157,158]. The SRM family encompasses three different groups of techniques that work on different principles and instruments[158]. These include structured illumination microscopy (SIM)[159], stimulated emission depletion (STED)[160] and single-molecule localization microscopy (SMLM)[161]. SMLM techniques offer some of the best resolutions, single-molecule sensitivity, and quantitative molecular counting and for these reasons this group has been chosen in this thesis and discussed more extensively in the following paragraphs.

2.1. Single-Molecule Localization Microscopy

SMLM techniques have an excellent resolutions ranging from 5-20 nm lateral (x,y) and 50 nm axial (z) depending on technique, they offer multi-color imaging and can achieve quantification at a single molecule and particle level[158,162,163]. They are based on the localization of single molecules (Figure 12), such that only scarce number of emitting molecules are in an "on" (emitting) state at one time, whilst the majority are in an "off" (dark) state. To perform an accurate fit, the emission profile must display minimal overlap in each image. A centroid position of each emitting molecule is identified and statistically fitted to a Gaussian function, and the localization precision is determined by the number of photons identified. The centroid positions from thousands of frames are superimposed into one super-resolved image. Several techniques form part of the SMLM family, and they differ mainly by how the "on" and "off" switching is achieved.

SMLM techniques include Photoactivated Localization Microscopy (PALM)[164], Stochastic Optical Reconstruction Microscopy (STORM)[165] and Points Accumulation for Imaging Nanoscale Topography (PAINT)[166,167], each displaying different methods of achieving temporal separation of emitters.
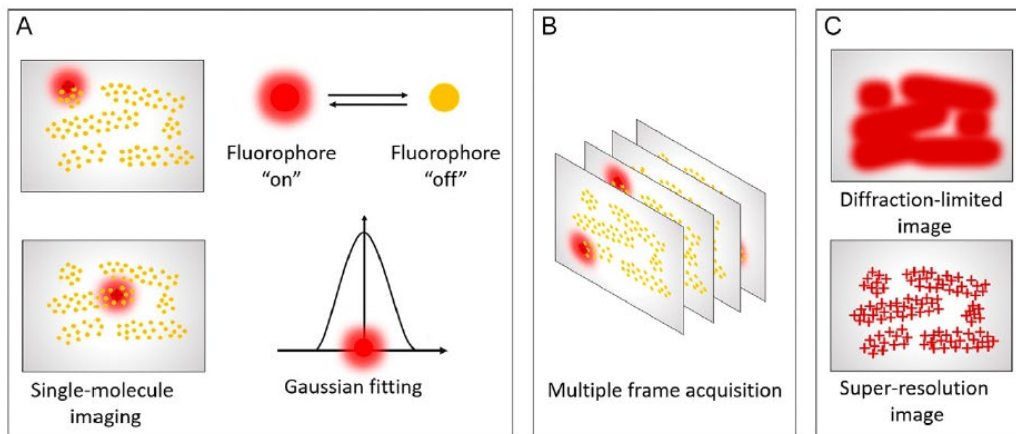
Figure 12 *The principles of Stochastic Optical Reconstruction Microscopy (STORM)[168]. A) Only a scarce number of fluorescent dyes are in the emitting "on" state at one time, whilst the majority are in a dark "off" state, achieving imaging of individual fluorophores without spatial overlap and with high resolution. The centroid position of each emitting dye is identified and plotted with a gaussian fitting and its exact position is localized. B) The positions of many emitting dyes are determined over thousands of frames. C) A super-resolved image is reconstructed made up of localizations (red crosses). Reprinted from reference 168 with permission, copyright © 2020 Elsevier Inc..*

2.1.1. dSTORM

Direct Stochastic Optical Reconstruction Microscopy (*d*STORM) is a SMLM technique that is gaining popularity in cellular biology and material science. It is based on the photoswitching and photoactivation of organic dyes, fluorescent proteins and even quantum dots[165]. In *d*STORM, fluorophores are intermittently switched "on-off" as a result of the photoswitching behavior of the dyes used and special buffer solutions[169] (Figure 12). The *d*STORM buffer solution consists of i) reducing agents (e.g. mercaptoethylamine MEA) that induce photochemical reactions which cause most of the dyes to be transferred to an "off" state, ii) oxygen scavenging systems (e.g. glucose oxidase, glucose and catalase) to reduce photobleaching and iii) buffer (e.g. PBS) for pH control. Unfortunately, different dyes blink optimally in different imaging buffers, hence multi-color acquisition with *d*STORM is challenging [170], but possible in 2-3 colors through the use of specific buffers such as Oxyrase/MEA (OxEA)[161]. Alternatives to these limitations include sequential labeling and imaging using a single fluorophore[171] or spectral demixing *d*STORM (SD-*d*STORM), that combines the benefits of red-emitting carbocyanine dyes with spectral demixing[172].

Through the use of spectrally distinct photoswitchable fluorophores, *d*STORM enables multi-color imaging with reduced cross-talk[172–174]. Still, although two-color *d*STORM has been achieved by imaging different structures using spectrally separated dyes[175,176], the limited availability of spectrally different photoswitchable fluorophores hinders the use of more colors. Most organic fluorescent dyes display photoswitching

properties, but not all of them meet the criteria required for *d*STORM imaging. Generally red fluorophores such as Alexa Fluor 647 and Cy5 perform significantly better than the best-performing dyes in other spectral regions. Therefore, even if one chooses four spectrally different dyes, those in the blue (480-540 nm), yellow (545-600 nm) and NIR (740-805 nm) will be considerably dimmer than those in the red (640-700 nm) spectrum, which may negatively affect the image resolution. It is important to note that in order to improve multi-color imaging, the longer wavelength color (i.e. 647 nm) should be imaged first to reduce the cross-talk caused by the shorter wavelength laser (i.e. 561 nm) due to the overlapping spectra of the two dyes[177].

*d*STORM has proved its potential initially in cellular biology, with important discoveries made regarding intracellular structure and protein organization[178] and more recently it has also contributed to the study of various complex molecular nanostructures[179]. Albertazzi and Meijer were the first to report the use of SRM to study the monomer exchange in supramolecular polymers, using 2-color *d*STORM imaging. Following this, other studies used similar approaches to reveal how hydrophobicity and chirality[180], as well as functional groups[181], affect supramolecular polymers[179]. *d*STORM was also applied to investigate the inner and surface morphology of polystyrene and poly(methyl methacrylate) (PMMA) blends[182].

Apart from material characterization, *d*STORM has also been applied to quantify NPs cellular interactions and trafficking, for example polystyrene NPs of diameters 80-800 nm and HeLa cells. Using 2-color imaging, co-localization studies were used to assess the interactions of these NPs with the cellular membrane[176] (Figure 13), and to quantify the molecular interactions between nanomaterials and biomolecules present in biological fluids such as the protein corona[183].
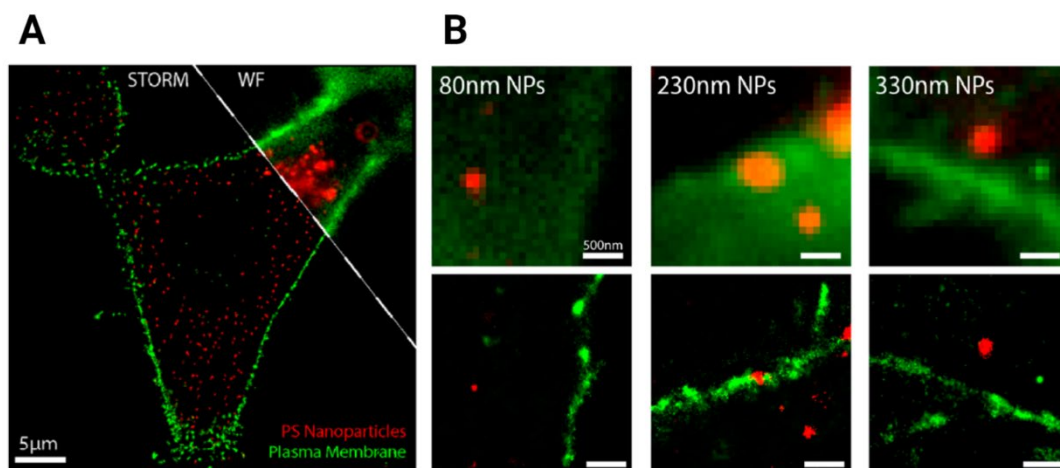
Figure 13 dSTORM images showing uptake of fluorescently tagged polystyrene NPs (red) by membrane-stained HeLa cells (membrane, green)[176]. A) large view of a cell by dSTORM compared to conventional wide-field (WF) image. B) Zoomed in images of NPs of different diameters (80 nm, 230 nm and 330 NP) by conventional wide field imaging (upper row) and dSTORM (lower row), highlighting the difference in resolution between the two imaging modalities. Adapted from reference 176 with permission, copyright © 2016 American Chemical Society.

2.1.2. DNA-PAINT

Despite the numerous advantages of *d*STORM, it is limited by photobleaching and a lack of dyes that can be concomitantly used, hence has restricted multicolor imaging. These limitations have been overcome with the introduction of other SMLM techniques. In 2006, Sharonov et al.[184] described Points Accumulation for Imaging in Nanoscale Topography (PAINT), a SMLM technique that relies on the diffusion and stochastic transient binding of a fluorophore conjugated to a probe and the target structure. In 2010, Jungmann et al. developed a variant of this technique named DNA-PAINT[166]. In contrast to other SMLM techniques, here fluorescent blinking is produced by transient hybridizations between two complementary single DNA strands (Figure 14). Specifically, DNA strands attached to structures of interest (docking strands) are imaged using complementary DNA strands attached to a fluorescent dye (imager strand). Since there is no actual photoswitching of dyes, this technique is independent from the dye's photophysics, is less impacted by photobleaching and attains high multiplexing ability[163,185,186], including one of the best resolutions in SRM[187]. Due to controllable kinetics in DNA strand hybridization, quantification of molecules is possible using quantitative PAINT (qPAINT), an approach previously developed by Jungmann et al. on DNA origami[163].
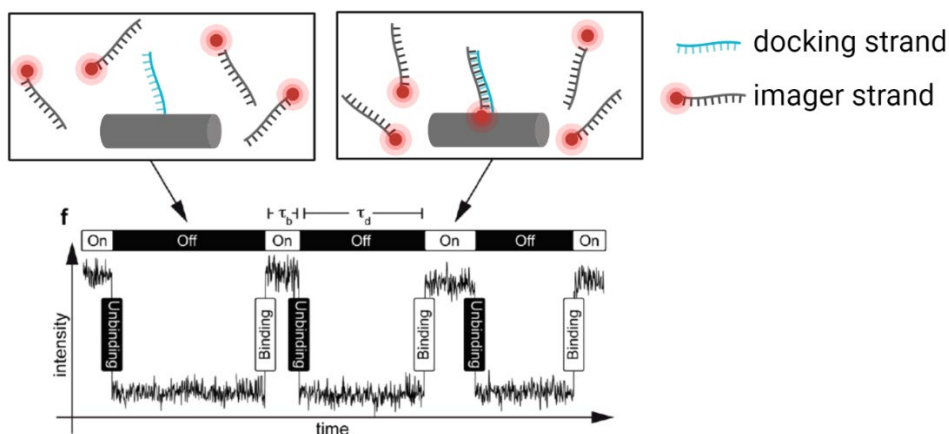
Figure 14 *The principles of DNA-PAINT. Single-stranded DNA (oligo/docking strand) is conjugated to structure of interest. Dye-labelled complementary single-stranded DNA (imager strand) is added in solution and leads to transient binding (DNA hybridization) with the docking strand. The transient binding is detected as "blinking" over a certain time trace. When in the bound state it is "on"/emitting fluorescence and when in the unbound state it is "off"/dark. Adapted from reference 166 with permission, copyright © 2010 American Chemical Society. Created with Biorender.com*

Delcanale et al. applied DNA-PAINT and qPAINT to quantify and map functional ligands on the surface of 330 nm streptavidin-coated carboxyl-polystyrene NPs. A high variability in the number of ligands/NPs was discovered, with a significant number of NPs exposing ligand numbers outside the Gaussian distributed population[188,189]. A similar approach was used to quantify functionalization of gold NPs for a range of ligand densities, observing just as in the previous example significant heterogeneity in functionalization[190]. These studies shine light on the particle-to-particle variations that

could affect the performance of functionalized NPs *in vivo*, and the importance of SMLM techniques as characterization methods in nanomedicine.

Indeed, SMLM techniques are revolutionary tools in nanomedicine unveiling the structure, dynamics and function of complex synthetic nanomaterials. Yet it is worth mentioning that the lack of fluorophores with minimal spectral overlap, particularly in *d*STORM, limits imaging of more than two simultaneous targets[191], preventing the localization of NPs in more than one specific location at a time. DNA-PAINT has been able to overcome this issue through the use of different sequences of docking strands, demonstrating 124-color imaging on DNA origami[185], and the application of eight color imaging in cells has been achieved[186]; however, these highly multiplexed experiments are limited by complicated labelling procedures, considerably long acquisition times (so fixed samples are used), sample penetration depth and low-throughput.

3. Electron microscopy

EM is an irreplaceable tool in the physicochemical and intracellular study of nanomaterials[146,192–195]. Compared to light microscopy, EM uses a beam of electrons rather than a beam of light, and since electrons have a shorter wavelength than visible light, this group of microscopes offer significantly improved resolutions[196]. Several EM techniques have been successfully applied in nanomedicine, including Scanning Electron Microscopy (SEM), cryo-EM and Transmission Electron Microscopy (TEM).

SEM is typically used for NP size and shape characterization. In this case, electrons interact with the sample to produce and reflect secondary electrons, backscattered electrons and characteristic X-rays. SEM offers 3D information and characterization of a nanomaterial's morphology and composition, but generally suffers of a lower resolution and inability to study material crystallinity or intracellular processes[197]. Cryo-EM offers the best preservation of biomaterials in a near-native frozen hydrated state, eliminating the need for chemical fixation or resin embedding, both of which can lead to loss of ultrastructure. Various methods exist to study nanomaterials with 2D cryo-TEM being the most common one to study virus-like NPs[198] and lipid-based NPs[199]; 3D cryo-TEM and cryo-Electron Tomography (cryo-ET) offer powerful alternatives to study 3D structures of complex structures such as icosahedral symmetries[198] but rely on heavy data processing and specialized equipment[148].

3.1. Transmission electron microscopy

In TEM an electromagnetic lens is used to focus electrons into a thin beam which is transmitted through an ultrathin sample (70-150nm); electrons then either scatter off the sample or pass through and hit a detector at the bottom of the microscope. The un-scattered electrons recreate an image of the footprint of the sample, with darker and brighter areas of the image representing that fewer or more electrons are transmitted through, respectively. Therefore, higher atomic mass/denser structures will be observed as darker since they absorb more electrons instead of allowing them to transmit through.

Thanks to its exquisite resolution, TEM has unmasked information on the morphology of various nanomaterials[106,107,200] and has become a standard technique in the material

characterization pipeline. Notably, it is simple to visualize inorganic nanoparticles such as gold NPs without any further staining, since they provide high contrast against the underlying supporting films found on TEM grids (e.g. carbon/formvar). However, organic nanomaterials require negative staining, in which a thin layer of heavy metals (e.g. uranyl acetate) is applied on top of the material, leading to a dark staining of surrounding regions, whilst the specimen itself is left unstained and its morphology is elucidated.

TEM has been widely used to study the fine relationships between NPs and cell/tissues, offering some of the most valuable information of uptake mechanisms[201] and intracellular voyage[146,193,202,203]. For example, TEM has been used to identify caveolin-mediated endocytosis as the main uptake pathway of polymeric coated gold NPs[204], and to quantify the amount of siRNA-conjugated colloidal gold NPs that escape from different endo-lysosomal compartments[193]. Plaza-GA et al. took inspiration from nature to functionalize gold NPs with a bacterial toxin, and demonstrated the formulation's endosomal escape properties using TEM[194], as seen in Figure 15. Furthermore, TEM allows the visualization of morphological changes within the cell such as shrinkage or swelling of mitochondria/endo-lysosomal compartments that are important hallmarks of cell damage, not easily detectable by light microscopy[205]. Markedly, the majority of cellular NP studies using TEM have been carried out on electron dense materials such as inorganic NPs (e.g. gold, silica, silver NPs, quantum dots)[136,194,206,207], since semi-transparent materials (e.g. polymeric/protein-based NPs) generally do not offer enough contrast to be accurately differentiated from the complex intracellular milieu.

Furthermore, it must be pointed out that dynamic changes cannot be studied since only fixed or frozen samples can be imaged. Since TEM requires thin, dehydrated samples, preparation of biological samples such as cells requires several stages, with various techniques and processes available, some of which can be exceptionally complicated. Typically, samples are first fixed, dehydrated and embedded in a resin, then sectioned into ultrathin sections of 70-150 nm thickness, before being contrasted with heavy metals and imaged[208]. Specificity is also a problem, making it difficult to distinguish between organic nanomaterials and cellular milieu.
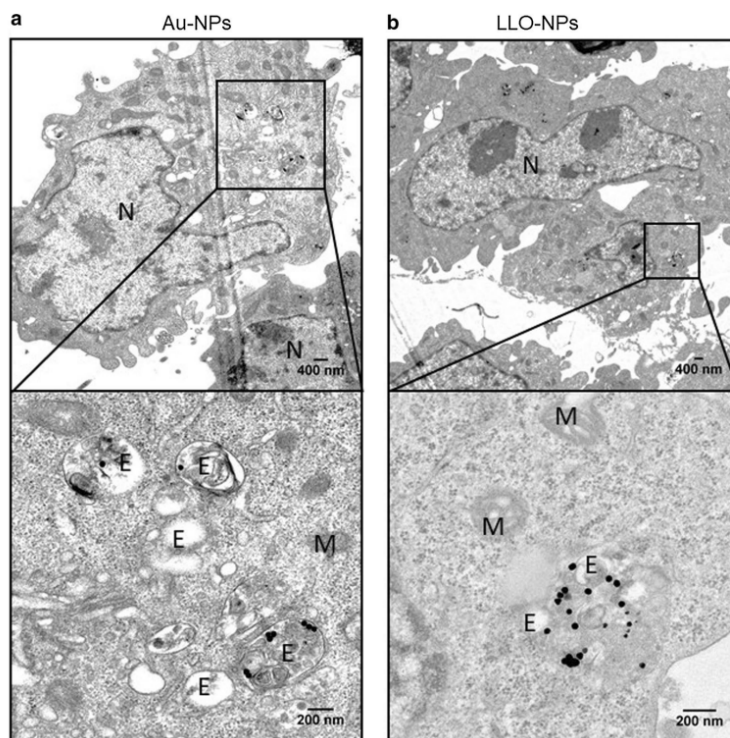
Figure 15 *TEM images of mouse embryonic fibroblasts (MEFs) incubated with a) gold NPs and b) with gold NPs functionalized with a bacterial protein. In b) the endosomal/lysosomal membrane is perforated because of the bacterial protein, allowing endosomal escape of the gold NPs. Bottom panels are zoomed in areas seen in top panels. Where N = nucleus, M = mitochondria and E = endosomes/lysosomes. Highlights the power in resolution of TEM to reliably identify nanomaterials within the cellular context. Reprinted from reference 194 with permission, copyright © 2019, Springer Nature, Ismael Plaza-GA et al.*

Advanced imaging techniques come with plenty of strengths but also weaknesses, and as such, a synergistic approach between different techniques would allow us to gain a much more comprehensive understanding of NP properties and biological behaviors.

4. Correlative Light and Electron Microscopy

As previously discussed, FM offers chemical specificity of molecules, multicolor imaging and ability to study biological processes. However, localization of molecules is not always straightforward due to many molecules remaining unlabeled, and multicolor imaging only allowing the detection of a couple of simultaneous targets/structures. Additionally, no information on ultrastructure can be gained, and the resolution of conventional FM does not provide detection of individual biomolecules or nanomaterials. A way to overcome the resolution gap is through SRM, but if ultrastructural content is needed, EM is the method of choice. EM however only offers analysis on grayscale images, making the detection of molecules cumbersome; biological samples are normally fixed and finding rare events in space and time is almost impossible.

Correlative light and electron microscopy (CLEM) are a group of techniques that integrate images of the same sample from both microscopies, overcoming their individual limitations by combing the strengths of the two imaging techniques, allowing the analysis of molecules in their cellular/morphological context[209,210]. In practice, CLEM protocols span to a variety of techniques, whereby FM can be wide-field, confocal, or SRM, whilst EM can expand to TEM, SEM, volume EM, cryo-EM and dark-field energy filtered TEM[211]. Due to the plethora of information that CLEM can provide, various advances in biology have been made such as the study of the segregation of chromosomes during cell division[212], membrane trafficking and organelle dynamics[213], , and identification of particle-rich cytoplasmic structures (PaCSs) in human disease[214].

A major limitation in conventional CLEM is the difference in resolution limits between the two microscopes. With the development of SRM, the resolution gap between FM and EM has narrowed, allowing molecular structures in cells to be imaged within the ultracellular context with unprecedented nanoscale resolution. Examples of established protocols include PALM-TEM for imaging intracellular fluorescent proteins[215], 3D interferometric PALM-SEM for studying organization of mitochondrial nucleoids[216] and STORM-TEM to track intracellular pathogens[168,217] (Figure 16).
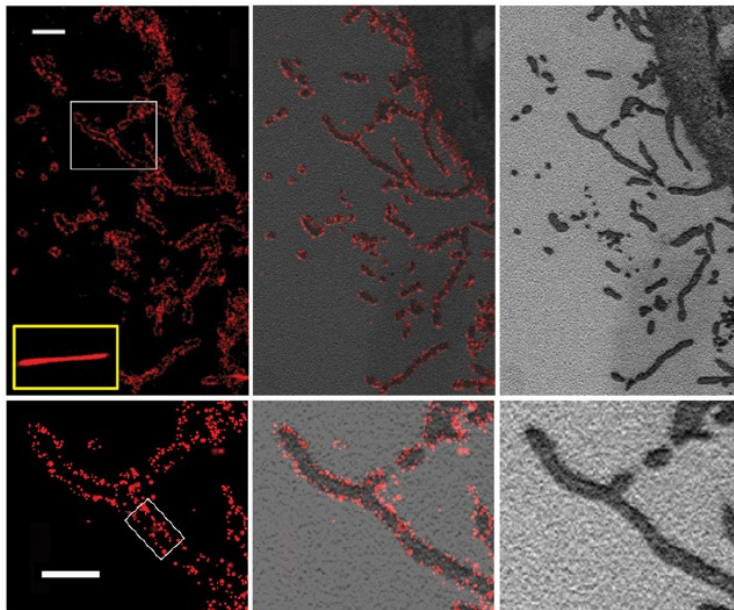
Figure 16 Correlative STORM and SEM images of resin-embedded sections of filamentous influenza viruses budding from infected cells[218]. Left panels show STORM only images, middle panel show correlative images and right panel SEM only images. Lower panels are zoom-in images of upper panels. Yellow box is a dSTORM image of an influenza virus filament, immuno-stained for haemagglutinin. Scale bars 500 nm. Figure adapted from reference 218 with permission, copyright © 2015 PLOS ONE.

4.1. Applications of CLEM in nanomedicine research

As we have previously seen, quality control that ensures the safety and effectiveness of nanomaterials requires their thorough and quantitative *in vitro* characterization at a

single particle level, and intracellular trafficking with detailed ultrastructure of the cell. Whilst advanced techniques such as TEM and SRM contribute greatly to this need, no single technique can achieve these tasks. The ability to combine the advantages of these two powerful techniques, whilst minimizing their individual weaknesses, opens many doors to better understanding and predicting nanomaterial properties and intracellular behaviors.

First, SRM-TEM correlative techniques could contribute with relevant information on the interplay between different physicochemical properties at a single particle level. However, no super-resolution CLEM protocols have been developed for this purpose. Secondly, it offers a means to specifically label a variety of nanomaterials and achieve high resolution analysis of their intracellular behavior within exquisite cellular context. At the start of writing this thesis only three articles using CLEM to study intracellular trafficking had been published. A 3-fold correlative microscopy approach between FM, SEM and ion beam analysis (IBA) was developed by Le Trequesser et al. to detect, track and quantify titanium dioxide NPs inside/outside of cells[219]. Han et al. developed a FM and energy-filtered TEM (EFTEM) correlative protocol with 3D tomography to allow the quantification of fluorescent nanodiamonds at a single particle level within different cellular compartments (Figure 17). Very recently and within the same research group, Frey et al. applied confocal laser scanning microscopy (CLSM)-TEM correlative microscopy to analyze protein-based nanocarriers intracellularly, demonstrating the relevance of CLEM in understanding metabolic pathways of nanocarriers[220]. Yet, it is important to note that no SRM-TEM protocols have been developed for nanomaterial tracking.
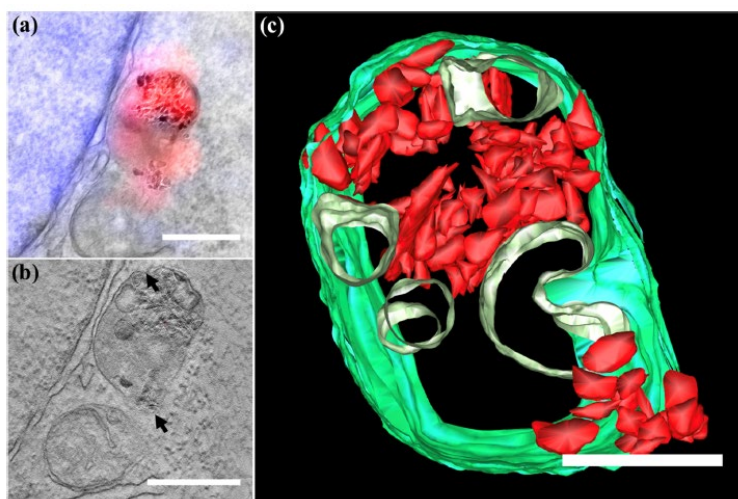
Figure 17 Correlative light and electron microscopy (CLEM) of fluorescent nanodiamonds (fNDs) in HeLa cells[221]. A) LM and TEM correlative microscopy image, whereby the localization of fNDs by LM is shown in red and cell nucleus appears in blue. B) Electron tomogram section of the same region where black arrows indicate the disappearance of endosomal membrane. C) 3D EM model of fNDs clusters inside endosomal vesicles, where fNDs appear in red and the cellular membrane is shown in green. Scale bar: (A,B) 500 nm and C) 250 nm. Reprinted from reference 221 with permission, copyright © 2019 American Chemical Society.

Whilst the aforementioned research clearly demonstrates the power of CLEM in understanding NP intracellular metabolism, only NPs visible by EM techniques were quantified; as such, a variety of NP formulations cannot be accurately analysed with these techniques. A main issue is that there is still a resolution gap between the FM and EM techniques used, preventing the assignment of fluorescently labelled single particles not visible in EM alone to specific compartments. We believe that there are still crucial unanswered questions in nanomedicine that could be answered using CLEM. To achieve this, it is necessary to go one step further and correlate the information given at a single particle and molecular level by SRM techniques such as DNA-PAINT and *d*STORM with the excellent morphological detail offered by TEM. We aim to develop such correlative techniques that can allow the nanomaterial community to a) better characterize nanocarriers at a single particle level and understand the interplay between different physicochemical parameters that govern nanoparticle behavior, and b) to track their intracellular distribution and thus better predict their efficacy and safety. Furthermore, due to the complexity of these correlative techniques, apart from describing the developed protocols and discussing the importance of the findings, another important objective will be to highlight some of the difficulties that arise from combining two different microscopies and to suggest how to overcome these, with the aim of guiding other scientists on how to apply these techniques to their own research.

Objectives

This Chapter summarizes the main objectives of this Thesis.

The **Introductory Chapter** highlights the promise that nanomedicine holds in treating various diseases, with a focus on cancer. However, despite the hype around this field in the last decades, the translation to the clinic has been relatively slow. Nanomedicine aims to increase the selective delivery of therapeutics to specific target sites such as a tumor, in turn improving the effectiveness of the encapsulated therapeutic and lowering its side effect profile. The ability of nanomaterials to act as effective and safe drug carriers relies on very specific physicochemical properties and biological behaviors that must be well controlled and studied. However, whilst the complexity of nanocarriers expands day by day, the types of methods used to accurately characterize their physicochemical properties and biological pathways remain generally the same as the ones used for small molecular entities. Yet, nanocarriers display intricate and complex characteristics as opposed to common therapeutics, which pose numerous problems to their efficacy and safety if not well understood. Some of these are mentioned in the main **Introduction** and include increased heterogeneity in crucial properties such as size and surface functionalization, and poor delivery of cargo to site of action due to intracellular barriers such as endosomal entrapment. There is currently a lack suitable techniques optimized to assess and quantify such parameters at a single particle level (rather than average values), to evaluate parameters in relation to each other, or track individual NPs within the intracellular milieu to understand their biological fate. In turn, this leads to poor clarification of regulatory standards for characterization of physicochemical properties and biological activity of nanomaterials. This is one of the main reasons why we are still seeing an unsatisfactory translation of nanocarriers from bench to clinic. To help fill part of this gap, we propose the development, optimization, and application of quantitative advanced imaging techniques such as SRM, TEM and CLEM to characterize, study and advance our understanding of nanocarriers more accurately. **Chapters 1 and 2** focus on the characterization of nanomaterials *in vitro*, whilst **Chapters 3 and 4** on the localization, quantification, and trafficking of nanomaterials within the cellular milieu.

In **Chapter 1** the main objective is to optimize and implement the novel DNA-PAINT technique for the quantification of ligand functionalization in various manually formulated PLGA-PEG formulations with increasing target group content. The aim is to first use DNA-PAINT and qPAINT to quantify the number of accessible functional ligands on the surface of these NPs and to account for interparticle heterogeneity in ligand functionalization. Using these results, we want to rationally redesign our current PLGA-PEG formulation as to achieve a greater exposure of accessible functional ligands.

In **Chapter 2**, the main objective is to develop, optimize and apply a super-resolution CLEM method consisting in the correlation of DNA-PAINT and TEM. Using this technique, the interplay between ligand functionalization and size at a single particle level will be studied, as well as the multiparametric heterogeneity between these two parameters in PLGA-PEG NPs. We further intend to show the advantage of our correlative technique as opposed to a one-method-at-a-time approach in studying NP sub-populations. Then finally to demonstrate the applicability of CLEM protocols in the characterization of other nanomaterials, such as supramolecular polymers.

In Chapter 3 the first main objective is to assess different *d*STORM-TEM CLEM protocols for biological samples, and to select and optimize a suitable protocol for the intracellular trafficking of PLGA-PEG NPs, with the goal of preserving cellular ultrastructure and fluorescence signal. The second objective is to use the optimized correlative protocol to quantify the distribution of NPs in different endo-lysosomal compartments at specific time points. Lastly, we aim to quantify the change in NP distribution (i.e. endosomal escape) upon the application of a lysomotropic agent.

In Chapter 4 the main objective is to apply the optimized *d*STORM-TEM correlative protocol in Chapter 3 for the intracellular trafficking of polyplexes. The aim is to quantify both polymer and cargo molecules using two color direct STORM and to track their specific location using TEM. Another objective is to quantify and compare the endosomal escape properties between two polyplexes with rationally designed polymeric backbones.

Chapter 1 | Quantifying the effect of PEG architecture on nanoparticle ligand availability using DNA-PAINT

This chapter reproduces almost literally the following published article:

Supportive information for this chapter can be found in Appendix 1.

Abstract: *The importance of PEG architecture on nanoparticle (NP) functionality is known but still difficult to investigate, especially at a single particle level. Here, we apply DNA Point Accumulation for Imaging in Nanoscale Topography (DNA-PAINT), a super-resolution microscopy (SRM) technique, to study the surface functionality in poly(lactide-co-glycolide)–poly(ethylene glycol) (PLGA–PEG) NPs with different PEG structures. We demonstrated how the length of the PEG spacer can influence the accessibility of surface chemical functionality, highlighting the importance of SRM techniques to support the rational design of functionalized NPs.*

1. Introduction

Nanomedicine aims to improve clinical outcomes and reduce the adverse side effects caused by the lack of selectivity for target tissues of small molecular drugs[1,222]. A popular strategy to achieve this aim is the tethering of functional moieties on the surface of nanoparticles (NPs), which improves the interaction between the drug delivery system and the target cells[78,223]. The grafting of targeting ligands to the surface of polymeric NPs is commonly implemented by using PEG as a spacer[224]. The hydrophilic nature of PEG also endows the formulation with "stealth" properties, reducing fouling by plasma proteins[225] and improving circulation times[226]. However, the architecture of PEG chains has been shown to influence the association of nanoparticles to their target receptors[227] and in turn their cellular uptake[228,229]. Notably, covering the surface of NPs with identical length PEG chains can reduce the ligand free motion and hinder the accessibility towards target receptors, whilst 'cocktail' PEGylation – where ligand-free shorter PEG chains and ligand-tethered longer PEG chains are covering the NP surface – can increase ligand mobility and improve its accessibility to target receptors, as well as maintaining stealth properties[227–230].

Despite the acknowledgement of this phenomenon, the effect of PEG architecture on ligand accessibility has mainly been studied with ensemble assays based on average population results. In a pioneering study using transmission electron microscopy (TEM) and antibody fragments conjugated to gold nanoparticles, the authors were able to map the accessible epitopes on the surface of NPs at a single-particle level[128]. Although TEM offers excellent resolution, quantification is limited by the density of ligands that can be quantified, and low throughput information that makes data analysis cumbersome.

Super-resolution microscopy (SRM) based on single-molecule localization (SMLM) techniques have demonstrated their superiority in the quantification of functional ligands[188,190,231], due to their nanoscale resolution (10-20 nm), molecular specificity and single-molecule sensitivity. DNA Point Accumulation for Imaging in Nanoscale Topography (DNA-PAINT) is a type of SMLM technique which offers various advantages over other microscopy techniques, such as greater multiplexing possibility[185,186], lower photobleaching rates and accurate molecule counting for a variety of functionalization densities[166,190]. Consequently, DNA-PAINT has been used to map functional ligands on the surface of polystyrene[188,189] and gold[190] NPs, exposing ligand distribution and heterogeneity on the NP surface. The exact number of functional ligands can be quantified using quantitative PAINT (qPAINT)[188,189], a technique initially developed for the quantification of docking strands in DNA origami[163].

In this work we used qPAINT to quantify the number of functional ligands on the surface of PLGA-PEG NPs and to study the role of spacer PEG length and target group content on their targeting ability. Finally, we studied the ligand availability (%) by comparing the number of available functional ligands quantified using qPAINT with the number calculated using commonly applied theoretical calculations. First, we formulated different NP formulations via the

nanoprecipitation method[232], by mixing PLGA, PLGA-PEG$_{5k}$-maleimide and PLGA-PEGx polymers, varying the amount of target group (maleimide) content and spacer PEG length in the PLGA-PEGx polymer (where x denotes molecular weight of 1k or 5k). Then, we conjugated the NPs to our model ligands - thiol-oligonucleotides (docking strands) – and quantitatively studied the number of available ligands and distribution using DNA-PAINT and qPAINT for the different formulations, highlighting marked heterogeneity within the formulations. Finally, we demonstrated at a single particle and molecular level how PEG architecture can influence ligand number and availability.

2. Results and Discussion

2.1. Nanoparticle formulation, ligand conjugation and characterization

A brief outline of the NP formulation and DNA-PAINT and qPAINT quantification protocols is given in Figure 1. NP were formulated manually via the nanoprecipitation method[232] by mixing of PLGA-PEG$_{5k}$, PLGA and PLGA-PEG$_{5k}$-Maleimide polymers with increasing maleimide content (10-100%) (1). Then they were conjugated with an excess of thiolated oligonucleotides (docking strands) via a thiol-maleimide reaction[233], which were used as DNA-PAINT probes and as a model for biological ligands (2).
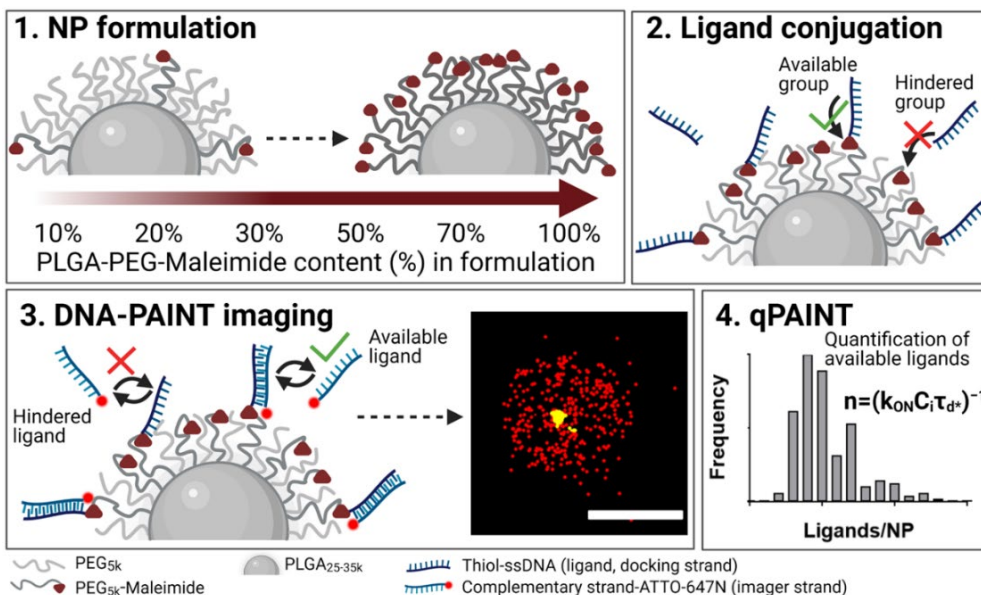
Figure 1 *Outline of DNA-PAINT and qPAINT protocol. (1) PLGA-PEG NPs were first formulated using varying maleimide contents (10-100%), then (2) functionalized by conjugation with a thiol-oligonucleotide (docking strand). (3) During DNA-PAINT imaging, complementary imager strands attached to ATTO-647N dye transiently bind and unbind to the available ligands on the NP surface, leading to the acquisition of a super-resolved image, whilst the hindered ligands are undetected. Red localizations are representative of ligands, and yellow of the encapsulated dye (DiI) used as a reference marker and drift corrector. Scale bar 100 nm. (4) qPAINT achieves quantification of the exact number of available ligands (n) by using the mean dark time between the binding events (τd*), the second-order association rate constant (kON) between the complementary strands, and the known concentration of imager strands (Ci) through the equation $n = (k_{ON}C_i\tau_{d^*})^{-1}$.*

Extensive NP characterization was carried out, including hydrodynamic diameter and polydispersity index (PdI) by DLS and zeta potential (ZP) measurements for surface charge for all formulations before ligand conjugation, immediately after conjugation and 7 days after conjugation, as shown in Figure 2. Control PLGA-PEG NPs were also formulated, without PLGA-PEG-Maleimide, but with the same PLGA ratio of 15%. Prior to conjugation the diameter was generally stable between all formulations, whilst after conjugation there was a slight increase with maleimide content. This increase could be caused by an increase in docking strands attached to the surface of the NPs with increased maleimide content. All formulations showed good stability, including after 7 days at 4 °C storage, as seen by the PdI values (less than 1) (Figure 2B). The ZP values were generally between -10 and -30 mV (Figure 2C), in range with previously reported values for PLGA-PEG NPs[234,235], suggesting colloidal stability of NPs in dispersion[236]. There was a slight decrease in ZP with maleimide content post-conjugation, which can be explained by the fact that docking strands are negatively charged due to their DNA nature, thus at higher maleimide contents a higher content of conjugated docking strands will lead to a decrease in ZP. For this reason, we also expected to see a decrease in ZP from pre to post conjugation, but this was not the case. We believe that this may be because the formulation of NPs is done in water whilst the conjugation is done in PBS; although ZP measurements are done in water, we believe that some PBS may remain near the NP surface, leading to a neutralization in ZP. Notably, the 20% maleimide batch was formulated on a different day to the rest of the formulations and could explain why it does not follow the general trend.
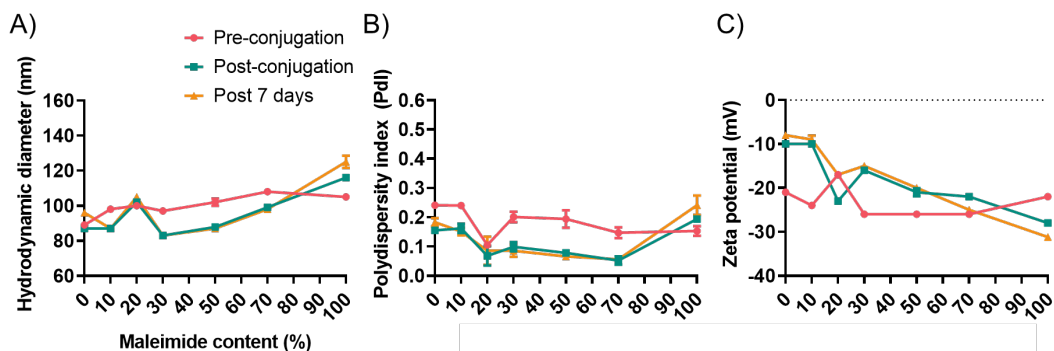
Figure 2 *Analysis of the A) hydrodynamic diameter (nm) and B) polydispersity index (PdI) by Dynamic Light Scattering and C) zeta potential (mV) using a Zetasizer Nano ZS (Malvern Panalytical) at 25°C in milliQ water pH 7.0 for the PLGA-PEG (PEG$_{5k}$) NP formulations (i) before conjugation, (ii) immediately after conjugation and (iii) 7 days after conjugation with functional ligands (docking strands). The diameter is given as the z-average (intensity). The standard deviation (+/-) for 3 repeats is given. See Materials and Methods for details on both maleimide and control NP formulations.*

Ligand conjugated NPs were also characterized by TEM, which offers size and morphological information at a single particle level as can be appreciated in Figure 3. Notably, since TEM requires samples to be under vacuum, NPs are imaged in a dry state with no interaction with the solvent, and hence their diameter is smaller as compared to the hydrodynamic diameter which is measured in solution.
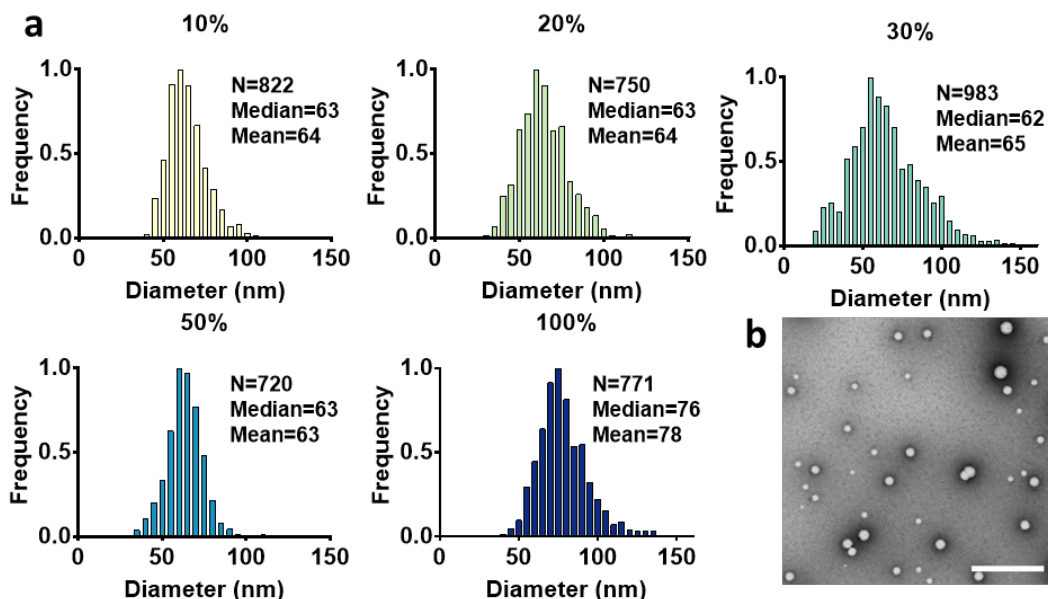
Figure 3 *a) Normalized frequency histograms of NP diameter (nm) from TEM images, of ligand-conjugated PLGA-PEG (PEG$_{5k}$) NPs with varying maleimide content (10, 20, 30, 50 and 100%). The number of NPs analyzed (N), and median and mean diameters are given for each. Bin widths=5 nm. b) TEM image representative of a 10% maleimide formulation (scale bar 500 nm).*

2.2. DNA-PAINT and qPAINT quantification protocols

After NP formulation and characterization, we then studied the availability of the conjugated functional ligands to the complementary imager strands using DNA-PAINT imaging[3] as depicted graphically in Figure 1 (3). During imaging, DNA hybridization mediates the transient binding and unbinding of the complementary imager strands to the docking strands. This allows the imaging and localization of single ligand molecules, depicted as red localizations in Figure 1 (3). An important aspect is that if the functional ligand is not properly exposed to the imager strands, it will not be available for detection and thus the localizations identified reveal the number of available functional ligands. It therefore offers useful information on orientation of functional ligands, which is of particular interest in more complex antibody approaches used for targeting and diagnostics, where wrong orientations can have detrimental effects on their activity[237–239].

Finally, whilst the number of localizations gives an estimation of the total number of ligands, the exact number can be quantified using qPAINT (4), which uses kinetic information based on the dark time between binding events to quantify available ligands. Specific parameters used are the mean dark time between the binding events (τ_{d^*}), the second-order association rate constant (k_{ON}) between the complementary strands, and the known concentration of imager strands (C_i) through the equation $n = (k_{ON}C_i\tau_{d^*})^{-1}$ [163]. The k_{ON} value relies on an experimental calibration, which is done by analyzing the reversible binding kinetics of one docking site (n=1) using a known concentration (C_i) as previously described[163,188]. To calculate the k_{ON} value, ideally the calibration is done on NPs

bearing one single active docking site. To achieve this, we formulated PLGA-PEG NPs with 1% maleimide content and conjugated them with a low docking strand concentration, whilst DNA-PAINT imaging was carried out using a higher than usual complementary imager strand concentration (10 nM) to improve the signal-to-noise ratio. Figure 4 shows an example NP chosen for calibration, where the docking site signal is shown in red and the DiI reference signal in green. Furthermore, the chosen NP shows a clearly identifiable localization cluster with a size of a few tens of nm consistent with that of a subdiffraction-sized docking site, found within the expected diameter of a NP. We chose NPs with clusters between 15-40 localizations, numbers above those expected from non-specific background signal as seen in our control experiments (Figure 5).

To obtain τ_{d*}, a cumulative distribution function (CDF) of individual dark times from calibration NPs was required which was fitted with an exponential model (Figure 4b). The respective k_{ON} was calculated as 2.3×10^6 M^{-1} s^{-1}, a value in agreement with those reported by Delcanale et al. on polystyrene NPs (3.3×10^6 M^{-1} s^{-1})[188]. Using the known k_{ON}, C_i and τ_{d*} values, we were then able to quantify the number of ligands per single NP, as described later.
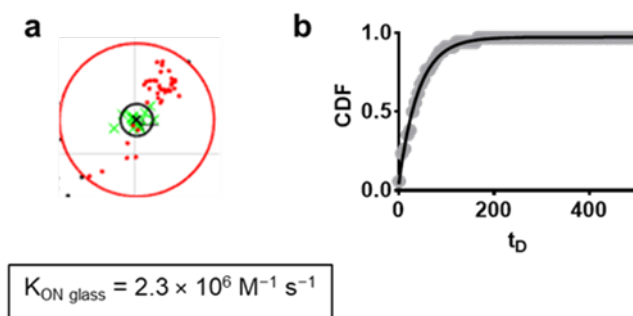
Figure 4 qPAINT calibration for PLGA-PEG NP imaging on glass. a) Representative PLGA-PEG NP used for the qPAINT calibration and b) corresponding cumulative distribution function (CDF) of individual dark times (t_D) obtained for the calibration NP (grey circles) and calculated kON value for glass measurement (2.3×10^6 M^{-1} s^{-1}). For calibration, NPs were loaded with approximately a single thiol-docking strand. DNA-PAINT localizations are seen in red and DiI in green. Analysis was done in MATLAB.

We also carried out two control experiments for our data, the first by using a non-complementary imager aimed to demonstrate that the DNA-hybridization between the docking and imager strand is specific, and the second control by imaging non-functional NPs using the correct imager aimed to demonstrate low non-specific attachment of imager strands to NPs. Both controls (Figure 5) show a much lower number of localizations compared to the experimental results in Figure 6, confirming the specificity of the method. Notably, DNA-PAINT offers a relatively high-throughput analysis, with 200-500 NPs analyzed per field of view, a clear advantage when compared to other single-particle microscopy techniques such as TEM.
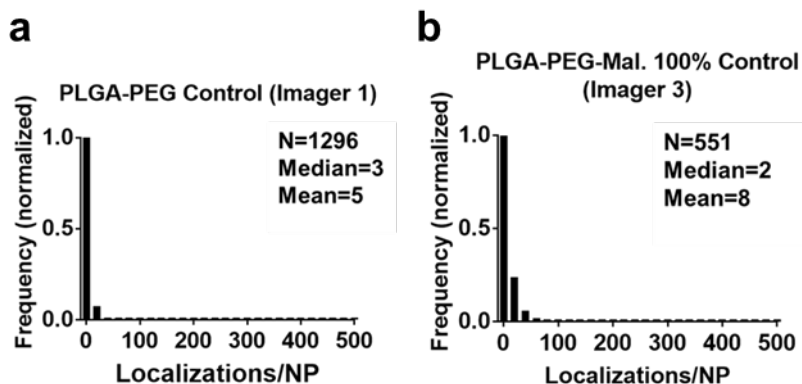
Figure 5 *a) Normalized frequency histograms of DNA-PAINT localizations for control PLGA-PEG (PEG$_{5k}$) NPs (with no maleimide content) after imaging with imager strand 1, and b) for PLGA-PEG (PEG$_{5k}$) NPs with 100% maleimide content after conjugation to functional ligands (docking strands) and imaging with imager strand 3 (non-complementary pairing). The number of nanoparticles analyzed (N), the median and mean number of localizations are also shown. The data were analyzed using MATLAB Software.*

Furthermore, since NPs are bound to a glass substrate, it is useful to know the amount of docking strands inaccessible to imager strands. Our group previously studied 330 nm polystyrene NPs by DNA-PAINT in 3D showing that the whole NP is clearly visible[188]. We also carried out a control experiment on PLGA-PEG NPs using longer docking strands and irreversible hybridization that showed only ~ 6% of conjugated docking strands to not be detected by the imager (Figure A1.1).

2.3. Ligand quantification using DNA-PAINT and qPAINT

Using the described protocol, we first showed DNA-PAINT and qPAINT results on the quantification of the number of available ligands per NP on 6 different PLGA-PEG NP formulations with increasing maleimide content (10-100%) and conjugated to an excess of functional ligand. Please note a constant time was kept between NP formulation and imaging for all formulations. Figure 6a shows a DNA-PAINT image of localizations clusters in red representative of surface ligand number. The localization clusters in yellow are illustrative of DiI dye encapsulated in the NPs, which was used for mechanical drift correction and as a reference for NP identification. In Figure 6b we observe images of representative NPs from each formulation, illustrating a visual increase in number of localizations with maleimide content, and thus an increase the number of conjugated ligands per NP. This demonstrates that DNA-PAINT can discriminate formulations with different contents of surface functionalization.

We then analyzed the x,y,t coordinates of the localizations using a previously described mean-shift clustering algorithm in MATLAB[188,189] and plotted the data of localizations/NP in frequency distribution graphs. The distributions showed a clear increase in localizations/NP with maleimide content but also an increase in the distribution width (i.e. heterogeneity), which is expected with greater target group contents. This emphasizes that the average number of ligands is not and should not be used as a representation of the whole NP population. Notably,

ligand conjugation and imager hybridization processes are both stochastic (random) in nature, therefore, ligand distributions should follow a Poisson distribution. However, what we observe are generally non-symmetrical (i.e. non-Poissonian) localization distributions. These results agree with previous results from Post et al. using *d*STORM quantification, whereby they found a negative binomial fit in ligand distribution and suggested this occurs due to additional heterogeneity[231]. Although the authors did not conclude the reasons for the overdispersion, we recently have recently attributed these results to an entanglement between ligand and size distribution using correlative microscopy[240], as will be explained in Chapter 2. In addition, we observed that for NPs with greater maleimide content the distributions tail towards higher localization numbers. As will be described later in Chapter 2, the sub-populations of NPs at the extreme right of the localization distributions generally represent NPs with larger than expected diameters.
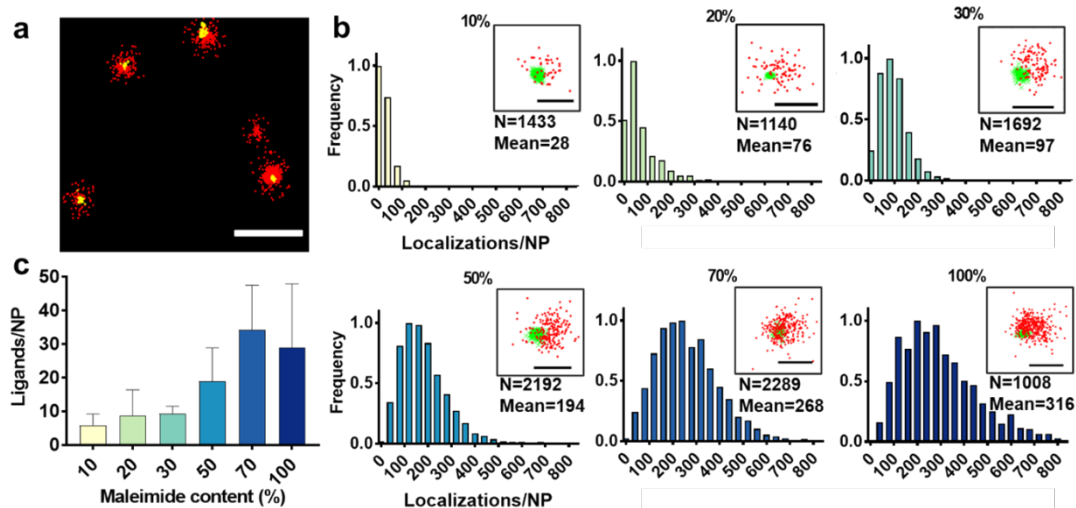
Figure 6 *a) Representative DNA-PAINT image of ligand-conjugated PLGA-PEG (PEG$_{5k}$) 50% maleimide NPs displaying the number of localizations (red) per NP (scale bar = 200 nm). The yellow signal is DiI dye encapsulated in NP, used for mechanical drift correction and as a reference in NP identification. b) Normalized frequency histograms of DNA-PAINT localizations for PLGA-PEG-Maleimide (PEG$_{5k}$) NP at various maleimide contents (10-100%), the number of NP analysed (N) and the mean number of localizations. Close-up images of representative NP for each formulation (scale bar = 100 nm), whereby DNA-PAINT localizations are seen in red and DiI in green. c) The number of available ligands/NP per formulation as retrieved by qPAINT. The data were analysed using MATLAB Software.*

We then counted the exact number of available ligands on the NP surface using the previously established method qPAINT[163,188,189]. Figure 6c illustrates a general increase in the quantified number of ligands per NP with maleimide content up to 70%, followed by a saturation in the number of ligands at 100% maleimide. Despite expected general increase in ligand number with maleimide content, unexpectedly low numbers of available ligands were observed for all formulations. For this reason, we next calculated the conjugation efficiency of our thiolated docking strands with the NPs.

We selected 3 formulations with maleimide contents typically used in literature (10%, 20% and 30%)[241] and calculated the docking strand conjugation efficiency (CE%) using spectrophotometry to be between 20-30% and confirmed the results by studying the CE% of a smaller molecule L-cysteine, with results between 40-50% (Table 1). For information on how CE% was calculated see Materials and Methods. Although the hydrophobic PLGA chains are assumed to form the core, and the hydrophilic PEG chains the outer layer, we expect that not all maleimide groups are be available for conjugation on the NP surface, since due to the miscibility of PEG and PLGA, some of the PEG-maleimide chains will be embedded in the NP core[241,242]. It has been shown that on average, only 50% of the maleimide groups are available for ligand conjugation[241], values which agree with our ligand CE% and L-cysteine assay results.

Table 1 Conjugation efficiency (CE%) of PLGA-PEG NPs (PEG$_{5k}$) formulations with varying maleimide content after conjugation with the thiolated docking strand and as comparison with the molecule L-Cysteine, to study maleimide availability. For protocol and calculations see Materials and Methods.

Formulation	Docking strand CE (%)	Cysteine CE (%)
PLGA-PEG-Mal. 10% (PEG$_{5k}$)	25	46
PLGA-PEG-Mal. 20% (PEG$_{5k}$)	21	41
PLGA-PEG-Mal. 30% (PEG$_{5k}$)	31	49

Then, as depicted in Table 2, average number of theoretical maleimide groups per NP per formulation was calculated, taking into account the potential number of ligands that could cover the surface of a NP, given its surface area and other relevant properties. Next, the average number of estimated ligands per NP (theoretical ligand number/NP) was calculated by considering the specific CE% values for each formulation. Finally, these values were compared with our qPAINT results. For all calculations see Materials and Methods. The experimental numbers were significantly lower than the estimated numbers e.g. 6 vs 77, 8 vs 129 and 9 vs 293 for 10%, 20% and 30% maleimide formulations, respectively. In addition to the issue of maleimide availability, it has also been reported that with increasing molecular weight (e.g. at 5 kDa), the PEG chain becomes more flexible[243], leading to conjugated ligands to be entangled in the PEG chains[244], a phenomenon which could explain the low numbers of quantified ligands compared to the expected numbers. This prompted us to analyze further the role of PEG length on the targeting ability of NPs.

Table 2 *Properties of PLGA-PEG NPs (PEG$_{5k}$) with varying maleimide content. For calculations of theoretical maleimide molecules/NP, CE%, theoretical ligand number/NP and ligand availability (%) see Material and Methods.*

Formulation	Diameter by TEM (nm)	Theoretical maleimide molecules/NP	CE (%)	Theoretical ligand number/NP	Quantified ligands by qPAINT
PLGA-PEG-Mal. 10% (PEG5k)	64 +/- 12	307	25	77	6
PLGA-PEG-Mal. 20% (PEG5k)	64+/- 15	612	21	129	8
PLGA-PEG-Mal. 30% (PEG5k)	65 +/- 23	962	31	293	9

PEG (typically 5 kDa[225]) is a common linker used for the tethering of target groups (e.g. maleimide) on the NP surface, and used as a spacer to improve formulation stability and to decrease the adsorption of serum proteins[225,245]. Despite this, it has been argued that the effect of PEG length on NP targeting ability must also be seriously considered[128,227,229,230,244,246]. Particularly, it has been shown that PEGylation of NPs with identical spacer and ligand-tethered chain lengths at higher molecular weights can lead to a reduced number of accessible tethered ligands on the NP surface[128,246], as well as reduced target receptor accessibility[227,229,230]. This phenomenon is thought to be due to hampered ligand free motion[227,229], as well as an increase in the flexibility of the PEG chain with increasing molecular weight[243] which can lead to entangling of surface ligands into the PEG chains[244].

We used DNA-PAINT and qPAINT to quantify at a single particle and molecular level the effect of spacer PEG chain length and on ligand availability. To this end, we tested the effect of substituting the 5 kDa PEG (PEG$_{5k}$) spacer chain in the PLGA-PEG$_{5k}$ polymer with a shorter 1 kDa PEG (PEG$_{1k}$) chain whilst maintaining the length of the PLGA and PLGA-PEG$_{5k}$-Maleimide strands unchanged, at 3 different maleimide concentrations (10, 20, 30%). Whilst the polydispersity index (Table A1.1) and TEM diameter (Figure A1.2) were similar to the PEG$_{5k}$ formulations, we did note an increase in the hydrodynamic diameter prior to and post conjugation in the new PEG$_{1k}$ NPs (Table A1.1). It has been suggested that longer PEG chains such as 5 kDa can entangle among each other via Van Der Waals forces and hydrogen bonding, leading to a reduction in the size of the outer layer and thus hydrodynamic radius, as compared to shorter PEG chains[229,247]. This effect would not be visible in TEM since the NP are in dry condition.

With this approach we wanted to promote the sticking out of the PEG brushes bearing the maleimide groups for an improved conjugation efficiency (CE%) with ligands (docking strands) and increased ligand availability to imager strands (graphically shown in Figure 7a). Using spectrophotometry, we found on average a 2-fold increase in CE% at all maleimide contents using the shorter PEG$_{1k}$ chains (Table A1.2). Using qPAINT, we observed on average a 7-fold increase at both 10% and 20% maleimide and a 3-fold increase at 30% maleimide contents in quantified ligands using the shorter PEG$_{1k}$ chains (Figure 7b, Table A1.2). For localization distributions and negative controls see Figure

A1.3. These results indicate that varying surface PEG chain lengths can improve the exposure of target groups (e.g. maleimide) which in turn improves conjugation efficiency to the ligand, and can enhance the exposure of conjugated functional ligands on the surface of NPs, which is expected to improve target cellular receptor recognition.
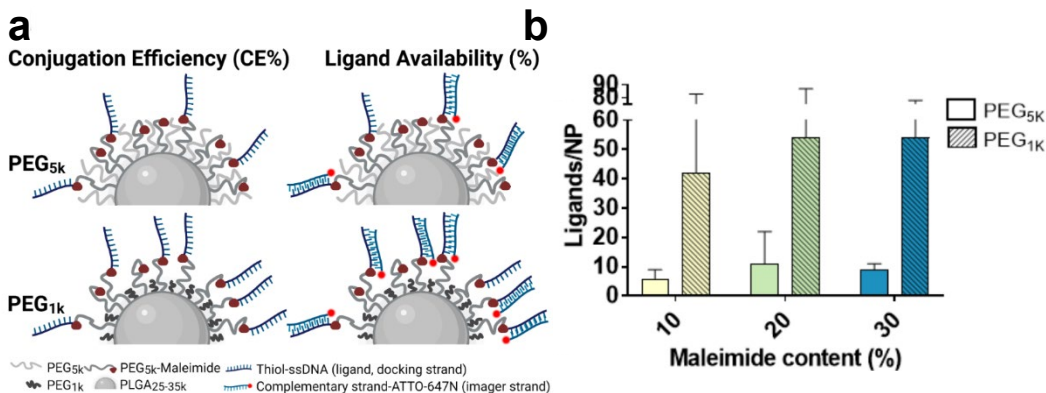
Figure 7 a) Schematic representation of the influence of spacer PEG chain length on the conjugation efficiency (CE%) and ligand availability (%) of PLGA-PEG NPs. Shorter PEG chains (PEG1k) are expected to achieve better CE% and imager availability due to improved maleimide and ligand free motion, and reduced flexibility and entanglement of PEG chains. b) Quantification of ligand number/NP by qPAINT with increasing maleimide content (10-30%) and varying spacer PEG chain length (PEG$_{5k}$ – blank, PEG$_{1k}$ – lined). Standard deviation bars are given for each formulation.

Lastly, we calculated the ligand availability (%) for each formulation by dividing the number of quantified ligands by qPAINT by the number of theoretical ligands (Table A1.2). A 3-fold average increase was found in ligand availability using the lower PEG$_{1k}$ chain, meaning that more docking strands were available in solution for binding with the imager strands. Notably, for both PEG$_{5k}$ and PEG$_{1k}$ ligand availability (%) was greater at lower maleimide contents. This is expected to be because at lower target group contents there are generally less conjugated ligands on the surface of the NPs, and therefore a reduced hindering effect, leading to an increase in ligand availability to imager strands/target receptors.

3. Conclusions

In summary, we demonstrated at a single-particle and single-molecule-level that ligand number and availability in polymeric NP could be greatly impacted by PEG architecture, with regular long PEG chain architecture causing entanglement of tethered groups and ligands within the polymeric chains. Still, although modification of PEG chain length generally improved ligand availability (maximum of 21% at 10% maleimide content), the overall picture is that the standard formulation method to conjugate functional ligands to polymeric NPs leads to NP with a low number of available ligands. Due to the unique single-particle and single-molecule properties and high-throughput capabilities of SMLM techniques, we strongly believe these results highlight their potential to

be used in the routine design, quality control and optimization of nanomaterials with improved biological efficacy.

4. Materials and Methods

Materials

Poly(lactide-co-glycolide)-methoxy-poly(ethylene glycol) GCW301 (Mw PLGA:PEG, 30:1 kDa, L:G in PLGA 50:50) was supplied from GenoTech. Poly(lactide-co-glycolide) AP082 acid endcap (PLGA, 50:50 LA:GA, Mw 25-35 kDa) and poly(lactide-co-glycolide)-poly(ethylene glycol) AK102 (Mw PLGA:PEG 30:5 kDa, L:G in PLGA 50:50) were purchased from PolySciTech. Poly(D,L-Lactide-co-glycolide)-poly(ethylene glycol)-Maleimide SKU 2794 (Mw PLGA:PEG:Maleimide 20:5:0.09707 kDa) was purchased from Nanosoft Biotechnology LLC. Tris(2-carboxyethyl) phosphine hydrochloride (TCEP, 0.5 M, pH 7.0) and Amicon Ultra-4 filters (regenerated cellulose, 100 kDa) were supplied from Merck Life Sciences. Acetonitrile (HPLC grade) was purchased from Carlo Erba Reagents.

Thiol-modified DNA strands (docking strands 1) and Atto647N-labelled DNA strands (imager strands 1 and 3) were designed and purchased from Integrated DNA Technologies. Docking strand 1 and imager strand 1 were used for DNA-PAINT imaging and qPAINT quantification of PLGA-PEG NPs, whilst docking strand 1 and imager strand 3 were used for control experiments. DNA strands were dissolved and stored in sterile TE buffer and used fresh. The DNA strands used have the following DNA sequences, and only 9 bases contribute to hybridization:

Docking strand 1: 3'ATC TAC ATA TT/thiol
Imager strand 1: 5'-CTA GAT GTA T/Atto647N/-3'
Imager strand 3: 5'-GTA ATG AAG A/Atto647N/-3'

Sterile phosphate-buffered saline PBS buffer pH = 7.4 was used for sample preparation. Buffer B which consists of 5 mM Tris-HCl, 10 mM $MgCl_2$, 1 mM EDTA, 0.05% Tween-20 pH=8 was used to dilute imager strands for DNA-PAINT imaging.

Nanoparticle formulation

PLGA-PEG NPs were formulated via the precipitation-solvent evaporation (nanoprecipitation) method according to literature[232] and to our previously reported data[240]. Briefly, 5 mg of polymers and 1.1 mM DiI (reference dye) were dissolved in 500 mL acetonitrile at room temperature. $PLGA_{25-35k}$ polymer was maintained at a ratio of 15% and mixed with $PLGA_{30k}$-PEG_{5k} (long PEG) or $PLGA_{30k}$-PEG_{1k} (short PEG) and $PLGA_{20k}$-PEG_{5k}-Maleimide polymers at alternating concentrations (10-100%). For example, for the PLGA-PEG 30% maleimide (PEG_{5k}) formulation: 75.0 mL PLGA from stock 10 mg/mL (0.75 mg), $PLGA_{30k}$-PEG_{5k} 152.8 mL from stock 18 mg/mL (2.75 mg), 100.0 mL $PLGA_{20k}$-PEG_{5k}-Maleimide from 15 mg/mL stock (1.5 mg) and 4.5 mL DiI from stock 10 mM (1.1 mM) were dissolved and made up to 500 mL with acetonitrile. The polymer solution was stirred at 200-300 rpm with a magnetic stirrer whilst milliQ water was pipetted at a 1:10 ratio (500 mL polymer solution is pipetted into 5 mL

milliQ water). Solvent extraction (evaporation) continued for 5 h under in a fume cupboard at room temperature. NPs were centrifugated and collected (Avanti J-26 XPI, rotor JA-14) using Amicon Ultra-4 filters according to manufacturer's instructions for 10 min at 5,000 x g at 20°C with milliQ water. NPs were stored in milliQ water at 10 mg/mL concentration at 4°C until further use. For the control PLGA-PEG (PEG$_{5k}$) formulation, no PLGA$_{20k}$-PEG$_{5k}$-Maleimide was added, the PLGA ratio was maintained at 15%, and PLGA$_{30k}$-PEG$_{5k}$ was increased to 85%. For the control PLGA-PEG (PEG$_{1k}$) formulation, no PLGA$_{20k}$-PEG$_{5k}$-Maleimide was added, however it was replaced with PLGA$_{30k}$-PEG$_{5k}$, whilst the PLGA ratio was maintained at 15%, and PLGA$_{30k}$-PEG$_{1k}$ varied depending on the formulation.

Conjugation to functional ligands (docking strands)

In order to remove the protective disulphide bonds on the thiol group of the docking strands, the reducing agent TCEP was used at a 10:1 molar excess compared to thiol[248]. Briefly, for a PLGA-PEG 30% maleimide formulation, 2.6 µL of 0.5 M TCEP and 116.6 µL of 1.1 mM thiol-docking strand were added to 380.9 µL PBS (pH=7.4) and allowed to stir for 20 min at room temperature. To prevent the re-formation of disulphide bonds[248], argon gas was bubbled inside the glass vial before closing the lid. Then, optimal conjugation was achieved by using a 3:1 molar ratio of thiol to maleimide. During the conjugation process, 500 µL of 10 mg/mL NP stock was added to the solution and mixed for an extra 2 h in the absence of oxygen. Unconjugated docking strands were separated via centrifugation using Amicon Ultra-4 filters as per filter instructions for 10 min at 5,000 x g (rcf) at 20°C with filtered milliQ water. NPs were stored in milliQ water at a concentration of 10mg/mL in the dark at 4°C.

DNA-PAINT chamber preparation

A 40 mL volume flow chamber was assembled from a glass microscopy slide (FisherBrand) and a coverslip (Corning Cover Gass, thickness 1 ½, 22 x 22mm), attached by double-sided tape. Prior to assembly, the coverslips were cleaned first with acetone, then with ethanol 96% for 10 min each by bath sonication, then dried under nitrogen flow. This process removes impurities and improves the NP retention on the coverslip. A 1000x dilution in PBS of the 10mg/ml NP stock was pipetted into the chamber, which was then turned upside down and allowed to adsorb for 20 min. PBS promotes the adsorption of NPs. Unattached NP were washed away with Buffer B. Finally, the chamber was filled with imaging buffer solution (Imager strand diluted in Buffer B to the required concentration) and sealed with nail varnish to avoid evaporation. An imager concentration of 5 nM and 2.5 nM was used for PLGA$_{30k}$-PEG$_{5k}$ and PLGA$_{30k}$-PEG$_{1k}$ respectively.

DNA-PAINT
DNA-PAINT imaging

Imaging was carried out with a Nikon N-STORM system configured for highly inclined and laminated optical sheet (HILO) imaging using a Perfect Focus System (PFS). Atto647N-Imager strand signal was collected using the 647 nm (160 mW) laser at 60% laser power and the DiI drift correction signal using the 561 nm laser (80 mW) at 2% laser power. No UV activation was required.

Fluorescence was collected using a Nikon 100x, 1.49 NA oil immersion objective and passed through a quadband pass dichroic filter (97335 Nikon). Images were acquired onto a 256 x 256-pixel region (pixel size 0.16 mm) of a Hamamatsu ORCA Flash 4.0 camera at 70 ms integration time. For the Atto647N-Imager strand 20,000 frames were acquired in the 647 channel and for the drift correction one frame was acquired every 100 frames in the 561 channel. The time taken for each image acquisition was ~ 25 min.

DNA-PAINT analysis

DNA-PAINT analysis on NPs was previously described by our group[188,189]. Briefly, A MATLAB script was used to count the number of localizations in the 647 channel and the 561 (DiI-fiducial marker) channel from the x,y,t coordinates of the txt files. Firstly, the localization clusters from the fiducial 561 channel were identified using a mean-shift clustering algorithm. These clusters were used to identify the center of each individual NP. A second filter was applied allowing the user to manually select specific parameters such as maximum size/minimum localizations per NP to filter out noise/aggregates/elongated shapes. In this case, the manually selected parameters were: minimum points=10, bandwidth=50, maximum particle diameter=160. Then, the localizations from the 647 channel found within a distance of 160 nm from the center of the NP were detected, and then the number and x,y,t coordinates of the localizations and diameter were calculated for each NP. The radius of each NP was estimated as the distance from the mass center making up 90% of the cluster localizations.

Drift Correction

This parameter was previously described in detail by our group[188,189]. Briefly, DiI was encapsulated within PLGA-PEG NPs as it is spectrally different to the dye used on the imager strand, allowing two channel acquisition for two reasons: 1) it allows the correction of the mechanical drift during image acquisition, 2) since the DiI dyes labelling the same NP are simultaneously emitting upon photoexcitation, the resulting clusters of DiI localizations in the reconstructed image correspond, with an uncertainty of a few tens of nm, to the center of the NP. This is an important parameter for further analysis, especially when few docking strands are available on the NP surface. Finally, the amount of DiI dyes per NP is rather low and there is no evidence that it significantly affects the docking−imager interaction. Thanks to the emission of DiI, the NPs themselves acted as subdiffraction-sized fiducial markers for the correction of the mechanical drift, without the need for introduction of additional probes. The low frequency (100 times lower than for imager strand excitation) and power of DiI excitation ensured negligible bleaching of the dyes during image acquisition. To obtain the multicolor images found in Fig. 1 and Fig. 2, the drift-corrected one-color images of the same field-of-view, acquired using different imager strands, were merged and aligned using ImageJ software, using the clusters of DiI localizations to align the centers of the single NPs.

qPAINT analysis

Data analysis for qPAINT on NPs was previously described by our group[188,189]. Briefly, the x,y,t coordinates of 647 localizations belonging to each NP was analyzed in MATLAB using a mean-shift cluster algorithm whereby the diameter and number of localizations was analyzed for each NP. A binary intensity versus time trace was created for each NP, assigning a value of 0 to the frames with 0 localizations and a value of 1 to the frames with one localization. The individual dark times were calculated for each NP, acquiring the corresponding CDF, then fitted with the exponential model and the value of the mean dark time τ_d* was extracted. The number of ligands per NP was quantified using the equation $n=(k_{ON}c_i\tau_{d*})^{-1}$ using k_{ON} to be $2.3 \times 10^6\,M^{-1}\,s^{-1}$ as previously calculated on PLGA-PEG NPs[240], and the known imager concentration, of 5 nM for PLGA-PEG (PEG_{5k}) NPs and 2.5 nM for PLGA-PEG (PEG_{1k}). Furthermore, linking is performed using the Nikon software, such that localizations in the very same position that are detected in 10 consecutive frames are counted as 1, while longer are rejected. Thus, if a binding event lasts longer than 1 frame and less than 10 it is counted as one. This affects ON-times but does not affect dark times and qPAINT.

TEM imaging

An in-house carbon-coated copper TEM grid (CF200-CU, 200 mesh, Electron Microscopy Sciences) was first treated using UV glow discharge for 30s using BAL-TEC CTA 005 Glow Discharge Unit to improve the attachment of NPs. Using a fine tweezer, the grid was placed on top of a 40 µL drop of NP solution (2mg/mL) (10mg/mL diluted x5 in MilliQ water) for 3 min for NP attachment. Please note NP solution was vortexed well before attachment to the grid to avoid aggregates. Then the grid was washed to remove impurities and unattached NPs on 40 µL MilliQ water drops for 1 min, 30 sec and 30 sec, then negatively stained using filtered uranyl acetate 2% (UA 2%, in MilliQ water) for 1 min. Excess UA was removed by tapping the edge of the grid on Whatman filter paper. The grid was then allowed to dry overnight in a desiccator. Next, the grid was imaged using a Jeol 1010 (Gatan, Japan) from the Electron Cryomicroscopy Unit from the CCiTUB, equipped with a tungsten cathode. Images were acquired at 80kV with a CCD Megaview 1k x 1k, with a magnification of x20 000-50 000. The NPs diameter was measured using ImageJ software.

Calculations for Table 1 and Table S2
Calculation of Conjugation Efficiency (CE%)

After conjugation of PLGA-PEG NPs to 3-fold molar excess of docking strands, the NP solution was spun down via centrifugation using a bench-top centrifuge (Eppendorf Microcentrifuge 5415 R Sigma-Aldrich) for 20 min at 16.1 x g (rcf) at 20°C leading to a NP pellet formation. The supernatant was collected, then spun down again and the process was repeated for 2 times more to the resulting supernatant until no pellet was observed. The negative control consisted of PLGA-PEG NPs (no maleimide) undergoing the conjugation process and centrifugation steps identically to the test NPs. The final supernatant solutions

were analyzed using a NanoDrop ND-1000 Spectrophotometer (at 260 nm) and the CE % was calculated as:

$$\left(1 - \frac{Thiol-oligo\ in\ Test\ supernatant\ (abs)}{Thiol-oligo\ in\ Control\ supernatant\ (abs)}\ x\ 3\right) x\ 100\%$$ (Equation 1)

Where x 3 denotes the 3-fold molar excess of docking strands compared to maleimide content.

Calculation of theoretical maleimide groups per NP:

Based on Spherotech's instructions[249]:

Calculating the number of particles in suspension:

$$\left(\frac{(6\ x\ Polymer\ Weight\ (g))}{(3.14\ x\ Polymer\ Density\left(\frac{g}{cm^3}\right) x\ NP\ Diameter\ (\text{um})^3}\right) x\ 10^{12}$$ (Equation 2)

Calculating the number of maleimide molecules in suspension:

$$\left(\frac{Polymer\ Mass\ (g)}{Polymer\ Molecular\ Weight\left(\frac{g}{mol}\right)}\right) x\ Avogadro's\ Number$$ (Equation 3)

Calculating the number of theoretical maleimide molecules per NP:

$$\frac{Number\ of\ Maleimide\ Molecules}{Number\ of\ Particles\ in\ Suspension}$$ (Equation 4)

Calculation of theoretical ligands per NP:

Theoretical number of maleimide molecules/NP x CE% (Equation 5)

Calculation of ligand availability (%):

$$\frac{Quantified\ ligands}{Theoretical\ number\ of\ ligands}\ x\ 100$$ (Equation 6)

Cysteine assay protocol and calculation:

NP were conjugated with x5 molar excess of L-Cysteine (Sigma Aldrich, MW=175.63 g/mol) in comparison to maleimide content, for 2h in PBS and at RT. under spinning conditions. Then, the NP solution was spun down via centrifugation (Eppendorf Microcentrifuge 5415 R Sigma-Aldrich) for 20 min at 16.1 x g (rcf) at 20°C leading to a NP pellet formation. The supernatant was collected, and the process was repeated on the supernatant for 2 times more until no pellet was observed. The negative control consisted of PLGA-PEG NP

(without maleimide) undergoing the conjugation process and centrifugation steps identically to the test NP. The final supernatant solutions were analyzed using Ellman's test as per manufacturer's instructions[250]. Each sample was then analyzed using a NanoDrop Spectrophotometer at 412 nm and using the molar extinction coefficient of TNB ($14,150$ M^{-1}cm^{-1}). The conjugation efficiency was calculated as per Equation 1 in Supplementary Information.

qPAINT calibration on grid and glass

For the calibration experiment, PLGA-PEG 1% maleimide NP were conjugated to thiol-docking strands 1 at a 1:1 molar ratio under the usual conditions and imaged with 10 nM and 20 nM imager 1 in Buffer B for glass and grid samples, respectively. Experiments were carried out according to a previously published protocol by our group[188], with some differences. Briefly, under TIR conditions using a 647 nm laser (~30 mW) 40% power for the excitation of imager strands; emission was detected in a 256 x 256-pixel region of the camera for 20 000 frames at a rate of 10 Hz (camera exposure time 100 ms); a 561 nm laser (~3 mW) power 2% was used for DiI excitation; one frame in the 561 channel was collected every 100 frames in the 647 channel. The time for acquisition of one image was roughly 30 min; temperature was controlled at 25°C. Firstly, the localization clusters from the fiducial 561 channel were identified using a mean-shift clustering algorithm. These clusters were used to identify the center of each individual NP, with an uncertainty of a few tens of nm from the center of the NP. Another filter was used allowing the user to select parameters to filter out noise/aggregates/elongated shapes. Then, the localizations from the 647 channel found within a distance of 120 nm from the center of the NP were detected, and then the number and x,y,t coordinates of the localizations and diameter were calculated for each NP. Using a qPAINT algorithm, a binary intensity time trace was reconstructed for each NP, designating a value of 0 to the frames without localizations and a value of 1 to the frames with 1 localization. Individual CDF were assigned per NP from individual dark times (corresponding to consecutive 0 values in the time trace), fitted with an exponential model $y(t) = 1 - Ae^{-t/\tau_d*}$. qPAINT uses kinetic information based on the mean dark time (τ_{d*}) between binding events to quantify accessible ligands, which is associated to the number of ligands (n) through the equation $n = (k_{ON}c_i\tau_{d*})^{-1}$. This requires a calibration to calculate the second-order association rate of the docking strand-imager strand pair (k_{ON}). Using PLGA-PEG 1% maleimide NP conjugated to thiol-docking strands at a known imager concentration (c_i) in Buffer B, we calculated the k_{ON} for the binding kinetics of a single docking strand to be 2.3×10^6 M^{-1} s^{-1} for glass measurements and 8.8×10^5 M^{-1} s^{-1} for grid measurements.

Chapter 2 | Correlating super-resolution microscopy and transmission electron microscopy reveals multiparametric heterogeneity in nanoparticles

This chapter reproduces almost literally the following published article:

*Andrian T, Delcanale P, Pujals S, Albertazzi L. **Correlating Super-Resolution Microscopy and Transmission Electron Microscopy Reveals Multiparametric Heterogeneity in Nanoparticles.** Nano Lett. 2021;21(12):5360-5368. As the first author of this paper, I performed all the experimental protocols, I contributed to protocol design, data analysis and manuscript writing. Dr. P. Delcanale was responsible for statistical analysis. All authors participated in the planning, writing, and correction of the written work.*

Supportive information for this chapter can be found in Appendix 2.

Abstract: *The functionalization of nanoparticles with functional moieties is a key strategy to achieve cell targeting in nanomedicine. The interplay between size and ligand number is crucial for the formulation performance and needs to be properly characterized to understand nanoparticle structure−activity relations. However, there is a lack of methods able to measure both size and ligand number at the same time and at the single particle level. Here, we address this issue by introducing a correlative light and electron microscopy (CLEM) method combining super-resolution microscopy (SRM) and transmission electron microscopy (TEM) imaging. We apply our super-resolution CLEM method to characterize the relationship between size and ligand number and density in PLGA−PEG nanoparticles. We highlight how heterogeneity found in size can impact ligand distribution and how a significant part of the nanoparticle population goes completely undetected in the single-technique analysis. This protocol holds great promise for the multiparametric analysis of other parameters and nanomaterials.*

1. Introduction

The field of nanomedicine is rapidly expanding in light of its expected impact on health care[1,50,251]. Nanoparticles (NPs) conjugated with functional ligands have been developed for various applications, including imaging and diagnosis[252,253], and targeted drug delivery[80,254]. Yet, despite many optimization efforts, only a small fraction of the injected dose has shown to reach the target site[144], exposing the gap in our understanding of how the properties of ligand functionalized NPs can affect their biological responses. Common methods to characterize ligand functionalized NPs rely on average results, which do not provide an accurate picture of the material at a single-particle level, and generally underestimate the magnitude of heterogeneity in ligand number and distribution[130].

It is particularly important to study the heterogeneity in size and functional ligand distribution as they are the main determinants of the formulation's *in vivo* fate. As previously described in the **Introduction** of this thesis, firstly, NP size is a major determinant of cellular uptake[255,256], blood circulation half-life[93,257], biodistribution[95,96], tumor permeability[97] and immune response[98]. Secondly, the functionalization of NP surface with targeting ligands is the most used strategy to achieve tissue and cell-selective delivery of drug carriers through the recognition of biomarkers on the cell surface. In this context, ligand number, affinity and distribution govern the NP biodistribution, cell selectivity and internalization and as a consequence its therapeutic efficiency[258,259].

Size is generally characterized by dynamic light scattering (DLS), whilst electron microscopy (EM) and atomic force microscopy (AFM) are used to reinforce the results as they can provide direct characterization of the size distribution and morphology of nanomaterials at the single particle level[192,260,261]. On the contrary, quantification of ligand numbers and ligand distribution proves to be more challenging and it is often carried out with indirect assays based on averaged values which mask the heterogeneity in a nanoparticle formulation[129,130,133]. Moreover, analysis at a single particle level with high throughput is still suffering from a lack of accurate and standardized techniques[129].

Recently, super-resolution microscopy (SRM) techniques based on single-molecule localization (SMLM) have been used for the analysis and quantification of synthetic nanomaterials *in vitro* and within cells[183,188,262–264], as well of functional ligands[188,190,231], thanks to their superior resolution (10-20 nm), molecular specificity and sensitivity[179]. DNA Points Accumulation for Imaging in Nanoscale Topography (DNA-PAINT), a type of SMLM technique[166], can be used to quantify single molecules (i.e. molecular counting) and achieves high multiplexing, low photobleaching and is accurate for a wide range of functionalization densities[166,265]. It been applied to map the functional sites on the surface of polystyrene NPs, and to explore the spatial distribution and surface heterogeneity of the active sites on their surface[188]. In **Chapter 1** of this thesis, we have applied this technique to quantify functional ligands on the surface of PLGA-PEG NPs, and to make rational decisions on their surface architecture design to improve ligand availability[266]. Quantitative PAINT (qPAINT) - a technique originally used to quantify docking strands in DNA origami[163] - can quantify the exact number of

functional ligands on the surface of NPs[188–190,266], highlighting the applicability of SMLM in nanomedicine research.

Still, despite the advances in SRM that allow us to characterize NPs at a single particle level, we are only able to study the population of NPs that are labelled and thus lose information on NP size and morphology. Consequently, the relationship between various physiochemical properties (i.e. multiparametric) such as size and ligand number and distribution remains unclear. Although it is good practice to characterize samples with multiple techniques, a correlation between individual physiochemical parameters and biological performance cannot be made. As such, we lose important information on the entanglement between different physicochemical parameters[267,268].

Correlative light and electron microscopy (CLEM) are a powerful and well-established group of multimodal imaging systems that combine the benefits of both microscopies through detailed images of the same region[209]. CLEM has proved its potential in structural biology[211,215,217,218,269,270] and recently to track specific NPs intracellularly[220,221], but to the best of our knowledge, it has not yet been explored for the structural characterization of nanomaterials. To address this issue, we have developed a correlative super-resolution microscopy (SRM) and transmission electron microscopy (TEM) (super-resolution CLEM) method. It combines the ability of SRM to quantify the number of surface ligands, with the potential of TEM to characterize the size and morphology with nanometric precision and at a single particle level.

Here, we propose a super-resolution CLEM workflow for the characterization of functionalized polymeric poly(lactide-co-glycolide)-poly(ethylene glycol) PLGA-PEG NPs. Polymeric NPs have been applied in targeted drug delivery systems due to their biocompatibility, biodegradability, and general ease in surface customization[271–273]. A common strategy for surface grafting of NPs with targeting ligands is by surface modification with the spacer PEG[274], which also offers stealth behavior[275,276]. In **Chapter 1** of this thesis, we demonstrated using DNA-PAINT that a 'cocktail' PEGylation of PLGA-PEG NPs – where ligand-free shorter PEG chains and ligand-tethered longer PEG chains are covering the NP surface – improves the functional ligand availability. For this reason, we formulate NPs via the nanoprecipitation method[232] consisting of PLGA, PLGA-PEG$_{5k}$-maleimide and PLGA-PEG$_{1k}$ polymers, using the 'cocktail' PEGylation approach. Then, we functionalized PLGA-PEG$_{5k}$-maleimide chains to thiol-oligonucleotide ligands (model ligand) *via* a maleimide-thiol conjugation, a conjugation approach that provides high reactivity and good final stability under most conditions[241,277,278].

We first described our super-resolution CLEM method and its applicability in investigating the relationship between ligand number, ligand distribution and ligand density versus size, at a single-particle level and with nanometric resolution. We surprisingly discovered the presence of a large population of NPs with no ligands on their surface, as well as 'invisible NPs' that go undetected by DNA-PAINT imaging alone. Finally, we quantified the amount of accessible surface ligands per particle using our multiparametric correlative method and demonstrate its advantage over a one-method-at-a-time approach. The applicability of our correlative method spans to a plethora of other different nanomaterials, with the only requirement being the attachment of docking strands to the ligands of interest, although other DNA-free

PAINT approaches could also be used[279,280]. Therefore, our approach holds great promise for the multiparametric analysis of various other parameters and nanomaterials.

2. Results and Discussion
2.1 Introducing super-resolution CLEM methodology

Our super-resolution CLEM method is outlined in Figure 1 and extra information can be found in Figure A2.1 and in the Materials and Methods. Briefly, polymeric NPs were formulated manually via the nanoprecipitation method[232] using combinations of PLGA-PEG_{1k}, PLGA and PLGA-PEG_{5k}-maleimide polymers (1). Then, NPs were conjugated to functional ligands through a thiol-maleimide reaction[233,241]. The ligand consisted of a thiol group conjugated to a short (9 bases) oligonucleotide strand (i.e. docking strand) (2). The NPs were attached to a carbon-coated copper TEM grid previously treated with UV glow discharge and prepared into a glass imaging chamber. Then, a complementary oligonucleotide strand labeled with Atto-647N (i.e. imager strand) was flown into the chamber (3). To relocate the region of interest (ROI) later in TEM, we collected large field-of-view (FOV) bright field (BF) images of the grid to distinguish its orientation (4). In DNA-PAINT imaging, DNA hybridization drives the transient binding of the imager strands to the docking strands on the surface of the NPs, leading to fluorescence signal and localization of single molecules over thousands of frames[166] (5). After image acquisition, space-time coordinates of individual molecules were analyzed to precisely quantify the number of available surface ligands per NP through the quantitative PAINT method (qPAINT)[163,188,190], as thoroughly described in Chapter 3 (6). Following negative staining with 2% uranyl acetate, the grid was transferred to TEM, for size analysis and morphological inspection. Using the reference images, the ROI was established and sequentially imaged, since the FOV in TEM is smaller due to its higher resolution. Then the sequential images were stitched manually in Adobe Photoshop to create a 'TEM canvas' of the ROI (7). Then, the SRM image was scaled and rotated to match the size and orientation of the TEM stitched image, and manually correlated to obtain a TEM canvas with overlapping clusters of localizations per single particle (8). The number of surface ligands as quantified by qPAINT and size of each NP as analysed by TEM was correlated at a single-particle level (9).

1 - NP formulation
2 - Tagging ligands with DNA
3 - TEM grid and chamber preparation
4 - Reference acquisition
5 - DNA-PAINT imaging
6 - Ligand quantification by qPAINT
7 - TEM imaging, stitching and size quantification
8 - Image correlation
9 - Size and ligand correlation

no. ligands=39   diameter=89 nm

PEG1k
PEG5k-Maleimide
Docking strand (thiol-DNA oligonucleotide, ligand)
Imager strand (complementary strand + Atto647N Dye)

Figure 1 Overview of the super-resolution CLEM method. Formulation of PLGA-PEG NPs via nanoprecipitation (1). Conjugation of NP maleimide groups to thiol-DNA 9-mer oligonucleotides (docking strands) acting as functional ligands (2). NPs are attached to a TEM grid, which is assembled into a chamber, followed by flow of complementary imager strand buffer solution (3). A reference image of the region of interest (ROI) is taken using a stitching function (4). Then the DNA-PAINT image is acquired, through transient binding and unbinding of the complementary imager strands attached to ATTO-647-N fluorophore (5). The txt. file consisting of the x,y,t localizations coordinates is extracted and analyzed into number of localizations per NP. The exact number of available ligands is quantified using qPAINT analysis (6). For TEM imaging, the NP-coated TEM grids are negatively stained, then the ROI is imaged sequentially. The sequential images are manually stitched, and NP size can be quantified (7). DNA-PAINT and TEM images are correlated manually (8). Size and ligand number are quantified and correlated at a single-particle level (9). Schematic NP and arrow in (9) were created with BioRender.com.

2.2 Characterization of NPs at a single-particle level

We first tackled the characterization of PLGA-PEG NPs with DNA-PAINT and TEM separately. We formulated NPs with 5% and 30% maleimide content and conjugated them to an excess of ligand and used DNA-PAINT and qPAINT to quantify and analyze the ligand number and distribution. For further characterization see Tables A2.1 (DLS), and Figure A2.2 (ZP). To demonstrate that the DNA-hybridization is specific between

the docking strand and imager strand we carried out control experiments whereby the formulations were imaged under the same conditions using non-complementary imager strands (Figure A2.3). Furthermore, to accurately quantify ligand numbers by qPAINT, we recalculated the k_{ON} value from **Chapter 1** for 'on-grid' measurements, to account for any changes in binding events on the TEM grid compared to a glass substrate (Figure A2.4).

Figure 2A shows a reconstructed DNA-PAINT image where the functional groups are represented as red localizations, and the encapsulated reference DiI dye as yellow localizations. Notably, NPs without the corresponding DiI signal get disregarded as since they correspond to unspecific signal in the MATLAB algorithm used for NP analysis, as described in Materials and Methods. Interparticle heterogeneity in surface ligand distribution was found, as can be seen by the distinct number of localization events between different NPs. Figure 2B and Figure 2C present quantification of the number of localizations/NP by DNA-PAINT and the average number of ligands per NP by qPAINT, for formulations with 5% and 30% maleimide content, respectively. Since a higher number of localizations ligands were quantified for the 30% maleimide formulation, these results reflect the expected increase in relation between maleimide content and number of ligands conjugated to the surface of the NPs.
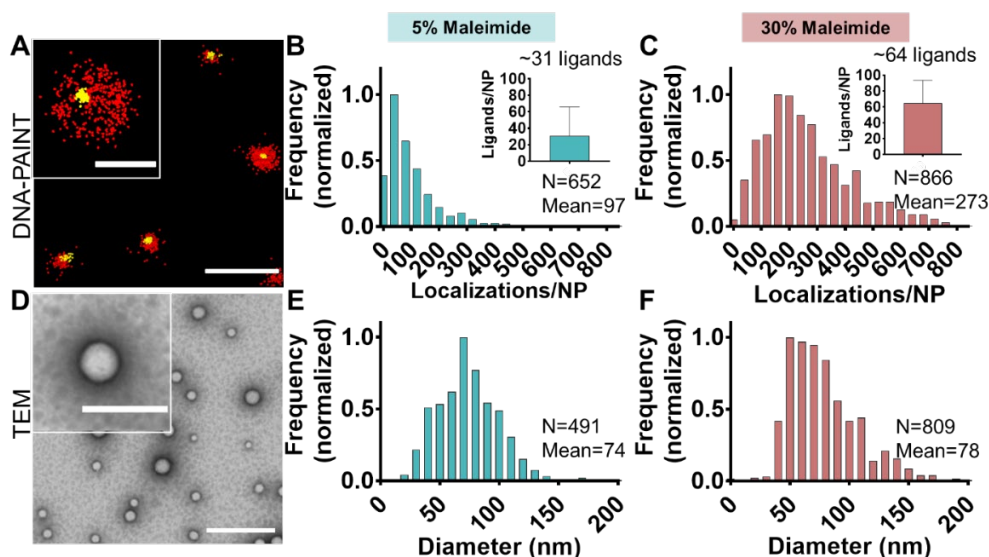
Figure 2 *Characterization of localization distribution and ligand number and diameters for PLGA-PEG nanoparticles conjugated to thiol-docking strands using DNA-PAINT and TEM. A) DNA-PAINT images of PLGA-PEG 30% maleimide NPs in a large field (scale bar 1000 nm) and a small field (upper left, scale bar 100 nm). DNA-PAINT localizations are shown in red and DiI signal used for drift correction and as a reference in yellow. Normalized frequency histograms of DNA-PAINT localizations per NP for B) PLGA-PEG 5% and C) 30% maleimide formulations, including the number of NPs analyzed (N) and the mean number of localizations per NP (Mean), as well as a bar graph depicting the number of ligands per NP quantified with qPAINT, and the average number of ligands per NP. Bin widths=40. D) Transmission Electron Microscopy (TEM) images of PLGA-PEG (30% maleimide) NPs a large field (scale bar 1000 nm) and a small field (upper left, scale bar 200 nm). Normalized frequency histograms of NP diameter (nm) for E) PLGA-PEG 5% and F) 30% maleimide formulations, including the number of NPs analyzed (N) and mean diameter in nm (Mean). Bin width=10.*

A non-symmetrical and broader distribution (i.e. more heterogeneous) is observed at the 30% maleimide content compared to 5%. By calculating the coefficient of variation (CV) of number of localizations per NP, we found that NPs formulated in the same way and in the same batch display a number of localizations that spans by 60-90% from the mean value, highlighting marked ligand heterogeneity in these formulations (Figure A2.5). It must be noted that manual bulk mixing methods for NP formulation are inherently prone to heterogeneity in both size and surface functionalization[129], since the mixing of the polymer solution and antisolvent phase is not homogeneous. Advances in formulation such as by microfluidic and Particle replication in non-wetting templates (PRINT) technologies offer more precise control over NP composition and size[106,135,281], and would indeed offer interesting comparisons in these studies.

Notably, DNA-PAINT is a fully random process, as the DNA strand molecules in solution have equal probability to attach to a complementary strand on a NP[231]. The conjugation process of ligands to maleimide groups on NP surface is also expected to be stochastic (Poissonian), unlike the distributions observed here. A possible reason is that the stochastic process of ligand conjugation is entangled with other parameters, such as size, resulting in non-Poissonian distributions. We therefore used TEM to study NP size heterogeneity. A typical TEM image depicting PLGA-PEG NPs is seen in Figure 2D. Figure 2E and Figure 2F show the distributions in diameter at a single-particle level for the PLGA-PEG 5% and 30% formulations, respectively. Although a nearly symmetrical distribution is seen for particles formulated with 5% maleimide content, at 30% we observe a more heterogeneous distribution, similar to that observed in localizations/NP with DNA-PAINT.

Observing heterogeneity in both size and functional ligands, we next correlated DNA-PAINT with TEM images to identify a possible relationship between NP size and the ligand functionalization at a single particle level.

2.3 Multiparametric characterization of NPs using super-resolution CLEM

In Figure 3, we introduced a representative correlative image obtained using the proposed super-resolution CLEM method on ligand conjugated PLGA-PEG NPs. We first obtained a DNA-PAINT image (Figure 3A) prior to sample preparation required for TEM, to preserve the surface docking strands intact for the hybridization with the complementary imaging strands. In this image, particles are visible as red clusters of localizations – representative of the number of surface ligands - with an appreciable heterogeneity among them. Then, a TEM image was acquired on the same field of view (Figure 3B), clearly highlighting NPs of different sizes. The merging of these two images results in the final super-resolution CLEM image (Figure 3C), which allowed us to make two important qualitative observations: a marked heterogeneity in both number of localizations and size per NP, and the presence of particles without the reference DiI signal, that would otherwise be invisible to DNA-PAINT imaging alone (i.e. 'invisible particles').

Furthermore, we used highly inclined and laminated optical sheet (HILO) as the mode of imaging in DNA-PAINT that results in a greater imaging depth than total internal

reflection fluorescence (TIRF) mode. This is necessary to be able to image NPs that are on the surface of a TEM grid and not directly on a glass slide.
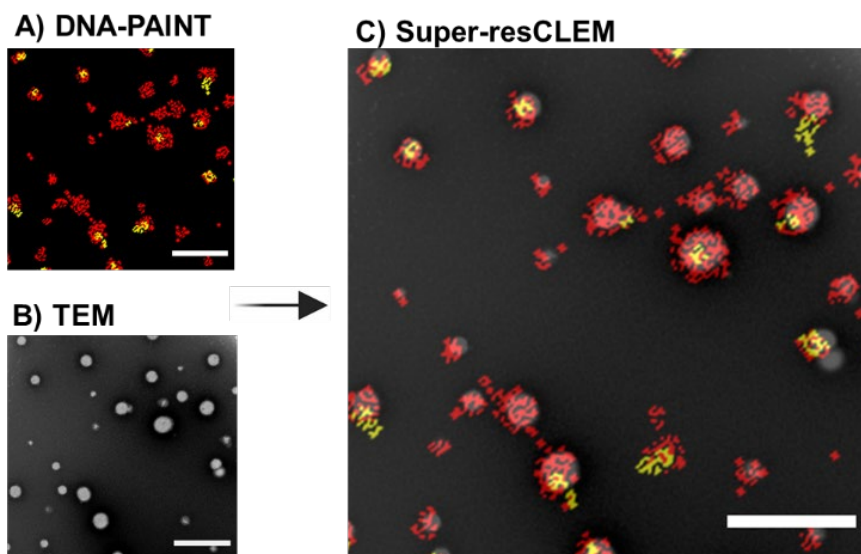
Figure 3 *Correlative DNA-PAINT and TEM (super-resolution CLEM) image of PLGA-PEG NPs. A) DNA-PAINT image where red localizations are representative of ligand number and yellow localizations of encapsulated DiI dye used as a reference marker and B) TEM image, both corresponding to the same PLGA-PEG 30% maleimide NPs. C) Overlaid super-resolution CLEM image. NPs without the reference DiI signal ('invisible particles') would be discarded in DNA-PAINT imaging alone. All scale bars=500 nm. For details of image acquisition and data analysis see Materials and Methods. Arrow was created with BioRender.com.*

Using the correlative images for both 5% and 30% formulations (Figures 4A and 4B, respectively), we studied the relationship between the number of ligands per NP versus TEM diameter at a single particle level for both formulations (Figure 4C and 4F, respectively). By observing these scatterplots – where every NP is one cross – we saw that the number of surface ligands per NP increased exponentially with increasing NP size, but also that both formulations displayed heterogeneity in the trend as shown by the broad data clouds. To better understand the trend, particles were binned according to their diameter and the average ligand number was obtained for particles within each bin (Figure 4C and 4F, black circles). The obtained averaged data were well fitted with a power model (grey line). The results demonstrated that the number of ligands per NP increased roughly as a power of 2 (1.8 for 5% and 2.5 for 30% maleimide formulations) with increasing diameter. This suggests that the number of ligands is directly proportional to the area of a particle, approximated as a sphere. Although the averaged bins clearly followed the power law, the single particle data (i.e. the crosses) showed a much broader relationship, notably, with more heterogeneity observed for NPs with 30% maleimide content and greater than 120 nm in diameter. For more statistical information see Figure A2.6. Next, we plotted a scatter graph of ligand density per NP versus diameter for both formulations. At 5% maleimide (Figure 4D), NPs with diameters between 50-120 nm showed the expected trend between these parameters i.e. the number of ligands per μm^2 does not generally change with diameter. A similar trend is observed at 30% maleimide (Figure 4G) albeit with a much

broader heterogeneity, particularly for diameters >120 nm. In both formulations we also observed a cloud of NPs with 0 ligand density for nearly all NP sizes.
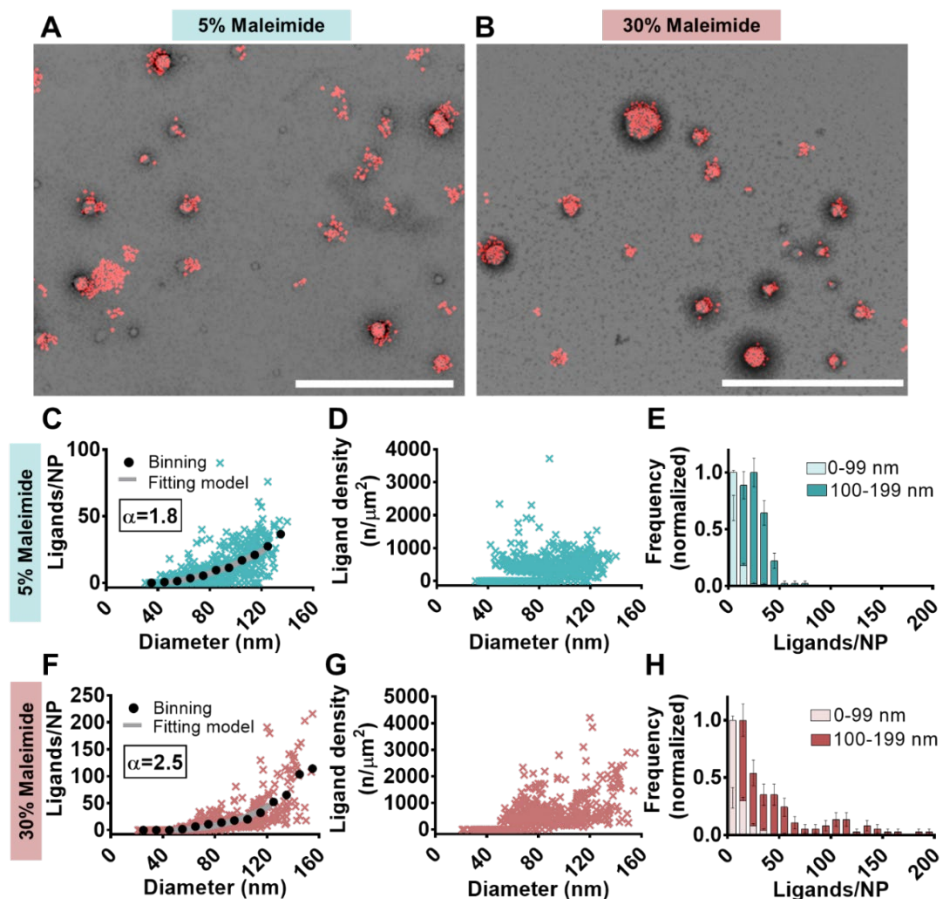
Figure 4 Multiparametric characterization of PLGA-PEG NPs using super-resolution CLEM. Super-resolution CLEM image of A) PLGA-PEG 5% and B) 30% maleimide NP formulations (scale bars=1000nm). The relationship between the number of ligands per NP as quantified by qPAINT, and the corresponding diameter as measured by TEM of C) PLGA-PEG 5% and F) 30% maleimide formulations. Black dots show the same data binned on TEM diameter (bin size 10 nm) where the average number of ligands is shown for each bin. Grey lines show the results of the fitting of binned data with a power-law model. The relationship between ligand density (number of ligands per NP surface area in µm^2) and the corresponding diameter by TEM for D) PLGA-PEG 5% and G) 30% maleimide NP formulations. Distributions of ligand number per NP based on diameter ranges by TEM of 0-99 nm and 100-199 nm for E) PLGA-PEG 5% and H) 30% maleimide formulations. Note: The DiI signal is not present in the CLEM images in A and B as it was not used as a reference in the analysis. In this case, TEM is used to confirm true NPs in DNA-PAINT. Details of image acquisition, data analysis and surface area calculation can be found in the Materials and Methods section.

To better understand these results, we analyzed the distributions of ligands per NP for smaller (0-99 nm) and larger (100-200 nm) NP populations in both formulations. We noted that the ligand distribution was more heterogenous at 30% maleimide (Figure 4H) than at 5% maleimide (Figure 4E) content, particularly in the larger size population; this was similar to the results observed in the relationship between ligand number and ligand density versus diameter. These findings - as well as other previously published

studies[282,283] - may suggest that heterogeneity found in NP size can affect the surface composition, and as described here, disrupt the expected trends in ligand number and in ligand density. Consequently, the presence of NP populations with distinct physiochemical properties in the same batch can lead to different outcomes in therapeutic efficacy[129].

Super-resolution CLEM endows us with the possibility to study the whole NP population at a single particle level, including those NPs without any reference signal that would otherwise be invisible if analyzed solely by SRM as depicted in Figure 3. To better understand the various sub-populations within our formulations, we subdivided the whole NP population according to the quantified number of ligands on their surface, then calculated the percentage of each sub-population with respect to the total amount of NPs. We found a remarkably substantial percentage of NPs without any functional ligands: 42% and 28% at 5% (Figure 5A) and 30% (Figure 5B) maleimide contents, respectively. Similar results were observed also on dendrimers, whereby over 45% of the entire material showed no surface ligands and very heterogenous populations[130,284], which opens up the door to a multitude of questions regarding the performance of these nanoparticle sub-populations that are in fact non-functional, which could also lead to toxicity and undesirable biological immune responses[129]. This highlights the need to better characterize and understand physicochemical properties in NPs and the impact these can have on their biological fates.
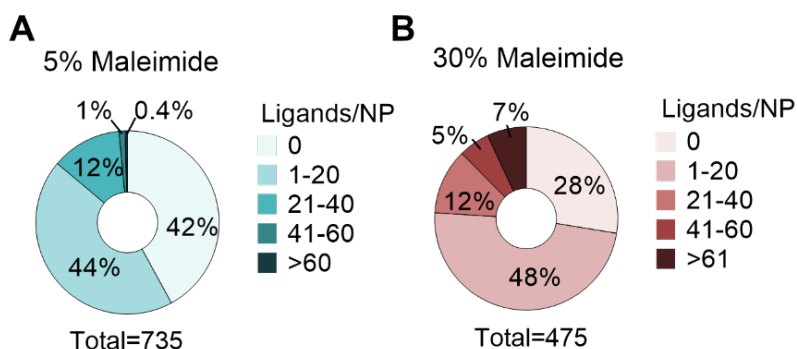
Figure 5 Pie charts depicting NP populations (%) with 0, 1-20, 21-40, 41-60 or >60 ligands/NP in A) PLGA-PEG 5% and B) 30% maleimide NP formulations, as quantified and analyzed by super-resolution CLEM. The total number of NPs analyzed per formulation is shown below each pie chart.

We then compared our results for the number of ligands per NP with the average theoretical calculations that are normally used in literature (Table 1). Firstly, we calculated the conjugation efficiency (CE%) of our NP formulations to the functional ligands (Table 1) and found these values to be 23% and 70% at 5% and 30%, respectively. Theoretical calculations assume that all the hydrophilic PEG-maleimide chains will migrate and be exposed to the NP surface, whilst the hydrophobic PLGA will form the core. However, due to the miscibility of PEG and PLGA[242,285], the NP core in fact also includes PEG-maleimide chains. It has been estimated that only about 50-60% of the maleimide groups added are available for conjugation on the NP surface[241], values in close accordance with our results. We then calculated the ligand availability (%) (i.e. the percentage of surface ligands per NP accessible to imager strands) for both formulations with the results obtained by a one-method-at-a-time approach using

TEM and qPAINT data separately (Table 1, white rows) and compared these with the results calculated by super-resolution CLEM (Table 1, grey rows). The ligand availability (%) is generally lower than the CE (%), meaning that not all conjugated surface ligands are accessible to the imager strands, which could be due to various reasons. Firstly, there is still a risk of ligand embedding in the PEG brush after conjugation[246,286], and secondly, the functional ligands could be poorly orientated to the imager strands. For these reasons, these results show that the accessibility of therapeutic ligands can be hampered by such factors.

Table 1 Calculation of ligand availability (%) values using DNA-PAINT alone and super-resolution CLEM.

Formulation	Diameter TEM (nm)	Theoretical maleimide molecules/ NP	CE (%)	Theoretical ligand number/NP	Accessible ligands (qPAINT)	Ligand availability (%)
5% Mal.	74 +/- 26	321	23	49	26	47
30% Mal.	78 +/- 29	1630	70	1141	54	5
5% Mal.	77 +/- 25	357	23	83	8	10
30% Mal.	82 +/- 31	2746	70	1922	19	1

Average TEM diameter, theoretical maleimide molecules per NP, conjugation efficiency (CE %), theoretical ligand number per NP, accessible ligands per NP as quantified by qPAINT, and resulting average ligand availability (%) for PLGA-PEG 5% and 30% maleimide formulations. These results were obtained either by a one-method-at-a-time approach using qPAINT and TEM separately (white rows) or by a correlative method using super-resolution CLEM (grey rows). For calculations see Materials and Methods.

We observed a general 5-fold overestimation in ligand availability (%) with a one-method-at-a-time approach compared to our super-resCLEM method. Using the latter approach, we are not limited to only imaging the population of NPs with a reference signal, but are indeed able to analyze the whole population, including the 'invisible particles' as generally all particles are visible in TEM. As depicted in Table 1, a single parametric approach would also overemphasize the therapeutic performance of the formulation and prevent the determination of a sufficiently effective NP dose.

3. Conclusions

In the present work, we introduced an efficient method based on super-resolution CLEM imaging to study the relationship between size and ligand number and density at a single particle level and with nanometric resolution. Firstly, we demonstrated that the heterogeneity found in NP parameters may be a result of the collective impact between different physiochemical properties such as size and surface ligand number. Secondly, we found a remarkable percent of NPs without any surface ligands, which in a therapeutic formulation would be ineffective and could even lead to toxicity and undesirable biological immune responses. Thirdly, we showed that the characterization of nanomaterials using a one-method-at-a-time approach limits the information obtained as compared to a multiparametric technique. For example, omitting sub-populations of NPs with no reference signal and importantly no surface ligands. The latter leads to an over-estimation of the number of ligands and ligand availability (%)

as observed by DNA-PAINT alone, which in hindsight would prevent the determination of an adequately efficient therapeutic dose.

The study of other nanomaterials using super-resolution CLEM – particularly with different morphologies – would shine light on the relationship between size and morphology and surface functionalization; and although the multiparametric characterization of the tens of different physiochemical properties relevant to nanomaterial performance is still out of our reach, we hope that this work will pave the way to a more robust characterization using correlative imaging techniques.

4. Outlook

The versatility of CLEM protocols such as the one described in this Chapter has prompted us to optimize and apply a similar correlative technique to study a more complex type of nanomaterial, namely supramolecular polymers. This group of polymers have been gaining importance because of their non-covalent nature that grants them various advantages as opposed to conventional polymers e.g. easy formulation, high processability, fine tuneability and responsiveness[287–289]. This last feature is exploited to externally control the supramolecular polymers, changing their properties upon exposure to different stimuli such as temperature, pH, or light[288]. Albertazzi et al. have designed a method using *d*STORM to study the molecular exchange pathways and mechanical properties of a specific group of supramolecular polymers[290], highlighting the significance of this technique in the analysis of such polymers. For this reason, we chose to optimize a *d*STORM-TEM correlative approach, that could be used to study the changes in these properties as a function of their supramolecular nature.

We specifically used a supramolecular polymer designed in our group, based on the C3-symmetric benzene-1,3,5-tricarboxamide (BTA) core, extended with a linear peptide-like amphiphile (BTA-Azo-C$_8$). This monomer was labelled with a Cy3 dye for microscopy purposes. Monomers were formulated in water to obtain fibrillar aggregates, and then attached to a nickel-hexagonal 200 mesh TEM grid coated with a formvar-carbon layer. The grid choice is particularly important when carrying out *d*STORM imaging (as opposed to DNA-PAINT imaging) since grids made from reactive metals such as copper can react when in contact with reducing components in the *d*STORM buffer, leading to peeling of the supportive layer. Next, the grid was imaged by *d*STORM and TEM microscopy, as detailed in Materials and Methods of this Chapter.

We first obtained a *d*STORM image of a supramolecular polymer fiber (Figure 6A, left panel), and then a TEM image of the same field-of-view (FOV) (Figure 6B, middle panel), and successfully overlapped the respective images, to create a correlative *d*STORM-TEM image of supramolecular polymers (Figure 6A right panel). Interestingly, initially *d*STORM showed fibers of greater lengths (> 3000 nm) compared to previously reported sizes on a similar fiber system[288] (250-1000 nm). To understand this better, we acquired higher resolution images by TEM of the same fiber and carried out the *d*STORM-TEM correlation on a smaller FOV (Figure 6B). The results demonstrated that the fibers were in fact polymer bundles (~ 80 nm) made of much smaller fibers, roughly 8 nm in diameter. Since the resolution of *d*STORM is ~ 20 nm,

molecules with a smaller size will not be distinguished from one another when closer to each other by less than 20 nm. For this reason, *d*STORM alone was unable to show the true structure of these fibers.
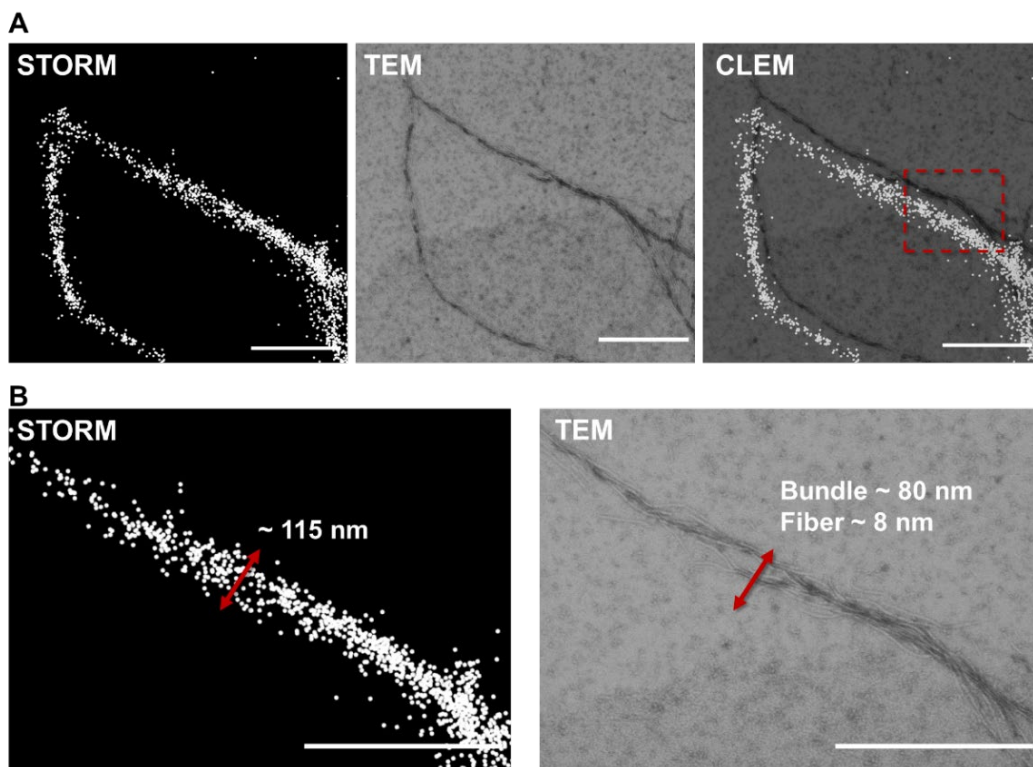
Figure 6 A) Large field views of BTA-AZO-C_8 supramolecular fibers by dSTORM, TEM and by correlative STORM-TEM, of the same area. B) Zoom-in images of the area highlighted with the lined red box in A), showing that the single fiber observed by dSTORM is a bundle of smaller fibers. Scale bars = 500 nm.

As a next experiment, it would be interesting to study the monomer exchange of a highly stable polymer such as BTA-Azo-C_8. Monomer exchange between these fibers has been demonstrated to be extremely slow, and CLEM could provide some valuable information on this process. To do so, fibers including BTA-Cy3 and BTA-Cy5 would be assembled separately. Upon mixing the two fibers, monomers would start to exchange between fibers, mixing BTA-Cy3 with BTA-Cy5. By this means we could study the monomer exchange along the fiber using *d*STORM, whilst TEM could offer an insight on whether the monomers pack together onto a single fiber or remain in separate fibers in a bundle. Notably, we could also identify if the exchanges occur isotopically along the fiber (monomer intercalation) or localized at the ends (monomer addition). We foresee the application of *d*STORM-TEM in polymer science to go beyond the results shown here and to give unique insight into their morphology.

5. Materials and methods

Materials

Materials for nanoparticle formulation

The polymer poly(lactide-co-glycolide)-methoxy-poly(ethylene glycol) GCW301 (Mw PLGA:PEG, 30:1 kDa, L:G in PLGA 50:50) was supplied from GenoTech. The polymers poly(lactide-*co*-glycolide) AP082 acid endcap (PLGA, 50:50 LA:GA, Mw 25-35 kDa) and poly(lactide-*co*-glycolide)-poly(ethylene glycol) AK102 (Mw PLGA:PEG 30:5 kDa, L:G in PLGA 50:50) were supplied from PolySciTech. The polymer poly(D,L-Lactide-co-glycolide)-poly(ethylene glycol)-Maleimide SKU 2794 (Mw PLGA:PEG:Maleimide 20:5:0.09707 kDa) was supplied from Nanosoft Biotechnology LLC. Amicon Ultra-4 filters (regenerated cellulose, 100 kDa) were purchased from Merck Life Sciences. The solvent acetonitrile (HPLC grade) was purchased from Carlo Erba Reagents. The reducing agent Tris(2-carboxyethyl)phosphine hydrochloride (TCEP) 0.5 M pH 7 was supplied by Merck Life Science.

Materials for DNA-PAINT imaging

Thiol-modified DNA oligonucleotides (docking strands 1) and Atto647N-labelled DNA oligonucleotides (imager strands 1 and 3) were designed and purchased from Integrated DNA Technologies. Docking strand 1 and imager strand 1 were used for DNA-PAINT imaging, whilst docking strand 1 and imager strand 3 were used for control experiments. DNA oligonucleotides were dissolved and stored in sterile TE buffer (10 mM Tris-HCl pH 8, 0.1 mM EDTA) and used fresh. The DNA oligonucleotides used have the following DNA sequences, and only 9 bases contribute to hybridization:
Docking strand 1: 3'ATC TAC ATA TT/thiol
Imager strand 1: 5'-CTA GAT GTA T/Atto647N/-3'
Imager strand 3: 5'-GTA ATG AAG A/Atto647N/-3'
Sterile phosphate-buffered saline PBS buffer pH = 7.4 was used for NP sample preparation in the imaging chamber. Buffer B (5 mM Tris-HCl, 10 mM MgCl$_2$, 1 mM EDTA, 0.05% Tween-20 pH=8) was used to dilute the imager strands for DNA-PAINT imaging.

Materials for TEM imaging

Copper TEM grids (200 mesh) were coated with a carbon layer in-house. Microscopy slides (dimensions 76x26 mm, thickness 1/1.2 mm) were supplied by RS France and coverslips (dimensions 24x24 mm, thickness 0.13-0.16 mm) were supplied by Deltalab, and used for DNA-PAINT measurements. Uranyl acetate 2% in MilliQ water was prepared in-house and used within 3 months for TEM negative staining.

Nanoparticle formulation

PLGA-PEG NPs were formulated *via* the precipitation-solvent evaporation (nanoprecipitation) method according to literature[232]. Briefly, 5 mg of polymers and 1.1 mM DiI (reference dye) were dissolved in 500 µL solvent phase (acetonitrile) at room temperature. PLGA polymer was maintained at a ratio of 15% and mixed with PLGA$_{30k}$-PEG$_{1k}$ and PLGA-PEG-Maleimide polymers at 5% or 30% maleimide content. For

example, for the PLGA-PEG 30% maleimide formulation: 75.0 µL PLGA from a stock of 10 mg/mL (0.75 mg), PLGA-PEG 152.8 µL from a stock of 18 mg/mL (2.75 mg), 100.0 µL PLGA-PEG-Maleimide from a stock of 15 mg/mL stock (1.5 mg) and 4.5 µL DiI from a stock of 10 µM (1.1 mM) were dissolved and made up to 500 µL with acetonitrile. For control PLGA-PEG formulations, no PLGA-PEG-Maleimide was added and was instead replaced with $PLGA_{30k}$-PEG_{5k}, whilst the PLGA amount was maintained at 15%, and $PLGA_{30k}$-PEG_{1k} varied depending on the formulation. The polymer solution was stirred at 200-300 rpm whilst the anti-solvent phase (MilliQ water) was pipetted at a 1:10 ratio (500 µL polymer solution is pipetted into 5 mL milliQ water). Solvent extraction (evaporation) continued for 5 h under magnetic stirring in a fume cupboard at room temperature. NPs were then collected by centrifugation (Avanti J-26 XPI, rotor JA-14) using Amicon Ultra-4 filters as per filter instructions for 10 min at 5,000 x g at 20°C with filtered MilliQ water. NPs were stored in MilliQ water at a 10 mg/mL concentration in the dark at 4°C until further use.

Conjugation of docking strands to NPs

First, the protective disulphide bonds on the thiol group were reduced using TCEP at a 10:1 molar excess compared to thiol[248]. Briefly, for PLGA-PEG 30% maleimide, 2.6 µL of 0.5 M TCEP and 116.6 µL of 1.1 mM thiol-DNA docking strand were added to 380.9 µL PBS pH = 7.4 and allowed to stir for 20 min at room temperature. Prior to closing the lid, argon gas was bubbled in the glass vial, to prevent reformation of disulphide bonds[248]. Then, the conjugation between thiol-DNA oligonucleotide and NP maleimide was carried out at a 3:1 molar ratio of thiol-DNA oligo to maleimide, to ensure optimal conjugation. For this, 500 µL of 10 mg/mL NP stock was added to the solution and mixed for 2 h more in the absence of oxygen. Unconjugated thiol-DNA oligos were removed *via* centrifugation using Amicon Ultra-4 filters as per filter instructions for 10 min at 5,000 x g (rcf) at 20°C with filtered milliQ water. NPs were stored in milliQ water at a concentration of 10mg/mL in the dark at 4°C.

Calculation of ligand density per NP

For Figure 4D and Figure 4G, the ligand density was calculated for each NP individually, by dividing the number of ligands per NP (quantified by qPAINT) by the surface area (SA) of that NP, in turn calculated using its respective TEM diameter. The SA was calculated as per surface area of a sphere:

$$Surface\ area\ (\mu m^2) = 4\pi r^2 \quad (1)$$

Super-resolution CLEM protocol on TEM grids
DNA-PAINT chamber preparation

The carbon-coated copper TEM grid was first treated using UV glow discharge for 30s using BAL-TEC CTA 005 Glow Discharge Unit to improve the attachment of NPs. Using a fine tweezer, the grid was placed on top of a ~ 40 uL drop of NP solution 2mg/mL (10mg/mL diluted x5 in milliQ water) for 20 min for NP attachment. The grid was then washed through a drop of imager strand 1 in Buffer B solution (5 nM) and placed on a microscopy glass slide with the NPs attached side facing upwards. The coverslip was then placed on top of the grid and sealed using quick dry transparent

nail varnish to prevent evaporation. Prior to the experiment, coverslips were thoroughly cleaned in acetone and ethanol 96% for 10 min each in bath sonication, then dried using nitrogen gas flow. Prior to DNA-PAINT imaging, reference images of the region of interest were taken. These consisted of 1) a large view of the grid, by acquiring a 13x13 stitched image in bright field using the NIS-Elements stitch function and if required a large bright field image of the ROI (1024 x 1024) using the 100x oil objective. To remove the grid from the chamber, the nail varnish was gently removed using a tissue embedded in acetone, then it was placed in a petri dish filled with MilliQ water to aid in the smooth separation of the coverslip from the microscopy slide. The grid was then gently picked up using a tweezer. Please note these steps must be carefully carried out, as to not accidentally peel off the carbon film on the grid (Figure S1).

DNA-PAINT acquisition and drift correction

Imaging was carried out with a Nikon N-STORM system configured for highly inclined and laminated optical sheet (HILO) imaging, using a Perfect Focus System (PFS). Atto647N-Imager strand signal was collected using the 647 nm (160 mW) laser with 60% power and the DiI drift correction signal using the 561 nm laser (80 mW) with 2% power. No UV activation was required. Fluorescence was collected using a Nikon 100x, 1.49 NA oil immersion objective and passed through a quadband pass dichroic filter (97335 Nikon). Images were acquired onto a 256 x 256-pixel region (pixel size 0.16 mm) of a Hamamatsu ORCA Flash 4.0 camera at 70 ms integration time. For the Atto647N-Imager strand 20,000 frames were acquired in the 647 channel and for the drift correction one frame was acquired every 100 frames in the 561 channel. The time taken for image acquisition was ~ 25 min. For super-resolution CLEM, NPs were imaged using 5 nM imager strand 1 in Buffer B. During image acquisition, the NIS Elements Nikon software generates a list of localizations by Gaussian fitting the fluorescent blinking dyes of the conventional diffracted images. To avoid overcounting, blinking detected in consecutive frames are counted as single blinks by the software. The generated localization list is filtered to remove background due to free dyes attached to the glass, by applying a density filter of 5 localizations in a radius of 120 nm. The fluorescence signal of the encapsulated dye DiI is spectrally different from that of the imager strand, and thus was acquired in a different channel (561 nm). This allowed the correction of the mechanical drift during image acquisition without the addition of extra probes. Furthermore, there is no evidence that DiI significantly affects the interaction between docking strand and imager strand.

qPAINT calibration on grid

Unlike DNA-PAINT, qPAINT uses kinetic information based on the mean dark time (τ_{d^*}) between binding events to quantify accessible ligands, which is associated to the number of ligands (n) through the equation $n = (k_{ON}c_i\tau_{d^*})^{-1}$. This requires a calibration to calculate the second-order association rate of the docking strand-imager strand pair (k_{ON}). Using PLGA-PEG 1% maleimide NPs conjugated to thiol-docking strands at a known imager concentration (c_i) of 5nM in Buffer B, we calculated the k_{ON} for the binding kinetics of a single docking strand to be 8.8×10^5 M^{-1} s^{-1}, a value similar to previously reported values[163,188]. For full experimental procedure see Figure S5.

TEM imaging

In preparation for TEM imaging (Figure S1), the grid was first washed to remove buffer salts on MilliQ water drops for 1 min then 30 sec, then negatively stained using filtered uranyl acetate 2% (UA 2%, in MilliQ water) for 1 min. Excess UA was removed by tapping the edge of the grid on Whatman filter paper. The grid was then allowed to dry overnight in a desiccator. Next, the grid was imaged using a Jeol 1010 (Gatan, Japan) from the Electron Cryomicroscopy Unit from the CCiTUB, equipped with a tungsten cathode. Images were acquired at 80kV with a CCD Megaview 1k x 1k. Firstly, the ROI was located using a low-magnification function. Then, sequential images were taken of the ROI at a magnification of x20 000, which were stitched manually in Adobe Photoshop CS9.

Image correlation

The DNA-PAINT image was correlated to the stitched TEM image in Adobe Photoshop CS9. First, it was re-scaled according to the TEM image resolution. Then, a 'vividlight' layer filter was applied and the transparency was increased to 57% of the DNA-PAINT image, to allow better visualization of the CLEM image. This process also included rotation of the SRM image. At no point prior to data analysis are the original TEM images modified in any way, as these must be used for size and morphology analysis. However, for the purpose of showing super-resolution CLEM images the contrast of the TEM images was modified as to allow the correlation to be clearly seen.

Data analysis correlation

Diameters of individual particles were correlated to the number of ligands quantified by qPAINT from DNA-PAINT images. Data analysis for qPAINT on NPs was previously described by our group[188,189]. Briefly, the x,y,t coordinates of 647 localizations belonging to each NP was analyzed in MATLAB using a mean-shift cluster algorithm whereby each NP was assigned an identification number, and its diameter and number of localizations. For qPAINT analysis, a binary intensity *versus* time trace was reconstructed for each NP, assigning a value of 0 to the frames without localizations and a value of 1 to the frames with one localization. The individual dak times were computed for each NP, obtaining the corresponding CDF, which was then fitted with the exponential model and the value of the mean dark time τ_{d*} was extracted. The number of ligands per NP was quantified using the equation (1): $n = (k_{ON}c_i\tau_{d*})^{-1}$ using $k_{ON\ (grid)}$ to be 8.8×10^5 M^{-1} s^{-1} and the known imager concentration (Figure S5). Then, the diameter of each individual NP was measured in ImageJ from the stitched TEM image. Using the identification numbers of each NP in the DNA-PAINT image, each NP was correlated in terms of diameter by TEM and ligand number by qPAINT. Note that the DiI (561) channel is not used as a reference (unlike in the DNA-PAINT characterization measurements done on glass), as some NPs show to not encapsulate any DiI. In this case, the TEM stitched image is used as reference.

The following calculations are for the results described in Table 1

 a. *Calculation of conjugation efficiency (CE%):*

This was achieved using a NanoDrop ND-1000 Spectrophotometer. Briefly, after conjugation of PLGA-PEG NPs to thiol-DNA oligos, the NP solution was spun down *via* centrifugation using a bench-top centrifuge (Eppendorf Microcentrifuge 5415 R Sigma-Aldrich) for 20 min at 16.1 x g (rcf) at 20°C leading to a NP pellet formation. The supernatant was collected, and the process was repeated for 2 times more until no pellet was observed. The negative control consisted of PLGA-PEG NPs (no maleimide) undergoing the conjugation process and centrifugation steps identically to the test NPs. The final supernatant solutions were analyzed by NanoDrop spectrophotometry (at 260 nm) and the CE % was calculated as per Equation 2:

$$\left(1 - \frac{Thiol-oligo\ in\ Test\ supernatant\ (abs)}{Thiol-oligo\ in\ Control\ supernatant\ (abs)}\ x\ 3\right) x\ 100\% \quad (2)$$

 b. *Calculation of theoretical maleimide groups per NP as per Spherotech's instructions[249]:*

Number of particles in suspension:

$$\left(\frac{(6\ x\ Polymer\ Weight\ (g))}{(3.14\ x\ Polymer\ Density\left(\frac{g}{cm^3}\right) x\ NP\ Diameter\ (\text{um})^3}\right) x\ 10^{12} \quad (3)$$

Calculation of number of maleimide molecules in suspension:

$$\left(\frac{Polymer\ Mass\ (g)}{Polymer\ Molecular\ Weight\left(\frac{g}{mol}\right)}\right) x\ Avogadro's\ Number \quad (4)$$

Number of theoretical maleimide molecules per NP:

$$\frac{Number\ of\ Maleimide\ Molecules}{Number\ of\ Particles\ in\ Suspension} \quad (5)$$

 c. *Calculation of theoretical ligands per NP:*

Calculated by multiplying the theoretical maleimide molecules/NP by the CE % of the formulation.

 d. *Calculation of ligand availability:*

Calculating the percentage of ligands quantified by qPAINT out of the theoretical ligands per NP.

DNA-PAINT measurements on glass

i)   *Preparation of imaging chamber*

A 40 mL volume flow chamber was assembled from a glass microscopy slide and a coverslip, attached by double-sided tape. Prior to assembly, the coverslips were cleaned first with acetone, then with ethanol 96% for 10 min each by bath sonication, then dried under nitrogen flow. This process removes impurities and improves the NP retention on the coverslip. The NP 10mg/mL (x1000 dilution in PBS) were pipetted into the chamber, which was then turned upside down and allowed to adsorb for 20 min. PBS promotes the adsorption of NP. Unattached NP were washed away with Buffer B. Finally, the chamber was filled with imaging buffer solution (Imager strand diluted in Buffer B to the required concentration) and sealed with nail varnish to avoid evaporation.

ii)   DNA-PAINT for NP imaging on coverslips

This was carried out with a Nikon N-STORM system configured for total internal reflection (TIR), using a Perfect Focus System (PFS). Atto647N-Imager strand signal was collected using the 647 nm (160 mW) laser 60% laser power and the DiI drift correction signal using the 561 nm laser (80 mW) 2% laser power. No UV activation was required. Fluorescence was collected using a Nikon 100x, 1.49 NA oil immersion objective and passed through a quadband pass dichroic filter (97335 Nikon). Images were acquired onto a 256 x 256-pixel region (pixel size 0.16 mm) of a Hamamatsu ORCA Flash 4.0 camera at 70 ms integration time. For the Atto647N-Imager strand 20,000 frames were acquired in the 647 channel and for the drift correction one frame was acquired every 100 frames in the 561 channel. The time taken for image acquisition was ~ 25 min. All PLGA-PEG-Maleimide formulations were saturated with a 3:1 molar excess of thiol to maleimide. PLGA-PEG-Maleimide PEG NP were imaged with 2.5 nM Imager strand 1 in Buffer B or Imager strand 3 in Buffer B for the negative control.

TEM imaging protocol (no CLEM)

An in-house carbon-coated copper TEM grid (CF200-CU, 200 mesh, Electron Microscopy Sciences) was first treated using UV glow discharge for 30s using BAL-TEC CTA 005 Glow Discharge Unit to improve the attachment of NPs. Using a fine tweezer, the grid was placed on top of a 40 µL drop of NP solution (2mg/mL) (10mg/mL diluted x5 in MilliQ water) for 3 min for NP attachment. Please note NP solution was vortexed well before attachment to the grid to avoid aggregates. Then the grid was washed to remove impurities and unattached NPs on 40 µL MilliQ water drops for 1 min, 30 sec and 30 sec, then negatively stained using filtered uranyl acetate 2% (UA 2%, in MilliQ water) for 1 min. Excess UA was removed by tapping the edge of the grid on Whatman filter paper. The grid was then allowed to dry overnight in a desiccator. Next, the grid was imaged using a Jeol 1010 (Gatan, Japan) from the Electron Cryomicroscopy Unit from the CCiTUB, equipped with a tungsten cathode. Images were acquired at 80kV with a CCD Megaview 1k x 1k, with a magnification of x20 000-50 000. The NPs diameter was measured using ImageJ software.

NP diameter and localization script:

A MATLAB script was used to count the number of localizations in the 647 (Imager strand) channel and the 561 (DiI-fiducial marker) channel (Figure 1) and the diameter of the NP. Firstly, the localization clusters from the fiducial 561 channel were identified using a mean-shift clustering algorithm. These clusters were used to identify the center of each individual NP, with an uncertainty of a few tens of nm from the center of the NP (this is obvious when the 561 signal is not found on the center of the NP). Another filter was used allowing the user to select parameters to filter out noise/aggregates/elongated shapes. Then, the localizations from the 647 channel found within a distance of 160 nm from the center of the NP were detected, and then the number and x,y,t coordinates of the localizations and diameter were calculated for each NP. The radius of each NP was estimated as the distance from the mass center making up 90% of the cluster localizations.

dSTORM-CLEM correlative imaging on supramolecular polymers

BTA-Azo-C_8 monomers with 10% Cy3 dye labelling, with a final concentration of 50 µM in milliQ water were prepared by PhD student Edgar Fuentes at IBEC. The following steps were carried out by myself and Guillem Bracons, master student at IBEC. The polymers were allowed to reach equilibrium at RT. for 24 h, then placed in a water bath at 70°C for 1 h and allowed to settle at RT. for a further 24 h. A final polymer solution with 5% Cy3 dye labelling and a concentration of 25 µM were prepared by mixing equal volumes of monomer solution and milliQ water. Prior to *d*STORM imaging, another hot water bath was performed at 50°C, to push the equilibrium towards fiber formation. Glow discharge was carried out for 30 sec at 5 mA on a nickel-hexagonal 200 mesh grid with formvar-carbon coating, to improve fiber attachment. Fibers were diluted to 1 µM in milliQ water, then attached for 1 min onto the TEM grid, followed by a 30 second milliQ water wash to remove unattached polymers. The grid was prepared into a microscopy chamber as previously described, and a STORM buffer was flown in, consisting of a) 100 mM mercaptoethylamine (MEA), b) an oxygen scavenger system consisting of 5% glucose (wt/vol), 0.5 mg/mL glucose oxidase (Sigma-Aldrich) and 40 mg/mL catalase (Sigma), c) 15% glycerol, in PBS at pH 8.5. Fibers were imaged by STORM on a Nikon N-STORM system configured for highly inclined and laminated optical sheet (HILO) imaging using the 561 (80 mW) laser at 20 ms exposure for 10 000 frames. The grid was then removed from the chamber and washed on a milliQ water drop for 30 sec before negative staining for 1 min using 2% uranyl acetate. The same region was later imaged by TEM, and correlation was carried out manually using Adobe Photoshop CS9.

Chapter 3 | Development of a correlative *d*STORM-TEM method to track nanoparticles intracellularly

This chapter reproduces almost literally the following manuscript in the process of being submitted for review:

Andrian T, Pujals S, Albertazzi L. A super-resolution and transmission electron microscopy correlative approach to studying intracellular trafficking of nanoparticles. As the first author of this paper, I performed almost all the experimental protocols, I contributed to protocol design, data analysis and manuscript writing. High-pressure freezing, freeze substitution and ultramicrotome sectioning was carried out by the staff at the TEM facility in Parc Científic de Barcelona. Dr Silvia Pujals and Dr Lorenzo Albertazzi participated in the planning, writing, and correction of the written work.

Supportive information for this chapter can be found in Appendix 3.

Abstract: *Nanoparticles (NPs) are used to encapsulate therapeutic cargos and deliver them specifically to the target site. The intracellular trafficking of NPs dictates the NP-cargo distribution within different cellular compartments, and thus governs their efficacy and safety. Knowledge in this field is crucial to understand their biological fate and improve their rational design. However, there is a lack of methods that allows precise localization and quantification of individual NPs within distinct cellular compartments simultaneously. Here, we address this issue by proposing a correlative light and electron microscopy (CLEM) method combining direct stochastic optical reconstruction microscopy (dSTORM) and transmission electron microscopy (TEM). We aim to combine the advantages of both techniques to precisely address NP localization in the context of the cell ultrastructure. Individual fluorescently-labelled poly(lactide-co-glycolide)-poly(ethylene glycol) (PLGA-PEG) NPs were directly visualized by dSTORM and assigned to cellular compartments by TEM. We first tracked NPs along the endo-lysosomal pathway at different time points, then demonstrated the effect of chloroquine on their intracellular distribution (i.e. endosomal escape). The proposed protocol can be applied to fluorescently labelled NPs and/or cargo, including those not detectable by TEM alone. Our studies are of great relevance to obtain important information on NP trafficking, and crucial for the design of more complex nanomaterials aimed at cytoplasmic/nucleic drug delivery.*

1. Introduction

Nanoparticles (NPs) are used in medicine to encapsulate therapeutic molecules (e.g. chemotherapeutics, protein inhibitors and nucleic acids) in order to improve their target selectivity[291,292], solubility[7,8], and to reduce their toxicity[10,11,293]. Yet, although several NP formulations have been successfully marketed, achieving efficient intracellular delivery remains a significant bottleneck in nanomedicine [142–144,294]. Following cellular uptake, the next critical stage in NP delivery is intracellular trafficking, which determines the NP-cargo distribution within cellular compartments and hence the therapeutic efficacy and safety[86,154]. For example, a pre-requisite for RNA and DNA delivery is for the molecules to reach the cytoplasm or nucleus intact to perform their therapeutic function. Thus, NPs carrying such degradation-prone molecules must overcome several cellular barriers, including trafficking to acidic endosomes and lysosomes that can lead to NP disassembly, cargo degradation and loss of efficacy[145,148,295]. In order to improve the therapeutic efficacy of nanomaterials it is thus essential to understand their biological interaction with cells, including intracellular trafficking[146,296,297].

However, considerable uncertainties still remain about the exact intracellular pathways taken by nanocarriers, and this largely stems from a lack of reliable methods to visualize and quantify with enough resolution NPs at a single particle level within the ultracellular environment[146–148]. NP uptake and intracellular trafficking are typically assessed using flow cytometry, fluorescence microscopy (FM) and/or transmission electron microscopy (TEM)[146,147,151,152]. Notably, flow cytometry measures relative fluorescence intensity and does not distinguish the NPs location (e.g. membrane-bound, endosomal, cytosolic). FM lacks the adequate resolution to resolve individual NPs, and objects that are found closer together than the resolution of the microscope (≈ 250 nm) can falsely appear co-localized[152]. It is also limited by the number of targets that can be labelled and lacks ultrastructural information. An upgrade to classical FM are super-resolution microscopy (SRM) techniques that allow localization of single molecules and single NPs down to tens of nanometres[179]. For example, direct stochastic optical reconstruction microscopy (*d*STORM) is based on the localization of individual, photoswitchable fluorophores, offering a resolution of ≈ 20 nm, and has been previously applied for the intracellular trafficking of several types of nanomaterials[176,298–302]. Despite this achievement, it still lacks cellular ultrastructural information, and can typically be used to image co-localization in only two simultaneous targets. In contrast, TEM offers a powerful approach to study intracellular trafficking pathways, due to its excellent resolution (< 1 nm) and ultracellular detail, but it only offers analysis on grayscale images and is restricted to nanomaterials with adequate atomic contrast (e.g. metallic NPs)[203,205,303].

To overcome the individual limitations of FM and EM, a group of techniques that combine both microscopies through detailed images of the same field-of-view (FOV) have been developed, namely correlative light and electron microscopy (CLEM)[209,211]. Despite the potential of combining two very powerful techniques, only a handful of articles demonstrate the applicability of CLEM on intracellular trafficking of nanomaterials[220,221]. Whilst these studies clearly demonstrate the power of CLEM in understanding NP intracellular metabolism, there is still a resolution gap between the

FM and EM techniques used, preventing the assignment of single particles to specific compartments.

To bridge the resolution gap between FM and EM, the correlation of SRM-EM has been established, albeit not in the nanomedicine field, substantially improving image quality[209,211,304]. Various combinations of SRM-EM approaches have been used in biology to image intracellular fluorescent proteins[215], track intracellular pathogens[168,217] and to study budding of influenza viruses from infected cells[218]. Recently, we have developed a DNA-PAINT-TEM correlative approach to study the relationship between NP functional ligand numbers and size at a single particle level[240]. However, despite the potential of CLEM in this field, and to the best of our knowledge, SRM-TEM correlative approaches have not yet been applied for the intracellular trafficking of NPs. At a cellular level, SRM-TEM correlation would offer a means to specifically label a variety of nanomaterials including their cargo, and to track them within specific cellular compartments with nanoscale precision.

To address this issue, we propose a *d*STORM-TEM correlative protocol to track fluorescently labelled polymeric poly(lactide-co-glycolide)-poly(ethylene glycol) (PLGA-PEG) NPs at a single particle level within different cellular compartments. Polymeric NPs were chosen as a standard NP formulation for this protocol due to their well-studied properties; however they also show great promise for targeted drug delivery systems due to their biocompatibility, biodegradability, design flexibility and safety[1,3,51,52]. Notably, these NPs are undetectable by TEM alone in the cellular milieu due to their low contrast, highlighting the relevance of this correlative approach for imaging a wide range of nanomaterials.

We first discuss the roadmap of CLEM techniques available, considering their strengths and weaknesses, and optimize the most suitable protocol for our biological question. We then describe our adapted *d*STORM-TEM correlative method and demonstrate that the superior resolution of *d*STORM, as opposed to low-resolution FM, offers localization of single NPs within specific cell compartments in TEM. First, we use the proposed technique to track NPs within different compartments (early and late endosomes, lysosomes and non-endosomal compartments) at different time points. Second, we study the effect of the lysomotropic agent chloroquine on the NP intracellular distribution. We envision that this technique will be applicable to answer various questions on intracellular trafficking and endosomal escape, and to study more complex nanomaterials such as polyplexes for nucleic acid delivery, overall offering unique information that we are currently lacking on the biological fate of nanomaterials.

2. Results and Discussion
2.1 Overview of CLEM Protocols

A variety of CLEM workflows exist for cell biology applications[211], and despite their initial complexity to novice scientists, they typically follow TEM sample preparation steps (Figure 1). This section will only briefly discuss the main protocols, and for more extensive information readers are directed to specialized CLEM handbooks/reviews[209–211,305–307].
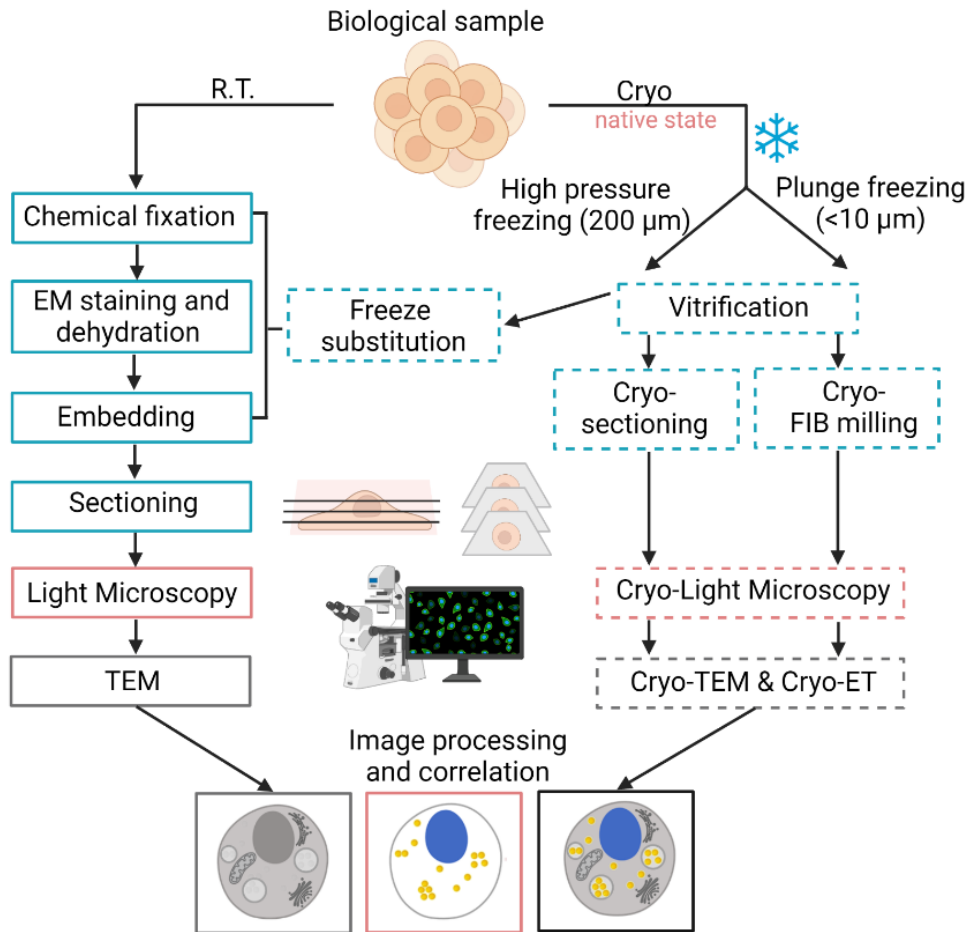
Figure 1 Standard correlative light and electron microscopy (CLEM) workflows in cell biology. Created with Biorender.com

The first step in TEM sample preparation is typically fixation and this can be done via chemical fixation or cryo-fixation using high-pressure freezing (HPF) or plunge freezing. Chemical fixation is normally achieved at room temperature (RT) and thus does not require any special equipment and is normally followed by further fixation and staining with osmium tetroxide (OsO_4). These harsh fixing conditions and heavy metals can lead to fluorescence quenching if fluorescence is present. HPF allows the vitrification of samples with a thickness of 200-300 µm at high pressures, freezing the specimen whilst avoiding the formation of ice crystals, and preserving an almost intact ultrastructure, as opposed to chemical fixation[308]. Following HPF samples can be either further prepared at cryo-temperatures for cryo-imaging or using freeze substitution (FS) for RT imaging. Plunge freezing achieves vitrification of samples thinner than 5-10 µm, by plunging into liquid ethane at cryogenic temperatures. The samples can be sectioned using cryo-focused ion beam milling.

The second step is resin embedding, a step necessary to harden the biological sample and to dehydrate it prior to TEM imaging. At RT, dehydration typically includes gradual

exposure to a solvent such as ethanol, which is then progressively replaced with a resin, that will eventually be polymerized into a hard block. Samples prepared by HPF are normally hard enough to allow direct sectioning using a cryo-microtome, or if the sample must be eventually processed at RT, freeze substitution (FS) is used instead. The latter includes the exposure of the sample to a solution containing typically acetone and a fixative/contrasting agent, which is then gradually replaced by slow resin infiltration and polymerization; these steps are carried out for several days whilst the temperature slowly increases to RT. The advantage of FS is that as opposed to chemical fixation, the cellular structure and membranes are much more well preserved. Several resins are available, with epoxy resins being probably the most common, offering hard resin blocks with great contrast in TEM, but that cause protein denaturation and thus cannot be used for immunolabelling. Softer resins include Lowicryl and LR White, that allow better preservation of protein structure and hence immunolabelling[210,309]. One can also remove the need for resin embedding, by using the Tokuyasu method[310], whereby the fixed sample is infiltrated with a cryo-protectant and frozen in liquid nitrogen, followed by cryo-sectioning. This allows for immunolabelling, but results in inferior preservation of ultrastructure.

Sectioning is required to ensure that samples are thin enough to allow the electron beam in TEM to pass through. This step can be done using a normal ultramicrotome if imaging is to be done at RT, or a cryo-ultramicrotome for subsequent imaging in cryogenic conditions. Typically, successive sections of a thickness of 50-100 nm (ultrathin sections) are cut and collected on the surface of metal grids or glass coverslips for TEM and SEM, respectively. Post-staining is then done using heavy metals such as uranyl acetate (UA) and lead citrate (Reynolds) for samples aimed at TEM. Cryo-EM does not require further staining since the contrast is provided by the native cellular environment, but as a result has much lower contrast. Notably, consecutive sections can be imaged individually by 2D TEM, or by 3D using serial sectioning. Electron tomography (ET) also offers 3D images but uses thicker sections of roughly 200-300 nm, which are imaged from different directions that are later automatically aligned to offer a 3D projection of the sample.

For CLEM protocols, FM can be combined with TEM at different time points in the protocol. FM imaging can be carried out i) before resin embedding, ii) on the resin block or on thin sections after embedding or iii) on thin sections for cryo-EM without embedding. The first protocol allows for dynamic data from live-cell imaging or imaging on whole cells, and the issue of fluorescence quenching due to certain fixation and staining protocol is circumvented. However, structural changes can occur during the fixation steps between FM and TEM imaging, leading to correlation mismatches and poorly understood data. The second protocol allows much more precise correlation between the two images and is particularly useful for imaging small structures that move fast. However, if the fluorescent label is present before sample preparation, then the fixation and heavy metal steps can lead to quenching of fluorescence [209,269,311], so parameters (e.g. heavy metal content, labelling percentage) must be optimized. For near native state imaging in both microscopes, the third protocol is the most suitable, however it requires very specific and expensive equipment and offers much lower sample contrast.

In CLEM, matching the region of interest (ROI) between the two microscopes is a necessary yet sometimes complicated task. TEM grids containing markings (finder grids) can be used for a coarse alignment and ROI identification. More specialized sample holders are available from Carl Zeiss and Jeol/Nikon with navigation markers recognized by the microscope software that offer automated ROI retrieval[209]. For high precision overlay of FM and EM images, fiducial markers recognizable in both imaging techniques are used, such as nanoparticles[168], quantum dots[312], and polymer beads[313], that can be correlated either manually or through automated software such as ec-CLEM[314]. Commercially integrated microscopes are also available, such as iLEM (iCorr) which contains an integrated single-color wide-field FM microscope in a TEM[315] or airSEM which comprises FM and SEM[316]. These microscopes avoid problems related to ROI identification, precision overlay, and sample distortion between imaging techniques, but are expensive and are not commercially available.

2.2 Choosing the right protocol

Clearly, there are a variety of different protocols that one can choose from. However, in practice not many research laboratories have the liberty to pick and choose the winner, due to a lack of available equipment and trained personnel. For this project, we attempted 3 different protocols found in literature for CLEM imaging[218], and these are described more thoroughly in Figure A3.1. They all shared some common aspects, that fluorescently labelled NPs were present in the sample from the start, *d*STORM imaging was carried out directly on the thin sections and both FM and EM were done at RT. Notably, we were interested in imaging small NPs that are rapidly taken up by the cell and distributed to different compartments, thus we chose to carry out *d*STORM on ultrathin sections (after resin embedding) as it reduces the risk of morphological changes between the two microscopies. However, for 2 out of the 3 protocols, we had the issue of fluorescence quenching due to harsh fixation steps and the use of osmium tetroxide.

For the first protocol we chose the typical RT. pathway using an epoxy resin (Figure A5.1A) but using a lower OsO4 concentration (0.6% as opposed to the typical 2%) to reduce the risk of fluorescence quenching. As seen in Figure A3.1B, the ultrastructure preservation was poor, probably due to using milder fixation protocols, and the fluorescence signal quenched in the process as can happen even at low osmium tetroxide concentrations and upon epon resin embedding. The second protocol consisted of a soften hydrophilic acrylic resin, namely LR white, that has been previously used for both EM and LM. No osmium tetroxide was used as per manufacturer's instructions[317]. Whilst the ultrastructure preservation was slightly better than with the previous resin (Figure A3.1C), the fluorescence signal was once again quenched which came as a surprise since no osmium was used but could have been caused by the high temperatures used during resin polymerization.

The third and final protocol we attempted was using Lowicryl HM20 resin together with high-pressure freezing (HPF) and freeze substitution (FS) as explained below and seen in Figure A3.1D. This combines a great structural preservation with the advantage of imaging with high numerical aperture lenses at RT.[318]. We hoped that aside from the ultrastructural preservation, the reduction in chemical fixatives used,

avoidance of both osmium tetroxide and high temperatures would also prevent fluorescence quenching.

2.3 dSTORM-TEM correlative method

To track NPs within different cellular compartments at a single particle level, we developed a *d*STORM-TEM correlative approach that benefits from nanometer-scale resolution in both techniques. The method described here (Figure 2) is an adaptation of the confocal microscopy – TEM correlative protocol used by Katheder et al. to assess autophagy in *Drosophila* tumor growth[319] and based on previous findings that demonstrate that fluorescent signal is maintained and ultrastructure is preserved in cells which have been high-pressure frozen, freeze-substituted and embedded in lowicryl resin sections[313,320,321].
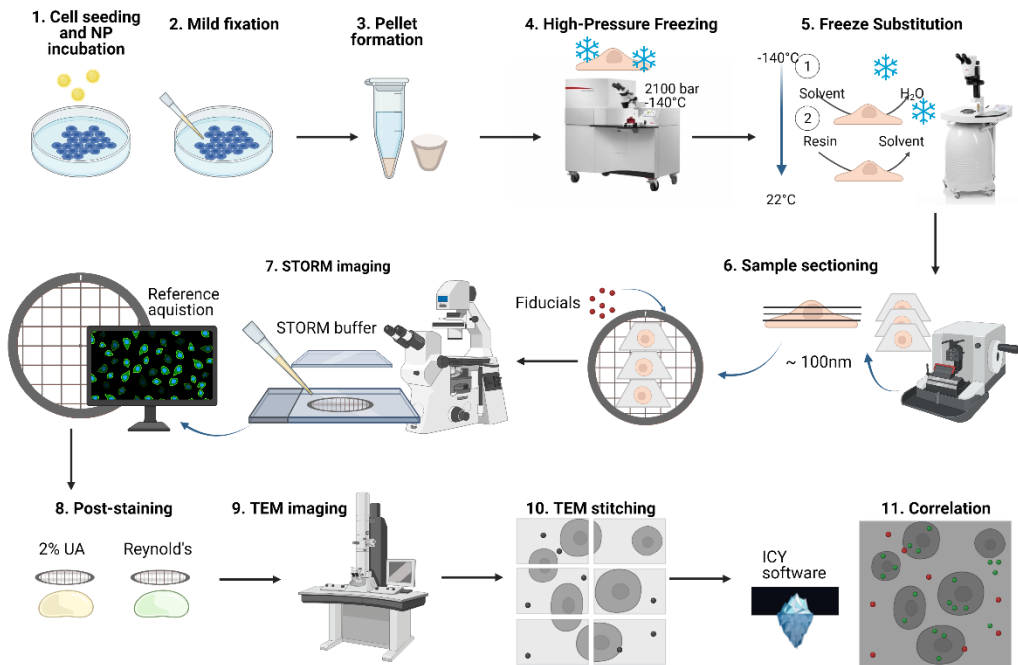
Figure 2 *Overview of dSTORM-TEM correlative protocol. After the formulation of PLGA-PEG DiI loaded NPs, the NPs were incubated with HeLa cells for specific time periods, and mildly fixed. Then, after scraping, the cells were centrifuged, and the resulting pellets were high-pressure frozen, and freeze substituted, then thin-sectioned (70-100 nm sections) using an ultramicrotome. The thin sections were picked up on a TEM grid and fiducials markers attached to aid in correlation. The grids were first imaged by dSTORM microscopy using a dSTORM buffer, and reference images of the region of interest (ROI) were acquired. The sections were then post-stained using the heavy metals 2% uranyl acetate and 3% lead citrate (Reynolds). Then, the ROI was found in TEM and imaged by sequential imaging, followed by stitching of the sequential images. Finally, the respective dSTORM and TEM images of the same ROI were overlapped using the open-source software ICY (ec-CLEM) by using the fiducial markers in both images.*

Briefly, PLGA-PEG DiI loaded NPs were formulated via the nanoprecipitation method[232,240,266] and characterized using TEM for diameter and morphology (Figure A3.2), dynamic light scattering (DLS) for the hydrodynamic radius (Figure A3.3) and

zeta potential for the surface charge (Figure A3.3). HeLa cells were then incubated with the NPs for specific time points. The cells were then mildly chemically fixed as this aids in cross-linking cellular structures and preserving membrane structures, without quenching fluorescent signal[319]. The cells were then pelleted and high-pressure frozen (HPF), ensuring vitrification at high pressures without the formation of ice crystals. The samples were then processed by freeze-substitution (FS; Table 1 Materials and Methods). During this process, cells were further stained and fixed and resin embedded at low temperatures which were gradually increased to ambient temperature. As a fixing and staining agent uranyl acetate (0.1% UA) was used, since stronger fixatives such as osmium tetroxide can strongly quench fluorescence even at low concentrations[218,269]. A lowicryl HM20 resin was chosen, as it is designed for low-temperatures and due to its low viscosity, it can allow penetration of *d*STORM imaging buffers into the resin-embedded samples. The resin-embedded cells were then sectioned to ultrathin sections (70-100 nm) using an ultramicrotome and sections were picked up on formvar-coated nickel TEM grids. These specific grids were used since formvar layer allows an easier pick up of ultrathin sections, whilst the nickel grid does not react with any chemicals in the *d*STORM buffer. 100 nm Tetraspeck beads were then attached to the thin sections and used as fiducial markers, due to their visibility in both microscopes. Next, the grid was sandwiched between a coverslip and a glass-slide with the *d*STORM buffer and sealed. The sample was first imaged by *d*STORM, as subsequent staining steps for TEM quench fluorescence, and reference images were acquired showing the location of the region of interest (ROI) on the grid. To enhance the contrast, the grids were post-stained after *d*STORM imaging with 2% UA and 3% lead citrate (Reynolds), then later imaged by TEM. Due to its superior resolution, the field-of-view (FOV) is smaller than that in *d*STORM, thus consecutive images were acquired to cover the required FOV, and later stitched automatically in Adobe Photoshop CS9. The *d*STORM-TEM image correlation was achieved using the open access eC-CLEM software package[314]. For extra protocol details see Materials and Methods in this Chapter.

2.4 NP intracellular trafficking

An example CLEM image using both low-resolution FM and *d*STORM images is shown in Figure 3. The TEM canvas of the cells is appreciated in Figure 3A, with the respective PLGA-PEG NP fluorescence visible in green in Figure 3B and fiducial markers in red in Figure 3C. The resulting low-resolution FM-TEM overlap of these images is shown in Figure 3D. Whilst the low-resolution FM images gives a clearer representation of the NP signal at larger FOVs (Figure 3D), the superior resolution of *d*STORM is better appreciated at greater magnifications (Figure 3E vs Figure 3F). Due to the greater match in resolutions between *d*STORM and TEM, single NPs can be accurately assigned to specific cellular compartments as observed in Figure 3F.
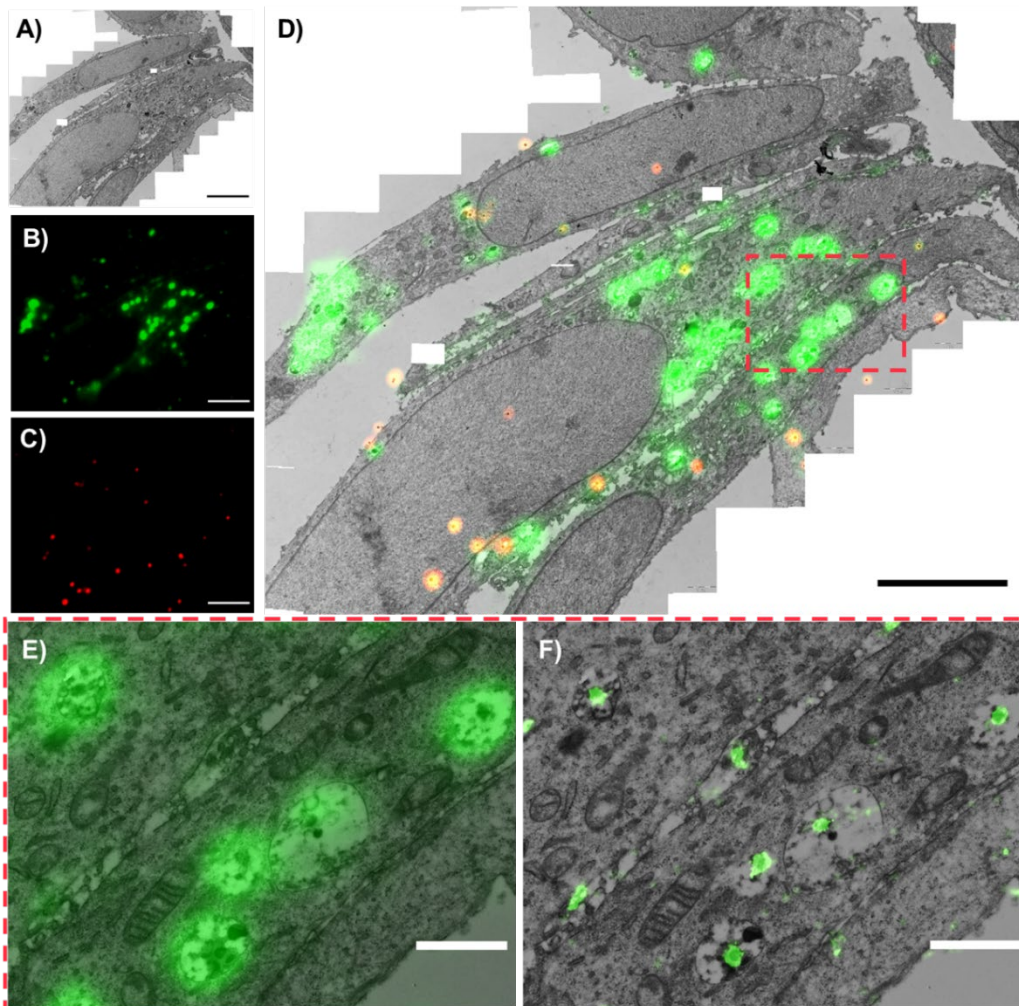
Figure 3 *Correlative low-resolution FM/dSTORM and TEM images of PLGA-PEG DiI loaded NPs internalized in HeLa cells. Large view images of the ROI of A) the stitched TEM image, B) PLGA-PEG NPs (DiI) signal and C) fiducial markers both in low-resolution FM, and D) correlative low-res FM-TEM image (scale bars A-D = 5 µm). Magnified views of the boxed region in D), where E) low-resolution FM-TEM correlated image of PLGA-PEG NPs and F) dSTORM-TEM correlated image of PLGA-PEG NPs, highlighting the difference in resolution between the two FM techniques (scale bars E and H = 1 µm).*

The ultrastructure in TEM was very well maintained even after using high laser power by *d*STORM (Figure 4), allowing the morphological detection of various cellular organelles, including early endosomes (EEs), late endosomes (LEs), lysosomes, mitochondria, and nuclei.
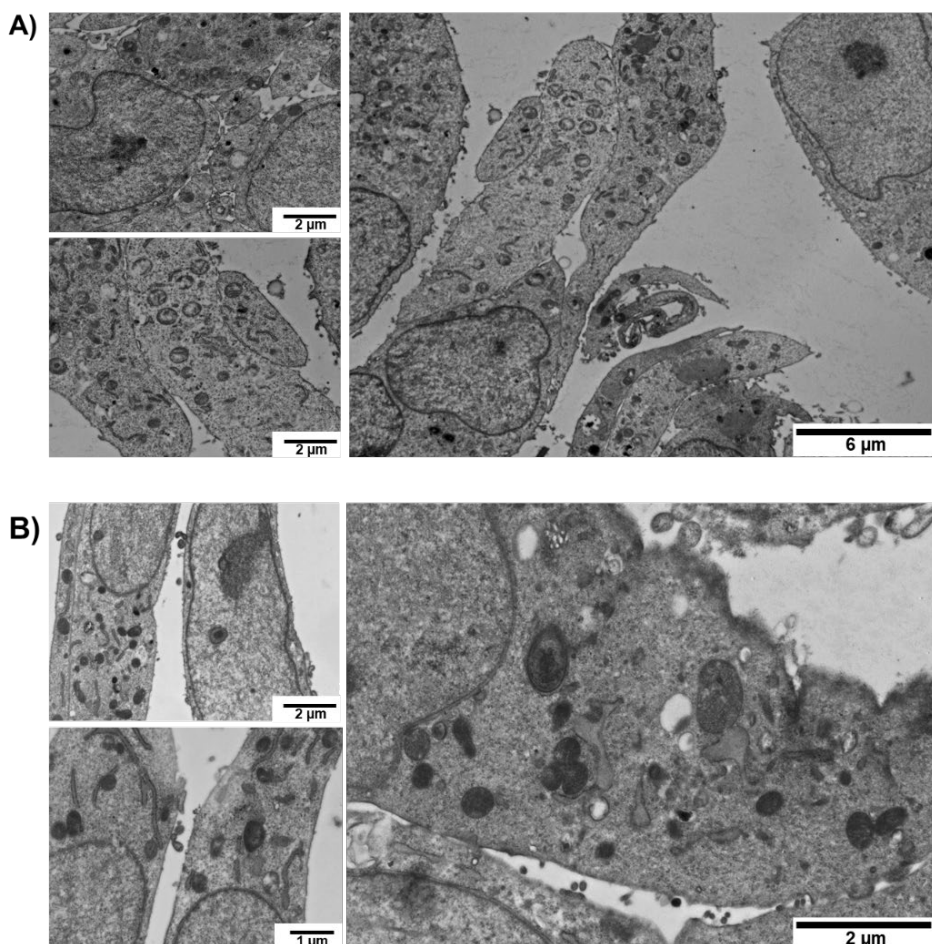
Figure 4 *Ultrastructural preservation after dSTORM-TEM protocol treatments. A) Ultrastructure of HeLa cells incubated with PLGA-PEG DiI loaded NPs and imaged with dSTORM. B) ultrastructure of HeLa cells without NP incubation and without dSTORM imaging (control).*

Markedly, the mild chemical fixation protocol prior to HPF and FS did not lead to background autofluorescence (Figure A3.4). Additionally, our protocol did not rely on the use of osmium tetroxide (OsO_4) as a contrast enhancer/fixative, whilst the use of low concentration of UA (0.1%), resin and UV polymerization treatments maintained an adequate fluorescence signal viable for further measurements and did not affect cellular ultrastructure. These are necessary pre-requisites when optimizing a CLEM technique, and due to their successful realization, we were able to assign single NPs within specific cellular compartments and track their cellular voyage at different time points.

The accuracy error in correlation was calculated automatically using the eC-CLEM plug-in in ICY[314] which ranged between 40-60 nm depending on the number of fiducial markers in the FOV. For this image, 20 fiducial markers were present, and the accuracy was of 52 nm (Figure A3.5), in line with other values reported using super-resolution

CLEM and fiducial markers of similar size[322]. Briefly, if the registration error of the fiducials is greater than the predicted registration error, a non-rigid transformation is applied (warping), which is useful if any deformations occur during preparation steps such as chemical fixation/dehydration[314]. Notably, correlation between two techniques can be limited by i) the limit of resolution of the least resolved technique and ii) the correlation accuracy between the two techniques. Since the correlation accuracy error is slightly greater than the resolution limit of *d*STORM (approx. 20 nm)[165], *d*STORM-TEM provides a more accurate assignment of single NPs to specific organelles as opposed to correlation with low-resFM (approx. 250 nm). This can be clearly visualized in Figure 3E and 3F.

We used the proposed correlative protocol to explore the intracellular fate of PLGA-PEG NPs. To do this, we first incubated HeLa cells with NPs for different periods of time (1 h, 8 h and 24 h) and treated the cells as described in the previous section. A 4 h pulse was done for the 8 h and 24 h time-points and then NPs were chased for the remaining respective time. We first correlated the low-resolution FM images with the respective TEM images as this allows a clearer correlation at a large FOV (Figure 5). Notably, at 1 h NPs were still found attached to/surrounding the cell membrane, which reduced with increasing incubation times. Punctate intracellular signal was seen at all time points, indicating NP uptake into endo-lysosomal compartments had started prior to 1 h, agreeing with previous results under similar conditions[323–325].

We then correlated the *d*STORM and TEM images, since the increase in resolution from *d*STORM allowed precise tracking of individual NPs within the cellular milieu and understanding of their intracellular pathways. Briefly, NPs are typically taken up via endocytosis, an energy-dependent mechanism (caveolae- and clathrin mediated), phagocytosis, macropinocytosis and pinocytosis[137]. After endocytosis, NPs are engulfed by endocytic vesicles that fuse to form early endosomes (EEs), and then mature to late endosomes (LEs) and lysosomes[154,326–329] (Figure 5A). This intracellular pathway is thought to be an important limiting step for various formulations that require cytosolic/nuclear delivery of cargo such as chemotherapeutics/RNA/DNA. The lack of methods that allow single NP tracking within the ultrastructure of the cell prevents gaining important insights into their intracellular trafficking and developing more effective nanomaterials. Although in this work we use standard non-functionalized PLGA-PEG NPs to demonstrate the capability of super-resolution CLEM, the protocol is extendable to other fluorescently labelled nanomaterials and/or their cargo.

NPs were imaged during their cell uptake (Figure 6B, left panel), to their distribution in EE (Figure 6C), LE (Figure 6D) and lysosomes (Figure 6E). The NPs were assigned to different compartments by morphological comparison between distinct vesicles as previously described by Fermie et al. using a CLEM approach[213]. EE typically have a diameter between 100-500 nm with an electron-lucent lumen and loosely packed intraluminal vesicles (ILVs); LE have a diameter between 250-1000 nm with densely packed ILVs; lysosomes have diameters between 200 to >1000 nm with an electron-dense lumen and membrane whorls. For extra correlative images at 1 h, 8 h and 24 h see Figure A3.6, Figure A3.7 and Figure A3.8, respectively. Occasionally we were also able to detect non-endosomal NPs (NE), i.e. found inside the cell but not in any of the three compartments/nucleus. Notably, polymeric NPs such as PLGA-PEG may be

slightly visible at the cell membrane but not at all visible within the cellular milieu by TEM alone, showing the suitability of this method to a wide range of nanomaterials.
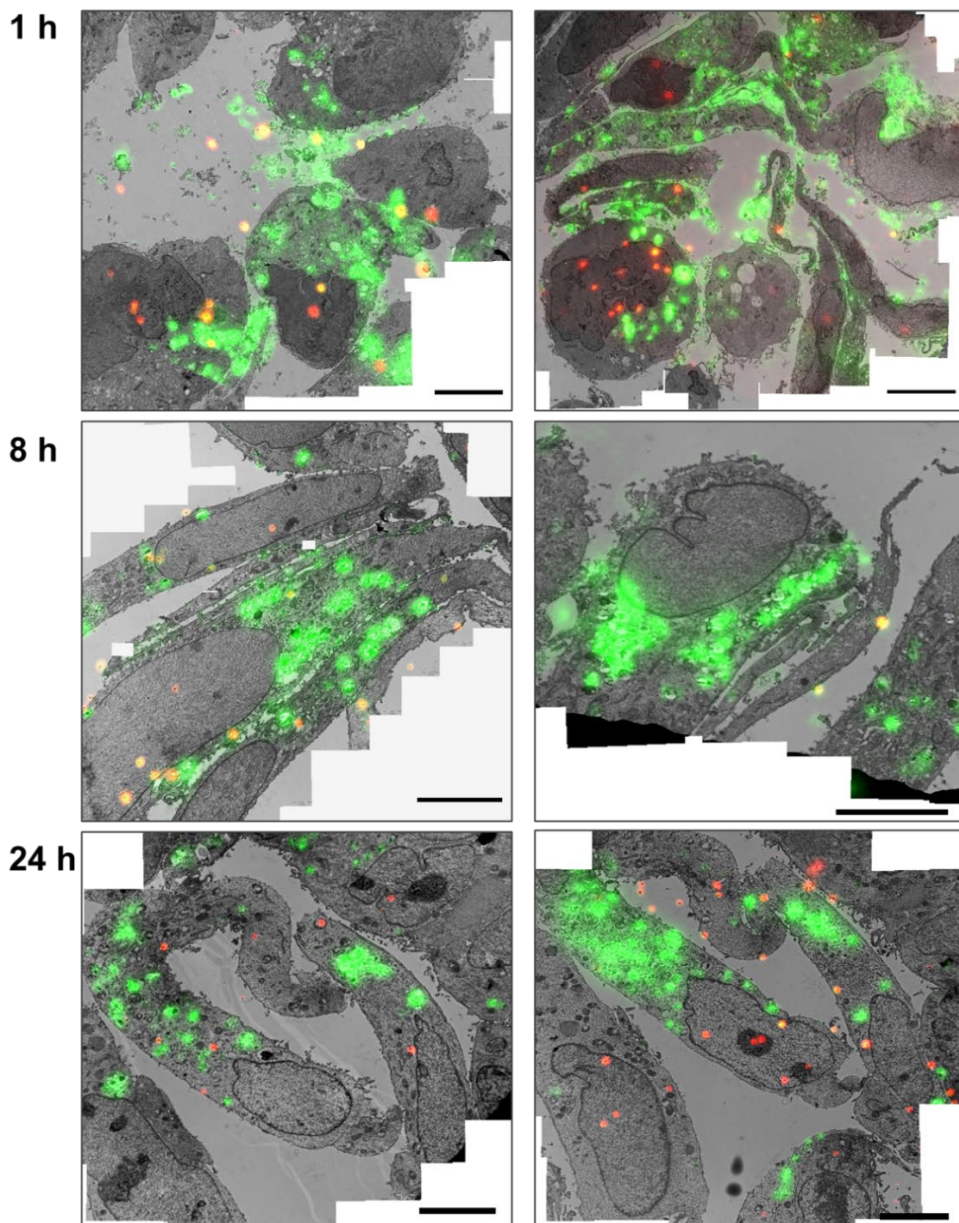
Figure 5 *CLEM (low resolution-TEM) images of PLGA-PEG NPs incubated with HeLa cells at different time points (1 h, 8 h and 24 h). NP signal is seen in green and fiducial marker (Tetraspeck) signal is seen in red/orange. Scale bars = 5 μm.*
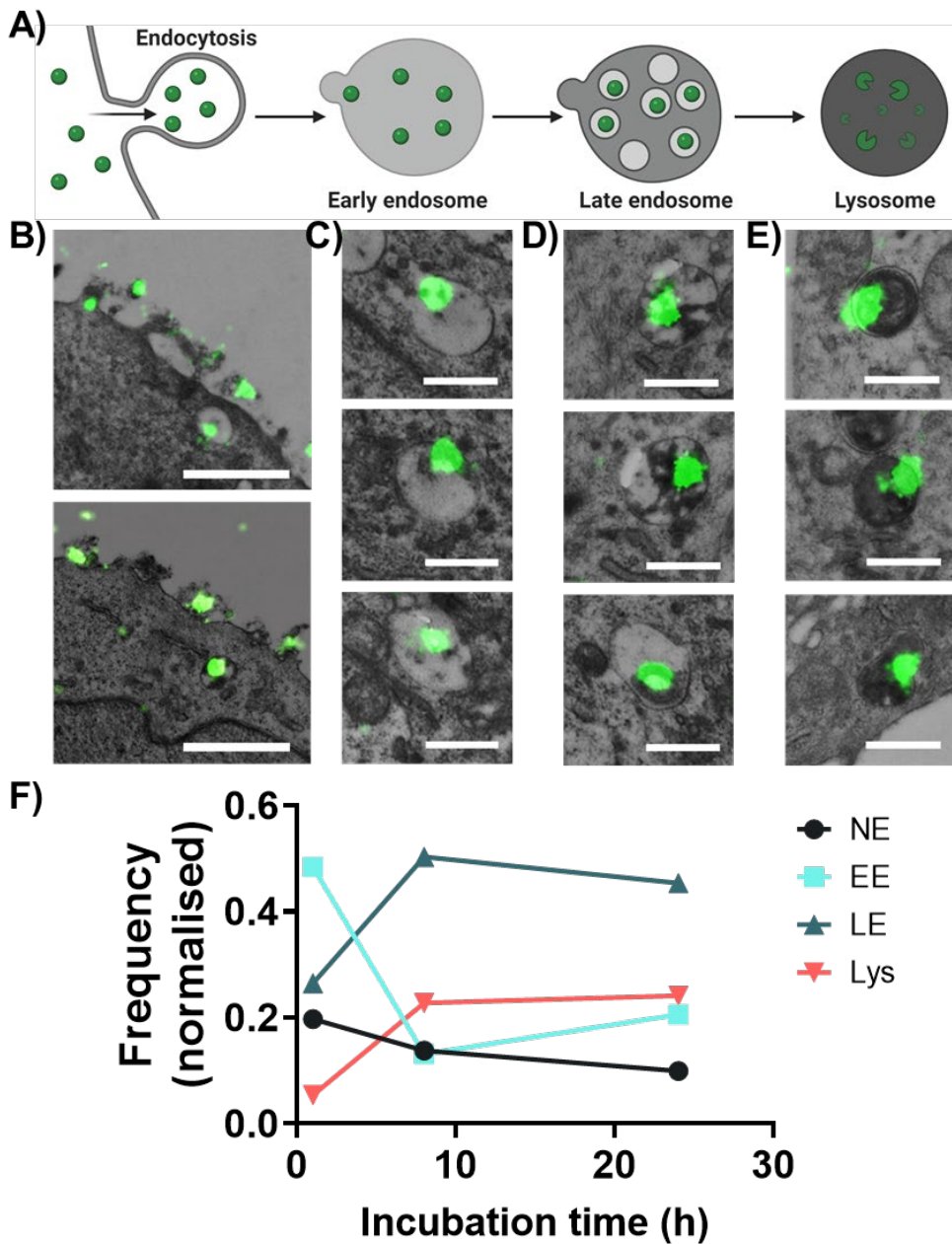
Figure 6 *dSTORM-TEM correlation for intracellular trafficking of PLGA-PEG NPs. Scheme of A) Endo-lysosomal pathway consists of NP endocytosis, and trafficking by early endosomes (EE) to late endosomes (LE) and to lysosomes in HeLa cells. B) PLGA-PEG DiI loaded NPs detected by dSTORM and localized within different cellular compartments by TEM: B) during endocytosis, C) in EE, D) in LE and E) in lysosomes. F) Time course of quantitative dSTORM-TEM analysis of PLGA-PEG NPs progressing through EE, LE, lysosomes and non-endosomal compartments (NE). Normalization was done using the total number of NPs at each time point. At 1 h N=223, at 8 h N=145 and at 24 h N=141. Scale bar B = 1 μm, C-E = 500 nm.*

For the quantification, NP clusters were counted in each compartment and normalized based on the total number of NPs (Figure 5F). At 1 h, most NPs were found within the EE ($\sim$ 48%), followed by LE ($\sim$ 26%) and NE ($\sim$ 20%), with the minority in lysosomes ($\sim$ 5%). This suggests that PLGA-PEG NPs were taken up by cells via endocytosis and then transported through the classic endocytic pathway, as has been previously reported[329,330]. As the incubation time increased to 8 h, the population of NPs in EE decreased to $\sim$ 13%, whilst it increased in LE to $\sim$ 50% and in lysosomes to $\sim$ 23%, suggesting that NPs have progressed along the endo-lysosomal pathway. At 24 h the distribution of NPs within the specific compartments remained similar to that at 8 h. This could be explained by the fact that at 8 h more NPs were still found at the membrane compared to 24 h (Figure 5, Figure A3.9), suggesting that between 8-24 h NPs were still being endocytosed and transported through the endocytic pathways, agreeing with previously reported results[327].

As previously stated, NPs were also found in NE compartments (Figure 7A), albeit in small amounts. Since PLGA-PEG NPs are not expected to achieve endosomal escape, we believe these results could be due to broken organelles releasing NPs into the cytoplasm as previously shown[331], as partially broken endo-lysosomal compartments containing NPs were seen by *d*STORM-TEM (Figure 7B). However, these results could also be due to NPs that have degraded and released the dye – this could be tested by labelling the polymer using a spectrally different dye, in order to track both carrier and cargo. Although in this experiment we were not interested in studying endosomal escape, being able to localize and quantify NPs outside of endo-lysosomal compartments indicates that our technique is well-tailored to study this process as will be demonstrated later.
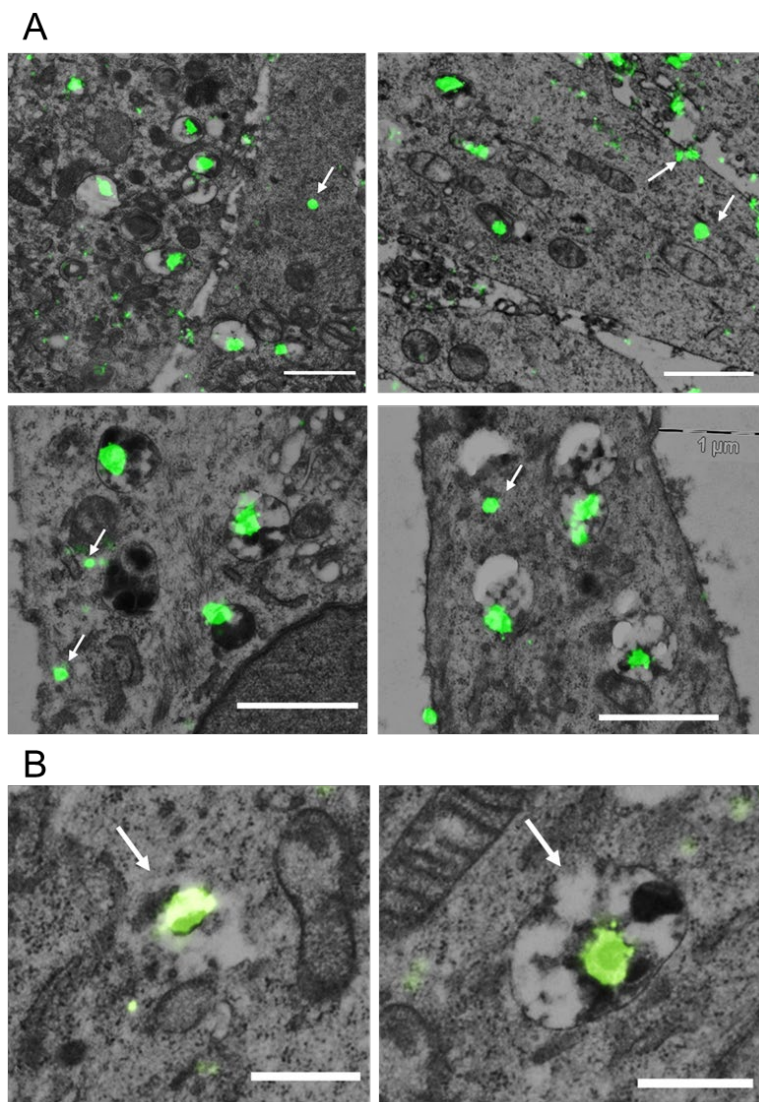
Figure 7 dSTORM-TEM images of PLGA-PEG NPs incubated with HeLa cells. A) White arrows highlight NPs found outside of endo-lysosomal compartments and denoted as 'non-endosomal (NE)' throughout the main article (NPs found on the cell membrane were not included in this group). Scale bars = 1 µm. B) White arrows highlight ruptured cellular compartments. Scale bar = 500 nm.

Notably, a 72-h incubation was also carried out, which showed no visible fluorescence signal in 500 nm semi-thin sections, as opposed to the other time points (Figure 8). This result was surprising since DiI loaded PLGA-PEG NPs were previously shown to still be internalized at 72 h in MCF7 cells[106]; however, the authors of this paper used a 6-fold greater NP concentration for the incubation as compared to our experiment.
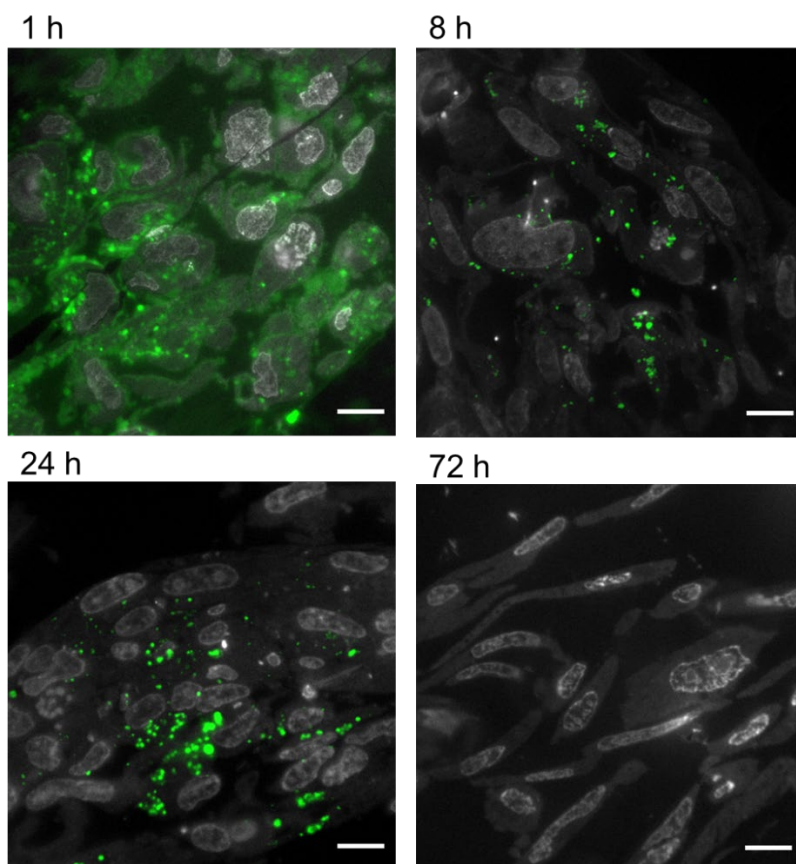
Figure 8 *Fluorescence signal of PLGA-PEG NPs incubated for different time points (1 h, 8 h, 24 h
and 72 h) with HeLa cells in 500 nm semi-thin sections after CLEM protocol. At 1 h signal looks
diffuse around the cells, with some localized signal inside cells. At 8 h and 24 h the signal looks more
localized in specific intracellular compartments. At 72 h there is a lack of signal. Scale bar = 10 µm.*

To get a better understanding of NP internalization at the different time points, a flow-
cytometry assay was carried out (Figure 9). As expected, the lowest internalization is
seen at 1 h, followed by a significant increase at 8 h. At 24 h there was a decrease in
the number of internalized NPs, followed by a further decrease at 72 h, comparable to
the uptake at 1 h. These results agree with the decrease in fluorescence seen at 72 h
in Figure 8 and could be due to a release of NPs from the cells through the recycling
endosome system and/or through the exocytosis pathway as demonstrated previously
for PLGA NPs[329,330] and other nanomaterials[137,332–334]. Since these NPs reach the
lysosomes, it is also possible that they are degraded, as previously shown for PLGA
NPs[329]. Another possible reason is that since HeLa cells have a doubling time of
roughly 33-35 h[335], after this time intracellular NP load is expected to decrease as a
result of cell division[336]. Finally, CLEM is still a low-throughput technique, meaning that
if the NP load is low or has been diluted/degraded, there is a high chance that NP
presence will not be detected. Further systematic analysis of more time points would
be required to fully understand these observations.
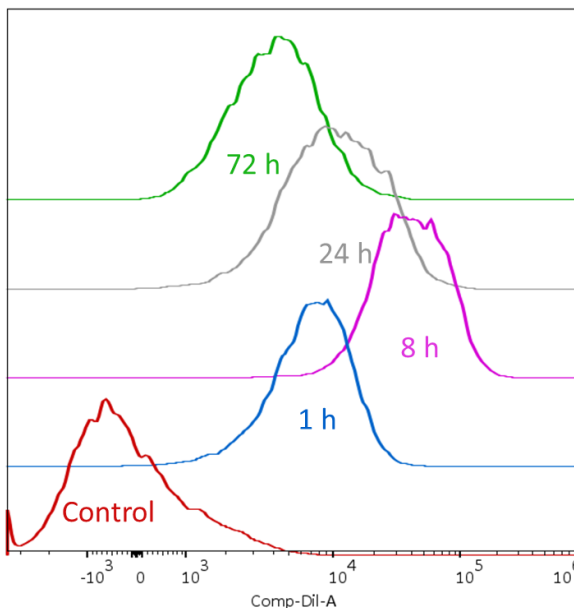
	Sample Name	Subset Name	Count	Freq. of Parent	Mean : Comp-DiI-A
	E2 72.fcs	cells	9917	74.8	5299
	D2 24.fcs	cells	9959	68.4	14316
	C2 8.fcs	cells	9928	69.5	47709
	B2 1.fcs	cells	9897	70.0	8452
	A2 C.fcs	cells	9832	69.6	-128

Figure 9 Cellular uptake using flow cytometry of PLGA-PEG NPs in HeLa cells at different incubation times. The highest number of NPs within/on the cells is found at 8 h (purple) > 24 h (grey) > 1h (blue) > 72 h (green). The red color indicated background fluorescence due to cells only (control).

Using the information from *d*STORM-TEM correlative images, we were able to assign and quantify the distribution of NPs among different cellular compartments at a given time point. This is not possible with the classical confocal colocalization analysis that is generally limited to two structures at a time and suffers from resolution issues (structures in proximity tend to colocalize due to lack of resolving power). Overall, these results demonstrate the applicability of *d*STORM-TEM correlative imaging in tracking individual nanomaterials and/or their cargo intracellularly, for a better understanding of their biological fates. However, there is a clear need to develop more high-throughput protocols that would result in more user-friendly technique, more significant statistics, and the ability to catch rare events in the act.

2.5 The effect of chloroquine on NP intracellular distribution

Our previous results showed that PLGA-PEG NPs were mainly entrapped within the endo-lysosomal pathway. Endosomal entrapment is a process that typically happens after endocytosis, whereby the carrier-drug ensemble is entrapped and degraded in endo-lysosomal compartments, and thus presents a key bottleneck in ensuring effective therapeutic delivery using nanocarriers[122,143,146,147]. As previously mentioned, current ensemble techniques used in this field prevent the thorough understanding of endosomal escape mechanisms. We therefore wanted to demonstrate the applicability

of our proposed *d*STORM-TEM protocol on studying endosomal escape. To promote
the escape of PLGA-PEG NPs from endo-lysosomal compartments, we used the
lysomotropic endosomal escape enhancing compound chloroquine[337,338] (Figure 10).
Cells were incubated with 100 µM chloroquine for 4 h, followed by a 4 h NP pulse and
a 4 h chase (total 8 h), before being treated and thin sectioned (+CQ, Figure 10B), and
compared with an identical sample without chloroquine treatment (-CQ, Figure 10 A).
After imaging by *d*STORM-TEM, NP clusters were counted in each compartment and
normalized according to the total number of NPs (Figure 10C).

For the cells not treated with chloroquine (-CQ), PLGA-PEG NPs were found mainly in
LE and lysosomes, with a minority found in EE and NE compartments. In contrast,
chloroquine treatment (+CQ) caused a 4-fold and a 2-fold decrease in NPs found in
lysosomes and LE, respectively, whilst causing a 3-fold and a 2-fold increase in NPs
found in EE and NE compartments, respectively (Figure 10C). For extra *d*STORM-
TEM images see Figure A3.10. These results agree with the documented behavior of
chloroquine as a damage-inducing agent for vesicles in the late stages of the endo-
lysosomal pathway (low pH compartments), leading to less NP found in LE and
lysosomes, but more within the EE and cytoplasm.
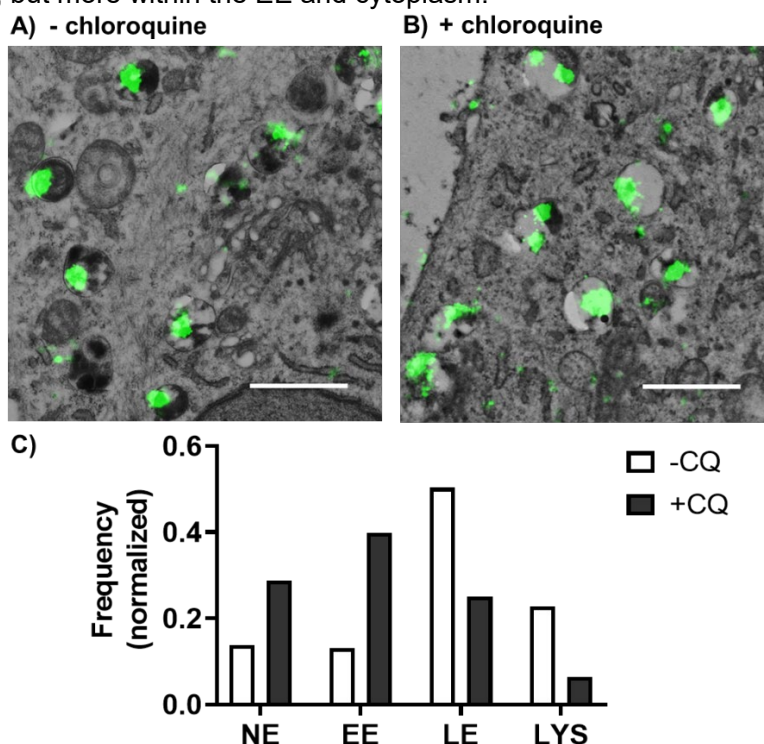
Figure 10 *dSTORM-TEM correlation for studying the effect of chloroquine on PLGA-PEG NP
intracellular trafficking. PLGA-PEG DiI loaded NPs were detected by dSTORM and localized within
different cellular compartments using TEM. dSTORM-TEM correlative images of A) NPs incubated
with HeLa cells for 8 h, and B) HeLa cells treated with 100 µM chloroquine for 4 h prior to 8 h NP
incubation. A 4 h NP pulse and a 4 h NP chase were carried out for both samples. Scale bars = 1000
nm. C) Quantitative analysis of NP distribution within different cellular compartments without (-CQ)
and with chloroquine treatment (+CQ). Normalization was done using the total number of NPs at each
condition: -CQ N=145, + CQ N=236.*

Endosomal entrapment is a recognized bottleneck in drug delivery and for this increasing research is aimed at designing formulations with endosomal escape in mind. However, whilst the arsenal of nanomaterials is increasing, there is still a tendency in the field to use qualitative and inconsistent techniques (e.g. co-localization studies using confocal microscopy) to study their endosomal escape properties. To be able to design more successful nanocarriers, we must be able to track their intracellular pathways using more quantitative and direct techniques, and this work highlights the relevance of *d*STORM-TEM in achieving this quest.

3. Conclusions

In this work, we have introduced an efficient *d*STORM-TEM correlative protocol to study the intracellular pathway of PLGA-PEG NPs in HeLa cells, that allows the localization of single NPs (*d*STORM) within cellular compartments (TEM) with nanometric resolution in both microscopies, whilst maintaining NP fluorescence and preserving cellular ultrastructure.

PLGA-PEG NPs were localized in different cellular endo-lysosomal and in non-endosomal compartment at several incubation times. We showed that at early time points, NPs were found mainly in EE, whilst at later time points in LE and lysosomes. After 72 h however we were unable to image NPs by CLEM due to a loss of fluorescence, which we attributed to various already proven factors, including exocytosis, cell division and/or particle degradation. Since PLGA-PEG NPs were entrapped within the endo-lysosomal pathway, we then studied their endosomal escape upon incubation with the lysomotropic agent chloroquine. Using our *d*STORM-TEM protocol we quantified the cellular distribution of NPs, and showed a decrease of NP localization within low pH compartments (LE and lysosomes), and an increase in EE and NE compartments (i.e. endosomal escape).

Importantly, the proposed *d*STORM-TEM protocol can image and localize NPs that are not detectable by TEM alone and thus we envision that it could be applied to track many fluorescently labelled nanomaterials and/or their cargo within the ultracellular environment. Particularly, limiting steps in intracellular delivery such as endosomal entrapment could be studied for more complex nanomaterials such as polyplexes or lipoplexes that require nucleic acid delivery to the nucleus. We believe that advanced microscopy techniques such as CLEM are of great relevance in obtaining complex information that we are currently lacking and could facilitate the rational and efficient design of nanomaterials for drug delivery.

Although commercial systems for integrated microscopy have been developed[209], they are still a long way from being incorporated into general laboratories. Our protocol requires only equipment typically found within light and electron microscopy facilities, thus allows a wider implementation by the scientific community. Yet, for correlative techniques to be picked up as standard techniques in nanomaterial characterization and demonstrate their worth, more automated, and high-throughput imaging protocols will be required. We believe that a synergistic effort from various scientific disciplines could soon make this a reality.

4. Materials and Methods

Nanoparticle formulation:

PLGA-PEG NPs were formulated via the precipitation-solvent evaporation (nanoprecipitation) method according to literature[232] and to our previously reported data[106,240,266]. PLGA (PLGA, 50:50 LA:GA, Mw 25-35 kDa; PolySciTech, Akina) and PLGA-PEG (PLGA LA:GA 50:50, Mw. 30 kDa and PEG 5kDa; PolySciTech, Akina) were dissolved in the solvent acetonitrile (ACN, Chem-Lab, HPLC grade, Sigma Aldrich) to give stock solutions. To ensure maximum dissolution, the solutions were maintained at RT. for 2h, with 1 min vortex every 30 min, followed by a final 10 min bath sonication. Fresh milliQ water was filtered with a 0.22 μm sterile filter (Merck Milipore, Millex GP) and used as the antisolvent phase. 1,1′-dioctadecyl-3,3,3′,3′-tetramethylindocarbocyanine Perchlorate (DiI, lipophilic cationic carbocyanine dye; Sigma Aldrich) was weighed and dissolved in ACN to a concentration of 1.1 mM and used as a stock solution. PLGA and PLGA-PEG stock solutions were mixed to give a 15:85 (wt:wt) ratio, respectively, and DiI stock solution was added to give a final concentration of 30 μM.

4 mL of the anti-solvent phase (water) was added to a glass vial (5mL) with a magnetic stirring bar (VWR, 8x3mm) and placed on a magnetic stirring plate (IKA3050009 Big Squid White) at 200-300 rpm. Maintaining a 10:1 ratio between antisolvent and solvent, 400 μL of the solvent phase (polymeric solution) was added dropwise to the stirring antisolvent phase using a 20-200 μL pipette. The final NP suspension was allowed to stir for 5h to enhance solvent evaporation. The capped glass vial was then kept in the fridge at 4-8 ˚C until further use.

Cell plating and nanoparticle incubation:

HeLa cells (ATCC) were seeded on a 92 x 17 mm cell culture dish (Nunc™, Fisher Scientific) and incubated for 24h in Dulbecco's Modified Eagle Medium (DMEM, with L-Glutamine 10 mM, 4.5 g/L D-glucose and pyruvate, Gibco) supplemented with FBS 5% (Gibco) and penicillin/streptomycin 1% (Biowest), at 37 ˚C and 5% CO_2, to full confluency. After the incubation, the medium was removed and the cells washed thrice with warm PBS (1x, pH 7; Thermo Fisher). Then PLGA-PEG NPs diluted to 1.5mg/5mL in OptiMEM™ (Thermo Fisher) were added to the cell plate and incubated for either 1h, 8h, 24h or 72h at 37 ˚C and 5% CO_2. For the latter 3 time points, the NP solution was removed after 4h and washed thrice with PBS (at 37 ˚C), then replaced with medium for the remaining incubation time.

Next, the cells were first fixed for 30 min at RT. by adding an equal volume of Fixative 1 (4% paraformaldehyde, 0.1% glutaraldehyde, in 0.1M PHEM (240 mM PIPES, 100 mM HEPES, 8 mM MgCl2, 40 mM EGTA; pH 6.9)), in an equal volume of the FDMEM found in the cell culture dish. Then, fixative solution was discarded and replaced with 5mL Fixative 1 for another 30 min at RT. Then, the solution was removed and replaced with 1.5mL of Fixative 2 (2% paraformaldehyde in 0.1 M PHEM) for 5 min at RT., ensuring that the cell dish is evenly covered. The cells were then scraped off (whilst in Fixative 2) using a cell scraper and transferred to a 1.5mL Eppendorf. These were then

pelleted using a centrifuge (Eppendorf 5804 R) at 2500 rpm (1200 rcf) for 10 min at RT. The supernatant was replaced with 1 mL Fixative 2, then centrifuged again. The pellet was kept in Fixative 2 at 4 °C and covered from light until next steps.

High-pressure freezing, freeze substitution, resin embedding and ultramicrotomy:

The following protocol is an adaptation of the protocol used by Katheder et al.[319], with some modifications. Briefly, pellets were suspended in 20% dextran (in PBS), pipetted to 200-µm-depth planchettes and high-pressure frozen (Leica HPM100). The freeze substitution and resin embedding steps were carried out using a temperature-controlled AFS2 (Leica). For full details on freeze substitution protocol see **Table 1**. Briefly, sample carriers were transferred to 4 mL freeze substituent (0.1% (w/v) uranyl acetate in acetone) inside the pre-cooled AFS2 chamber, and the freeze substitution steps occurred from -140 °C to -45 °C (steps 1-5). Then, the samples were washed 4 times in acetone at -45 °C (steps 6-9), followed by infiltration with increasing concentrations of Lowicryl HM20 resin (25%, 50%, 75%, and 100%; steps 10-14; Electron Microscopy Sciences). Finally, two last steps of HM20 infiltration take place, whilst the temperature is increased slowly from -48 °C to 22 °C (steps 15-16). UV-polymerization occurred in steps 14-16.

Two semithin sections (500 nm) were obtained for each sample on an Ultracut UC7 ultramicrotome (Leica). One was stained using methylene blue, for a first visual check-up of cell morphology. The second semithin section was stained using 20 µg/mL Hoechst (Sigma-Aldrich) in PBS for 10 min at RT. and imaged using a Nikon N-STORM microscope to check for fluorescence. Then, ultrathin sections (70-100 nm) were obtained and collected on a 200-mesh formvar film-coated hexagonal nickel grids.

Table 1. Freeze substitution steps.

Step	T_{start} (°C)	T_{end} (°C)	Slope (°C/h)	Time (hh:mm)	Reagent	%	UV
1	-140	-140	0	01:00	Acetone/UA 0.1%	100%	
2	-140	-90	50	09:00	Acetone/UA 0.1%	100%	
3	-90	-90	0	80:00	Acetone/UA 0.1%	100%	
4	-90	-45	5.6	08:00	Acetone/UA 0.1%	100%	
5	-45	-45	0	04:00	Acetone/UA 0.1%	100%	
6	-45	-45	0	01:00	Acetone	100%	
7	-45	-45	0	01:00	Acetone	100%	
8	-45	-45	0	01:00	Acetone	100%	
9	-45	-45	0	01:00	Acetone	100%	
10	-45	-45	0	24:00	3 Acetone/1 Lowicryl HM20	100%	
11	-45	-45	0	08:00	2 Acetone/ 2 Lowicryl HM20	100%	
12	-45	-45	0	24:00	1 Acetone/ 3 Lowicryl HM20	100%	
13	-45	-45	0	24:00	Lowicryl HM20	100%	
14	-45	-45	0	24:00	Lowicryl HM20	100%	+
15	-45	22	4.7	14:24	Lowicryl HM20	100%	+
16	22	22	0	48:00	Lowicryl HM20	100%	+

Preparation for dSTORM imaging:

As per Figure 11, the grids were first placed on top of 40 µL drops of nuclei stain Hoechst 20 µg/µL (in PBS) for 10 min at RT. using a fine tweezer. The grids were then washed in 40 µL x3 consecutive milliQ water drops (1 min each). Next, for addition of fiducial markers, the grids were placed on a 40 µL drop of Tetraspeck (0.1 um diameter, ~1.8 × 10^{11} particles/mL in 2 mM sodium azide; Invitrogen) diluted x500 in PBS for 10 min, then washed through a drop of milliQ water.

A 40 µL drop of GLOX imaging buffer was placed on top of a glass microscopy slide (FisherBrand), containing a) 100 mM mercaptoethylamine (MEA), b) an oxygen scavenger system consisting of 5% glucose (wt/vol), 0.5 mg/mL glucose oxidase (Sigma-Aldrich) and 40 mg/mL catalase (Sigma), c) 15% glycerol, in PBS at pH 8.5. This was covered with a glass coverslip (Corning Cover Glass, thickness 1 ½, 22 x 22mm). The imaging chamber was then sealed using transparent nail polish to prevent buffer evaporation.
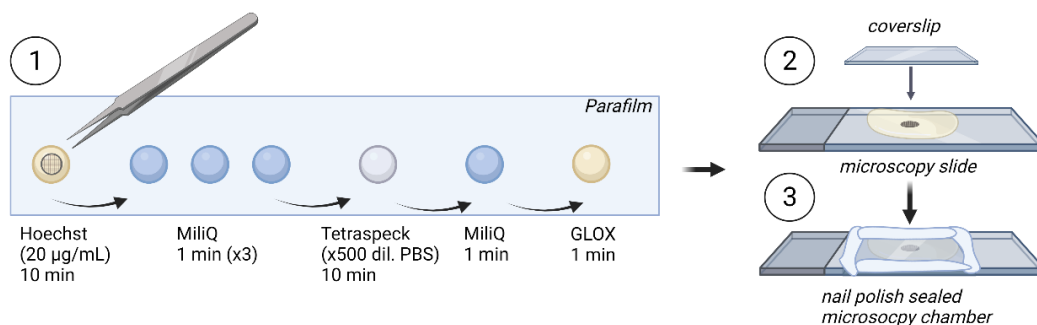
Figure 11 *Preparation of grids for dSTORM imaging.*

dSTORM imaging:

First, several reference images were taken as seen in Figure 12. The EPI lamp on DAPI filter was used to take a 13x13 stitch (1024x1024) of the distribution of the thin sections on the grid, using the NIS-Elements stitch function. 2) The second reference image was taken using the same lamp and filter at 1024x1024 inside the grid hexagon of interest, showing the cell nuclei, then 3) one image was acquired at 256x256, which gives the exact FOV that will be imaged by *d*STORM. Then, using the Nikon N-STORM system configured for highly inclined and laminated optical sheet (HILO) imaging, a low-resolution image of NPs was taken using the 561 nm (80 mW) laser, and a low-resolution image of the fiducial markers using the 647 (160 mW) laser, both at 2% laser power and 300 ms. These latter two images are used for correlation of low-resCLEM images.
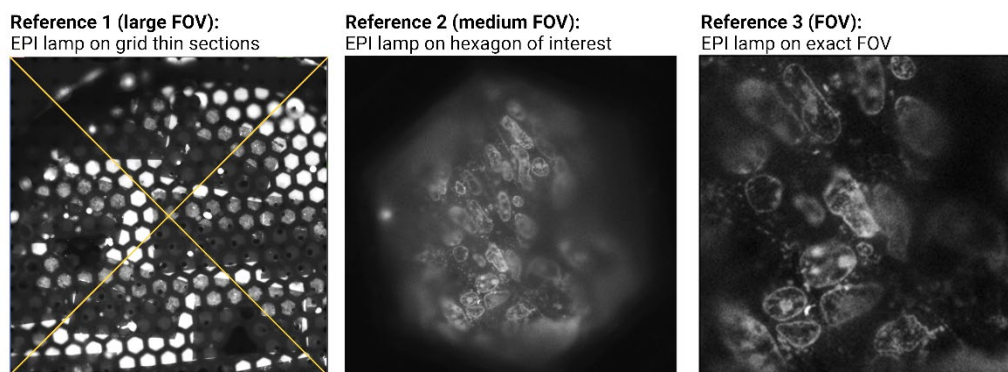
Figure 12 *Reference image acquisition in STORM. Where FOV is field of view.*

NPs were imaged by *d*STORM by illuminating the sample with the 561 nm (80 mW) laser at 100% power, and the fiducial markers with the 647 nm (160 mW) laser at 5% power. Fluorescence was collected using a Nikon 100x, 1.49 NA oil immersion objective and passed through a quadband pass dichroic filter (97335 Nikon). Images were acquired onto a 256 x 256-pixel region (pixel size 0.16 mm) of a Hamamatsu ORCA Flash 4.0 camera at 20 ms integration time. For the 561 channel 10,000 frames were acquired, and for the fiducial markers one frame was acquired every 100 frames in the 647 channel. Single molecules localization movies were analyzed with NIS element Nikon software. Data was analyzed with NIS Elements (Nikon) and ImageJ. No filters were applied to the STORM images presented in the article.

Preparation for TEM imaging:

To remove the grid from the microscopy chamber without ripping/damaging the grid, it is important to be as gentle as possible whilst doing the following steps. First, tissue embedded in acetone was used to gently remove the nail polish around the edges of the coverslip, trying to not move the coverslip whilst doing this. Then, as seen in Figure 13, the microscopy chamber was placed in a petri dish filled with milliQ water, and the coverslip was gently moved left and right, until detached from the microscopy slide, then with a tweezer, gently lifted. Next, the grid was picked up using a tweezer and washed to remove buffer salts on 5 x 40 µL milliQ water drops for 1 min each. The grid was allowed to dry for at least 15 min, and then stained.

For staining of the ultrathin sections, the grid was first placed on a 20 µL drop of 2% uranyl acetate (in milliQ water) for 30 min at RT. Then, the grid was removed using a tweezer and rinsed thoroughly in 200 mL milliQ water using a jet of water. If the grid dropped in the beaker, it was gently removed and washed with another 200 mL of milliQ water. The grid was then allowed to dry for at least 15 minutes. To prevent precipitation of lead in Reynolds' solution (prepared in house) by exposure to atmospheric CO_2, a pellet of NaOH was placed underneath a small petri dish, to exclude atmospheric CO_2. Then, a 20 µL drop of 3% lead citrate (Reynolds') was placed quickly underneath the petri dish, next to the NaOH pellet. The grid was then stained for 1 min and washed thoroughly using a 200 mL jet of milliQ water. The grid was then allowed to dry inside a desiccator for at least 2 h before imaging in TEM.
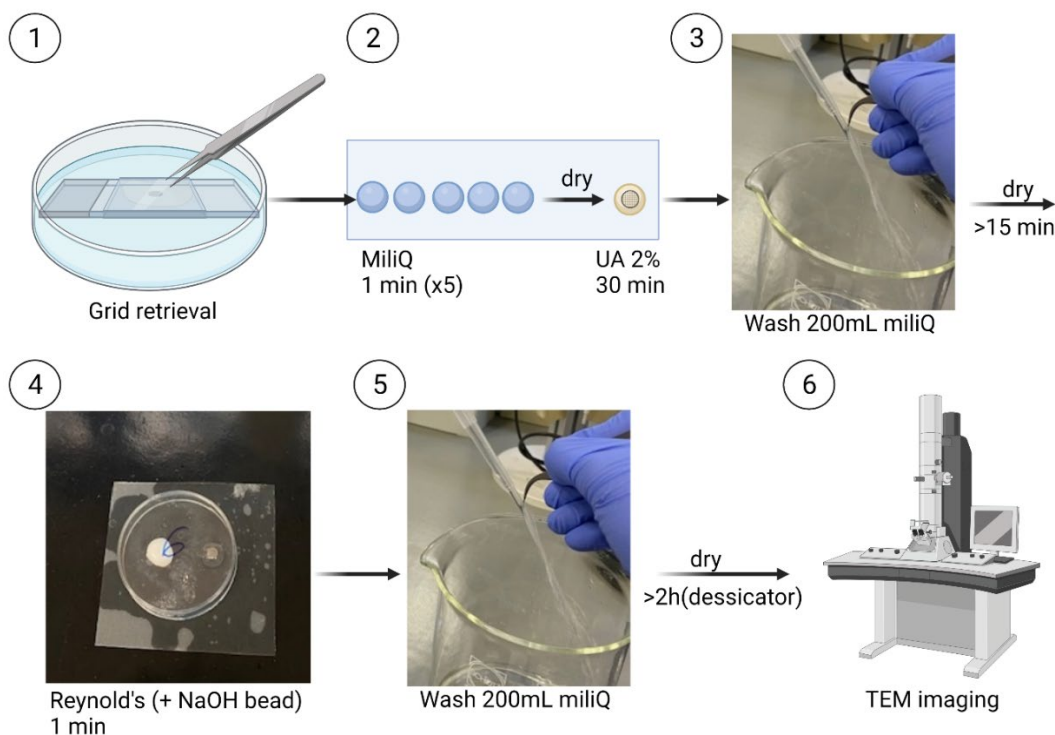
Figure 13 *Grid retrieval and contrasting steps for TEM imaging.*

TEM imaging:

The grids were imaged using a Jeol 1010 (Gatan, Japan) from the Electron Cryomicroscopy Unit from the CCiTUB, equipped with a tungsten cathode. Images were acquired at 80 kV with a CCD Megaview 1k x 1k and the Analysis 3.2 software. First, the ROI was located using a low-magnification function and the reference images acquired previously. Then, sequential images were taken of the ROI at a magnification of x15 000, which were later stitched using the 'photomerge' function in Adobe Photoshop CS9. Images were also taken at greater magnifications such as x30 000 to highlight in better resolution structures of interest.

Correlation and data analysis:

The low-resolution/STORM and TEM images were first pre-processed to enhance contrast and brightness, and overlay was achieved using the open access eC-CLEM plugin using the ICY bioimage analysis platform. To do this, fiducial markers visible in both images were selected, and the program would achieve the correlation. Typically, a non-rigid (warping) transformation would be carried out if the registration error of the fiducials was greater than the predicted registration error. Briefly, as seen in Figure 14, around 20-30 fiducial markers were localized in both images, and a non-rigid transformation was applied. The correlation accuracy (in nm) was calculated and was between 40-60 nm when using 20-30 fiducial markers. Note that the greater the number of fiducials per image, the greater the accuracy and vice versa.
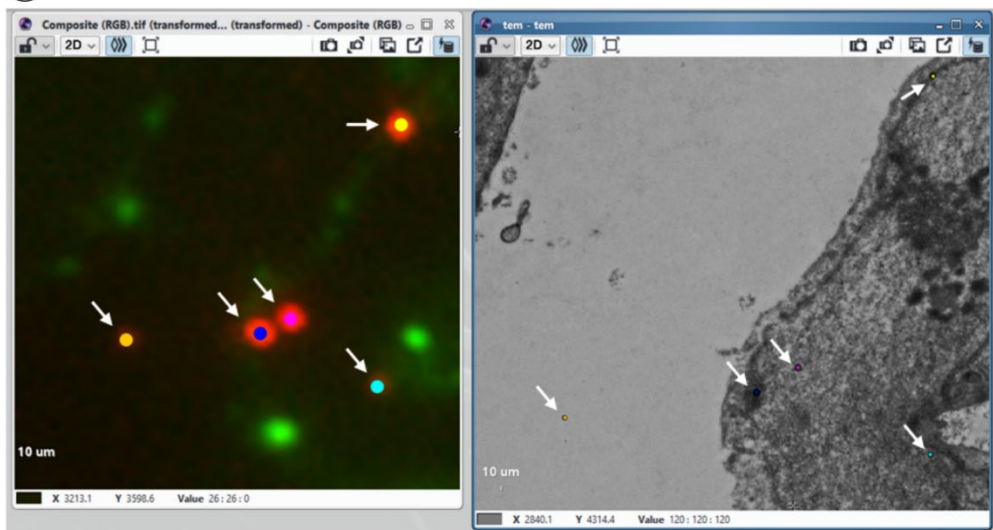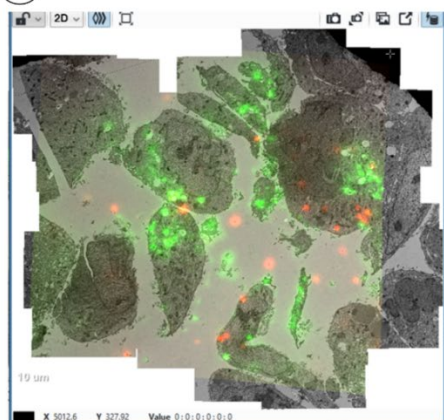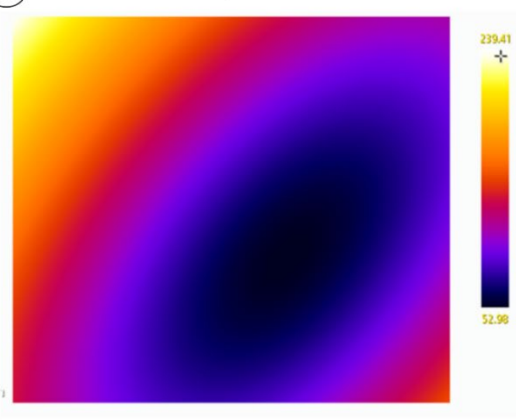
Figure 14 CLEM correlation using ec-CLEM.

STORM images were reconstructed using the NIS Elements software in Nikon using a 2D Gaussian fitting and a threshold of 180 for both channels. The threshold is the difference between the photon number in the peak pixels and the background pixels. The trace length parameter was set to 5 to avoid different molecules blinking consecutively, meaning that molecules identified in 5 consecutive frames would be counted as 1, or removed if more than 5 frames.

For NP quantification, STORM signal with 50-300 nm diameter and 10 or more localizations was considered a true NP. If signal of 2 or more NPs was clearly distinguishable as single NPs, then these were counted as independent NPs. Larger signal (200-300 nm diameter) was considered a single NP. As opposed to TEM, if NPs are closer to each other than the resolution limit of STORM (~ 20 nm) they are not

distinguishable as individual NPs, and thus a limitation of this method is that the number of NPs may be understated.

Flow cytometry assay:

A 12-well NuncTM cell culture plate (dDBiolab) was seeded with HeLa cells (ATCC) and incubated for 24 h in Dulbecco's Modified Eagle Medium (DMEM, with L-Glutamine 10 mM, 4.5 g/L D-glucose and pyruvate, Gibco) supplemented with FBS 5% (Gibco) and penicillin/streptomycin 1% (Biowest), at 37˚C and 5% CO2, to achieve an approximate confluency of 100 000 cells/well. After the incubation, the medium was removed and the cells washed x3 with warm PBS (1x, pH 7; Thermo Fisher). Then, the PLGA-PEG NPs were diluted as to achieve the original concentration of NPs per number of cells in the CLEM experiments (20 µg/mL, 1 mL per well) in OptiMEMTM (Thermo Fisher). NPs were added to the wells and incubated for either 1 h, 8 h, 24 h or 72 h at 37 ˚C and 5% CO2. For the latter 3 time points, the NP solution was removed after 4 h and washed x3 with PBS (at 37 ˚C), then replaced with full medium for the remaining incubation time. One well was kept as control (no NP incubation). Next, the medium was removed, and the cells were washed x3 with PBS (at 37 ˚C). Then, cells were detached by incubating with 500 uL of trypsin-EDTA (0.25%; Thermo Fisher) for 5 min at 37 ˚C. 1.5 mL of full medium was added per well to inactivate the trypsin. The cells were then centrifuged at 5000 rpm (Eppendorf 5415 R) for 3 min at 4 ˚C, and resuspended in cold PBS, followed by two more rounds of centrifugation and resuspension. The final resuspension was done in 400 µL cold PBS and the samples were stored on ice until analysed. Data was analysed using a SA3800 (Sony) spectral flow cytometer equipped with 4 lasers (405, 488, 561, and 635-640 nm), using the 561 laser for NPs. A total of approx.10 000 counts were acquired per sample.

Chapter 4 | Two-color *d*STORM-TEM correlative microscopy for the intracellular trafficking of polyplexes

This chapter was carried out in collaboration with Navalón López María, Dr Cristina Fornaguera Puigvert and Dr. Salvador Borrós Gómez at Institut Químic de Sarrià, Universitat Ramon Llull. Maria synthesized and fluorescently labelled the polymers and plasmid DNA. My work consisted of polyplex formulation, cell incubation and imaging, dSTORM-TEM correlative protocol and data analysis. High-pressure freezing, freeze substitution, resin embedding and ultramicrotomy was carried out by the staff at the TEM facility in Parc Científic de Barcelona.

Abstract: *Successful gene therapy relies on the design and formulation of efficient and safe gene carriers. Cationic polymers such as poly(β-aminoesters) (pBAEs) can be complexed with nucleic acids to form polyplexes, allowing nucleic delivery into the cell and specifically into the cell nucleus, where the gene is expressed. Tailoring polyplexes with cationic polymers can overcome endosomal entrapment, a major bottleneck in nanoparticle-mediated drug delivery. However, there is still much debate regarding the endosomal escape mechanisms, limiting the rational design of effective and safe polyplexes. One of the problems is that intracellular trafficking is typically studied using methods that do not provide single-particle information or enough ultrastructural detail. In this work, we propose a super-resolution correlative light and electron microscopy (CLEM) method combining two-color direct stochastic optical reconstruction microscopy (dSTORM) and transmission electron microscopy (TEM). We selected two polymers, the first containing a combination of two end-capped pBAEs with tri-RH (arginine – histidine), and a second polymer with only tri-R end-cap. Using qualitative correlative images, we were able to demonstrate that RH polyplexes achieved endosomal escape at 6 h, whilst the R polymers may have been trafficked through the endo-lysosomal pathway and exocytosed/degraded. Then, we quantified the number of RH polymer and cargo molecules using dSTORM in different cellular locations to demonstrate endosomal escape. Finally, using dSTORM-TEM, we were able to capture macropinocytosis cellular uptake for larger RH polyplex structures. These results confirmed the reason for improved transfection efficiency observed in RH polyplexes from previous studies. Although these studies are still in their infancy, they could enable a more thorough understanding of intracellular pathways of polyplexes, and hence a more polymer rational selection.*

112

1. Introduction

Gene therapy – the delivery of nucleic acids to cells - has gained importance at a preclinical and clinical stage in different therapeutic areas such as oncology, infectious or cardiovascular diseases[339], whilst the recent COVID-19 pandemic has demonstrated the global impact that gene delivery can achieve. Despite the potential in this field, the delivery system has been a significant bottleneck in ensuring successful gene delivery[340]. Typically, RNA and DNA must be delivered to the cytoplasm or nucleus, respectively (Figure 1). For these sensitive molecules to reach the site of action intact, they must overcome different physiological barriers: i) resist degradation in systemic circulation, ii) reach the target cells, iii) get taken up by the cells, iv) evade degradation by the endo-lysosomal system and v) deliver cargo to cytosol/nucleus. Unsurprisingly, nanomedical research has been heavily aimed at formulating synthetic delivery systems that are stable and efficient enough to deliver these nucleic acids, and these mainly include positively charged cationic polymers and lipids[56].
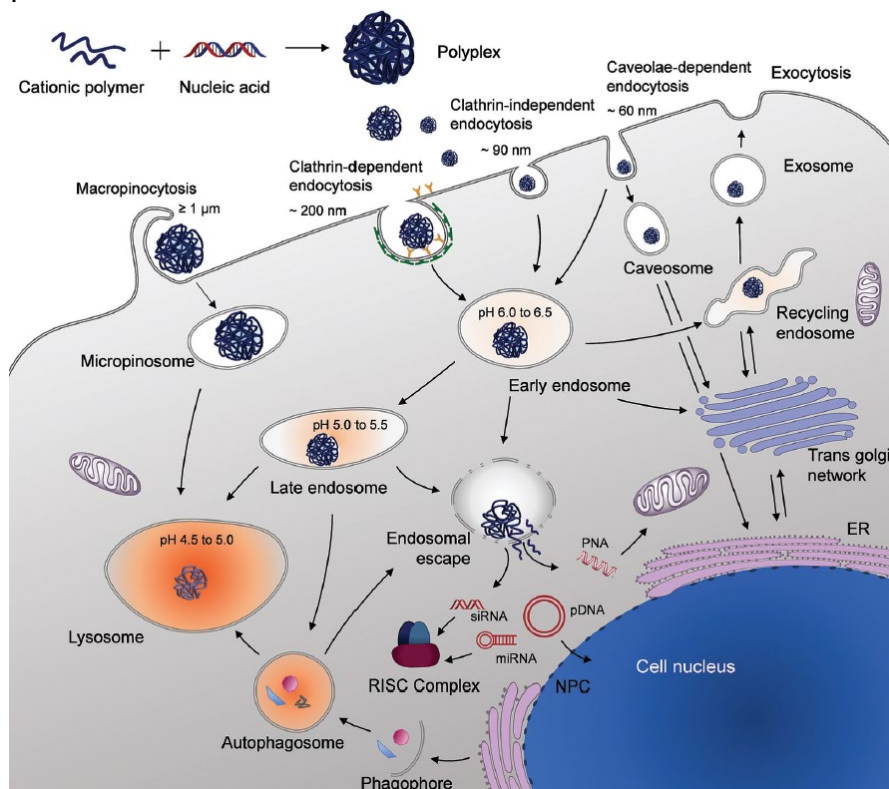
***Figure 1** The delivery of genes (siRNA, miRNA and pDNA) using cationic polymers (polyplexes). Cellular uptake mechanisms include macropinocytosis and various endocytosis pathways and can dictate intracellular pathways. Intracellular trafficking via different routes, endosomal escape into the cytoplasm and exocytosis are also illustrated. Finally, endosomal escape into the cytoplasm, polymer release of cargo and delivery to the specific site (cytoplasm/nucleus) is depicted. ER: endoplasmic reticulum, NPC: nuclear pore complex. Reprinted with permission from reference 122, Copyright ©The Royal Society of Chemistry 2018.*

As emphasized in the **Introduction** of this Thesis, polyplexes are nanocarriers that form through the complexation of cationic polymers and nucleic acids through electrostatic interactions. This class of nanomaterials typically offers low toxicity, flexible design chemistry and promising transfection rates[341]. Despite this, polyplexes have still not reached the clinic, and this is partially due to a limited knowledge on their interactions with biological components and varied activity profiles[342]. For this reason, it is necessary to gain more in-depth information on their biological fate. We previously described in our review[343] and in the **Introduction** that achieving efficient intracellular delivery remains a significant challenge in nanomedicine. One of the main causes is endosomal entrapment, leading to degradation of the carrier-drug ensemble, and loss in bioavailability in the intracellular environment[145,147,148,343]. This phenomenon represents one of the main bottlenecks for using NPs as drug carriers in gene delivery[138,139,145,337]. The careful design of polyplexes with cationic polymers with a high buffering capacity in the endosomes has been shown to increase transfection efficiency. This is believed to be due to an increase in osmotic pressure that disrupts the endosomal membrane[338,344,345], although this mechanism has also been disputed[122,346–348]. Additionally, their intracellular trafficking pathways are still not well understood, and several suggestions include endo-lysosomal, the Golgi or endoplasmic reticulum (ER) pathways[345,349–351]. These pathways are also heavily influenced by their uptake mechanism as depicted in Figure 1, which can consist of endocytosis (clathrin dependent and independent, and caveolae-mediated) and macropinocytosis[122]. Therefore, a thorough understanding of both uptake mechanisms and intracellular pathways is required to gain a full picture of polyplex behavior.

Notably, intracellular trafficking studies are still limited to indirect and qualitative methods such as flow cytometry, inhibition of specific pathways, transfection assays and/or co-localization studies using fluorescence microscopy[346,350–354]. One of the main issues of co-localization techniques is that they test one pathway at a time and miss out on the greater ultrastructural picture, as well as being unable to track NPs at a single particle level.

Furthermore, due to their nanometric size (50-200 nm), commonly used techniques cannot discriminate between nucleic acid and polymer and thus cannot be used to reliably track their complexation state intracellularly. Recently, our group has demonstrated the applicability of two-color *d*STORM for structural characterization[175] and intracellular trafficking at a single particle and molecule level of both polymer and cargo[300,355]. Yet, despite the ability of *d*STORM to identify nanocarrier and cargo at a single particle level, due to a lack of spectrally distinct fluorophores, in practice it cannot image more than 2 or 3 targets, and thus does not offer the ultrastructural context necessary to accurately localize these nanocarriers and their cargo within the cellular milieu.

Whilst in the previous chapter we applied one-color *d*STORM-TEM to track PLGA-PEG NPs, in this chapter we proposed the use of two-color *d*STORM-TEM imaging to unveil the intracellular trafficking of more complex nanomaterials that are formulated with endosomal escape in mind. Furthermore, *d*STORM was applied to track both carrier and cargo. We focused on two types of polyplexes consisting of poly(β-aminoesters) (pBAE) polymers complexed with plasmid DNA (pDNA). pBAE polyplexes have

demonstrated high transfection efficiency and biodegradability as well as low toxicity both *in vitro* and *in vivo*, making them promising gene delivery nanocarriers[344,356–358]. The first polyplex was formulated using both tri-arginine (R) and tri-histidine (H) end capped pBAEs and pDNA and was expected to achieve endosomal escape due to its buffering capacity at endo-lysosomal pH, whilst the second consisting only of tri-R end-capped pBAE and pDNA was not. The structure of the polymers is depicted in Figure 2A. To track both polymer and cargo, we labelled the polymer using a Cy5 dye and the cargo using a spectrally distinct dye Cy3 (Figure 2B). Whilst these results have been demonstrated using indirect and qualitative transfection assays[344], our *d*STORM-TEM correlative approach offers direct quantification of intracellular polyplex distribution (Figure 2C).
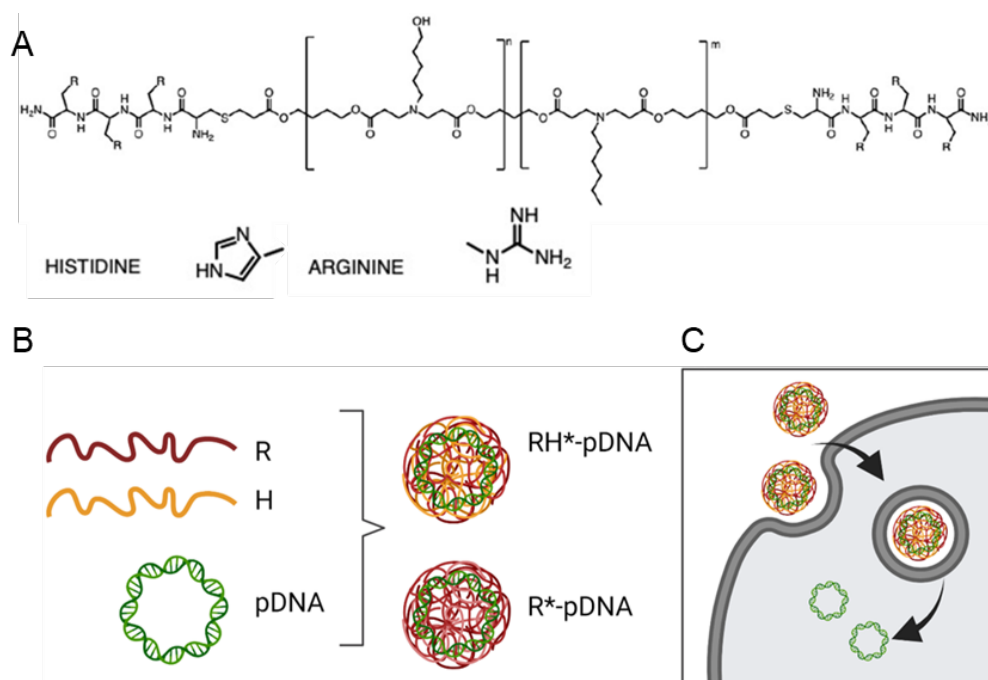
Figure 2 A) Chemical structure of the polymers used for polyplex formulation. Polymers were oligopeptide end-modified poly (betaaminoesters) consisting of terminal peptides composed of a cysteine plus three arginine (R) or histidine (H). B) Formulation of two different polyplex formulations consisting of either R and H or R only polymers. For the RH formulation the H polymer was labelled and for the R formulation the R was labelled. Polymers were labelled with Cy5 (red) and pDNA with Cy3 (green). C) Correlative imaging allows localization of polyplexes or decomplexed polymer/pDNA (by dSTORM) within the intracellular environment (by TEM). Adapted from Reference 355 © 2022 Riera et al. ChemMedChem published by Wiley-VCH GmbH. Created with Biorender.com.

First, we used *d*STORM to image cellular internalization of RH-pDNA polyplexes in A549 (cancerous human lung epithelial) cells at different incubation times, to pick valuable time points and to optimize labelling percentages. A549 cells were chosen due to their good polyplex transfection[344] and large cytoplasmic area suitable for TEM imaging. Second, we applied our *d*STORM-TEM correlative method to track both RH-pDNAand R-pDNA polyplexes at 2 h and 6 h incubation times. We used a mixture of qualitative correlative images and quantitative molecular data from *d*STORM to

compare intracellular trafficking between the two polyplexes. Third, we shine light on the possible uptake mechanisms for the RH and R polyplexes. In this work, we show the potential of *d*STORM-TEM gain useful information on the uptake mechanisms and intracellular behavior of polyplexes which is expected to lead to rational design of optimized polyplex formulations.

2. Results and Discussion

In this work, the intracellular behavior over time of two different polyplex formulations with different pBAE compositions (Figure 2, Table 1) was studied using *d*STORM-TEM correlative imaging. The cargo consisted of plasmid DNA (pDNA; 5.3 kb) codifying for the GFP gene typically used as evidence of transfection. Notably, transfection was not assessed in this study but elsewhere[359]. The optimization and detailed steps of the *d*STORM-TEM correlative protocol have been described in **Chapter 3** and will therefore not be discussed in this Chapter. Notably, the protocol has demonstrated to be very robust, allowing two-color imaging of polyplexes without modifications, proving its capability to evaluate different types of nanomaterials. Physicochemical characterization of hydrodynamic diameter, polydispersity (PdI) and labelling are given in Table 1. Both formulations presented the expected diameters between 50-200 nm, and PdI values within the accepted range, implying formulation stability. The labelling strategies will be explained in the next section.

Table 1 *Polyplex formulations, physicochemical characterization of size and polydispersity and labelling. Size and polydispersity were measured using Dynamic Light Scattering at 25°C in milliQ water pH 7.0. The labelling refers to the percentage % of polymer/pDNA molecules labelled.*

Polyplex	Zeta-average (nm)	Polydispersity index (PdI)	Polymer combination (%)	Labelling (%)
RH-pDNA	189.3 +/- 2.9	0.340 +/- 0.013	R 60:H 40	H-Cy5 (12%) pDNA-Cy3 (25%)
R-pDNA	188.8 +/- 4.8	0.180 +/-0.006	R 100	R-Cy5 (12%) pDNA-Cy3 (25%)

2.1 dSTORM imaging of polyplexes in vitro and in cells

Polyplexes were formulated by nanocomplexation as previously described in literature[344] and in Materials and Methods. Example *d*STORM images of RH-pDNA polyplex are shown in Figure 3 to highlight the ability of this technique to detect the two components with nanometric resolution. The polymers and pDNA were labelled using spectrally distinct dyes, compatible with *d*STORM imaging; Cy5 was used to label polymers and Cy3 to label pDNA. *d*STORM imaging was previously optimized by our group, such that the average dye:polymer ratio was 1:1 and dye:plasmid ratio was 10:1[300]. The labelling density (i.e. ratio labeled: unlabeled molecules) of the polymer was increased from the original 1% to 12%. The pDNA labelling was maintained at 25% in both formulations. We increased the labelling % of polymer to account for the loss of area imaged in *d*STORM-TEM correlative imaging (thin section as opposed to larger cell areas) as well as any possible photobleaching during the CLEM protocol, to ensure polyplex identification. Please note that the optimal dye labelling is still under

optimization for CLEM experiments. The size of the polyplexes by *d*STORM is approximately 200 nm, in agreement with DLS measurements (Table 1).
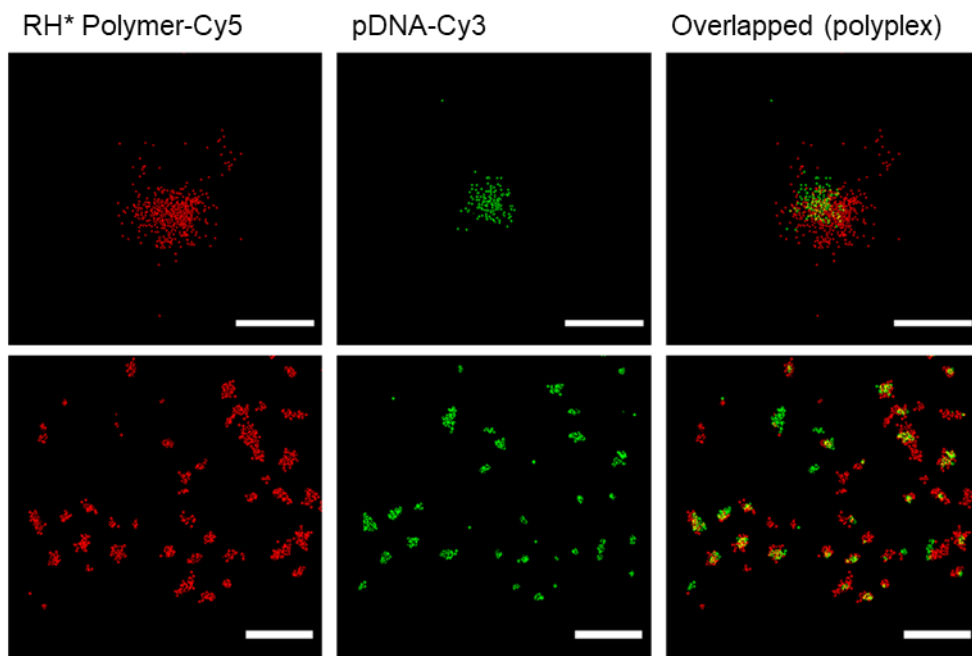
Figure 3 *dSTORM images of RH-pDNA polyplexes on a glass, whereby the H polymer is labelled using Cy5 and pDNA using Cy3. Zoom-in images in each channel and overlayed of a single polyplex are shown in the upper rows, whilst multiple polyplexes are shown below. * Denotes which polymer is labelled (H). Scale bars top = 200 nm, scale bars bottom = 2 µm.*

Next, we studied the internalization of labelled RH-pGFP polyplexes at different time points in A549 cells by *d*STORM alone (Figure 4). After 1 h polyplex incubation in low-serum medium (pulse), cells were washed and allowed to incubate for 1 h, 5 h and 11 h (chase) in full medium, then fixed and stained using Hoechst for nuclei recognition. We were able to detect single polyplexes, which seemed to be internalized after the 1 h pulse, such that at 2 h some complexed polyplexes and free polymer/pDNA were found in the cytoplasm. At 6 h, polyplexes were observed nearer to the nucleus with more freely dispersed polymer in the cytoplasm, whilst at 12 h more polyplexes are seen near the nucleus and even inside it. As we will see later on, *d*STORM imaging is quantitative in nature, such that the number of polymer and pDNA molecules can be quantified at different time points as shown by Riera et al. previously[300,355].
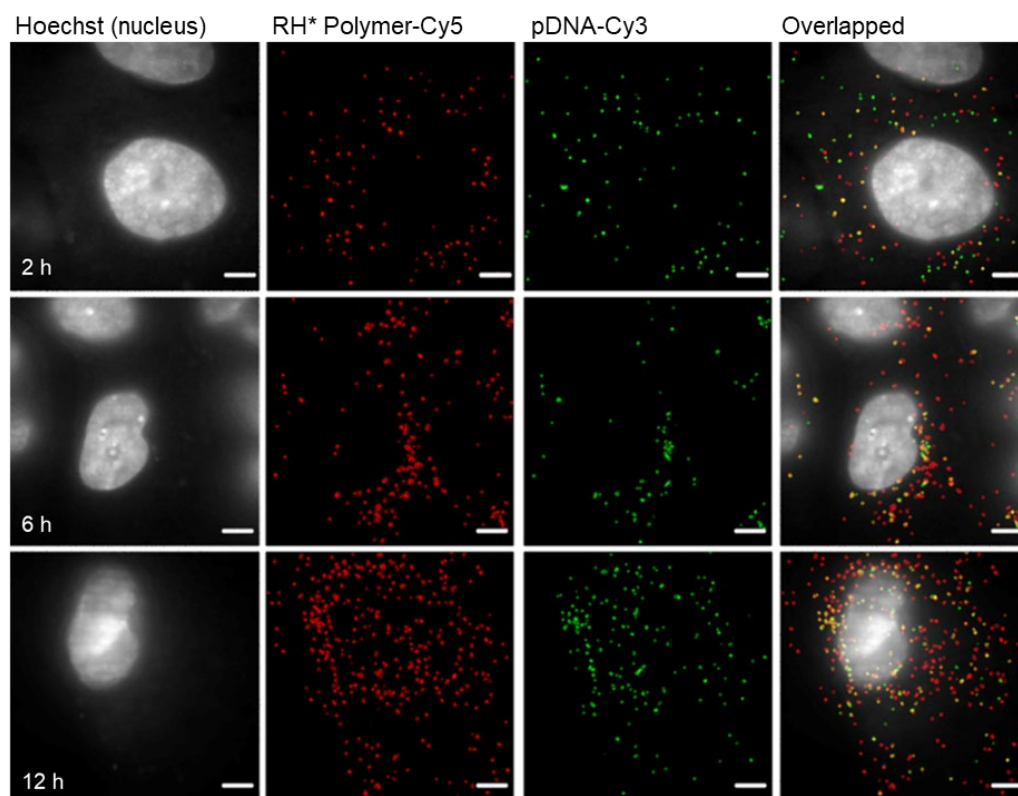
Figure 4 *dSTORM images of RH-pDNA polyplexes in A549 cells at 2 h, 6 h and 12 h incubation time points. Left panels show cell nuclei stained with Hoechst by EPI lamp, center left and right panels show dSTORM localizations of RH polymer and pDNA, respectively, and right panels show all panels combined. * Denotes which polymer is labelled (H). Scale bars = 5 µm.*

It is important to note that when carrying out multi-color imaging, the longer wavelength dye (i.e. Cy5) should be imaged first to reduce cross-talk caused by overlapping spectra of the shorter wavelength dye (Cy3). To check if there is crosstalk between the two dyes Cy3 and Cy5, two control formulations were prepared and imaged (Figure 5), whereby Polyplex 1 consisted of RH polymers with unlabeled polymer and labelled pDNA, and Polyplex 2 of RH polymers with labelled polymer and unlabeled pDNA. As it can be appreciated from the *d*STORM images, there was insignificant crosstalk from either channel. For this reason, no further action (i.e. subtraction of background) was necessary.
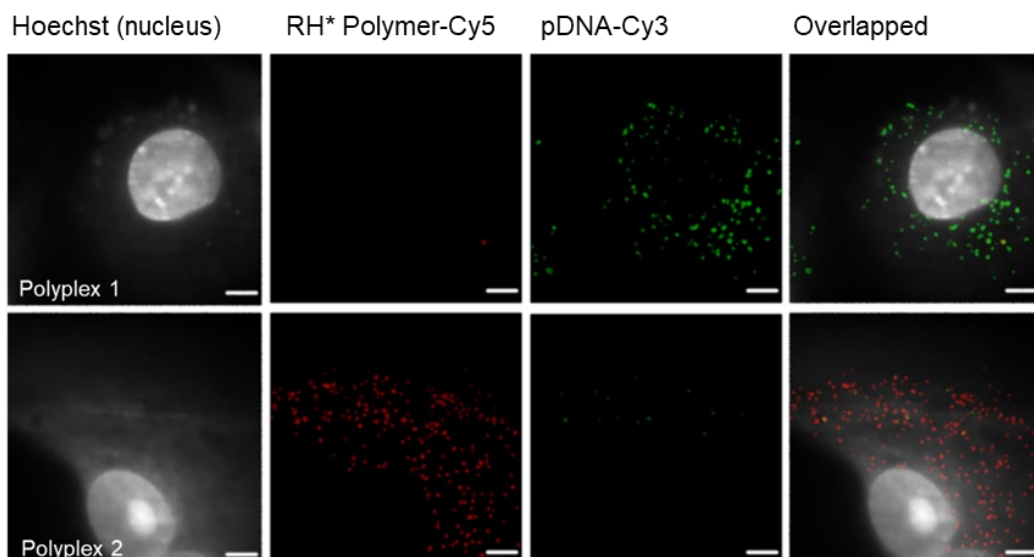
Figure 5 *Control dSTORM images showing no crosstalk between Cy5 and Cy3 signals. Polyplex 1 (top row) consisted of RH-pDNA where only pDNA was labelled using Cy3, and Polyplex 2 (bottom row) consisted of RH-pDNA where only RH polymer was labelled using Cy5. Both polyplexes were incubated for 12 h with A549 cells. Left panels show nuclei labelled with Hoechst by EPI lamp, center left and right panels show dSTORM localizations of RH polymer and pDNA respectively, and right panels show all panels combined. * Denotes which polymer is labelled (H) Scale bars = 5 μm.*

2.2 Correlative imaging of polyplexes in cells

Despite the extremely useful quantitative information provided by *d*STORM on polyplex complexation, it offers little information on their intracellular location, since FM imaging generally lacks ultrastructural detail. For this reason, we correlated the information gained from *d*STORM with that from TEM, by overlapping the same field-of-view (FOV) in both microscopies. For this experiment, polyplex internalization was studied at 2 h and 6 h, with an initial 1 h pulse followed by a chase for the remaining time. These specific times were chosen since at 6 h polyplexes were already expected to have achieved endosomal escape, based on previous unpublished results. The intracellular distribution of both polyplexes described in Table 1 (i.e. RH-pDNA and R-pDNA) was studied and compared using this technique. As previously stated, the RH-pDNA polyplex was expected to achieve endosomal escape due to its buffering capacity at endosomal pH.

Briefly, sample preparation for this imaging protocol consisted of i) a mild fixation step, ii) high-pressure freezing (HPF) to vitrify the sample, iii) freeze substitution (FS) to further fix, contrast and resin-embed the sample, iv) sectioning the sample using an ultramicrotome down to 70-100 nm ultrathin sections and v) preparing the sample for imaging in each technique and correlation. For full methodology on CLEM protocol see Materials and Methods in **Chapter 3**.

This protocol can be carried out using low-resolution (Figure 6A) or *d*STORM imaging (Figure 6B) and TEM on the same FOV. However, as previously explained and as can

be seen in Figure 6, *d*STORM offers a much better resolution that more closely matches that of TEM, whilst being able to offer relevant quantitative information on the number of polymer and pDNA molecules, as previously demonstrated[300]. For this reason, we have chosen to present the *d*STORM-TEM correlative images in this Chapter, whilst the low-resolution-TEM images can be found in Appendix 4.
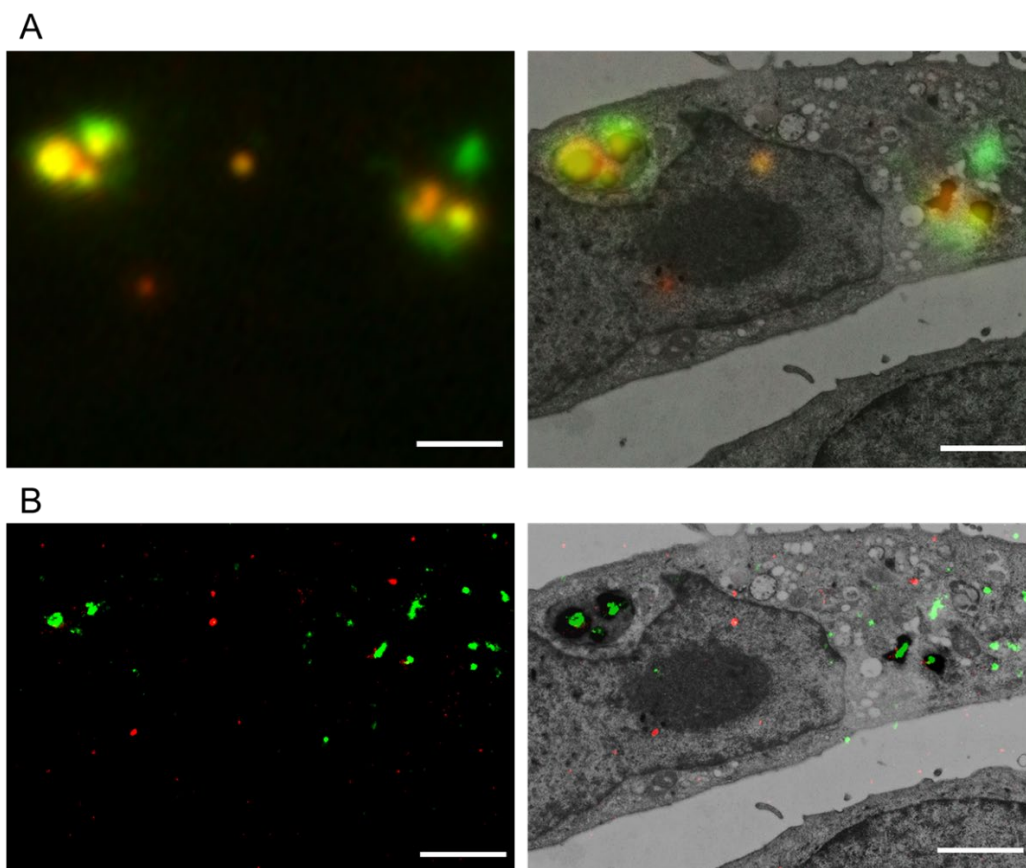
Figure 6 A) Low-resolution FM (left panel) and correlative low-resolution FM-TEM (right panel) images, and B) dSTORM (left panel) and correlative dSTORM-TEM (right panel) of RH pBAE polyplexes in A549 cells. The difference in resolution can be clearly appreciated between FM and dSTORM. Green signal depicts pDNA and red signal pBAE polymer. Scale bars = 2 µm.

First, *d*STORM-TEM correlations were carried out and analysed at 2 h incubation time with the RH-pDNA (Figure 7A) and R-pDNA (Figure 7B) polyplexes. For the RH formulation, polyplexes were seen close to the cell membrane (outside) as well as inside the cells entrapped within endo-lysosomal compartments, as pointed out by the white arrows. In contrast, the R formulation was found both inside and outside of the cells, mainly outside the cells near the cell surface, depicting a slighter slower cellular uptake. Please note, that at this incubation time point only, the labelling % of the R polymer was 24% instead of 12%, as can be seen from the increased number of red (Cy5) localizations in Figure 7B. Currently the optimal labelling percentages are still being optimized for CLEM experiments.

121

A) RH* + pDNA
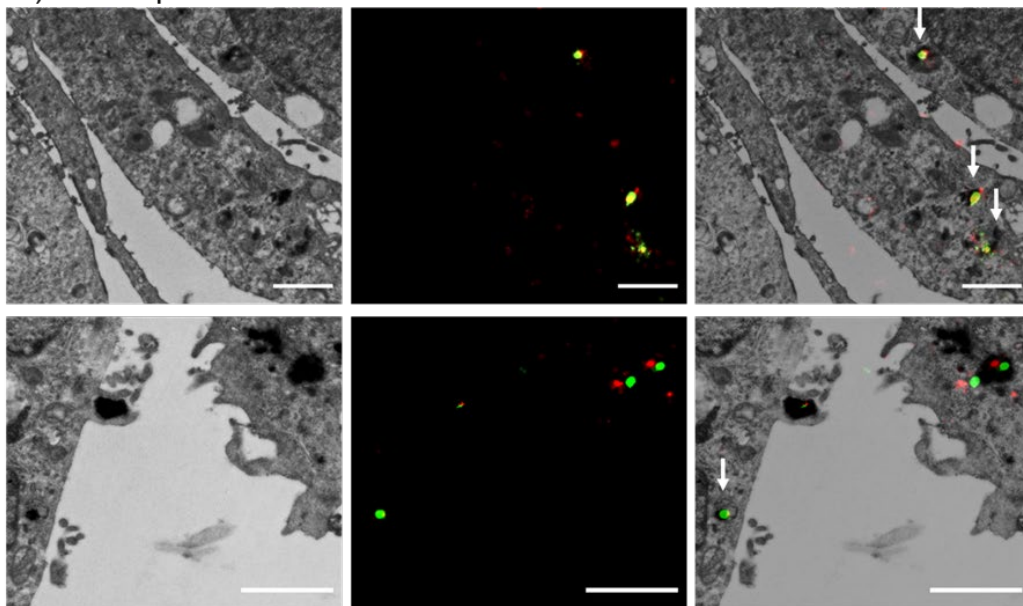
B) R* + pDNA
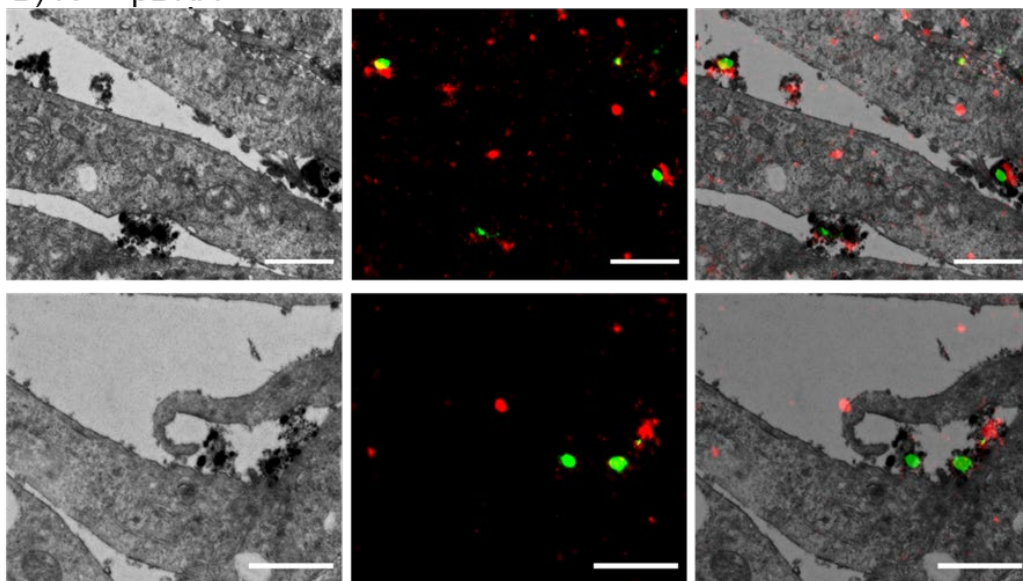
Figure 7 Correlative dSTORM-TEM images of pBAE polyplexes consisting of complexed A) RH* polymer and pDNA and B) R* polymer and pDNA, incubated for 2 h with A549 cells. Left panels show TEM images, middle panels show dSTORM images of the same region of interest, and right panels show the correlation between dSTORM-TEM images. Asterix (*) denotes the polymer labelled. Green signal depicts pDNA and red signal the respective pBAE polymer. White arrows depict polyplexes found in endo-lysosomal vesicles. Scale bars = 1 µm.

At 6 h incubation time, the RH polyplexes were mainly found inside the cell and as expected mainly in the cytoplasm (Figure 8A). The histidine (H) groups provide a higher

buffering capacity in the endosomes as compared to arginine (R) alone, thus can lead to polyplex endosomal escape through processes such as the proton sponge effect, agreeing with the results observed here at 6 h. These results also agree with previous data showing that cationic polymers delivering nucleic acids can escape the endo-lysosomal pathway within 8 h[350]. Notably, bigger aggregates still seem to be intact polyplexes, whilst individual polyplexes seem to have disassembled suggestive of degradation, in agreement with previous *d*STORM results[355].

A) RH* + pDNA
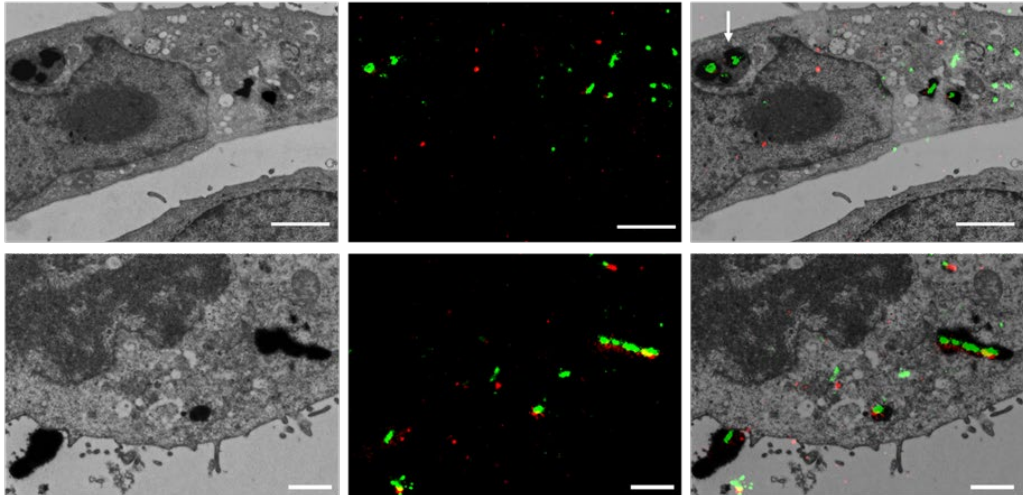
B) R* + pDNA
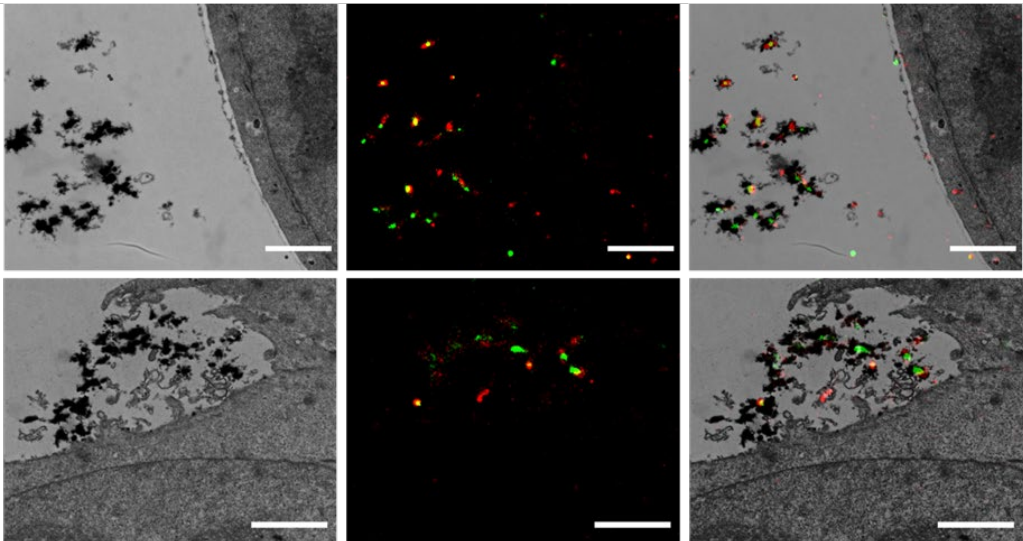
Figure 8 *Correlative dSTORM-TEM images of pBAE polyplexes consisting of complexed A) RH* polymer and pGFP and B) R* polymer and pDNA, incubated for 6 h with A549 cells. Left panels show TEM images, middle panels show dSTORM images of the same region of interest, and right panels show the correlation between dSTORM-TEM images. Asterix (*) denotes the polymer labelled. Green signal depicts pDNA and red signal the respective pBAE polymer. White arrows depict polyplexes found in endo-lysosomal vesicles. Scale bars = 2 µm.*

The R polyplexes were found predominantly outside of the cell at both time points, although at 2 h they were found mainly attached to the cell membrane (Figure 7B), whilst at 6 h they were found further away from it (Figure 8B). Since R polymers are more positively charged than their RH counterparts[344], they have better cell penetration[116–118], thus we hypothesize that R polymers could have achieved cellular uptake. We expect that during the blind 2 h – 6 h time points, the R polyplexes may have been taken up and distributed via the endo-lysosomal pathway – since they do not achieve endosomal escape and were potentially expulsed via exocytosis into the intercellular space, a process previously documented in nanomaterials[137,329,330,332]. This could also explain why the NPs found outside of the cells at 6 h are much further away from the cell membrane (NP cellular expulsion) than at 2 h (NP cellular uptake). However, polyplexes that have entered the cell could have also been degraded. To truly understand these results further investigation is required, such as carrying out shorter time points to study the early stages of the intracellular pathway.

Importantly, *d*STORM does not just offer well-resolved images of nanostructures, it also enables extraction of quantitative information at the single molecule level. Such information cannot be gained with other techniques used in polyplex characterization (e.g. DLS/confocal microscopy). Using our correlative images, we quantified the number of polymer and pDNA molecules for the RH-pDNA polyplex formulation at 2 h and 6 h incubation time points, in non-endosomal compartments (NE) and in endosomes per cell, to demonstrate quantitatively its endosomal escape. Notably, NE consisted in the *d*STORM localizations found in the whole cell minus those in endo-lysosomal compartments. To do this, we used a MATLAB script designed in-house by Gutierrez et al[360].

At 2 h incubation, both RH and pDNA generally showed higher values in endosomal compartments, although some molecules were also found in NE compartments (Figure 9A). These results suggest that polyplexes were trafficked through the endosomes, and that some molecules had already achieved endosomal escape within 2 h. At 6 h incubation, the amount of both polymer and pDNA increased notably in the non-endosomal space (NE) and reduced drastically in the endosomal compartments, suggestive of endosomal escape. Furthermore, at 2 h there was greater dispersity between number of localizations in different compartments and between cells. This is probably because at shorter time points there were still many polyplexes found on the cell membrane which were still achieving cellular uptake, whilst others were dynamically progressing through endo-lysosomal routes, and some were already achieving endosomal escape, leading to a greater general variability in localizations. Even though cellular uptake can still happen at later time points, we noticed that at 6 h the dispersion in localizations between compartments and cells was lower, which was probably because the majority of polyplexes already achieved endosomal escape by this point and were thus mainly found in NE compartments.
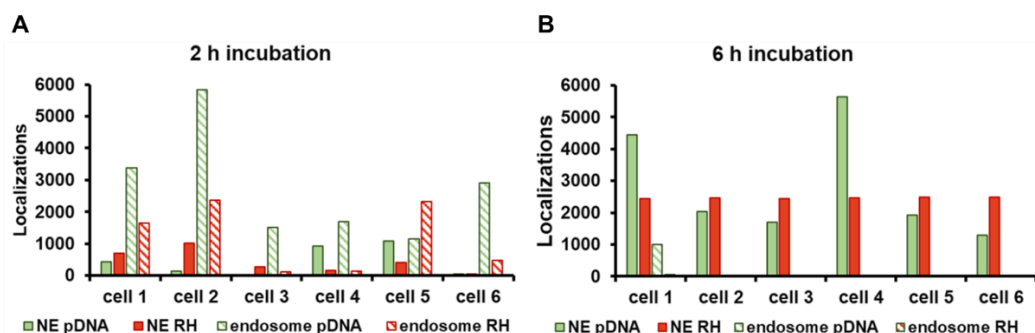
Figure 9 *Quantification of polyplexes from dSTORM-TEM images for the RH-pDNA polyplex at A) 2 h incubation and B) 6 h incubation with A549 cells. Localizations for RH polymer are shown in red (non-endosomal) and red-lined (endosomal) bars and for pDNA in green (non-endosomal) and green-lined (endosomal bars). Non-endosomal refers to all intracellular localizations minus endosomal localizations+nucleus, and endosomal refers to all localizations found in endo-lysosomal compartments. Results are shown for 6 different cells.*

Markedly, these results do not account for the type of endosomal escape mechanism, a topic which is under current debate in the scientific community[338,344–348]. Specifically, the non-endosomal (NE) compartments in this work consisted of all intracellular areas besides endosomes/lysosomes, therefore an assumption on cytosolic escape cannot be made. In fact, several studies have showed that polyplexes can have various fates after endosomal trafficking, such as Golgi or recycled vesicles[345,349–351]. Further CLEM analysis could shine light on such information. Moreover, it must also be noted that only 6 cells were studied for each condition, and as such a more systematic study will yield better statistics; however, such an undertaking is beyond the scope of this project and would require a significant amount of time to achieve.

2.3 Correlative imaging of polyplex uptake

Uptake of cationic polyplexes can be described by various routes, as depicted in detail in Figure 1. During the analysis of the correlative images of RH polyplexes, we surprisingly discovered plasma membrane extensions engulfing the polyplex structures, a phenomenon indicative of macropinocytosis (Figure 10), a route that provides efficient uptake for nonselective endocytosis. These results agree with others in literature[353,361–363], although some authors have reported additional routes such as clathrin-dependent and independent endocytosis, and caveolae-mediated endocytosis[361,364,365]. Notably, we did not notice macropinocytosis uptake behavior for the R polyplexes, which could be because macropinocytosis is a rare event to be observed by EM, or it could be indicative of other uptake mechanisms. This uptake mechanism in RH polyplexes agrees with our other results in two ways. First, RH polyplexes were found in larger and more compact structures compared to R polyplexes as can be seen clearly in Figures 8, 9 and 10, which we attributed to their more neutral charge that causes increased NP aggregation[236]. Since macropinocytosis typically involves engulfing of large structures (≥ 1 µm), size results by TEM agree that RH polyplexes were taken up via this route. Second, we hypothesized that the R polyplexes found outside of the cells at 6 h were exocytosed, which typically occurs for structures taken up via the endocytotic routes, once again agreeing with a lack of

macropinocytosis observed in R polyplexes. However, it must also be noted that RH polyplex aggregation probably occurred upon cell incubation with low-serum medium, due to the impact of the complex biological medium consisting of proteins and high ion content[366], particularly for RH polyplexes that already have a lower colloidal stability due to more neutral net charge. DLS and *d*STORM measurements showed smaller sizes prior to incubation (Table 1), but it must be noted that the measurements were carried out in milliQ water and PBS respectively, and thus extra measurements in the same medium should also be carried out to test their stability before cell incubation.
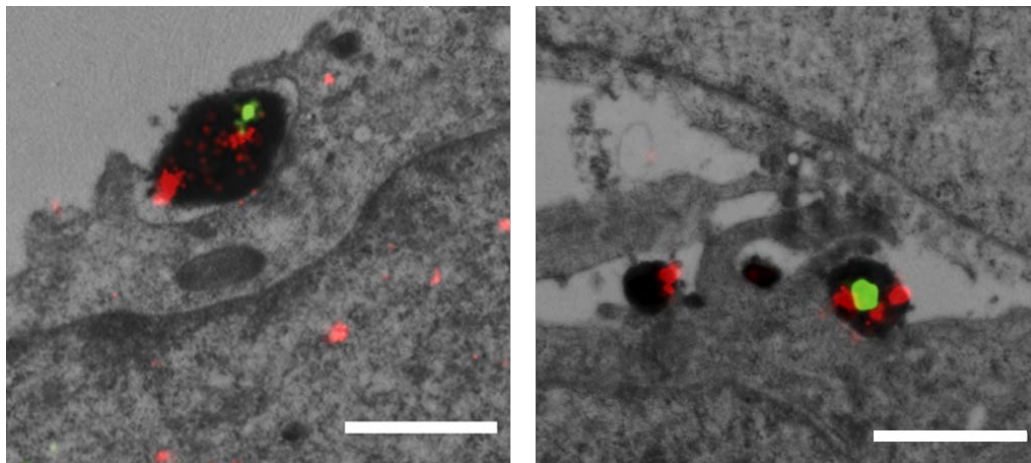
Figure 10 *Correlative dSTORM-TEM images showing plasma membrane extrusions around RH polyplex aggregates indicative of macropinocytosis cellular uptake. Scale bars = 1 µm.*

Uptake pathways are typically studied using specific pathway inhibitors (e.g. cytochalasin D for macropinocytosis[367]) and/or fluorescence co-localization with fluorescently-tagged fluid phase markers (e.g. dextran/albumin)[353,368], whilst live-cell imaging offers time information on fast uptake processes and indeed remove any doubts as to whether fixation protocols affect the uptake route. However, these techniques are typically qualitative in nature and do not allow the imaging of more than 2 targets simultaneously nor morphological detail. Electron microscopy can also be used for this purpose with added resolution and ultrastructural detail, but care must be taken when analyzing images, since precipitations formed by heavy metal staining can resemble polyplex structures. Therefore, to give an accurate representation of cell uptake mechanisms, a combination of CLEM with the aforementioned techniques would be the most appropriate.

As technical notes and points for further optimization, as opposed to PLGA-PEG NPs, these polyplexes give a much greater dark contrast in TEM. This is because the pH of uranyl acetate in water is between 4.2 - 4.9 depending on the concentration, and uranyl species are mainly positively charged, thus negatively charged molecules such as the pDNA in the polyplexes stain more. Whilst this proved useful in the correlation and validation of fluorescent signal, it did hamper with the ability to discriminate between different endo-lysosomal compartments, since the dark staining overshadowed the intrinsic morphological characteristics of different compartments such as early endosomes, late endosomes and lysosomes, that were clearly distinguishable in the

correlative images in **Chapter 3** of this thesis. Probably this problem could be overcome by optimizing the percentage of uranyl acetate used and/or the time of contrasting, or even by switching to another staining agent such as Uranyless. Furthermore, some of the dark polyplex structures in TEM seemed to not be fluorescently labelled, which could be due to photobleaching occurring during the CLEM protocol leading to a loss of fluorescence. Since these are preliminary results, the next logical step is to compare the difference in photon intensity between polyplexes in fixed cells (no CLEM protocol) vs intensity after CLEM protocol in order to find a more optimal labelling percentage.

3. Outlook

Future work that could be considered using the developed correlative protocol could be to show whether polyplex decomplexation occurs outside or inside of the cell, and to study uptake at shorter time points to better understand the behavior of R polymers. Another important intracellular barrier to be overcome is the nuclear membrane since nuclear entry is required for the pDNA to reach its target site. This is typically studied using transfection experiments using fluorescence microscopy to quantify GFP expression[300,344], although *d*STORM has also been applied to quantify the number of polyplex molecules in the nuclear region. This would typically require longer incubation times up to 48 h. Since our correlative protocol images ultrathin sections made by slicing of cells, it could be used to reliably quantify molecules found within the nuclear space and thus to study and quantify delivery of nucleic acids to the nucleus.

4. Conclusions

This Chapter demonstrates the flexibility of *d*STORM-TEM protocols in studying nanomaterial trafficking in cells. In this instance, qualitative images showed that RH-pDNA polyplexes were found on the cell membrane and internalized mainly in endo-lysosomal compartments at 2 h, whilst R only polyplexes were mainly found on the cell membrane. At a longer incubation time of 6 h, the RH polyplex already demonstrated endosomal escape, whereas the R polyplex was found generally still outside of the cells, suggesting possibilities such as that they had achieved exocytosis, were degraded intracellularly, or did not achieve cellular uptake at all. We took advantage of the molecular counting properties of *d*STORM to quantitively determine endosomal escape of the RH-pDNA polyplex by counting the number of RH and pDNA molecules within endo-lysosomal and within non-endo-lysosomal compartments at 2 h and 6 h time points. Finally, *d*STORM-TEM allowed us to capture macropinocytosis of large RH polyplex structures. We also highlighted some of the limitations of our technique such as low throughput and heavy staining of polyplexes in TEM, and made suggestions to overcome these in the future, as well as discussing other experiments that could be potentially achieved with this technique. Overall, we believe that advanced imaging techniques, particularly when used in correlation, can bring further important information on the intracellular trafficking of nanocarriers for gene therapy, such as studying their decomplexation over time in the extensive intracellular milieu, clarifying the intracellular pathways taken by different formulations and designing formulations with better endosomal escape properties. Although this work is still in its

infancy, further commitment could lead to a more comprehensive understanding of polyplex behavior and the design of more effective nanocarriers for gene delivery.

5. Materials and Methods

Polyplex formulation

Arginine (R) and histidine (H) end-modified poly(β-aminoester) (pBAE) polymers were synthesized as previously described in literature via a two-step procedure[344,358,369]. Briefly, a C6 acrylate-terminated polymer (ref) was synthesized by using a primary amine:diacrylate addition reaction (1:1.2 M). The resulting acrylate-terminated polymer was further modifyed by end-capping modification with either 3 arginine (R) or 3 histidine (H) molecules, through a thiol attachment of a terminal cystein. The polymer was later labelled with Cy5 at a 1 dye per pBAE molecule ratio, as previously described[300,355]. Plasmid pMAX-GFP (plasmid DNA - pDNA) (3486 bp) was produced and purified from E. coli and labelled with Cy3 Label IT® Tra2cker™ Intracellular Nucleic Acid Localization Kit (Mirus Biotech), as per supplier instructions. Labelling density was adjusted to 10 dye molecules per pDNA. This was determined from the ratio of Cy3 and DNA concentrations measured in Tecan Infinite 200 Pro instrument (Tecan, Barcelona, Spain), as previously described[355]. Polyplexes were formulated as previously described[344]. Briefly, equal volumes of pGFP (plasmid-DNA):pBAE polymer were mixed at a 1:25 weight ratio (w/w) in NaOAc buffer solution (12.5 Mm, pH 5.2). Notably, the pGFP solution was added to the pBAE solution, mixed vigorously by pipetting, then incubated for 30 min at RT. The mixture was then added to an equal volume of mili-Q water and mixed vigorously as described and used fresh. For optimal *d*STORM imaging for CLEM studies, polyplexes were prepared using 12% Cy5-labelled pBAE polymer and 25% Cy3-labelled pGFP.

Sample preparation for STORM imaging of free polyplexes

A microscopy chamber was prepared by sealing a microscopy slide (FisherBrand) and a coverslip (Corning Cover Glass, thickness 1 ½, 22 x 22mm) using double sided tape. Approximately 40 µL of freshly prepared polyplexes diluted in 1/100 PBS was flown into the microscopy chamber and allowed to attach for 15 min at RT. Then, unbound polyplexes were removed by washing the chamber twice with PBS. To image the polyplexes, *d*STORM GLOX buffer was added to the chamber, consisting of: 5% glucose (wt/vol), 0.5 mg/mL glucose oxidase (Sigma-Aldrich) and 40 mg/mL catalase (Sigma), c) 15% glycerol, in PBS at pH 8.5.

Sample preparation for in vitro dSTORM imaging of polyplexes

A549 cells (ATCC) were seeded at a density of 30 000 cells per well with 400 µL Dulbecco's Modified Eagle Medium (DMEM, with L-Glutamine 10 mM, 4.5 g/L D-glucose and pyruvate, Gibco) supplemented with FBS 5% (Gibco) and penicillin/streptomycin 1% (Biowest), at 37°C and 5% CO_2, for 24 h. The medium was washed out and polyplexes were incubated at a concentration of 1.9 ng pGFP/µL in OptiMEM™ (Thermo Fisher) (400 µL per well). The cells were incubated first for 1 h with the polyplex solution (pulse) before being washed with PBS and incubated in full DMEM for an extra 1 h, 5 h and 11 h before fixation (chase). The fixation step consisted

of 15 min of RT. incubation with 4% paraformaldehyde (200 µL per well). The cells were then washed 3 times with PBS and stored in 400 µL PBS at 4°C in the dark or imaged in 400 µL GLOX STORM buffer. Before imaging, Nuclei were stained with 10 µg/mL Hoechst (Sigma-Aldrich) in PBS for 10 min then washed 3 times with PBS.

Sample preparation for dSTORM-TEM correlative imaging of polyplexes

A549 cells were seeded on a 92 x 17 mm cell culture dish (Nunc^{TM}, Fisher Scientific) and incubated for 24h in full DMEM at 37 °C and 5% CO_2, to full confluency. The medium was removed, and the cells were washed with PBS, then the polyplexes were incubated at a concentration of 1.9 ng pGFP/µL in OptiMEM^{TM} (Thermo Fisher) (4 mL per well). The cells were incubated first for 1 h with the polyplex solution (pulse) before being washed with PBS and incubated in full DMEM for an extra 1 h and 5 h before fixation (chase). The next steps were followed in accordance with the same protocol as in Chapter 5: mild fixation using Fixative 1 and Fixative 2 (2), high-pressure freezing (HPF) (3), freeze substitution (FS), cutting of ultrathin sections (70-100 nm) using an ultramicrotome and preparation steps for *d*STORM imaging (4), preparation for TEM imaging (6) and TEM imaging (7).

The steps for dSTORM imaging and correlation and data analysis differ from those in
Chapter 3 *and are thus explained:*
dSTORM imaging

First, several reference images were taken as seen in Figure S17: 1) The EPI lamp on DAPI filter was used to take a 13x13 stitch (1024x1024) of the distribution of the thin sections on the grid, using the NIS-Elements stitch function. 2) The second reference image was taken using the same lamp and filter at 1024x1024 inside the grid hexagon of interest, showing the cell nuclei, then 3) one image was acquired at 256x256, which gives the exact FOV that will be imaged by *d*STORM. Then, using the Nikon N-STORM system configured for HILO (highly inclined and optical sheet) imaging, a low-resolution image of pGFP was taken using the 561 nm (80 mW) laser, and a low-resolution image of the polymer using the 647 (160 mW) laser, both at 2% laser power and 300 ms. These latter two images were used for correlation of low-resCLEM images. NPs were imaged by *d*STORM by illuminating the 561 nm (80 mW) and 647 (160 mW) laserS sequentially at 100% power. Fluorescence was collected using a Nikon 100x, 1.49 NA oil immersion objective and passed through a quadband pass dichroic filter (97335 Nikon). Images were acquired onto a 256 x 256-pixel region (pixel size 0.16 mm) of a Hamamatsu ORCA Flash 4.0 camera at 20 ms integration time. 10,000 frames were acquired in each channel. Single molecules localization movies were analyzed with NIS element Nikon software. Data was analyzed with NIS Elements (Nikon) and ImageJ. No filters were applied to the *d*STORM images presented.

Correlation and data analysis:

For low-resolution/*d*STORM and TEM image overlay, correlation was achieved manually using Adobe Photoshop CS9, by rotating and scaling the *d*STORM image on top of the TEM image. *d*STORM images were reconstructed using the NIS Elements software in Nikon using a 2D Gaussian fitting and a threshold of 180 for both channels.

The threshold is the difference between the photon number in the peak pixels and the background pixels. The trace length parameter was set to 5 to avoid different molecules blinking consecutively, meaning that molecules identified in 5 consecutive frames would be counted as 1, or removed if more than 5 frames. For the quantification of localizations, a MATLAB code developed in our group by Gutierrez et al. [360] was used. Briefly, a XYT-coordinate file of the *d*STORM image is imported in MATLAB, from which the number of localizations are extracted. A second file, which is the representative *d*STORM-TEM correlative image is used to trace the region of interest (ROI). ROI or multiple ROIs are selected around the cells of interest (from the *d*STORM-TEM image), and a list of the number of localizations and area are reported (from the XYT file). To count the localizations inside endo-lysosomes, the same script is used and the ROIs with polyplex signal inside these compartments are selected instead. To calculate the number of localizations in non-endosomal (NE) compartments, the number of localizations per endosomal compartments are discounted from the number of localizations per whole respective cell.

Discussion

This section summarizes and discusses the work presented in the previous Chapters. It focuses on the applications of super-resolution microscopy, transmission electron microscopy, and correlative light and electron microscopy on the characterization and intracellular studies of nanocarriers. Their strengths and limitations are assessed, as well as the impact their application would have on the nanomedical field.

Discussion

Nanomedicine offers the promise of selective delivery of therapeutics to specific target sites, and thus an increase in the effectiveness of the encapsulated drug, with a minimized toxicity profile. So far despite the extensive arsenal of nanocarriers developed, the field is still lacking in regulatory approvals and successful translation to the clinic, particularly for active targeting formulations[23,71,143]. One of the main issues is that more clarification is required in terms of physicochemical characterization and biological activity of nanomaterials. Currently, this is achieved similarly to small molecular entities, using ensemble techniques that only offer bulk measurements and average values[129,147,148,343]. Yet, the physicochemical complexity of these entities spans way beyond that of regular therapeutic compounds. Firstly, the properties of individual NPs prepared in the same batch are far from uniform, and present high heterogeneity in size, surface chemistry, encapsulation efficiency and ligand functionalization, among others; this is in part due to manual synthesis protocols that lead to incoherent trends in NP properties. As such, average values lead to understudied heterogeneity and poorly characterized nanomaterials, with unpredictable biological outcomes[129,130,284]. Secondly, nanocarriers must be able to successfully enter their target cells and overcome intracellular barriers to release their therapeutic cargo, ideally in the cytoplasm or nucleus[122,147,148]. Tracking their biological pathways early in the design process would allow stratification of promising formulations, saving time and money and lead to more successful regulatory approvals. However, characterization tools must keep up with the complexity found in nanotechnology formulations. Bulk measurements and/or qualitative information provided by techniques such as DLS and flow cytometry and microscopies with insufficient resolutions should not be the sole characterization tools in this field. Advanced microscopy techniques can overcome various drawbacks intrinsic in ensemble techniques, including improved resolution and quantification, and as such have ever-growing applications in nanomedicine. These are particularly promising in expanding our understanding of their physicochemical properties and intracellular pathways, and thus the formulation of more effective nanocarriers.

The aim of this thesis was to develop and apply advanced imaging techniques such as SRM, TEM and CLEM, to characterize and track nanocarriers intracellularly at a single particle level. These techniques are of crucial importance to move away from bulk characterization using average values, and towards more accurate quantitative approaches. SRM allowed us to quantify at a single particle and molecule level the NP surface functionalization and to demonstrate the effect of surface PEG architecture on functional ligand availability **(Chapter 1)**; as such, rational changes were made to improve the design of the nanocarrier formulation. The developed SRM-TEM technique was aimed to shine light on the relationship between surface functionalization and size at a single particle level, and to establish the importance of multiparametric analysis in nanomaterial characterization **(Chapter 2)**. Similarly, the rational optimization and development of an SRM-TEM correlative protocol led to the study the intracellular pathways of PLGA-PEG NPs, allowing localization of single NPs in specific cellular compartments **(Chapter 3)**. The applicability of the same technique to study polyplexes formulated with endosomal escape properties was also demonstrated **(Chapter 4)**. The following paragraphs will serve as take home messages from the previously presented Chapters.

Chapter 1 of this thesis introduced and discussed how SRM techniques are emerging as revolutionary tools in nanomaterial characterization; due to their excellent resolution and molecular counting properties, they are able to image and track NPs at a single particle level, to quantify single molecules such as functional ligands and to account for heterogeneity in NP populations[188,190,302,370,371]. Quantification of functional molecules is pivotal if the intended use of the nanomaterial is drug delivery and molecular biosensing, since these applications require NPs to have sufficient well orientated functional groups to selectively recognize targets. However, studies in literature rarely consider the dispersity in ligand number per NP; instead, average values are used that are not a reliable measure since they leave a large population of NPs in the dark. It comes to no surprise that no nanomaterial formulations with active targeting properties have been approved so far if their functionalization is not accurately studied. Despite the advances in quantitative microscopy techniques, their application towards the study of nanomaterials, particularly polymeric ones, remains poorly explored.

In **Chapter 1** DNA-PAINT and qPAINT were employed to quantify the surface functionalization of various PLGA-PEG NP formulations with increasing target group content[266]. As opposed to standard techniques (e.g. spectrophotometry or theoretical calculations based on particle properties) DNA-PAINT permitted the clear visualization of the interparticle heterogeneity in ligand functionalization and the comparison between different formulations. In contrast to the results from theoretical calculations (i.e. the potential amount of ligands that could cover the surface of a NP, given its surface area and other relevant properties), the experimental ligand numbers were significantly lower. Importantly, since DNA-PAINT only identifies ligands that are well exposed in solution, it was hypothesized that the low experimental values could be due an entanglement of the ligands in the long PEG linker chains to which they were attached. This prompted the redesign of the PEG architecture in the original formulation using a 'cocktail' approach (i.e. combining shorter spacer PEG length with longer ligand-tethered PEG length), which resulted in a notable increase in the number of accessible functional ligands. Without information at a single-particle level, the true targeting abilities of a formulation cannot be properly understood. Since this parameter heavily governs the specific distribution and toxicity of nanomaterials, poor characterization can lead to unnecessary time spent on formulations that do not possess the expected biological behaviors. Size is a major determinant of NP biological fate[95,255–257], and as such, characterization and morphological assessment at a single particle level is fundamental to predict and understand a nanomaterial's destiny. TEM was chosen for this purpose, since it confers the best possible resolution, and allows analysis of heterogeneity. These findings demonstrated that the structural characterization using quantitative techniques such as SRM and TEM should be more universally utilized in the rational design and formulation of nanocarriers.

The results in **Chapter 1** highlighted another important finding. Since ligand conjugation and imager hybridization processes are both stochastic (i.e. random) in nature, ligand distribution was expected to be Poissonian. However, upon DNA-PAINT quantification, the ligand distributions observed were non-Poissonian, suggesting that functionalization is not as random as previously thought, and that there is an extra factor inducing heterogeneity in these parameters. We hypothesized that the stochastic process of ligand conjugation could be entangled with other parameters

such as size, leading to increased variability and poorly predictable results. Despite the importance of understanding the relationship between various physicochemical properties, such information is not available in literature, mainly due to a lack of methods that can assign different parameters on the same particle. Since a single technique cannot provide all the answers; thus, a synergistic approach was implemented.

CLEM techniques were presented in the **Introduction** as powerful multimodal imaging systems that combine the benefits of both types of microscopies by sequential imaging of the same region[209,210]. Remarkably, no such CLEM techniques were explored for the structural characterization of nanomaterials at the time of drafting this thesis. To address this gap in literature, and to study the interplay between ligand functionalization and NP size, **Chapter 2** described the development of a correlative technique combining the power of DNA-PAINT and qPAINT to quantify surface functionalization, with the ability of TEM to characterize the size and morphology at a single particle level[240]. The results obtained with this technique established that the heterogeneity found in surface functionalization and size may be a result of the collective impact between different physicochemical properties. The results also found sub-populations of NPs that did not expose surface ligands, which in hindsight means that part of the formulation would be ineffective in cellular targeting and could pose a risk of systemic toxicity. Moreover, the characterization of NPs using a one-method-at-a-time approach resulted in the omission of sub-populations of NPs, leading to the overestimation in the number of surface ligands, that could lead to poorly calculated efficient doses. Thus, adopting comprehensive characterization tools that elucidate the interconnections between parameters is crucial when optimizing nanocarrier designs. To prove the applicability of correlative protocols for the characterization of more complex nanomaterials, a similar technique was applied, whereby *d*STORM was applied and correlated with TEM instead of DNA-PAINT (*d*STORM-TEM), to study supramolecular polymers. Although this work is still in its infancy, it stands as a pillar to show that with some optimization, correlative protocols can go beyond the characterization of polymeric NPs. Notably, *d*STORM imaging alone suggested that the signal observed corresponded to single fibers, but through the correlation of this information with the morphological detail of TEM, it was found that the single fibers were in fact bundles of smaller fibers, undetectable by the resolution of *d*STORM.

Nevertheless, a two-way relationship study is more than simplistic, when considering the vast number of parameters that could influence the biological fate and safety of these nanomaterials. Particularly, one must be careful when choosing which size characterization technique to use, since different techniques will result in incompatible values, depending on the material in question. In this case, we characterized the size of the nanomaterials in dry conditions, which may not realistically represent the formulation in biological conditions. Although the multiparametric characterization of tens of different relevant physicochemical parameters is still out of reach, we hope that **Chapter 2** will pave the way to more robust and innovative nanomaterial studies.

In theory, NPs offer great promise for the systemic delivery of therapeutics that have unfavorable physicochemical properties. However, in practice this is not easily achieved since the nanocarrier must overcome a variety of cellular barriers before releasing the cargo at the target site, some of which include crossing the plasma

membrane, escaping the endo-lysosomal system and in specific cases even cross the nuclear membrane[122]. In fact, extensive research has shown that less than 0.1% of the median I.V. administered NP dose is delivered to cancer cells[372], which is also observable in the lack of translation to the clinic, despite the great budget invested in this field. Nanomedicine success stories such as Abraxane and Doxil have been clinically approved due to their ability to reduce the toxic profiles of the encapsulated therapeutics but did not show clear or consistent enhancement in drug delivery[30]. Clearly, if we want to market nanocarriers that aim to improve the targeted delivery of their cargo, we need to better understand their biological behavior, starting with their cellular uptake and intracellular delivery. Some of the challenges in viable intracellular delivery of NPs were described in the **Introduction**, where we saw that NP entrapment in the endo-lysosomal system is a crucial bottleneck in the effective delivery of the therapeutic cargo to the cytoplasm/nucleus. A lack of reliable methods to visualize and quantify NPs at the nanoscale within the intracellular milieu worsens the matter, as it hampers the rational design and formulation of effective nanocarriers.

Typically, NP intracellular tracking is studied using co-localization with fluorescently tagged targets by confocal microscopy, which does not possess the necessary resolution to identify single NPs. Even if a SRM technique such as *d*STORM is used instead for improved resolution, due to a lack of spectrally distinct dyes, it is not possible to image more than 2-3 consecutive targets. Furthermore, if different targets are measured using sequential labelling, this greatly reduces the ability to track NPs within several compartments at the same time and in the same cell. TEM is the only technique that can be used to differentiate all the organelles in a field-of-view, and thus can be applied for the precise localization of NPs at a highly subcellular level. Nevertheless, for accurate localization by TEM, NPs typically must be electron dense enough to be discriminated from other cellular components; for this reason, polymeric/protein based nanocarriers that are semi-transparent are not typically studied intracellularly by TEM. Thus, the applicability of correlative imaging spans to a wider variety of nanomaterials that would otherwise not be identified by TEM alone.

In **Chapter 3** super-resolution CLEM, specifically *d*STORM-TEM, was employed as an efficient tool in tracking individual nanomaterials and/or their cargo within specific cellular compartments. First, a typical CLEM roadmap was presented, highlighting the most popular techniques used in cell biology including their individual advantages and weaknesses. Through rational optimization and by accounting for the biological question to be answered, a *d*STORM-TEM correlative method was developed that successfully maintained cellular ultrastructure preservation and NP fluorescence. As a proof of concept, the technique was first used to track non-functionalized PLGA-PEG NPs without endosomal escape properties. As such, these NPs were found progressing along and eventually entrapped in the endosomal pathway over a 24 h period. A lysomotropic agent (chloroquine) was then added to induce endosomal escape, prompting the quantification and comparison of intracellular distribution of NPs using our correlative approach. These results stand to show the promising value of super-resolution CLEM techniques in studying intracellular fates, as well as endosomal entrapment and escape of NPs.

Following on, **Chapter 4** confirmed the applicability of the developed *d*STORM-TEM technique for the intracellular tracking of more complex nanomaterials designed with endosomal escape in mind. For this purpose, two types of polyplexes were first

formulated consisting of distinct pBAE polymers complexed with plasmid DNA. Labelling each component with distinct fluorophores allowed the tracking and quantification of both nanocarrier and cargo by *d*STORM, and their cellular localization by TEM. This further permitted us to compare the endo-lysosomal escape properties between the two different formulations at different time points. Surprisingly, the correlative images allowed us to catch macropinocytosis uptake in the act for the larger polyplex structures, opening up a path of possibilities for such techniques in studying cellular uptake mechanisms of nanomaterials. The COVID-19 pandemic has placed nanocarriers for gene delivery in the spotlight, but we must remember that their translation to the clinic is still limited. Employing techniques such as CLEM for their characterization at early stages of drug development could improve the logical design and selection of nanomaterials that aim to deliver their cargo more efficiently to the cytoplasm or nucleus.

The aim of this thesis was to develop advanced imaging techniques to characterize nanomaterials and gain a better understanding of their intracellular fate and highlight the relevance of correlating information from different techniques as opposed to using a one-method-at-a-time approach. However, this does not imply that CLEM should be used in isolation for nanomaterial studies. In fact, to improve the quality of reported research, it is recommended to use multiple standard characterization tools that offer the necessary required information on material and biological characterization[134]. For example, we envision uptake mechanisms to be studied using a combination of 1) live-cell imaging using specific pathway inhibitors and co-localization experiments, 2) correlative imaging for a much in-depth quantitative and morphological analysis, and 3) flow-cytometry for high-throughput NP uptake studies and binding specificities. What is clear is that correlative techniques will empower us to obtain unique and in-depth understanding of NP batch characteristics, multiparametric information, as well as the ability to better understand the relationship between physiochemical properties and biological outcomes. What we propose is the introduction and standardization of advanced imaging and correlative techniques alongside other necessary and powerful techniques. Although this task is still in its infancy, a synergistic effort from various scientific disciplines must be made for the potential benefits of nanomedicine to be realized.

Outlook

This section presents new directions for the research Chapters presented in this Thesis as well as more generally for the nanomedicine and CLEM field.

Carrying out most of this research during a global COVID-19 pandemic has been challenging but it has also highlighted important messages in our field of research. First, the tremendous efforts made by the nanomedicine community in the last decade were not futile, in fact they were the solution to a devastating pandemic that has affected us all. Second, the innovative nature of the nanomedicine field is still to unlock its full potential in the treatment a variety of other diseases. For this to happen, a collaborative effort such as the one seen during this pandemic is required from all disciplines involved, from material science to biology and microscopy, to regulatory agencies. One of the main issues is that bench research as well as regulatory approval standards are still highly based on ensemble methods used for small molecular drugs. However, as explained in this thesis, nanomaterials cannot be accurately characterized based solely on standard ensemble techniques. Day by day, we witness the design of more complex nanomaterials, but to expand the potential of such formulations and provide patients with access to state-of-the-art and life-changing therapies, we must also pave the way for the standardization of more intricate techniques that will allow a more accurate characterization of nanomaterial physicochemical properties and a better prediction of their biological behavior.

In **Chapter 1**, the potential of SRM to characterize interparticle ligand heterogeneity, and to rationally design and optimize a nanomaterial formulation with increased accessible functional ligands was demonstrated. In addition to the results showed in this Chapter, there is a vast amount of other useful information that could be gained using SRM, and which we hope to see in the future. SRM could be used to compare various other PEG architectures to have a more robust understanding of the effect of PEGylation on ligand accessibility. To study the effect of different PEGylation approaches and even percentage of surface functionalization on the targeting abilities of NPs, one could conjugate NP formulations with an actual therapeutic ligand (rather than an oligonucleotide) and study their cell uptake in cells expressing the respective target receptors. Furthermore, although in our research maleimide was used as target group to which a model ligand was conjugated, DNA-PAINT would be particularly interesting for studying functional antibody orientation on the surface of NPs targeted for tumor imaging and treatment. Also, the multiplexing ability of DNA-PAINT using different oligonucleotides could be applied for the study of multivalent nanoparticles. Indeed, once NPs are injected into systemic circulation, they can lose their functionality upon biomolecular corona formation, and thus it would be interesting to study ligand availability in a more biological environment. Answering such questions would give the nanomedicine community a better insight into targeted nanomedicine.

In **Chapters 1 and 2**, we highlighted the presence of heterogeneity in different NP physicochemical properties and discussed the negative impact that omitting such information from research can have on their clinical translation. Notably, we formulated PLGA-PEG NPs via a bulk (manual) nanoprecipitation method, prone to reproducibility errors and inherently heterogeneous formulations. A useful comparison would be characterization of NPs formulated via a microfluidic device or PRINT technology, both of which offer more precise control over NP composition and size. It would be also extremely valuable to characterize the heterogeneity and interplay between physicochemical properties of already approved nanocarriers, as this would offer important information to researchers as to what level of heterogeneity is acceptable in a formulation. Importantly, regardless of the formulation method (e.g. manual vs.

microfluidic), there will still be some heterogeneity present. Therefore, until we find more accurate and scalable synthesis methods, we must focus on thoroughly characterizing nanocarriers, agreeing on an acceptable level of heterogeneity and ensuring it is maintained, and advanced microscopy techniques offer great potential for this purpose.

The development of a DNA-PAINT-TEM protocol for nanomaterial characterization *in vitro* was highlighted in **Chapter 2** and applied to study the entanglement between ligand functionalization and size in PLGA-PEG NPs. Then, in **Chapter 3** and **4**, a *d*STORM-TEM correlative protocol was optimized for the intracellular trafficking of PLGA-PEG NPs and polyplexes, respectively. Yet, our results and applications merely scratched the surface of the potential of such techniques, since there are numerous other nanomaterials to be studied and questions that these could help answer. Correlative protocols such as the one in **Chapter 2** could be applied characterize the relationship between other physicochemical properties e.g. functionalization/encapsulation efficiency and different morphologies, and cellular uptake. Using the protocol in **Chapter 3**, since both carrier and cargo can be imaged using *d*STORM, one could track specific site release of cargo of a multitude of other formulations, ranging from polymeric to lipid NPs and micelles. For example, instead of using non-functionalized carriers, it would be extremely useful to label and track more applicable formulations that target specific receptors on cancer cells e.g. fluorescently labelled NPs functionalized with labelled FDA approved antibodies (e.g. trastuzumab/cetuximab). A *d*STORM-TEM protocol would offer powerful resolution and information on the intracellular trafficking of both carrier and cargo.

Since this thesis referred to endosomal entrapment as a major bottleneck in clinical translation of nanomedicines, one could also apply advanced imaging techniques to explore this field further. Exciting topics to be explored would be i) how, and which NP physicochemical properties affect cellular uptake mechanisms and hence influence endosomal entrapment/escape, ii) confirm endosomal escape mechanisms and use the information to improve NP formulation design to exploit them, iii) study the time and location at which endosomal escape occurs intracellularly, and iv) study the degradation of the carrier/drug release over time.

In the correlative protocols in **Chapter 3 and 4** pre-labelled NPs were used. However, other protocols are possible if different biological questions are to be answered. For example, post-sectioning immunolabelling/labelling via biorthogonal click-chemistry using the Tokuyasu method are also possible alternatives, and such an example is described thoroughly in Appendix 6. The latter serves as an excellent method for tagging structures of interest with oligonucleotides for DNA-PAINT imaging, allowing fluorescent visualization of many more targets than by *d*STORM, and a much lower risk of fluorescence quenching, since fluorescence labelling is done after the sectioning step. Correlative microscopy can also be expanded beyond SRM and TEM. For example, whilst TEM offers morphological characterization in the dry state, atomic force microscopy (AFM) studies morphological and mechanical properties at a single particle level in solution. To overcome the risk of fluorescence loss/detachment of dye from NPs, label-free alternatives could be used instead of SRM, for example Raman imaging, that allows study of potential vibrational modes of the nanomaterial and thus could offer information on their chemical composition.

Furthermore, drawing conclusions based on 2D cell experiments does not provide sufficient translatable pre-clinical information. Bioengineered organs or tissues on microfluidic chips (e.g. cancer-on-a-chip) offer a much more accurate 3D alternative, as a precursor to *in vivo* studies. CLEM on tissues has been routinely carrier out, albeit not in the nanomedicine field. Also, TEM on thin sections of cellular 3D microfluid chips has been achieved, meaning that its correlation with other imaging techniques is only a matter of time. Such experiments would consider other drug delivery barriers such as the interaction of NPs with serum proteins and their extravasation through endothelial cells. Lastly, array tomography, comprising of sequentially cut and imaged thin sectioned tissue, could be implemented for a powerful 3D representation of nanomaterials intracellular trafficking in thicker samples.

In this Thesis, it was explained how the introduction of advanced imaging techniques - particularly super-resolution CLEM - as standard characterization techniques in nanomedicine could aid in NP translation to the clinic. Yet, it must be stressed that correlative techniques are inherently difficult and time consuming, with a whole protocol (such as the one discussed in **Chapter 3**) taking roughly 3-4 weeks to complete. The most important and cumbersome part is protocol optimization, to ensure that cellular ultrastructure preservation does not suffer at the expense of maintaining NP fluorescence, and vice versa. Thus, it is necessary to spend a good amount of time optimizing experimental conditions. The correlation of the images is also tedious task. Luckily, registration programs such as ec-CLEM (ICY) and Adobe Photoshop make this process slightly more automated. Needless to say, fast, and high-throughput data acquisition and analysis are necessary to achieve an unbiased characterization and statistically significant results, and the CLEM community must improve in this area. For example, microscopes that can automatically image large FOVs would reduce the amount of time spent by user at the microscope, whilst integrated microscopes would aid massively in improving retrieval of regions of interest and correlation, but these are not yet commercially available. Also, these complex protocols require good knowledge of both imaging techniques, as well as biology and nanomaterial science to ensure errors can be prevented and that results are well analysed; the most effective way to achieve this is through a strong collaboration across disciplines. We believe that by improving automatization of several steps and throughput in image acquisition, as well as supporting a greater collaboration between disciplines, advanced imaging techniques could become a critical part of standard protocols in nanomedicine studies. This in turn could pave the way for more effective and groundbreaking nanocarriers, including targeted ones, finally reaching the clinic.

Conclusions

This section summarizes the research findings in Chapters 1-4.

Conclusions

In **Chapter 1** PLGA-PEG NPs were formulated with increasing target group content and functionalized with surface ligands. Using DNA-PAINT and qPAINT, the number of accessible ligands at a single particle level was quantified and compared between each formulation. It was stressed that the average number of ligands should not be used as a representation of the overall NP formulation as it masks heterogeneity. Furthermore, it was observed that the ligand distributions were not stochastic in nature, suggesting that this could be an effect of interplay with other parameters. Surprisingly, a much lower number of accessible ligands were quantified compared to theoretical values, that was hypothesized to be due to ligand embedding into surface PEG chains. This prompted the redesign of the nanocarrier by modifying its PEG architecture, resulting in increased numbers of accessible surface ligands.

In **Chapter 2**, the interplay between ligand functionalization and diameter at a single particle level was explored. To do this, a CLEM method was developed combining the single molecule quantification properties of DNA-PAINT with the morphological analysis of TEM. First, this method allowed the study of multiparametric heterogeneity between NP ligand number and size at different target group contents. Second, large subpopulations of NPs with no accessible surface ligands were identified, which would offer no specific targeting in a biological setting. Third, it was demonstrated that characterization using a one-method-at-a-time approach limits the information obtained as compared to a multiparametric technique, which could lead to poor predictions of efficient therapeutic doses. As an outlook, the flexibility of correlative techniques was demonstrated by developing a *d*STORM-TEM correlative protocol to image and characterize supramolecular fibers.

In **Chapter 3** a CLEM roadmap used in cell biology was provided that prompted the optimization of a *d*STORM-TEM method for the intracellular trafficking of fluorescently labelled PLGA-PEG NPs. The resulting protocol maintained cellular ultrastructure and fluorescence signal. Single NPs by were directly identified by *d*STORM and assigned to specific cellular compartments using TEM. The results showed that at early time points NPs were found mainly early endosomes, whilst at later time points in late endosomes and lysosomes. Finally, chloroquine was used to promote NP endosomal escape, and its effect on the NP intracellular distribution was quantified.

In **Chapter 4** two different types of polyplexes were formulated using either RH or R pBAE polymers complexed with pDNA. Using our *d*STORM-TEM protocol, RH polyplexes were shown to achieve endosomal escape by 6 h, whilst the results for R polymers suggested trafficking through the endo-lysosomal pathway and exocytosis/degradation or no cellular uptake at all. Using *d*STORM, the number of RH polymers and pDNA molecules in different cellular locations was quantified at different time points, demonstrating endosomal escape. Finally, CLEM revealed that cellular uptake of RH polyplexes may occur via macropinocytosis.

Conclusions

Appendix 1

*This Appendix provides supportive information for the results described in **Chapter 1** of this Thesis. It Includes a control experiment to quantify the amount of docking strands inaccessible to imager strands and characterization of the PLGA-PEG (PEG 1_K) formulation.*
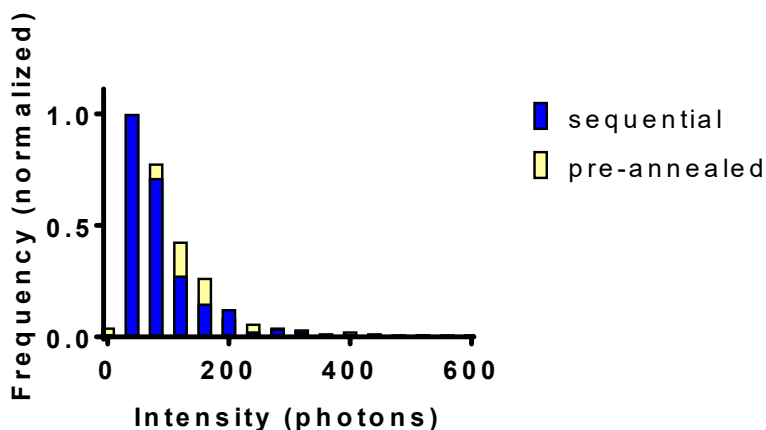
Figure A.1.1. *Distribution of emission intensity in photons of imager strands from individual PLGA-PEG-Maleimide (100%) NP acquired using low resolution images with two distinct labeling modalities, respectively 'sequential' (blue bars) and 'pre-annealed' (yellow bars).*

In this particular set of results, the NP formulation was conjugated to docking strands 21 oligos in length and imaged with a complementary imager strand also 21 oligos in length (as opposed to the normal 9 NT length), with 67% GC content to ensure irreversible hybridization between docking and imager strands. For the 'sequential' labelling the NP were conjugated to the thiol-docking strands at 3:1 excess of thiol to maleimide molar ratio, washed and then directly imaged with the imager strand. For the 'pre-annealed' labelling, the dockings strands were first mixed with the imager strands at a 1:1 molar ratio to achieve permanent hybridization. Then the pre-annealed strands were conjugated to the PLGA-PEG 100% Maleimide NPs at a 3:1 molar ratio thiol to maleimide, washed and imaged directly. Low resolution images were collected and roughly about 300 NP per labelling technique were detected and their fluorescence intensity (in photons) was measured. There is a clear overlap between the two distributions, suggesting that the number of active sites between both labelling modalities is similar, with comparable means of 68 and 72 for 'sequential' and 'pre-annealed' modalities, respectively. Therefore, there is only a low number of docking strands that target maleimide groups but that are not detected by imager strands (~6%).

PLGA-PEG NPs (PEG$_{1k}$) characterization

Please note that the PLGA-PEG 20% Maleimide formulation was formulated on a different day to the rest of the PLGA-PEG (PEG$_{1k}$) formulations.
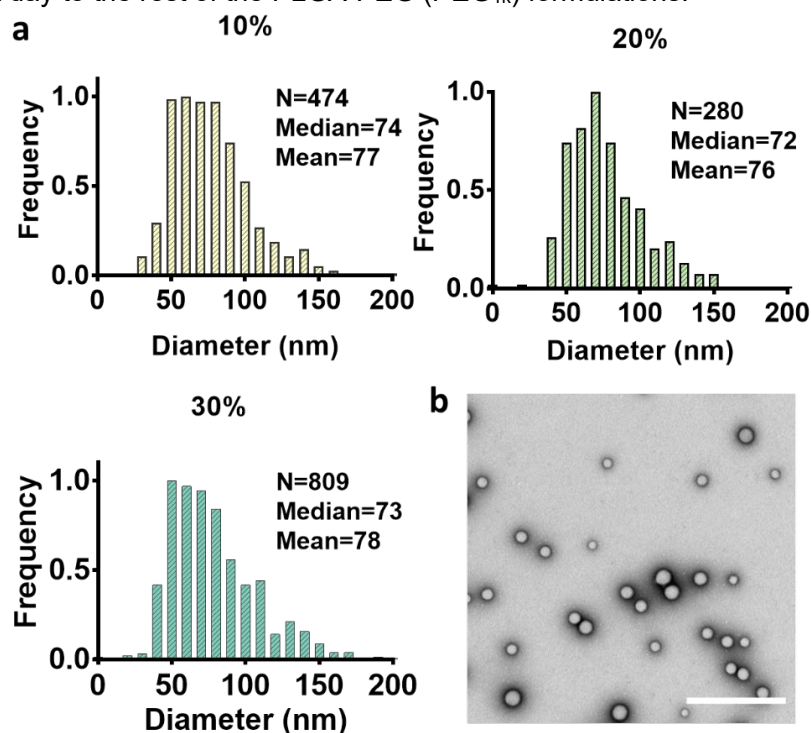
Figure A1.2. *(a) Normalized frequency histograms of NP diameter (nm) from TEM images, of ligand-conjugated PLGA-PEG NPs (PEG$_{1k}$) with varying maleimide content (10, 20, 30%). The number of NPs analyzed (N), and median and mean diameters are given for each. Bin widths=10 nm. (b) TEM image representative of a 10% maleimide formulation (scale bar 500 nm).*

Table A1.1. *Analysis of the hydrodynamic radius (diameter nm) and polydispersity index (PdI) by Dynamic Light Scattering and zeta potential (ZP, mV) using a Zetasizer Nano ZS (Malvern Panalytical) at 25°C in milliQ water pH 7.0 for the PLGA-PEG (PEG$_{1k}$) NP formulations (a) before conjugation, (b) immediately after conjugation and (c) 7 days after conjugation with functional ligands (docking strands). The diameter is given as the z-average. The standard deviation (+/-) for 3 repeats is given. The control formulations contain no maleimide, but the same ratio of PEG$_{5k}$ vs PEG$_{1k}$ (see Chapter 1, Material and Methods, Nanoparticle Formulation).*

a)

Formulation	Diameter (nm)	PdI	Z-average (mV)
PLGA-PEG 10% control	103.6 +/- 0.4	0.130 +/- 0.017	-29.9 +/- 0.6
PLGA-PEG 10% Maleimide	152.1 +/- 3.8	0.141 +/- 0.058	-37.5 +/- 0.5
PLGA-PEG 20% control	114.2 +/- 1.9	0.073 +/- 0.040	-18.9 +/- 0.1
PLGA-PEG 20% Maleimide	183.9 +/- 2.7	0.108 +/- 0.017	-25.4 +/- 0.5
PLGA-PEG 30% control	123.0 +/- 2.1	0.197 +/- 0.031	-37.1 +/- 1.4
PLGA-PEG 30% Maleimide	161.4 +/- 9.7	0.157 +/- 0.056	-28.7 +/- 0.6

b)

Formulation	Diameter (nm)	Pdl	Z-average (mV)
PLGA-PEG 10% control	117.0 +/- 0.9	0.101 +/- 0.018	-30.3 +/- 0.3
PLGA-PEG 10% Maleimide	165.9 +/- 6.4	0.071 +/- 0.050	-30.3 +/- 0.7
PLGA-PEG 20% control	113.4 +/- 1.6	0.094 +/- 0.017	-20.3 +/- 0.7
PLGA-PEG 20% Maleimide	191.3 +/- 4.5	0.108 +/- 0.029	-31.9 +/- 0.5
PLGA-PEG 30% control	120.9 +/- 1.6	0.142 +/- 0.031	-26.0 +/- 0.4
PLGA-PEG 30% Maleimide	156.9 +/- 4.9	0.157 +/- 0.056	-31.0 +/- 0.2

c)

Formulation	Diameter (nm)	Pdl	Z-average (mV)
PLGA-PEG 10% control	116.5 +/- 2.4	0.087 +/- 0.057	-23.7 +/- 0.4
PLGA-PEG 10% Maleimide	164.6 +/- 2.0	0.164 +/- 0.059	-26.4 +/- 0.9
PLGA-PEG 20% control	115.6 +/- 0.8	0.101 +/- 0.029	-20.5 +/- 0.7
PLGA-PEG 20% Maleimide	184.5 +/- 3.6	0.109 +/- 0.013	-30.7 +/- 0.7
PLGA-PEG 30% control	124.3 +/- 1.9	0.095 +/- 0.038	-21.6 +/- 0.3
PLGA-PEG 30% Maleimide	158.8 +/- 1-6	0.090 +/- 0.034	-25.0 +/- 0.4

Table A.1.2. Properties of PLGA-PEG NPs with varying maleimide content and spacer PEG length.

Formulation	Diameter by TEM (nm)	Theoretical maleimide molecules/NP	CE%	Theoretical ligand number/NP	Quantified ligands by qPAINT	Ligand availability (%)
PLGA-PEG-Mal. 10% (PEG5k)	64 +/- 12	307	25	77	6	8
PLGA-PEG-Mal. 20% (PEG5k)	64+/- 15	612	21	129	8	6
PLGA-PEG-Mal. 30% (PEG5k)	65 +/- 23	962	31	293	9	2
PLGA-PEG-Mal. 10% (PEG1k)	77 +/- 25	529	38	203	42	21
PLGA-PEG-Mal. 20% (PEG1k)	76 +/- 25	1025	35	359	54	15
PLGA-PEG-Mal. 30% (PEG1k)	78 +/- 29	1630	70	1141	54	5

For calculations of theoretical maleimide molecules/NP, CE%, theoretical ligand number/NP and ligand availability (%) see Material and Methods in Chapter 1.
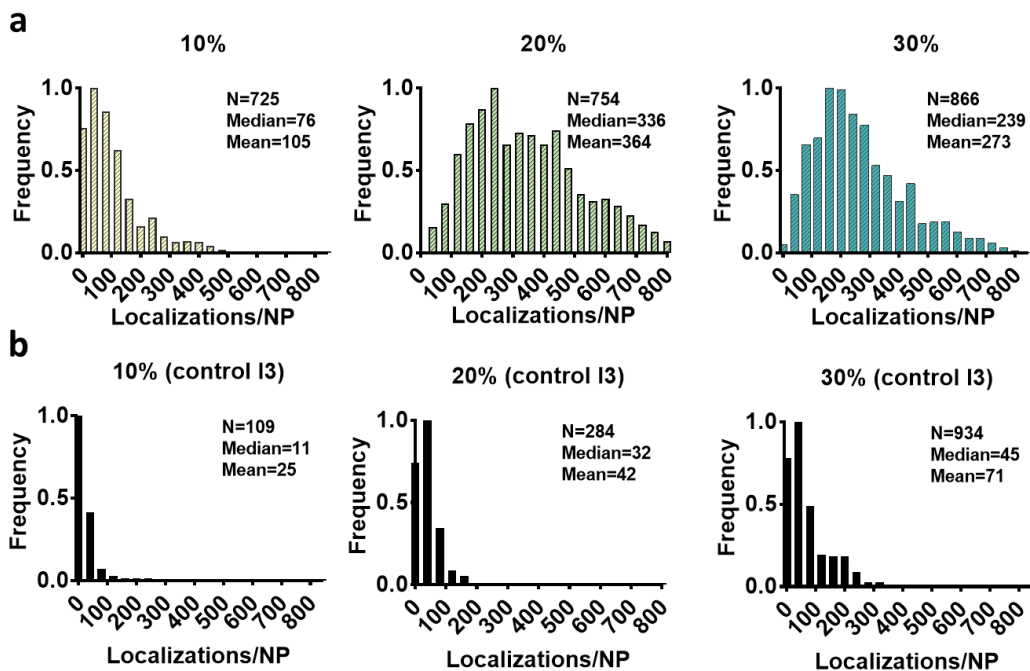
Figure A1.3. *(a) Normalized frequency histograms of DNA-PAINT localizations for PLGA-PEG (PEG$_{1k}$) NPs with varying maleimide contents (10, 20, 30%) after conjugation to functional ligands (docking strands) and imaging with imager strand 3 (correct pairing). (b) Normalized frequency histograms of DNA-PAINT localizations for PLGA-PEG (PEG$_{1k}$) NPs with varying maleimide contents (10, 20, 30%) after conjugation to functional ligands (docking strands) and imaging with imager strand 3 (non-complementary pairing). Bin width=40 nm. The number of nanoparticles analyzed (N), the median and mean number of localizations are also shown. The data were analyzed using MATLAB Software.*

Appendix 1

Appendix 2

*This appendix provides supplementary information to **Chapter 2** of this thesis. It includes extra graphical description of the CLEM protocol, nanoparticle characterization, DNA-PAINT controls, qPAINT calibration on TEM grid and extra data analysis.*
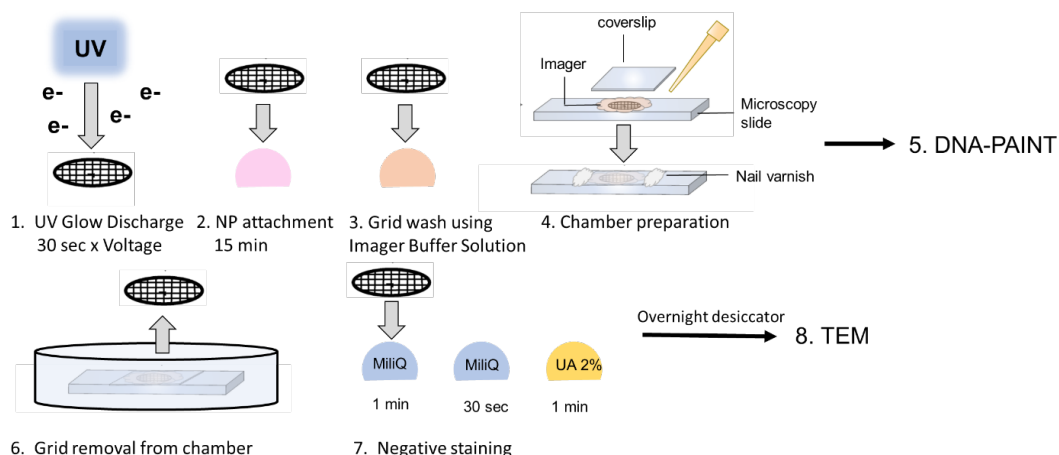
Figure A2.1 *Complementary schematic information for the super-resCLEM protocol described in Figure 1 and in Materials and Methods. Briefly, the carbon-coated copper TEM grid is treated with UV-glow discharge for 30s to improve the attachment of nanoparticles to the surface. The grid is immediately placed with the NP side on a 40 μL drop containing nanoparticle solution 10mg/mL (x5 diluted in MilliQ water) for 15 min. Then the grid is washed through the Imager Buffer solution (Imager strand in Buffer B). The grid is sandwiched between a coverslip and a microscopy slide with the NP side facing the coverslip. To prevent imager evaporation, the sides are sealed off using nail varnish. DNA-PAINT imaging then follows. After, nail varnish is gently removed from the chamber using acetone and tissue paper, then the chamber is placed inside a petri dish containing MilliQ water, and the coverslip is gently wiggled around until it detaches from the microscopy slide and is picked up with a tweezer. It is important to do this step carefully to prevent ripping of the carbon film on the grid. Then, the grid is placed in MilliQ water drops to remove buffers, for 1 min then 30 sec, then for 1 min in uranyl acetate (UA) 2% for negative staining. Excess UA 2% is removed by tapping it on Whatman filter paper. The grid is then left in a desiccator overnight to try. The final step is imaging by TEM, followed by correlation.*

Nanoparticle characterization

Table A2.1 *Analysis of the hydrodynamic radius (diameter nm) and polydispersity index (PdI) by Dynamic Light Scattering at 25°C in milliQ water pH 7.0 for PLGA-PEG nanoparticles with 5% and 30% maleimide content and their respective controls, (a) before conjugation, (b) immediately after conjugation and (c) 7 days after conjugation with thiol-DNA oligonucleotides. The diameter is from intensity distributions. The standard deviation (+/-) for 3 repeats is given.*

a)

Formulation	Diameter (nm)	PdI
PLGA-PEG 5% Maleimide control	111.1 +/- 0.5	0.104 +/- 0.028
PLGA-PEG 5% Maleimide	142.7 +/- 3.6	0.101 +/- 0.022
PLGA-PEG 30% Maleimide control	123.0 +/- 2.1	0.197 +/- 0.031
PLGA-PEG 30% Maleimide	161.4 +/- 9.7	0.157 +/- 0.056

b)

Formulation	Diameter (nm)	PdI
PLGA-PEG 5% Maleimide control	113.0 +/- 0.8	0.130 +/- 0.037
PLGA-PEG 5% Maleimide	156.5 +/- 2.7	0.076 +/- 0.012
PLGA-PEG 30% Maleimide control	120.9 +/- 1.6	0.142 +/- 0.031
PLGA-PEG 30% Maleimide	156.9 +/- 4.9	0.157 +/- 0.056

C=

Formulation	Diameter (nm)	PdI
PLGA-PEG 5% Maleimide control	113.6 +/- 2.5	0.133 +/- 0.023
PLGA-PEG 5% Maleimide	148.3 +/- 2.9	0.130 +/- 0.047
PLGA-PEG 30% Maleimide control	124.3 +/- 1.9	0.095 +/- 0.038
PLGA-PEG 30% Maleimide	158.8 +/- 1.6	0.090 +/- 0.034
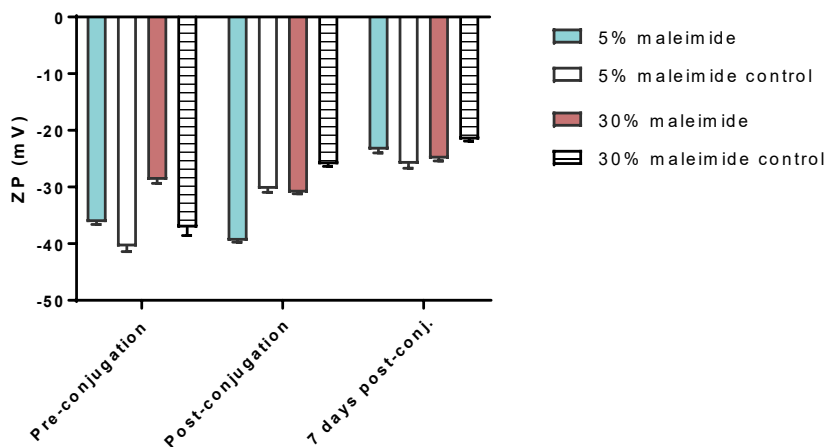
Figure A2.2 *Analysis of zeta potential (ZP, mV) by Dynamic Light Scattering (DLS) using a Zetasizer Nano ZS (Malvern Panalytical) at 25°C in milliQ water pH 7.0 of PLGA-PEG nanoparticles with 5% and 30% maleimide content and their respective control formulations, before conjugation (pre-conjugation), immediately after conjugation (post-conjugation) and 7 days after conjugation (7 days post-conj.) with thiol-DNA oligonucleotides. The error bars are the standard deviation for 3 measurement repeats.*
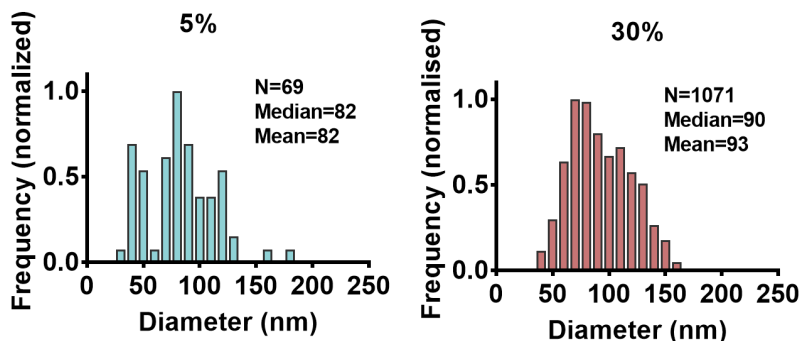
Figure A2.3 *Distributions of NP diameter obtained by DNA-PAINT imaging of PLGA-PEG NP with 5% and 30% maleimide content conjugated to thiol-oligonucleotides. The x,y,t coordinates were analyzed by a mean-shift cluster MATLAB algorithm (bandwidth=50, minimum points=20, maximum particle diameter=160).*
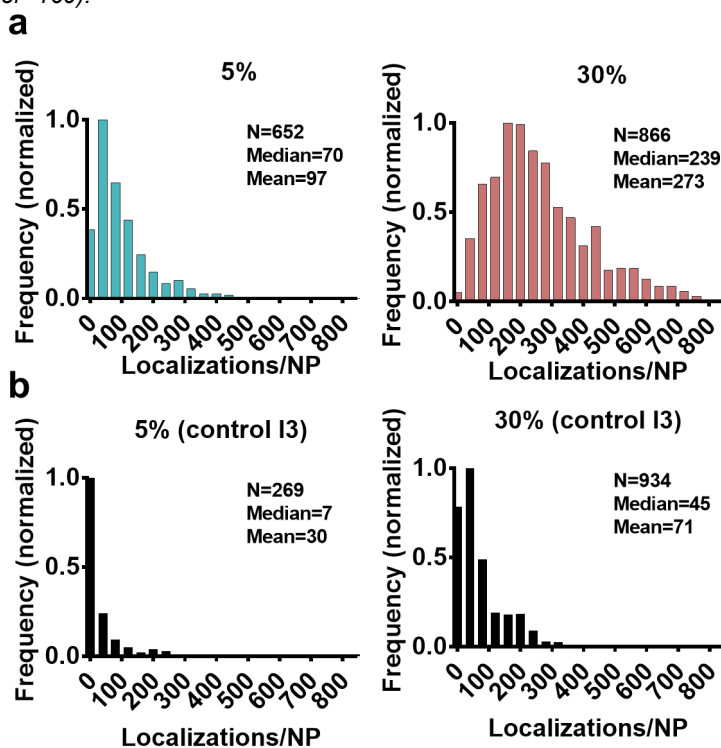
Figure A2.4 *(a) Normalized frequency histograms of DNA-PAINT localizations for PLGA-PEG nanoparticles with 5% (left) and 30% maleimide (right) contents conjugated to thiol-oligonucleotides after imaging with the correct complementary Imager strand 1. The number of nanoparticles analyzed (N), the median and mean number of localizations are also shown. (b) Normalized frequency histograms of DNA-PAINT localizations for PLGA-PEG nanoparticles with 5% (left) and 30% (right) maleimide contents conjugated to thiol-oligonucleotides after imaging with the non-complementary Imager strand 3. The number of nanoparticles analyzed (N), the median and mean number of localizations are also shown. The x,y,t coordinates were analyzed by a mean-shift cluster MATLAB algorithm (bandwidth=50, minimum points=20, maximum particle diameter=160).*

qPAINT calibration on grid and glass

For the calibration experiment, PLGA-PEG 1% maleimide NP were conjugated to thiol-docking strands 1 at a 1:1 molar ratio under the usual conditions and imaged with 10 nM and 20 nM imager 1 in Buffer B for glass and grid samples, respectively. Experiments were carried out according to a previously published protocol by our group[188], with some differences. Briefly, under TIR conditions using a 647 nm laser (~30 mW) 40% power for the excitation of imager strands; emission was detected in a 256 x 256-pixel region of the camera for 20 000 frames at a rate of 10 Hz (camera exposure time 100 ms); a 561 nm laser (~3 mW) power 2% was used for DiI excitation; one frame in the 561 channel was collected every 100 frames in the 647 channel. The time for acquisition of one image was roughly 30 min; temperature was controlled at 25°C. Firstly, the localization clusters from the fiducial 561 channel were identified using a mean-shift clustering algorithm. These clusters were used to identify the center of each individual NP, with an uncertainty of a few tens of nm from the center of the NP. Another filter was used allowing the user to select parameters to filter out noise/aggregates/elongated shapes. Then, the localizations from the 647 channel found within a distance of 120 nm from the center of the NP were detected, and then the number and x,y,t coordinates of the localizations and diameter were calculated for each NP. Using a qPAINT algorithm, a binary intensity time trace was reconstructed for each NP, designating a value of 0 to the frames without localizations and a value of 1 to the frames with 1 localization. Individual CDF were assigned per NP from individual dark times (corresponding to consecutive 0 values in the time trace), fitted with an exponential model $y(t) = 1 - Ae^{-t/\tau_{d^*}}$. qPAINT uses kinetic information based on the mean dark time (τ_{d^*}) between binding events to quantify accessible ligands, which is associated to the number of ligands (n) through the equation $n = (k_{ON}c_i\tau_{d^*})^{-1}$. This requires a calibration to calculate the second-order association rate of the docking strand-imager strand pair (k_{ON}). Using PLGA-PEG 1% maleimide NP conjugated to thiol-docking strands at a known imager concentration (c_i) in Buffer B, we calculated the k_{ON} for the binding kinetics of a single docking strand to be 2.3×10^6 M^{-1} s^{-1} for glass measurements and 8.8×10^5 M^{-1} s^{-1} for grid measurements.

$$K_{ON\ glass} = 2.3 \times 10^6\ M^{-1}\ s^{-1}$$

$$K_{ON\ grid} = 8.8 \times 10^5\ M^{-1}\ s^{-1}$$

Figure A2.5 *qPAINT calibration for glass and grid experiments. (a) Representative PLGA-PEG NP used for the qPAINT calibration on the glass. (b) Corresponding cumulative distribution function (CDF) of individual dark times obtained for the calibration NP (grey circles) and calculated kON value for glass measurements. (c) Representative PLGA-PEG NP used for the qPAINT calibration on the TEM grid. (d) Corresponding cumulative distribution function (CDF) of individual dark times obtained for the calibration NP (grey circles) and calculated kON value for TEM grid measurements. The representative NP images are loaded with a single available thiol-docking strand. DNA-PAINT localizations are seen in red and DiI in green. The red circle depicts the selected diameter for a true particle (100 nm) and the numbers 233 and 65 are the identifier numbers of the NPs, as analyzed by MATLAB.*

Further data analysis
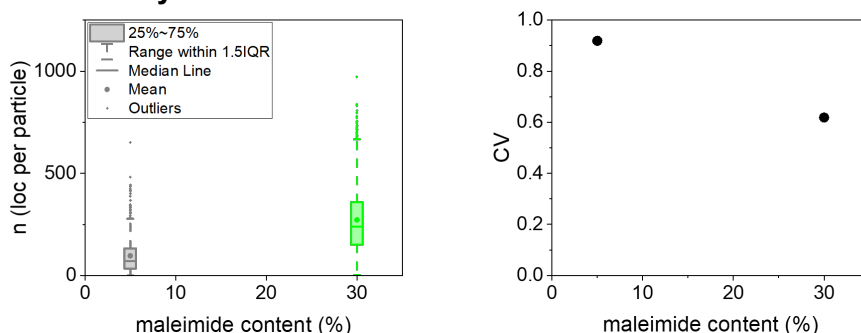
Figure A2.6 *Distribution analysis of number of localizations per NP for PLGA-PEG NP with varying maleimide content, as analyzed by DNA-PAINT. A) Distributions for number of localizations per PLGA-PEG NP with 5% and 30% maleimide content, indicating the interquartile range, median, mean and outliers. B) The coefficient of variation (CV) of number of localizations per NP with maleimide content. CV is calculated as CV= σ/⟨n⟩, where σ is standard deviation and ⟨n⟩ is the mean number of localizations per NP. Data used for analysis is the same as data found in Fig. 2B and Fig. 2C.*

Model	Power 1
Equation	Y= A*(abs(x-xc))^P
xc	34.83391 ± 18.7
A	0.00556 ± 0.018
P	1.87902 ± 0.680
Reduced Chi-Square	2.34413
R-Square	0.96111
Adj. R-Square	0.95463

Model	Power 1
Equation	Y= A*(abs(x-xc))^P
xc	35 ± 0
A	5.1E-4 ± 5.4
P	2.55161 ± 0.23908
Reduced Chi-Square	13.48786
R-Square	0.97451
Adj. R-Square	0.97132
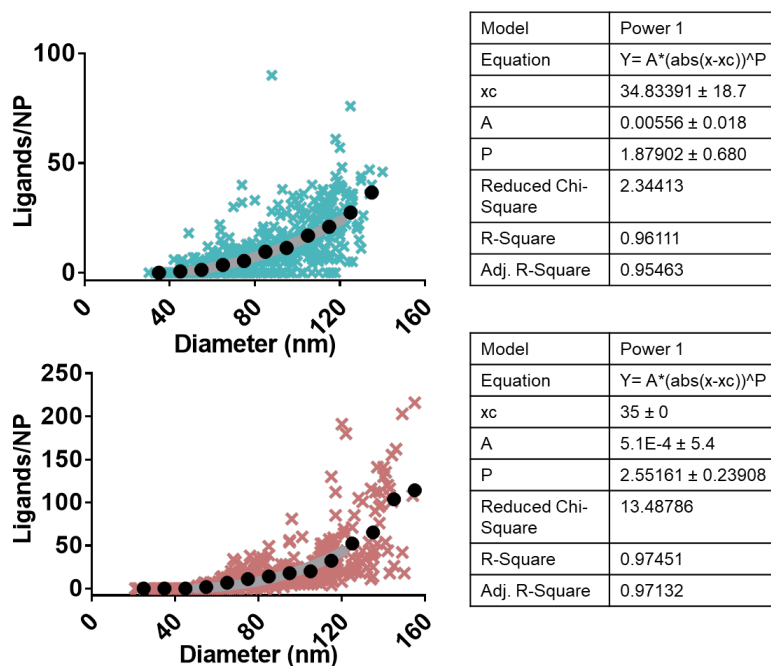
Figure A2.7 Extra statistical analysis corresponding to data and fitting model in Figures 4C and 4F. Note the fitting has been restricted to 50-120 nm diameters.

Cysteine assay protocol and calculation

Briefly, the NP were conjugated with x5 molar excess of L-Cysteine (Sigma Aldrich, MW=175.63 g/mol) compared to maleimide content, for 2h in PBS and at room temperature under spinning conditions. The control NP followed the same protocol. After conjugation, the NP solution was spun down *via* centrifugation using a bench-top centrifuge (Eppendorf Microcentrifuge 5415 R Sigma-Aldrich) for 20 min at 16.1 x g (rcf) at 20°C leading to a NP pellet formation. The supernatant was collected, and the process was repeated for 2 times more until no pellet was observed. The negative control consisted of PLGA-PEG NP (no maleimide) undergoing the conjugation process and centrifugation steps identically to the test NP. The final supernatant solutions were analyzed using Ellman's test as per manufacturer's instructions[250]. Each sample was then analyzed using a NanoDrop Spectrophotometer at 412 nm and using the molar extinction coefficient of TNB (14,150 $M^{-1}cm^{-1}$). The conjugation efficiency was calculated as per Equation 2 in Materials and Methods.

Table A2.2 Conjugation efficiency (CE%) of PLGA-PEG NP formulations with 5% and 30% maleimide content after conjugation with L-Cysteine, as a way of studying maleimide availability.

Formulation	Cysteine conjugation efficiency (%)
PLGA-PEG 5% Maleimide	67
PLGA-PEG 30% Maleimide	65

Appendix 2

Appendix 3

*This Appendix provides supportive information for the results described in **Chapter 3** of this thesis.*
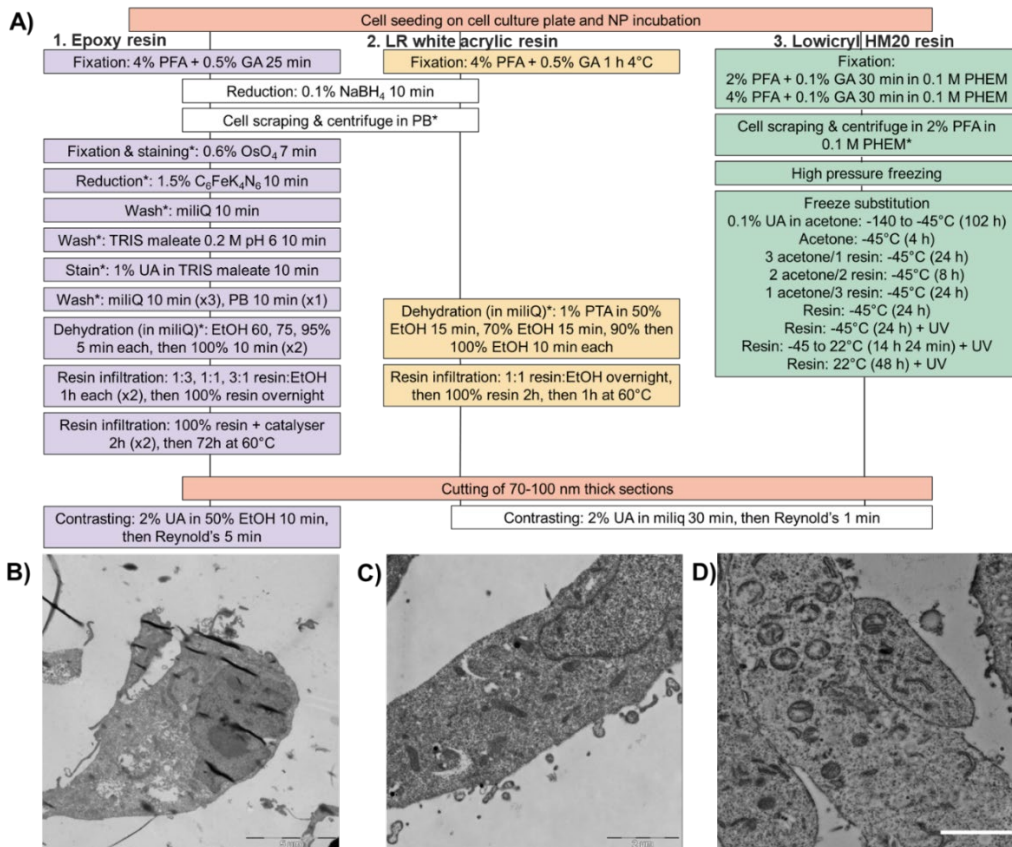
Figure A3.1. *Summary of CLEM protocols attempted and resulting TEM morphology. A) Methodology used for 1. an epoxy resin protocol (Embed-812; Electron Microscopy Sciences), 2. a LR white acrylic resin (medium viscosity, catalyzed; Agar Scientific) and 3. a lowicryl HM20 resin (Electron Microscopy Sciences). Unless stated otherwise, the steps were carried out at RT. * denotes a centrifugation step at 2500 rpm at RT. (Eppendorf 5804 R). B) TEM image of cell ultrastructure using the epoxy resin protocol; structure seems damaged with many empty cytoplasmic spaces (scale bar = 5 μm. C) TEM image of cellular ultrastructure using the LR white acrylic resin protocol; structure is better preserved than with the latter resin, but organelles are not easily distinguishable (scale bar = 2 μm). D) TEM image of cellular ultrastructure using lowicryl HM20 resin; structure is well preserved with organelles clearly distinguishable (scale bar = 2 μm).*

NP analysis:
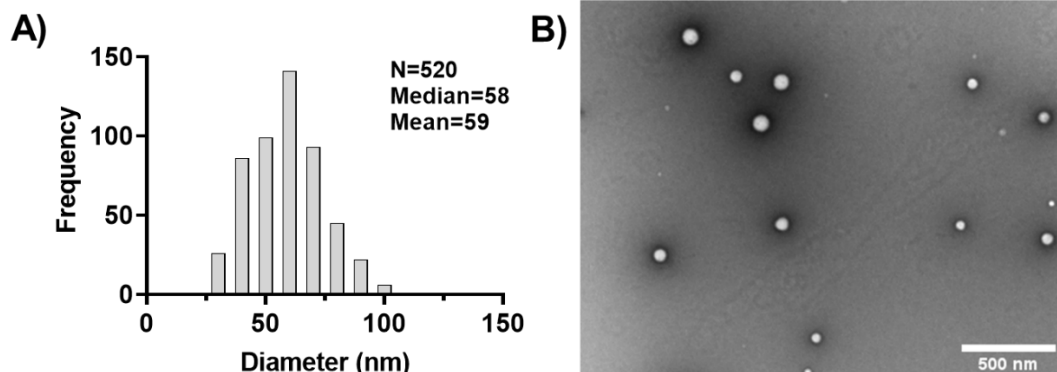
Figure A3.2. *TEM characterization of PLGA-PEG NPs.*

For negative staining, a 200-mesh carbon-layered copper grid was treated with UV-glow discharge (BAL-TEC CTA 005 Glow Discharge Unit) for 1 min to improve attachment. Using a fine tweezer, the grid was placed on top of a ~ 40 µL drop of NP solution 1mg/mL for 2 min. The grid was then washed to remove buffer salts using milliQ water drops for 1 min then 30 sec, then negatively stained using filtered uranyl acetate 2% (UA 2%, in milliQ water) for 1 min. Excess UA was removed by tapping the edge of the grid on Whatman filter paper. The grid was then allowed to dry overnight in a desiccator before TEM imaging.
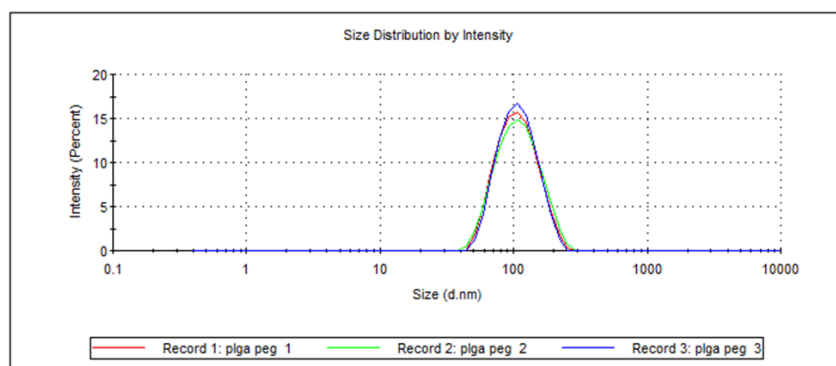
	Zeta average (nm)	STDEV	PdI	STDEV	ZP (mV)	STDEV
PLGA-PEG 30 µM Dil	100	(+/-) 0.6	0.099	(+/-) 0.009	-20	(+/-) 0.3

Figure A3.3. *DLS characterization of PLGA-PEG NPs. Analysis of the hydrodynamic radius (Zeta average nm) by intensity and polydispersity index (PdI) using Dynamic Light Scattering (DLS) at 25°C in milliQ water pH 7.0. Analysis of zeta potential (ZP, Mv) using a Zetasizer Nano ZS (Malvern Panalytical) at 25°C in milliQ water pH 7.0. Measurements were taken the following day after formulation. The standard deviation (STDEV) is for 3 measurement repeats.*
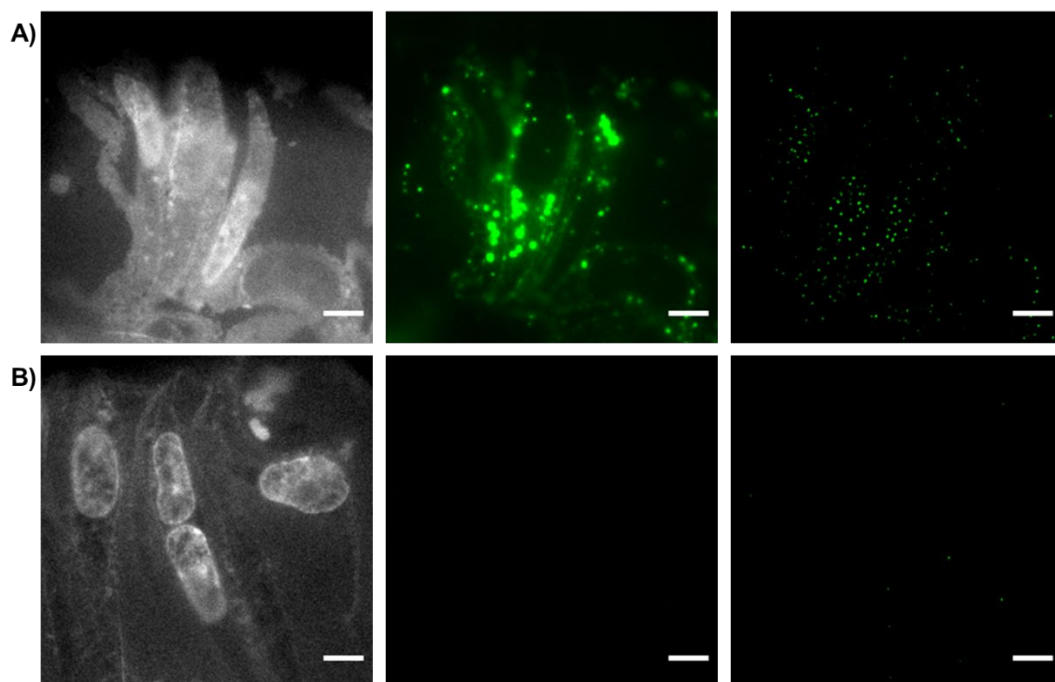
Figure A3.4. *Fluorescence signal after mild fixation, HPF and FS in preparation for STORM-TEM protocol on 70-100 nm thin sections for A) HeLa cells incubated with PLGA-PEG DiI loaded NPs for 8 h and for B) HeLa cells without any NP incubation. Left panel is of nuclei, middle panel is the low-resolution signal of NPs and right panel is the respective STORM image. Contrast for middle and right panels was kept the same. No significant background fluorescence was detected. Scale bars = 5 μm.*
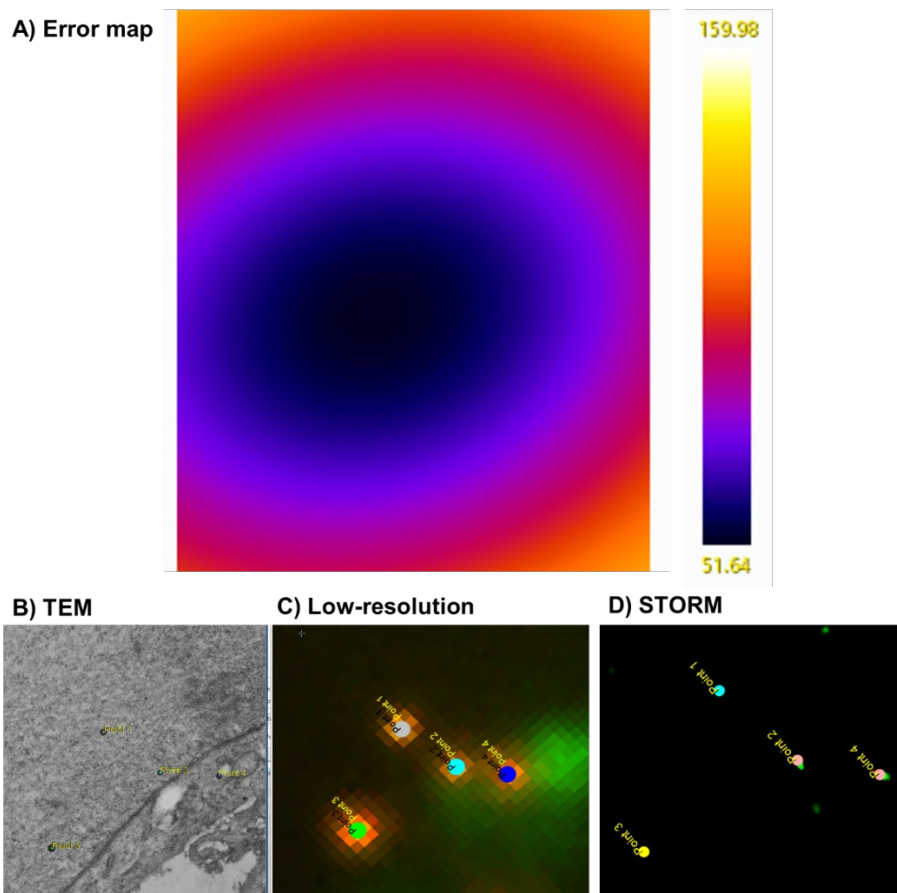
Figure A3.5. *The error map resulting from the correlation of a FM/STORM image with a TEM image as calculated by the open source ec-CLEM (ICY) software. Color gradient indicates an error of 51.64 nm in the center of the image to 159.98 nm on the extremities of the image. Tetraspeck fiducial markers were used for the correlation, as they are visible in TEM (B) and in FM (C)/STORM(D).*

Extra CLEM images:
1h
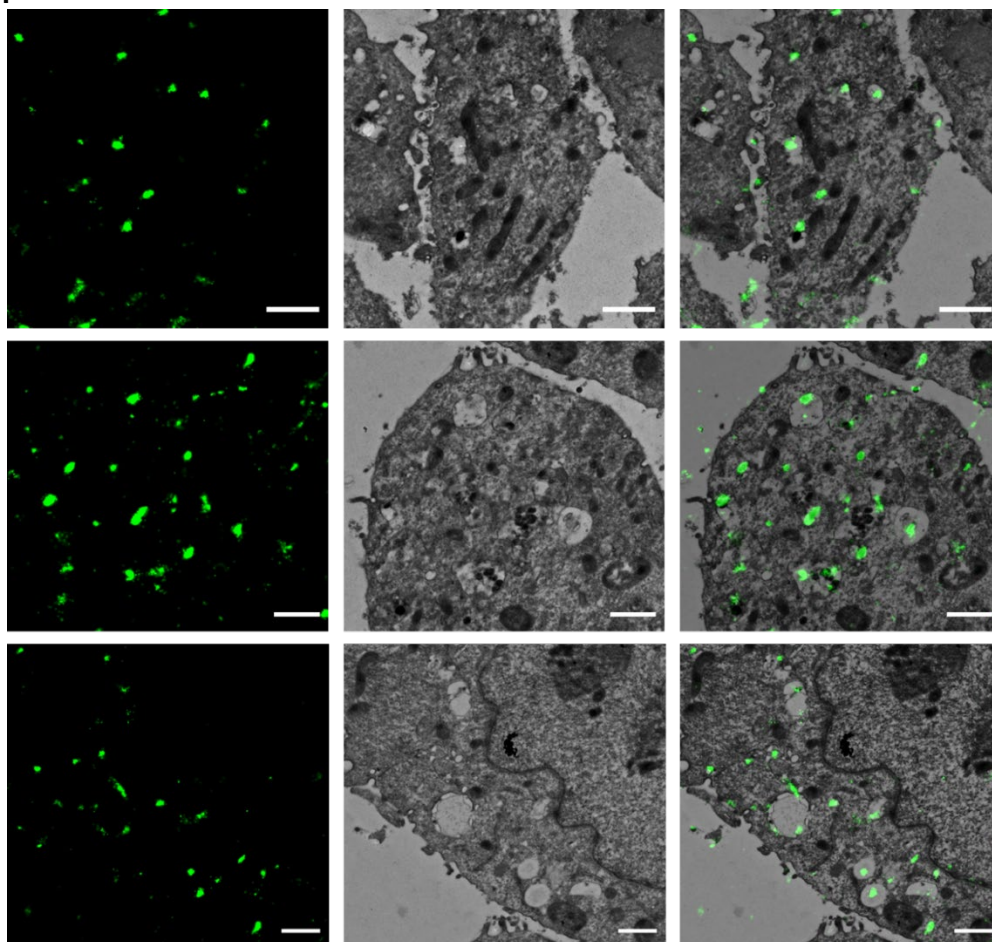
Figure A3.6. *CLEM (dSTORM-TEM) images of PLGA-PEG NPs incubated with HeLa cells for 1 h. Left panels are dSTORM images, middle panels are TEM images of the same region, and the right panels are the overlay of STORM and TEM images. Scale bars = 1 µm*

8 h
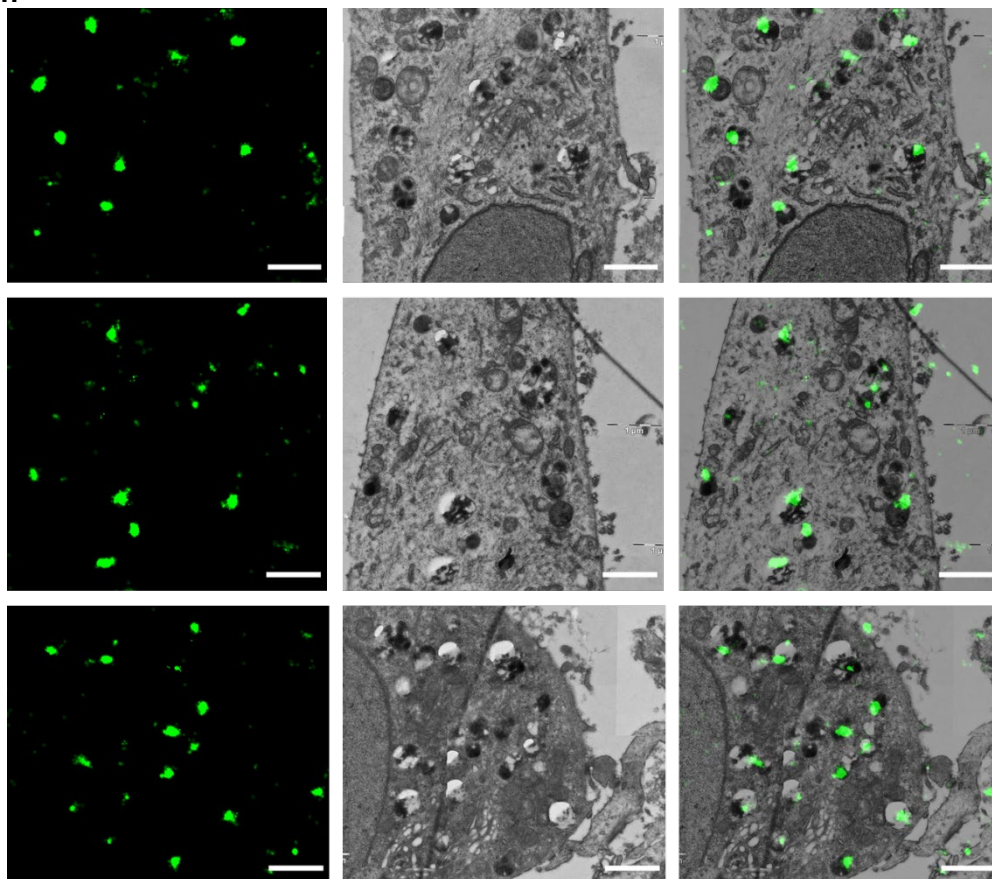
Figure A3.7. *CLEM (dSTORM-TEM) images of PLGA-PEG NPs incubated with HeLa cells for 8 h. A pulse-chase was done after 4 h of incubation. Left panels are dSTORM images, middle panels are TEM images of the same region, and the right panels are the overlay of dSTORM and TEM images. Scale bars = 1 μm*

24 h
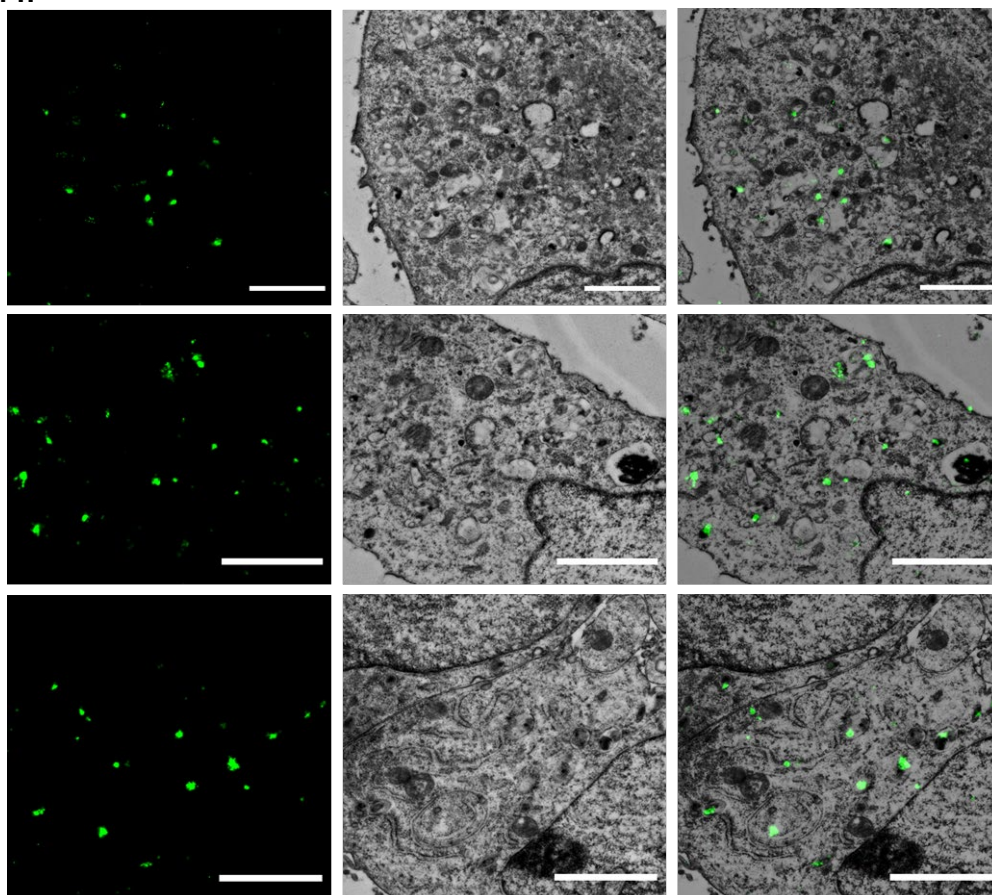
Figure A3.8 *CLEM (dSTORM-TEM) images of PLGA-PEG NPs incubated with HeLa cells for 24 h. A pulse-chase was done after 4 h of incubation. Left panels are dSTORM images, middle panels are TEM images of the same region, and the right panels are the overlay of dSTORM and TEM images. Scale bars = 1 μm*

1 h   **8 h**   **24 h**
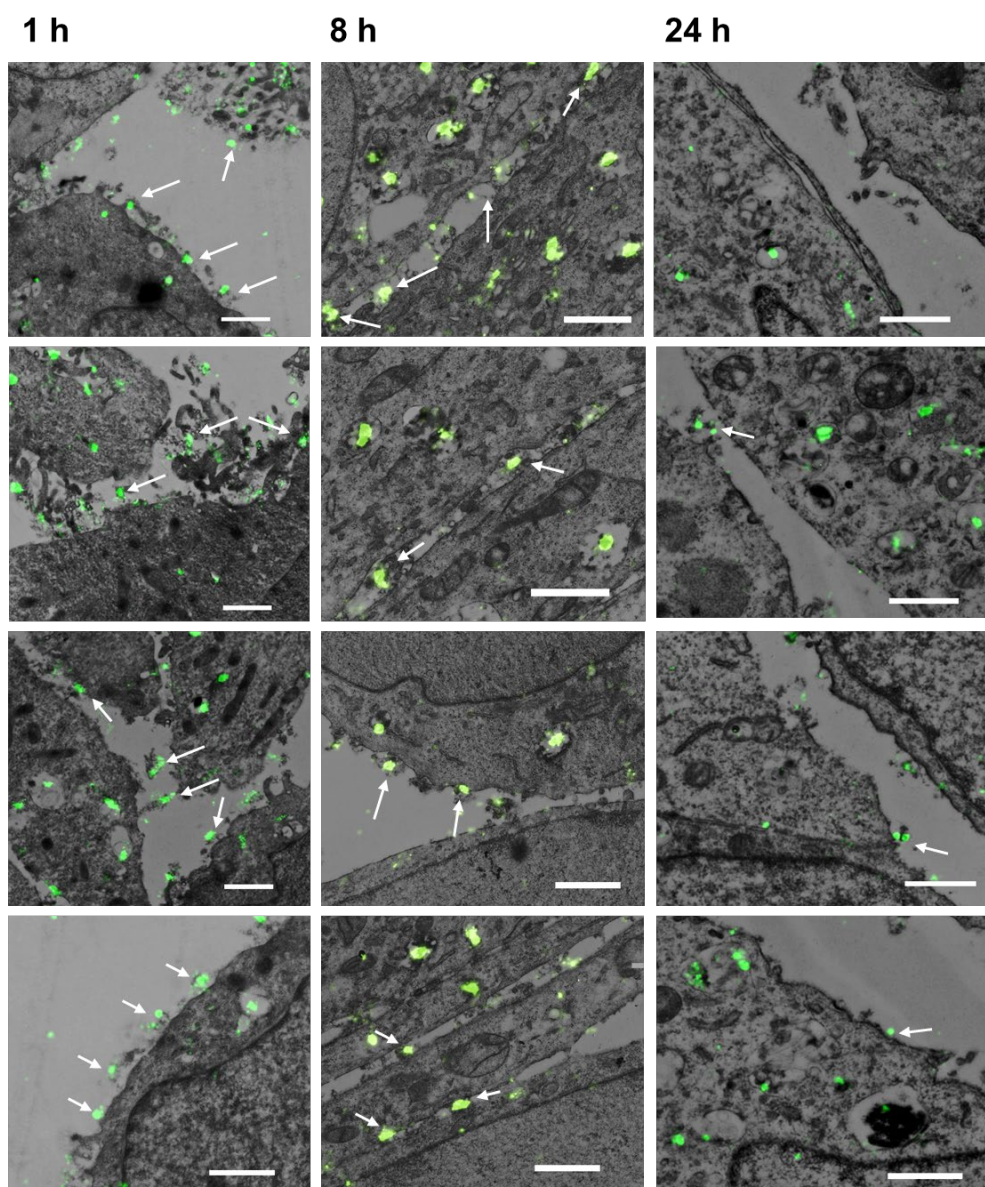
Figure A3.9. *CLEM (dSTORM-TEM) images of PLGA-PEG NPs on the surface or outside of HeLa cells, after incubation at different time points (1 h, 8 h and 24 h). dSTORM NP signal is observed in green. At 1 h, many NPs can be observed on the surface of cells, followed by less at 8 h, with 24 h showing the lowest number. White arrows are used to direct the reader to extracellular NPs that are not easily visible. Scale bars = 1 μm.*
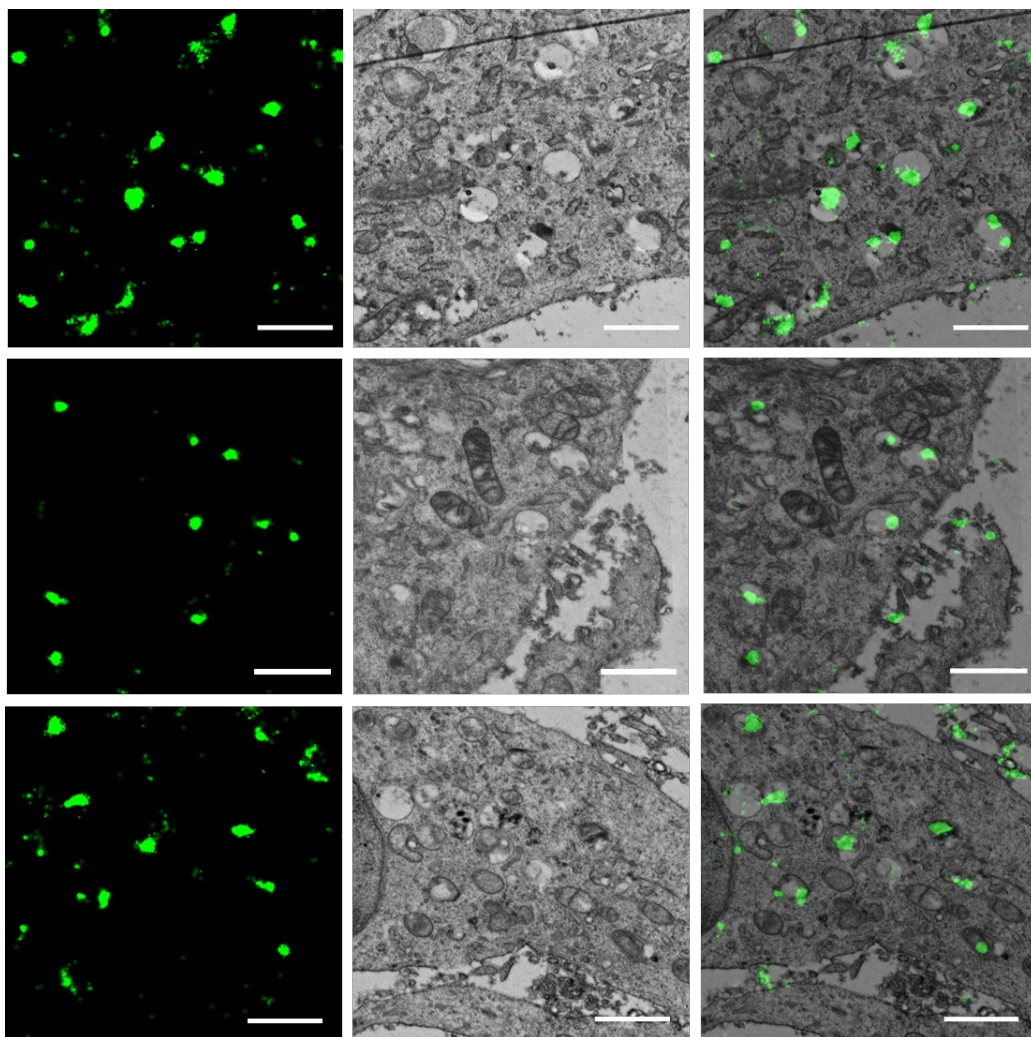
Figure A3.10. *CLEM (dSTORM-TEM) images of HeLa cells incubated with 100 µM chloroquine for 4 h, followed by a 4 h pulse and a 4 h chase incubation with PLGA-PEG DiI loaded NPs. Left panels are STORM images, middle panels are TEM images of the same region, and the right panels are the overlay of dSTORM and TEM images. Scale bars = 1 µm.*

Appendix 4

*This appendix provides supplementary information to **Chapter 4** of this thesis. It includes extra low-resolution FM-TEM correlative images.*

Appendix 4
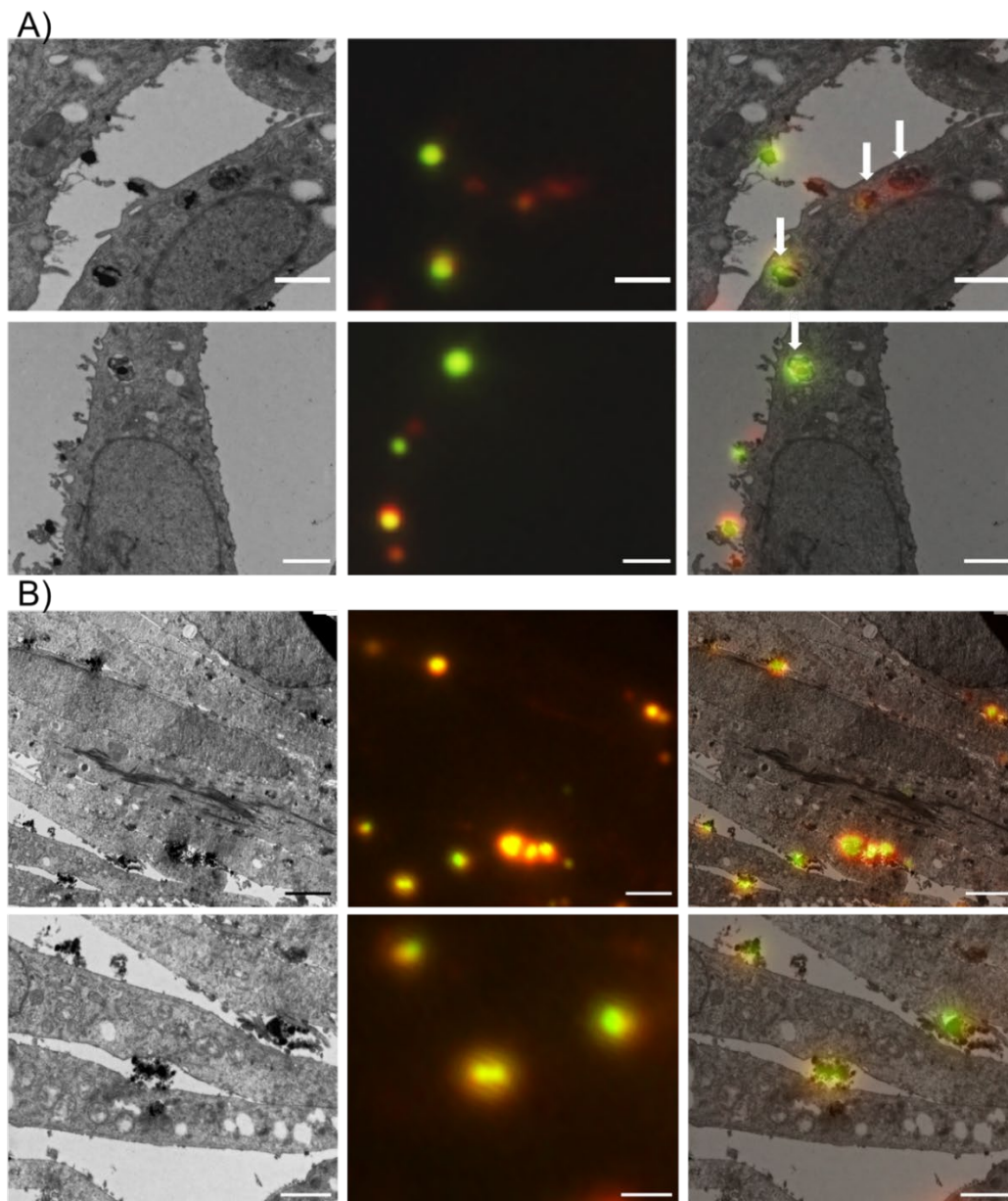
Figure A4.1. *TEM (left panels), low resolution FM (middle panels) and correlative low-resolution FM-TEM images (right panel) of A) RH-pDNA polyplex and B) R-pDNA polyplex at 2 h incubation time with A549 cells. Green signal depicts pDNA and red signal pBAE polymer. White arrows point to polyplexes found within endo-lysosomal compartments. Scale bars = 1 μm.*
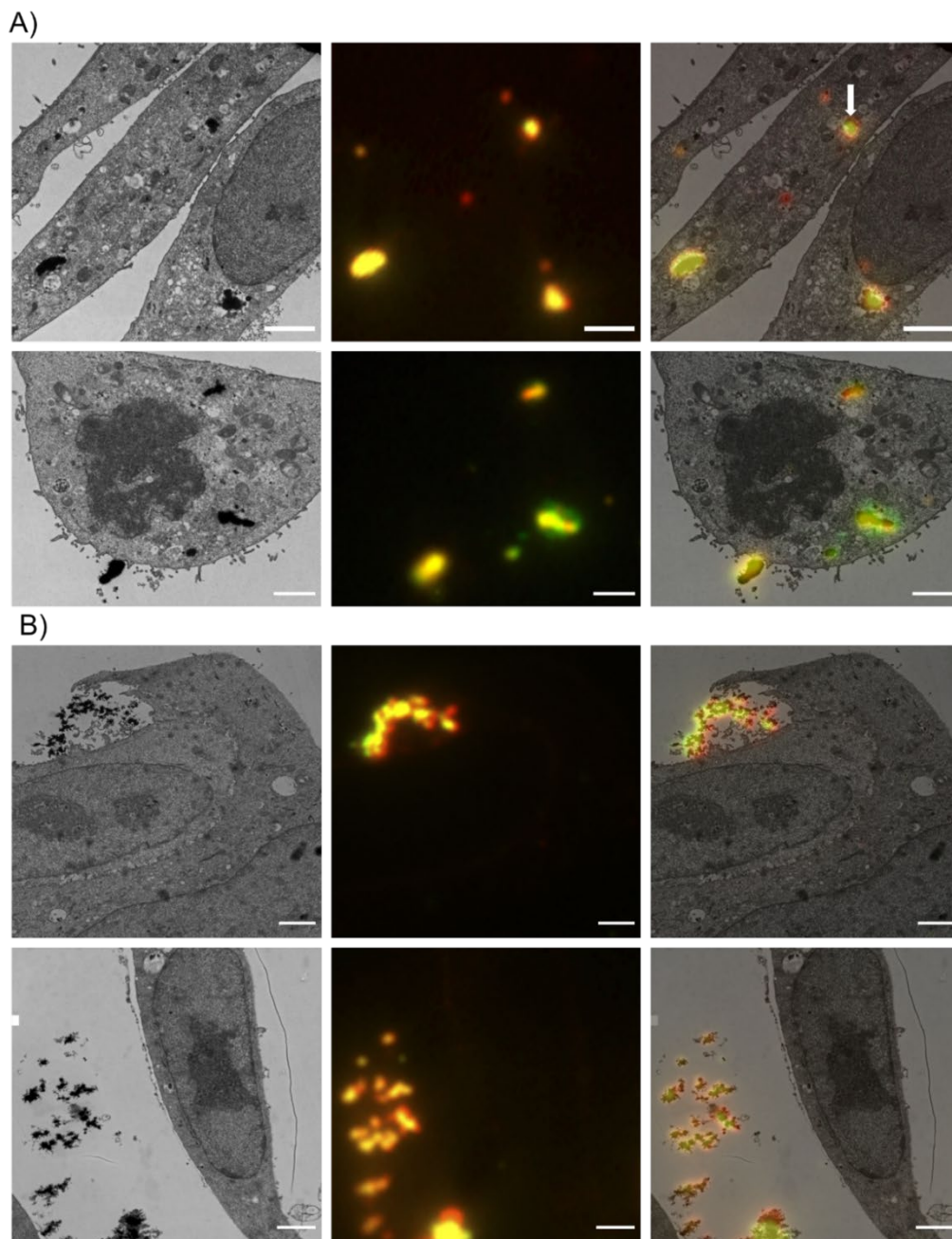
Figure A4.2. TEM (left panels), low resolution FM (middle panels) and correlative low-resolution FM-TEM images (right panel) of A) RH-pDNA polyplex and B) R-pDNA polyplex at 6 h incubation time with A549 cells. Green signal depicts pDNA and red signal pBAE polymer. White arrows point to polyplexes found within endo-lysosomal compartments. Scale bars = 2 μm.

Appendix 5

*This chapter reproduces almost literally the article **Andrian T.**, Riera R., Pujals S., Albertazzi L. **Nanoscopy for endosomal escape quantification**. Nanoscale Adv. 2021;3(1):10–23. As an author in this paper, I contributed to the overall organization, literature research, figure preparation and manuscript writing, together with Riera R. Pujals S and Albertazzi L contributed with providing periodic feedback and review for the manuscript.*

Abstract: *The successful delivery of nanoparticles is hampered by their endosomal entrapment and degradation. To push forward the smart development of nanoparticles we must reliably detect and quantify their endosomal escape process. However, the current methods employed are not quantitative enough at the nanoscale to achieve this. Nanoscopy is a rapidly evolving field that has developed a diverse set of powerful techniques in the last two decades, opening the door to explore nanomedicine with an unprecedented resolution and specificity. The understanding of key steps in the drug delivery process – such as endosomal escape – would benefit greatly from the implementation of the most recent advances in microscopy. In this review, we provide the latest insights into endosomal escape of nanoparticles obtained by nanoscopy, and we discuss the features that would allow these techniques to make a great impact in the field.*

Appendix 5

Introduction

Using nanoparticles (NP) to deliver drugs to cells (nanomedicine) was foreseen to be a true game-changer of the 21st century in improving the prevention, diagnosis and therapy of various therapeutic areas [50,373–377]. The potential of these nanosized carriers in pharmaceutical applications has been envisioned since the 1970's to improve the delivery of therapeutic and imaging agents to specific target sites [378–382]. The remarkable interest in NP is attributed to the plethora of physical and biological advantages they offer in comparison to conventional medicines, such as: improved efficacy and safety, enhanced solubility and pharmacokinetic profile, and increased target selectivity [6,21,383,384].

Although various NP formulations have been marketed [1,385], achieving efficient intracellular delivery still remains a significant challenge [143–145,294,295]. One of the main culprits is that the majority of NP – once taken up via endocytosis – are unavoidably distributed to endocytic vesicles. These acidic organelles can degrade the carrier-drug ensemble, reducing its bioavailability in the intracellular environment [147,386]. Within these vesicles, the pH gradually drops from neutral to acidic because of membrane-incorporated vacuolar-type ATPases. The cargo is first brought into the early endosome (pH ~ 6.3); this matures into a late endosome (pH ~ 5.5); then finally the late endosome fuses with the lysosome and the cargo is degraded by hydrolytic enzymes present in the acidic milieu (pH 5-4.5). The recycling endosome may direct some cargo back to the cell surface, whilst the majority remains entrapped in the endo-lysosomal pathway, where they are degraded [145,387] (Fig. 1). Endosomal entrapment thus represents one of the main bottlenecks in using NP systems for gene therapy [138,139,145,149] and proteins or small molecular drugs for the treatment of a variety of diseases [140–142,145].
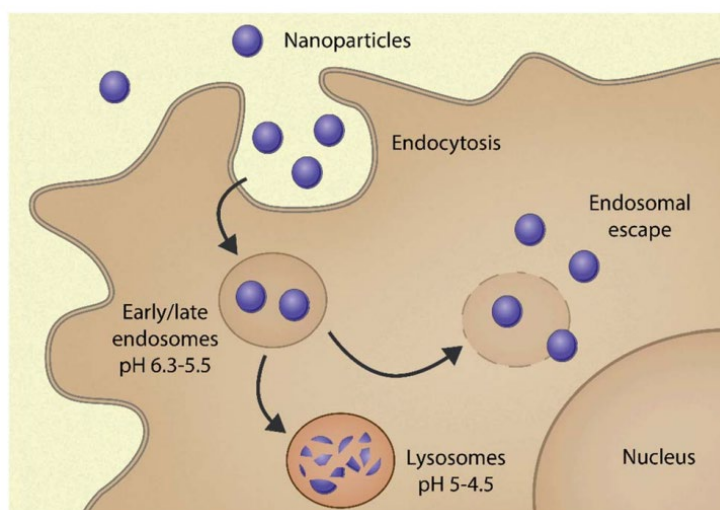
Figure 1. Scheme of the route followed by nanoparticles inside the cell. They are first internalized by endocytosis into early endosomes, where they are trafficked through the endolysosomal pathway and ultimately degraded in the lysosomes. Nanoparticles escaped from endosomes to avoid degradation and deliver their cargo into the cytoplasm.

Mechanisms through which NP – and more importantly the therapeutic cargo – can escape these degrading vesicles have become the subject of intense research over the past decades [122,145,147,295]. Inspired by the innate ability of bacterial toxins and viruses to escape endosomal vesicles, various hypothetical endosomal escape mechanisms have been proposed and reviewed in literature, such as: the "proton sponge" effect, membrane fusion, pore formation, membrane disruption, and vesicle budding and collapse [122,147,149,152,388–390]. Numerous strategies to enhance the escape of NP have also been suggested, including: endosomal buffering agents, membrane fusogenic peptides, lysosomotropic chemical agents [145,150,386,391–397], morphological-dependent changes [398] or external stimuli such as photochemical internalization (PCI) [399,400].

It is crucial to note that the endosomal escape hypotheses suffer from many inconsistencies. For example, the "proton sponge" hypothesis - based on the buffering capacity of polycations, that are suggested to cause an increase in lysosomal pH - has been heavily disputed in literature [348,401]. As a result, the mechanism of action of these formulation strategies are generally unknown. This is limiting the development of NP with efficient endosomal escape, and it is further worsened by the absence of effective methods to detect – and more crucially to quantify – this process. Consequently, it is challenging to determine which strategies are efficient in improving the escape ability of NP, hindering the development of successful formulations. Additionally, the lack of standardized methods leads to poor comparisons between different endosomal escape studies, leading to contradicting and inconclusive results [348,401–405].

Standard methods used to assess endosomal escape commonly employ fluorescence microscopy, flow cytometry or mass spectrometry. However, florescence microscopy cannot be used alone to quantify the total number of particles inside cells, as this requires cumbersome calibration of the fluorescence signal, and lacks the resolution to quantify individual NP below 250 nm. Flow cytometry measures relative fluorescence intensity rather than individual NP, and mass spectrometry leads to loss of spatial information [406]. Readers are directed to other available reviews for information on these techniques and how they may compare with nanoscopy methods [147,151,152,155]. Studying endosomal escape brings alongside certain challenges: it is a fast process, rare and occurs in the nanoscale. All these techniques have limited spatial resolution, are often poorly quantitative and fail to provide information on endosomal escape at the nanoscale and quantitative level, or with high molecular specificity within the cellular biological environment. Therefore, new, and improved techniques are necessary for quantification of NP-cell interactions to allow comparison and integration of data and push forward the smart development of NP.

Here we highlight the most prominent nanoscopy techniques and discuss the features that overcome the limitations of standard methods. We briefly emphasize on how they can be used for quantification of endosomal escape, and we provide a short perspective on how these techniques can help us gain more insight into the process of NP endosomal escape, leading to the development of more effective formulations.

Discussion

As previously highlighted, endosomal escape is a process that is fast, rare and at the nanoscale. Here we briefly discuss the pros and cos of various nanoscopy techniques that can be used to quantitatively study this process. For a summary of the techniques discussed see Table 1, and for extra information on how quantification can be achieved using these techniques, see Table 2. We put emphasis on the power of electron microscopy (EM), super-resolution microscopy (SRM) and correlative imaging to answer sought-after questions regarding NP endosomal escape, and ultimately on improving the development of NP with efficient therapeutic cytosolic delivery.

Table 1. *Comparison of the selected characteristics of the nanoscopy techniques and confocal microscopy. Bold indicates the best and italics the worst in each category.*

Technique	Resolution XY	Resolution Z	Live-cell imaging	Multi-colour	Temporal resolution	Quantification	Overall simplicity of technique
Confocal microscopy	*~200 nm*	*~400 nm*	Yes	Yes (3 colours)	ms–s	*Worst*	**Simple**
EM	**~1 nm**	NA	No	*No*	**ms**	Good	Complex
SMLM	~20 nm	~80 nm	No[a]	Yes (2–124 colours)	*min*	Good	Complex
STED	~50 nm	~150 nm	Yes	Yes (3 colours)	s	Good	Simple
SIM	~100 nm	~300 nm	Yes	Yes (3 colours)	ms–s	Bad	Simple
CLEM	~1 nm (EM)	Dependent on LM technique	No	Dependent on LM technique	Dependent on LM technique	**Best**	*Very complex*

[a] SMLM does not allow live cell imaging in most cases, but there are few examples.[87,89]

Electron Microscopy and Cryo-Electron Microscopy

With a near atomic resolution [407], EM is an irreplaceable tool in studying the physio-chemical properties of NP and quantifying their voyage through the endo-lysosomal pathway [141,192,194,195,203,391,408–420]. EM can even detect a low number (few hundreds) of single nanoparticles escaping endosomal structures, and since it is a label-free method, it will localise and quantify NP generally untraceable by standard light microscopy methods. TEM was demonstrated to quantify approximately 150-times more NP/cell compared to NP events/cell using a confocal laser scanning microscope [204]. EM allows direct visualisation and quantification of NP and endosomal compartments and can distinguish between intracellular/extracellular/intramembranous NP, both in 2D and 3D (Table 2).

Table 2. Overview of different types of quantification methods and how these can be achieved using nanoscopy and confocal microscopy, including information on throughput and disadvantages of the methods.

Technique	Quantification	Quantification process	Throughput	Disadvantages
[a]Confocal	Co-localization	NP endosomal vesicles are tagged with different fluorophores and average fluorescence intensity is calculated (*e.g.* using ImageJ – Color2/JACoP). Co-localization calculated using Mander's/Pearson's correlation coefficients[56,148]	Fairly good throughput – (*i.e.* a few cells, tens of lysosomes and tens of NP clusters)	-Limited resolution -Cannot resolve individual NPs -Localization precision is affected by resolution
	Particle tracking	The total number of particles and endosome co-localized NPs is tracked and counted with particle tracking software. As NPs cannot be individually detected, particle events are calculated instead, whereby a single NP event likely corresponds to one vesicle containing NPs[75,154]		-Invisible particles (*i.e.* due to bleaching of fluorophores or de-coupling of fluorescent dyes) -Number of particles is underestimated -Choice of fluorophore can influence results (*e.g.* pH sensitive dyes can have reduced signals in acidic vesicles) -Fluorescence must be quantified in relation to a control to account for fluorophore instability
EM	Direct visualization and quantification	The ratio between NPs found in the cytosol and endosomes is calculated[148,155,156]	Low throughput – (*i.e.* one cell, tens of NPs and a few endosomes per field of view)	-Complicated sample preparation
		Can distinguish between intracellular/extracellular/intramembranous nanoparticles		-Generally, samples are fixed and sectioned (*i.e.* no living cells)
	Serial sectioning or electron tomography	Imaging in 3D of sequential sample sections. Location, size, and the number of vesicles as well as NPs can be calculated in whole 3D cells[74,156]		-Difficulty in distinguishing different intracellular vesicles
	Stereological image analysis	Using the relative particle distribution within cells (RDI). Tests if NPs are localizing randomly or specifically within cellular compartments. The particle density of each compartment is calculated by relating the number of particle events in the specific compartment to the fractional volume of the compartment[157]		-Particles must be smaller than the section thickness (~150 nm)
		Correlating the total number of intracellular particles of a sample with the total cell number of that sample. Using the fractionator principle[54,158]		-Quantification from 3D reconstructions is difficult
		The density of intracellular particles is multiplied by the average cell volume to calculate the average number of NPs per cell[75]		-Restricted to samples with adequate atomic contrast

Table 2. continued.

Technique	Quantification	Quantification process	Throughput	Disadvantages
SMLM	Spatial analysis and clustering	Single-molecule localization microscopy techniques produce point cloud data as a result of multiple localizations in time. These data can be analyzed to identify objects, and determine densities or spatial correlations[93]	Intermediate – low throughput. The field of view may vary from one to few cells. The imaging time would greatly depend on the specific technique used (seconds to minutes)	-In some cases, there are undesired non-specific interactions or background noise
	Molecule counting	Single-molecule localization microscopy techniques are based on the identification of individual molecules. Therefore, it is possible to quantify the exact number of molecules on a specific area.[159,160] For example, the ligands or proteins on the surface of a nanoparticle[161,162]		-High amount of data that can make the quantification process slow
	Stability of NPs and vesicles	The increased resolution and precise molecule counting of super-resolution microscopy allow the determination of the stability of small objects such as nanoparticles and vesicles. It is possible to establish their shape[96] and observe the degradation in time[99]		
STED/SIM	Size and shape of NPs	The improved resolution of these techniques allows the measurements of the size and shape of smaller objects compared to confocal microscopy[109,113,114]	Good throughput – imaging times in the millisecond-second range	-No single-molecule quantification
	Co-localization	Standard colocalization coefficient calculations are also applied for these techniques, although better resolution yields more precise results[109]		
CLEM	Combination of FM and EM techniques	Generally, fluorescence microscopy is carried out prior to EM. Images can be manually aligned using plugins such as eC-CLEM. Quantification can be achieved either *via* EM or FM, or both.[74,163] Detection of 'invisible particles' in light microscopy is possible with CLEM, as well as compartment-specific quantification	Low throughput – still limited by EM	-Complex and time-consuming sample preparation -NPs must be detectable using both light and electron microscopes -Alignment mismatch can affect correlation

[a] Quantification is not absolute (not at a single particle level) due to the resolution of the microscope.

As a pioneering example, Gilleron et al. [391] achieved one of the most promising semi-automatic approaches using TEM, quantifying the amount of siRNA-conjugated colloidal gold NP escaping from various endo-lysosomal compartments (Fig. 2A, top left). The authors developed a gold detection software that automatically detects and quantifies the total number of gold NP in each image, based on the threshold intensity of gold. Using this, they quantified the ratio of siRNA-gold within the endosomes and in the cytosol to calculate endosomal escape and found that only <2% of siRNA-gold escaped the endosomes in HeLa cells. Furthermore, using distinct mathematical models in combination with a pharmacological blockade of endosomal progression, they observed that release occurs mainly from the early endosome. Additionally, developments in staining methods such as photoconversion of diaminobenzene (DAB) – that allows the conversion of a fluorescent dye into an electron-dense signal - in combination with immunoelectron microscopy demonstrate that EM can be used to examine the interactions of NP with cellular organelles and to detect if they are intact or degraded after endo-lysosomal breakdown [421,422].
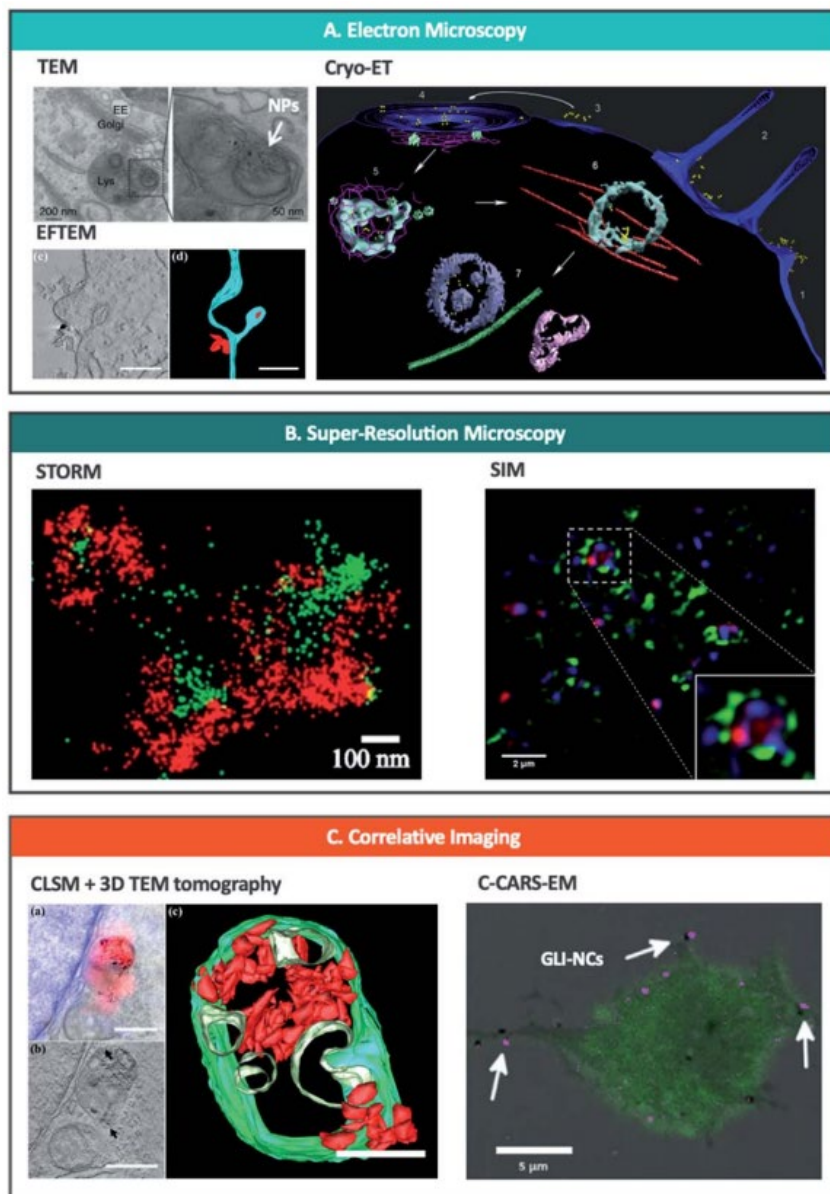
Figure 2. Nanoscopy techniques used to study and/or quantify endo-lysosomal trafficking of nanoparticles. (A) EM techniques including TEM (upper left)[149], EFTEM (lower left)[420] and Cryo-ET (right)[416] can be used to track and quantify nanoparticles in intracellular vesicles. Adapted with permission from ref. 149 Copyright © 2013 Nature America, Inc., from ref. 420 © 2019 American Chemical Society and from ref. [416] Copyright © Azubel et al. eLife. (B) Super-resolution microscopy has been used to image nanoparticles bursting out of endosomes with STORM (left)[299] and SIM (right)[423] Adapted with permission from ref. 299 and 423 Copyright 2018 American Chemical Society. (C) Correlative imaging combines different microscopic techniques such as CLSM and 3D TEM tomography (left)[420] or C-CARS and EM (right)[417] and offers spatiotemporal localization of labelled NPs and biomolecules with high specificity and sensitivity at a highly subcellular level. Adapted with permission from ref. 420 Copyright © 2019 American Chemical Society and from ref. 417 Copyright © 2018 The Authors. Biotechnology Journal Published by Wiley-VCH Verlag GmbH & Co. KGaA.

One of the limitations of conventional EM is that the image acquired corresponds to a distorted, dehydrated form of the natural specimen, due to the need for drying, staining or plastic embedding the sample. Using cryo-EM, the specimen exists in a near-native frozen-hydrated state, maintaining the structures of interest as they would be in solution [424,425]. However, up to date, the only paper exploiting cryo-EM to study the trafficking of NP within the endosomal pathway (albeit indirectly) is by Azubel et al. [416] who employed cryo-electron tomography (cryo-ET) to study the endosomal trafficking of fibroblast growth factor 21 tagged to gold NP (AuNP-FGF21) (Fig. 2A, right). By using 3D tomographic reconstruction, they were able to unequivocally identify gold NP inside/outside various cellular structures including endosomes. Although the authors did not focus on quantifying the gold NP, this technique has great potential to quantify the endosomal escape of various inorganic NP, as well as that of different proteinaceous ligands/protein-based cargo at a single-particle level and with great localisation precision.

Indisputably, EM is an irreplaceable asset in the visualization and quantification of NP endosomal escape. However, it can only be used on fixed or frozen samples and it is inappropriate for studying dynamic changes. Cellular samples must be cut into <200 nm thin sections and exposed to various staining and washing steps that can lead to the loss of NP [426]. Also, at the expense of high resolution, only a small field of view (a few endosomes and a few tens of NP) can be analysed at one time, making this a low-throughput technique. Lastly, TEM has reduced molecular specificity, thus makes it difficult to distinguish between different types of vesicles within the endosomal pathway [194].

Super-resolution Microscopy or Optical Nanoscopy

In the history of light microscopy, better lenses were used to improve resolution by focusing more light onto the sample, such as the pinhole in confocal microscopy [427]. However, Abbe´s diffraction's law [428] determines that the ultimate resolution of any light microscope is limited to 200-350 nm due to light diffraction. The advent of SRM [429] allows to overcome this limitation combining the advantages of fluorescent microscopy with nanometric resolutions. The specific labelling of proteins, multicolor ability and live-cell imaging at subcellular resolutions transformed this method into a new powerful tool to study endosome escaping.

i) Single-Molecule Localization Microscopy (STORM, PALM and PAINT)

Single-molecule localization microscopy (SMLM) is a group of fluorescent SRM techniques based on the localization of single molecules with resolutions down to tens of nanometres. It was in 2006 when SMLM was introduced bringing in the idea of stochastically having only a sparse subset of the fluorophores 'on' at a time and repeating the process until the whole sample is analysed [184,430–433]. Superimposing those sparse single-molecule images we can reconstruct the initial image at a higher resolution. The difference between the various techniques relies on how they cause the fluorophores to switch between 'on' and 'off' states. Stochastic optical reconstruction microscopy (STORM) [432,434] and photoactivated localization microscopy (PALM) [431,433] are based on the photoswitching and photoactivation of organic dyes

and fluorescent proteins respectively, meanwhile point accumulation for imaging in nanoscale topography (PAINT) [184,435–437] is based on the binding and unbinding of free diffusing fluorescent labelled probes to the target molecule.

The main advantages of these techniques are that they have an excellent resolution (5-25nm) to visualize NP and intracellular vesicles, and they can offer a powerful quantitative tool with single-molecule precision [438], i.e. molecular counting. Moreover, they offer multicolor imaging, bringing in the possibility of labelling multiple subcellular structures as well as delivery carriers at the same time. In particular PAINT, by multiple rounds of imaging with different target probes [436,439] or by kinetic fingerprinting the binding interaction, has recently proven 124 color super-resolution imaging [440]. The main disadvantage of SMLM techniques is that they also require long imaging times to reconstruct the final image (few minutes to an hour), making them generally not suitable for live cell imaging.

Recently, STORM has been applied to observe endosomal escape of siRNA polyplexes [441] (Fig. 2B). In this study, they imaged polyplexes carrying siRNA in early and late endosomes with 2-color STORM to direct visualize the rupture of endosomes and the release of polyplexes. They first measured the size of polyplexes under biological environments from 2D STORM images. Then, they observed the shape of individual endosomes and polyplexes inside cells to establish how the endosomal escape process was occurring. Finally, they combined 2-color STORM images to determine the level of colocalization of polyplexes and endosomes by counting individual polyplexes. In fact, STORM has also been used recently to study the trafficking and stability of NP in cells [442–444]. This and other techniques have shown the capability to image in 3D at the nanometric-scale resolution subcellular structures, such as endosomes and lysosomes, opening the door to a deeper understanding of endosomal escape [445].

ii) Stimulated Emission Depletion (STED)

Stimulated emission depletion (STED) is a SRM technique initially proposed by Stefan W. Hell in the 90s [446] and firstly applied on biological samples in 2000 [447]. It works by shrinking the focused excitation of a confocal by a second doughnut-shape laser. This second beam depletes fluorescence and as a result only fluorescence from the centre of the doughnut is collected. The main advantage of STED is that it offers diffraction unlimited resolution at imaging speeds similar to a confocal – seconds – as well as 3D and tissue imaging, as recently demonstrated by the imaging of NP internalization in 3D [448] and the crossing of the blood-brain barrier in brain tissue samples [449]. However, to effectively deplete fluorophore emission with the circular shaped beam, it requires a high intensity laser that may cause photodamage to cells [450], although live-cell imaging can be done at some extent [451].

STED nanoscopy has been applied in internalization and trafficking of NP [452–454]. Specifically, Li Shang and co-workers investigated the internalization of transferrin NP and measured the size of NP-loaded early endosomes with STED in live cells to conclude that particles were clustered inside the vesicles [454]. STED has not been used up to date to study endosomal escape of NP, however, due to the multiple advantages of this technique, we can foresee the potential of STED to contribute to this field.

iii)   Structured Illumination Microscopy (SIM)

Structured illumination microscopy (SIM) is a SRM technique based on the Moiré effect, in which the sample is illuminated with a known pattern in different orientations and the resulting images can be deconvoluted into a higher resolution image [455]. SIM can achieve a resolution half of Abbe´s theoretical limit, around 100-150nm, as well as fast imaging speed – below 1 second – and low light exposure to the sample compared to other SRM methods. This makes it the ideal SRM method for live-cell imaging.

SIM has had a great impact in studying cell-NP interactions due to its fast imaging speed, live-cell capabilities, and low restrictions on fluorophore selection. It has been applied to investigate NP internalization [456], trafficking [457] – as well as shape [458] and degradation [459] inside cells – and subcellular dynamic processes at few milliseconds time resolution [460,461]. Focusing on endosomal escape, SIM has been recently used to image the rupture of endosomes and the delivery of siRNA into the cytoplasm in breast cancer cells [423] (Fig. 2B). Moreover, SIM has revealed that PEI polyplexes are found close to the internal side of the membrane of lysosomes/late endosomes, rather than a central position in the vesicle [462]. These findings prove the potential of SIM to investigate endosome-NP interactions in live cells, where an intermediate resolution is sufficient.

Frontiers in Fluorescent Micro-/Nanoscopy

The field of microscopy is constantly evolving and releasing new tools to tackle the challenges at the micro- and nanoscopic scales. Recent developments have proven to be powerful techniques to study NP in the biological environment offering better resolution and live-cell imaging features. Specifically, AiryScan [463] and RESOLFT [464] came into play to reduce photobleaching in confocal and STED microscopy respectively, for improved live-cell imaging, dynamic studies and higher throughputs. Moreover, recently developed MINFLUX (minimum photon fluxes) has achieved an outstanding resolution of 1-3nm with low laser exposure in 3 dimensions [465,466].

Dynamic Imaging

Endosomal trafficking and escape of NP not only occurs at the nanoscale, but it is also a dynamic process. Some microscopy techniques can be combined with other tools to further investigate dynamic processes, such as fluorescence resonance energy transfer (FRET) [467–469], fluorescence correlation spectroscopy (FCS) [470,471] and single-particle tracking (SPT) [472–476]. Interestingly, SPT has been extensively used to study the co-localization and quantification of NP within endocytic vesicles [472,477–483]. For instance, Zahid et al. [477] used live-cell SPT in combination with multidimensional analysis to characterize intracellular distributions of quantum dots (QDs) properties and to quantify their endosomal escape. The knowledge provided by SPT data analysis - especially when combined with other techniques - can be used to understand the underlying biological mechanisms of what discriminates formulations that achieve endosomal escape from those that cannot.

Correlative Imaging

Various papers study the endosomal escape of NP using several independent microscopic techniques [141,408,415,484,485]. However, a correlative approach is more desirable, as it bridges the advantages of two distinct techniques by imaging the same region of interest and overlapping important information from the two methods. Despite a much greater image interpretation confidence - that would not be possible with either method individually [333] - there is a very low number of publications in the area. This is probably related to the complex and cumbersome procedures required for sample handling and image aligning [486].

Correlative light and electron microscopy (CLEM) are perhaps the most explored group of correlated techniques. The combination allows spatiotemporal localization of labelled biomolecules with high specificity and sensitivity (FM), and with (sub)-nanometer resolution and precise subcellular localization of NP within the cell (EM). In practice, quantification precision can be greatly improved using CLEM, as 'invisible particles' (i.e. not labelled with a fluorescent dye/semi-transparent in TEM) can be detected. Also, since it can be difficult to distinguish different endosomal compartments based just on TEM morphology, correlation with fluorescently labelled compartments in light microscopy can also improve NP localization precision.

Up to date, the only CLEM approach used to quantitatively study endo-lysosomal tracking of NP has been developed by Han et al. [420] (Fig. 2c, left). Using confocal laser scanning microscopy (CLSM) and 3D TEM tomography, they were able to demonstrate the localization of fNDs within endosomes, lysosomes and autophagosomes. Using the high-resolution TEM tomography results, they precisely quantified single fNDs found in clusters within the endosomal vesicles. However, quantification of single fNDs (not within clusters) was only possible at single-particle level by using EFTEM (energy filtered TEM) as an additional method (Fig. 2A, bottom left). Furthermore, EFTEM permitted autonomous TEM screening of the whole sample, demonstrating the potential of this technique to precisely identify and quantify intracellular NP.

Haruta et al. [487] used the local surface plasmon resonance (LSPR) of gold NP as tags for biological samples in CLEM. To alleviate the problem of the resolution mismatch of several orders of magnitude between the two techniques, EM has also been correlated with SRM. Fluorescent nanodiamonds (FNDs) have been studied at nanometer resolution using STED-TEM [488] and integrated light and scanning EM [489]. However, in these examples NP have been used for correlative purposes rather than to quantify or answer specific questions regarding intracellular trafficking. SRM-EM in fact offers a powerful tool to quantify and track endosomal escape and research in this area would benefit greatly the nanomedicine community.

A more distinct approach was achieved by Saarinen et al. [417] who used correlative coherent anti-Stokes Raman scattering and TEM (C-CARS-EM) to image glibenclamide-nanocrystals (GLI-NCs) in macrophages (Fig. 2c, right). The combination of label-free and chemically specific C-CARS technique with the excellent resolution and precision of TEM, allowed precise localization of GLI-NCs within endosomal vesicles. Although not achieved in this work, this technique also has the

potential to be quantitative. For example, using 3D information from C-CARS together with precise localization of nanocrystals from EM, one can calculate the ratio between NP found in the cytosol and in the endosomes (endosomal escape).

Conclusions and Perspectives

Whilst significant progress has been made on developing a rich formulation databank of NP for cytosolic delivery [1,385], our understanding of the physiochemical and biological requisites for achieving endosomal escape has loitered [138–142,145,149]. Our grasp of these mechanisms is hampered by the limitations of the standard techniques used to localise and quantify them. As discussed in this review, nanoscopy techniques – independently, or in correlation – hold the promise of answering some essential questions regarding endosomal escape. Some of these questions include: How and which physiochemical properties of NP influence endosomal escape? Which of the proposed endosomal escape mechanisms stand true and how can we improve the formulation of NP to exploit them? Can we relate endosomal escape to the time and location at which it occurs intracellularly?

Here we have highlighted the relevance of nanoscopy and some of the most recent discoveries in endosomal escape possible only using these methods. With a plethora of advanced microscopic techniques available, it is essential that we outweigh the pros and cons of each technique to best suit the scientific question proposed (Table 1 and Table 2). For a process such as endosomal escape - that is fast, rare and at the nanoscale – it may seem challenging to answer the various questions projected using individual methods. But as we have seen in this review, we are no longer restricted to a 'one method at a time' approach [333,417,420,487–489]. The benefits of correlative imaging – especially of SRM-EM – are of tremendous relevance in obtaining quantitative information on NP endosomal trafficking. Furthermore, as the amount of imaging data is increasing, automated quantification is becoming crucial in reducing manual analysis of images (and increasing throughput) and extracting more valuable data found in microscopic images, as well as making these techniques available to a broader research community.

Overall, these new developments in the field of imaging prospect exciting times ahead for the study of endosomal escape. We prompt the nanomedicine community to adopt the newest techniques available to achieve a better understanding of NP trafficking as well as to facilitate the rational design of NP able to overcome endosomal barriers.

Appendix 6

*This Appendix reproduces almost literally the article **Andrian T.,** Bakkum T., van Elsland D.M., Bos E., Koster A.J., Albertazzi L., van Kasteren S.I., Pujals S. **Super-resolution correlative light-electron microscopy using a click-chemistry approach for studying intracellular trafficking**. In: Methods in Cell Biology. Elsevier; 2021. As an author in this paper, I contributed to the overall organization, literature research, figure preparation and manuscript writing, together with Bakkum T. The rest of the authors contributed with providing periodic feedback and review for the manuscript.*

Abstract: *Correlative light and electron microscopy (CLEM) entails a group of multimodal imaging techniques that are combined to pinpoint to the location of fluorescently labeled molecules in the context of their ultrastructural cellular environment. Here we describe a detailed workflow for STORM-CLEM, in which STochastic Optical Reconstruction Microscopy (STORM), an optical super-resolution technique, is correlated with transmission electron microscopy (TEM). This protocol has the advantage that both imaging modalities have resolution at the nanoscale, bringing higher synergies on the information obtained. The sample is prepared according to the Tokuyasu method followed by click-chemistry labeling and STORM imaging. Then, after heavy metal staining, electron microscopy imaging is performed followed by correlation of the two images. The case study presented here is on intracellular pathogens, but the protocol is versatile and could potentially be applied to many types of samples.*

Appendix 6

Introduction
CLEM and super-resolution microscopy

Correlative light and electron microscopy (CLEM) is a group of powerful and well-established multimodal imaging techniques in biological research. With these techniques comes a wide scope of methodological advances that stems from the ability to place the molecular selectivity of fluorescence microscopy (FM) towards specific proteins and structures, within the subcellular context provided by the high imaging resolution of electron microscopy (EM) [209]. However, between the excellent resolution of EM and that of FM there is a wide gap, that imposes difficulties at the time of correlation.

An evident development in FM is super-resolution microscopy (SRM), a group of far-field optical techniques that are able to bypass Abbe's diffraction limit [157,158] and achieve a resolution down to tens of nanometers. These techniques can be divided into three groups: structured illumination microscopy (SIM) [159], stimulated emission depletion (STED) [160], and single-molecule localization microscopy (SMLM) [161]. SMLM methods overcome the diffraction barrier by ensuring that only a number of emitting particles are in an "on" (emitting) state at a time, whilst the majority are in an "off" (dark) state. The centroid position of each emitter is identified and statistically fitted to a Gaussian, with the localization precision being proportional to the number of photons emitted. By fitting the centroid positions of these emitters over thousands of frames without spatial overlap, a high-resolution image of single molecules can be produced (**Figure 1**). SMLM techniques have an excellent resolution (5-25 nm), offer multi-color imaging and can achieve quantification with single-particle precision [490]. Direct STochastic Optical Reconstruction Microscopy (dSTORM) [491] is one of the most popular choices of SMLM techniques and this is demonstrated through its significant achievements from cellular biology [492] to material science [176,179].
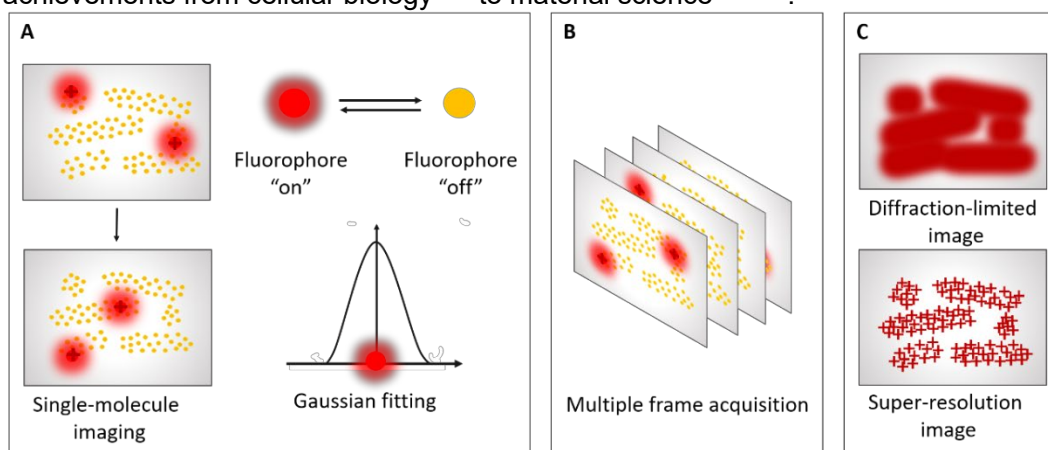
Figure 1. *The principles of STochastic Optical Reconstruction Microscopy (STORM). **(A)** Only a number of fluorophores are in the "on" (emitting) state at a time, whilst the majority are in the "off" (dark) state, allowing the imaging of subsets of fluorophores without spatial overlap and high resolution. The centroid position of each emitter is identified and statistically fitted to a gaussian. **(B)** The positions of many emitters are determined over thousands of frames and **(C)** a super-resolution image is reconstructed from these localizations. The diffraction-limited image is shown in the top right corner as a comparison.*

SMLM-CLEM, advantages over conventional CLEM

The past decade has witnessed the rapid rise of SRM techniques and their correlation with EM (SRM-CLEM), amongst others [493]. Each correlative method aims to add a new dimension of information, with minimal compromise to image quality and resolution upon correlation. STORM is able to achieve an x-y resolution of about 20 nm and a z resolution of about 50 nm [494], providing one of the best spatial resolutions in the SMLM group, compatible with that of TEM. Thus, the improved resolution of STORM leads to a nanoscale localization precision of the specific fluorescent labels in the ultrastructural reference space provided by EM [495]. Importantly, it is a powerful quantitative technique with single-molecule precision (able of molecule counting) [490]. Yet, despite its benefits over conventional CLEM, SRM-CLEM requires sample preparation strategies that agree with both imaging techniques, with minimal compromise to structure and resolution. These strategies focus mainly around the type of fixation and the choice of fluorophore.

Fixation in SRM-CLEM

It is well-established that chemical fixation and consequent dehydration steps used to preserve ultrastructure in EM can quench fluorescence, and since a strong signal-to-noise ratio is required for the performance of SRM, this step requires careful consideration [496,497]. Metal staining (e.g. using osmium tetroxide) used to enhance the structural contrast can further quench fluorescence, thus some SRM-CLEM studies approach this setback by lowering the osmium tetroxide (OsO_4) concentration during post-fixation [216,498]. A more compatible approach is the use of cryo-preparation techniques, such as the Tokuyasu cryo-sectioning method [499]. This was initially developed for immunostaining protocols, but has now been adapted to various CLEM procedures, with or without the need of immunostaining [500–502]. Although samples are fixed with aldehyde and dehydrated using a cryoprotectant, this approach provides good structural preservation, antibody accessibility, and ease of use. Also, lower concentrations of staining metals can be used as only a thin section (<200 nm) needs to be stained. Another more complicated method for cryo-sectioning is using high-pressure freezing (HPF) followed by subsequent freeze substitution (FS). This technique provides the best sample preservation, as it does not require resin embedding, chemical fixation or dehydration processes - though at the expense of longer preparation times [503].

Fluorescence labelling: advantages of click chemistry

The power of SRM-CLEM relies in its ability to image specific proteins or structures within cells with a high resolution. Although there are a plethora of approaches to fluorescently label the structures of interest, it is unlikely that one single probe can be suitable for all CLEM protocols [504]. Standard immunostaining has the advantage of high specificity towards endogenous molecules and avoids problems of probe expression. However, the fixation and permeabilization procedures necessary in the process can cause ultrastructural changes in the sample [505], and many antibodies are not compatible with thin sections due to insufficient sample penetration or loss of epitope recognition - even when a milder chemical fixation is used such as in Tokuyasu sectioning [506,507].

On the contrary, genetically encoded probes do not require permeabilization to gain entry to structures of interest, thus preserving the membrane structure, and improving the overall quality of EM. Single modality genetic probes (fluorescent proteins) can allow normal photoconversion in heavily fixed resin-embedded samples (OsO_4 0.5-1%) and are compatible with SRM-CLEM, as in the case of mEos4a [311]. Dual modality genetic probes such as miniSOG can convert fluorescent signal to electron dense signal using photoconversion, and preserve fluorescence even after the embedding stage [504,508]. However, the expression levels, fusion position and photophysical properties must be carefully optimized to not disturb biological processes.

Fluorescent proteins (FPs) are often touted for their broad applicability and ease of use but they have clear limitations as well [509]. They remain challenging in specific cases, such as pathogenic organisms, due to risks and license restrictions, or *in vivo* systems for various ethical and practical reasons. Moreover, even when successfully performed, the fluorescent protein may interfere with the tagged protein, or with the organism as a whole [509]. Another obvious limitation is the fact that FPs can only be used to label proteins, leaving many interesting biomolecules such as peptides, fatty acids, glycans and nucleic acids in the dark. Some of these non-protein biomolecules can be targeted with antibodies but these are highly specialized and suffer from the restrictions as mentioned above [510].

Chemical fluorescent modification with an organic fluorophore represents another way to label biomolecules of interest [511–514]. This can be done through chemical modification of the building blocks (amino acids, fatty acids, etc.) or direct modification of the macro molecule (proteins, glycans, etc.). Chemical fluorescent tags (~1 kDa) are much smaller than FP tags (~30 kDa), and are generally brighter and suffer from less quenching [515]. However, these can still severely interfere with the biological function, depending on the modification position, chemical properties of the fluorophore and number of fluorophores per biomolecule [509,512]. This effect is most pronounced in highly sensitive biological systems such as the immune system [516–518].

Bioorthogonal chemistry - also known as 'click' chemistry - uses a two-step labeling mechanism to first introduce a small chemical modification in the biomolecule of interest, followed by a secondary ligation (click) step to attach a fluorophore (or a different reporter) of choice [511]. The first modification – commonly referred to as click handle – can be as small as a few atoms in size (e.g. $-C\equiv C-$ vs $-CH_3$), minimizing the effect on the biological function [519]. The second step – clicking the fluorophore – can be performed at any time but if chemical fixation is possible or required (as for CLEM), this reaction should be performed afterwards to avoid interference with the biology altogether. This technique can be used to label any biomolecule, provided the structure is synthetically available and large enough to allow a small modification [511]. Various bioorthogonal reactions have been developed [520,521], that can be chosen based on the requirements of the biological question. The classic copper-catalyzed Huisgen cycloaddition (ccHc) [522] – or copper-click reaction – involves the ligation of a terminal azide to a terminal alkyne group, catalyzed by copper(I) (Figure 3). Either the azide or the alkyne can be incorporated into the biomolecule, depending on synthetic preferences and homology to the natural structure, but the alkyne is preferred due to significantly lower background of the cognate azide-modified fluorophore [523]. This

reaction is fast, high yielding and very selective, making it the ideal strategy for two-step labeling of biomolecules involved in sensitive biological processes. The well-known cytotoxicity of copper(I) [524] is irrelevant when performing the reaction after chemical fixation but can be avoided using a strain-promoted Huisgen cycloaddition (spHc) reaction, using a cyclooctyne-modified fluorophore [495].

Not only are these click handles small enough to avoid interfering with the biological processes, they are bioinert [524] and (bio)chemically stable [525]. This is of great importance when studying immunological processes, that include uptake of foreign material (e.g. bacteria), degradation and processing of the material for antigen presentation. We have previously shown that both the azide and alkyne groups are sufficiently stable to the harsh conditions that occur during degradation of bacteria, to allow the intracellular study of these foreign entities [523,526].

Case study: intracellular pathogens

The immune system employs a wide range of defensive strategies against foreign invaders, such as viruses, bacteria and multicellular parasites [527]. Immune cells sense their presence, process the molecular information and conclude on either a destructive response (clearance) or a non-destructive response (tolerance), to avoid unnecessary damage to the host [528]. Bacterial invaders are first internalized through a process called phagocytosis – employed by specialized phagocytic immune cells such as macrophages and dendritic cells – and subsequently killed and degraded in specialized anti-microbial compartments called phagolysosomes [529]. Intracellular pathogenic bacteria such as *Salmonella enterica* employ a parasitic lifestyle to avoid killing and clearance by the host cell (**Figure 2**) [530].

Classical microscopy techniques provide insufficient information on the intracellular behavior of pathogenic bacteria, due to the lack of either ultrastructural information, functional information, resolution, or a combination of both. Confocal-CLEM provides both functional information (through click labeling) and ultrastructural information on the subcellular behavior of the pathogen but lacks sufficient resolution to observe the precise label distribution. SRM-CLEM solves this problem and provides additional single-molecule sensitivity, that allows for visualization of sub-bacterial structures and rare events with low label density. We have previously shown that a combination of bioorthogonal labeling, STORM and TEM (STORM-CLEM) provides an effective tool to study the intracellular behavior of *Salmonella enterica* serovar Typhimurium (abbreviated here as *Salmonella*) [531]. The choice of SRM technique stands for achieving the best resolution and using a non-damaging laser power. We found STORM left the sample relatively unaffected, resulting in a well-preserved ultrastructure on EM.
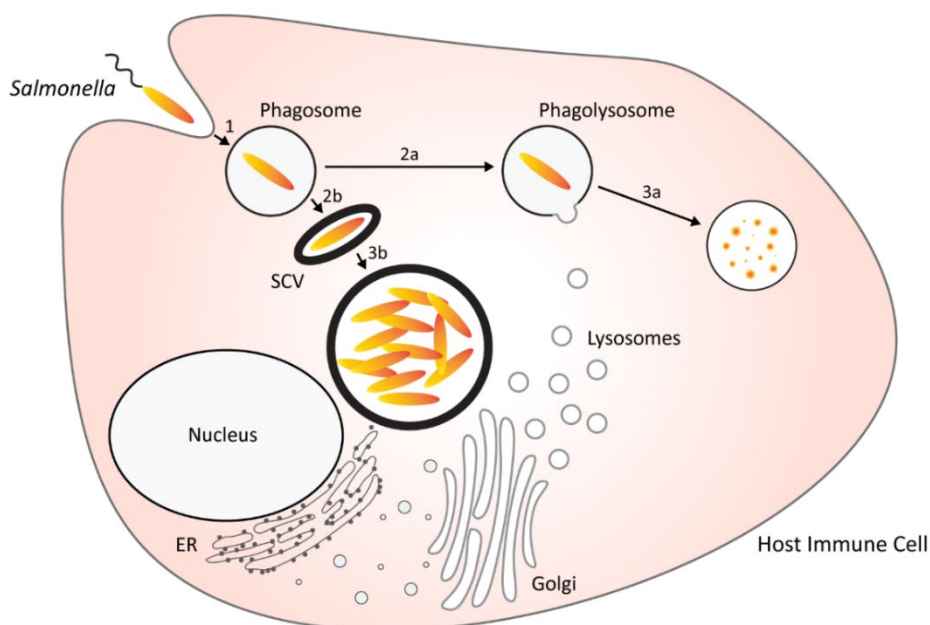
Figure 2. *Simplified schematic representation of the intracellular lifestyle of Salmonella enterica. Following uptake by a phagocytic immune cell (**1**), Salmonella bacteria initially reside within a host compartment called a phagosome. Phagocytic immune cells are specialized in degrading pathogenic bacteria through fusion of the phagosome with lysosomes (**2a**) to form a highly bactericidal phagolysosome, eventually resulting in the degradation of the pathogen (**3a**). However, Salmonella has evolved to evade degradation (**2b**), through the formation of a specialized compartment which is referred to as a Salmonella-containing vacuole (SCV). Through this immune-evading strategy, Salmonella is able to survive and even multiply freely (**3b**), usually resulting in host cell lysis and spreading of the pathogen.*

Methods

The method described here is primarily focused on the on-section click reaction and subsequent image acquisition and correlation of STORM-CLEM. More details about the original procedure for studying *Salmonella* in murine bone marrow-derived dendritic cells (BMDCs) can be found in the original publication (Elsland et al. 2018) [531]. Tips and alternatives to the protocol are indicated between asterisks (*). Steps that require extra attention or care are indicated between exclamation marks (!). A graphical summary of the protocol is illustrated in **Figure 3** and a simplified workflow with time indications is provided in **Figure 4.**

Bioorthogonal labeling of bacteria and cell infection experiment

It is strongly recommended to prepare all bacterial and mammalian cells, growth media and reagents beforehand, as the biological experiment requires a strict time schedule. A sufficient number of cells is crucial to obtain a large enough cell pellet for the subsequent sample preparation according to the Tokuyasu method (about 50-100 µL in volume). Generally, a 10 cm cell culture dish with a confluency of >70% should suffice for a single experimental condition (around 5-20 million cells, depending on the cell type).

0. Dilute an overnight culture of *Salmonella* (1:33) and allow to grow back to the exponential growth phase (OD_{600} between 0.3-0.5).
1. Replace the growth medium (LB) by a methionine-free alternative (SelenoMet) and supplement with a previously optimized concentration of L-homopropargylglycine (Hpg) (4 mM) for bioorthogonal labeling of the bacterial proteome, according to the BONCAT procedure [532,533].

    (*) The optimal label concentration can be determined by in-gel fluorescence and flow cytometry analysis [531]. Hpg can be easily substituted by L-azidohomoalanine (Aha) if preferred [526]. (*)
2. Incubate the bacteria for approx. 1-2 doubling times (30 min for *Salmonella*).

    (*) The effect of label incorporation on bacterial viability can be checked by comparing the growth rates of the bacteria in the presence or absence of the bioorthogonal label [531]. (*)
3. Infect the phagocytic immune cells (BMDCs) by co-incubating with the labeled bacteria (MOI 50) in antibiotic-free cell medium (e.g. IMDM + 10% FCS) for 45 min.
4. Wash away the non-internalized bacteria and further incubate the infected cells in medium, according to the biological research question (e.g. 3 hours for intracellular processing). Addition of gentamycin (f.c. 100 μg/mL for washes, 10 μg/mL for post-infection incubation) is desirable to kill extracellular bacteria and avoid uncontrolled bacterial growth.

Fixation and preparation of ultrathin cryo-sections

We previously discovered that the Tokuyasu cryo-sectioning technique is compatible with on-section click reaction [526], in addition to its well-known compatibility with immunofluorescence [507,534,535]. Here we briefly describe the method that has been used in the bioorthogonal STORM-CLEM publication, including some updates to the original Tokuyasu method. A complete and comprehensive protocol of the Tokuyasu method, including video tutorials, has been previously published by Peters et al. [536].

1. Fix the cells directly on the cell culture dish with a f.c. of 2% paraformaldehyde in 0.1 M phosphate buffer pH 7.2 for 24 hours at room temperature.
2. Rinse with PBS and 15 mM glycine in PBS to block potential aldehyde residues.
3. Harvest the fixed cells in pre-warmed (37°C) 1% gelatin in PBS using cell scrapers and collect in an Eppendorf tube.
4. Pellet cells by centrifugation and resuspend the pellet in pre-warmed 12% gelatin in PBS.
5. Incubate for 10 min at 37°C, then collect by centrifugation and solidify gelatin on ice.
6. Cut sample cubes of 0.5-1 mm^3 with a razor blade and allow sucrose infiltration by rotating in 2.3 M sucrose in PBS overnight at 4°C.
7. Transfer each sample cube to a metal support pin (to be mounted in the ultramicrotome) and plunge freeze by dropping the pin in a small container filled with liquid nitrogen.
8. Apply fiducials (0.1 μm FluoSpheres) to the Formvar/carbon-coated TEM grids grid (titanium, 100 square mesh, 3.05 mm, center-marked) by incubating the grids for 2 min on a droplet of prediluted (e.g. 1:2000) and sonicated (5 min at max power)

FluoSpheres. Wash 2 x 1 min on drops of PBS and 2 x 1 min on drops of milliQ water. Dry the grids by carefully touching the side of the grid on filter paper and store in a dry grid box until step 15.

9. Mount the sample pin on a cryo-ultramicrotome (Leica UC7 Ultramicrotome equipped with Leica EM FC7 Cryochamber and EM Crion ionizer/charger), pre-cooled to -115°C.
10. Trim the sample cube with a trimming knife (Diatome Trim 20°), leaving behind a block face of approx. 400 μm (h) x 300 μm (w) x 50 μm (d) for sectioning.
11. Using a cryo-immuno diamond knife (Diatome Cryo Immuno 35°), cut sequential ultrathin sections of 75 nm thickness.
12. Guide the growing ribbon with a micromanipulator (Diatome Micromanipulator[537]) to form a ribbon of 10-20 sections.
13. (!) Pick up the sample ribbon using a metal loop containing a droplet of pickup solution (1.15 M sucrose, 1% methylcellulose), making sure the droplet does not freeze before contact with the ribbon is made. (!)
14. Allow the pickup droplet to thaw inside a closed environment such as a 200 μL PCR tube. This avoids condensation from the air, which strongly increases folds in the sample.
    (*) Alternatively, a lift-up hinge can be used, as described elsewhere [538]. (*)
15. Place the droplet (sample down) on a fiducial-coated TEM grid.
16. Place the grid on a droplet of pickup solution (sample down), then place the grid (sample up) in a polyether-covered petri dish and store overnight at 4°C.

Click reaction and counterstaining of thawed cryo-sections

Various reaction conditions have been suggested and optimized [539–541] but the conditions described here work robustly in our hands for a wide range of applications, including in-gel fluorescence, flow cytometry, fluorescence microscopy and CLEM. Click reagents should be prepared freshly or stored at -20°C as single-use aliquots. The bioorthogonal reaction mixture (click mix) must be prepared following the indicated order.

1. Place the grid (sample down) on a prewarmed 2% gelatin PBS solution and incubate for 30 min at 37°C.
2. Prepare a clean surface for subsequent washing and staining steps by sticking some Parafilm onto a wet surface and removing the protective film from the top.
3. Prepare droplets of PBS containing 15 mM glycine and use a plastic loop to transfer the grid (sample down) on a droplet, then transfer to a second droplet.
4. Wash 5 x 2 min on droplets of PBS containing 15 mM glycine.
5. Prepare the click mix in an Eppendorf tube by mixing 4 μL 0.1 M copper sulfate, 4 μL 1 M sodium ascorbate, 4 μL 0.1 M THPTA, 4 μL 1 M aminoguanidine, 383 μL 0.1 M HEPES pH 7.4 and 1 μL 2 mM Alexa Fluor 647-azide (to react to the Hpg-labeled bacteria). Note that the reagents must be added in this sequence to obtain a working reaction mixture.
6. Incubate 60 min on a droplet of click mix.
7. Wash 3 x 2 min on droplets of PBS.

8. Wash 3 x 5 min on droplets of PBS containing 1% BSA.
9. Wash 3 x 2 min on droplets of PBS.
10. Incubate 5 min on a droplet of PBS containing 1 µg/mL DAPI.
11. Wash 5 x 2 min on droplets of PBS.

STORM imaging

The resolution of the confocal microscope is limited to about 250 nm by Abbe's law of diffraction of light, rendering this technique unsuitable for precise imaging of phagocyte-*Salmonella* interactions. STORM is able to circumvent the diffraction barrier and reach an x-y resolution of about 20 nm and a z resolution of about 50 nm [165,494], thus has an improved sensitivity of detection of intracellular pathogens and provides a better resolution alignment when used in correlation with TEM. Another important advantage of the STORM-CLEM protocol is that the fluorophore can be introduced after the biological course and sample preparation, hence we are not limited by the dyes available to use. We have chosen to label the bacteria using Alexa Fluor 647 – one of the best performing cyanine-based STORM dyes – through the ccHc ligation method described above. The protocol outlined here is aimed at combining the advantages of STORM and TEM (STORM-CLEM) to study the life cycle of *Salmonella* in BMDCs.

1. GLOX buffer is prepared as described in Materials section.
2. Microscopy slides are pre-cleaned with 100% ethanol and dried using a nitrogen gas flow. The grids containing the sample sections are washed on GLOX droplets (3 x 5 min) supplemented with 30% glycerol and placed on the glass slide with the thin section facing upwards. A small drop of GLOX buffer (20 µL) is placed on top of the grid and then covered with a glass coverslip #1.5H (24 mm x 24 mm, thickness 0.15 mm).
3. Low-magnification images are acquired using the 10x objective and the epifluorescence lamp, to map the grid and identify the location of interest in brightfield, 405 channel (nuclei) and 647 channel (bacteria).
4. The 10x objective is switched to the 100x oil immersion objective and a map is acquired of the area of interest from step 2, using both the transmitted light and fluorescence to specify the reference on the finder grid and the cell position. This will aid in tracing back the same area and cell in TEM.
5. Images are then obtained using the NIKON N-STORM system configured for HILO imaging, using an oil immersive objective (100x). Alexa Fluor 647 is excited using illumination from the 647 laser (160 mW, 1.9 kW cm^{-2}). Fluorescence is collected by means of a Nikon 100x, 1.4 NA oil immersion objective and passed through a quad-band-pass dichroic filter (97335 Nikon). 20,000 frames at 50 Hz are acquired for the 647 channel. Images are recorded onto a 256 × 256 pixel region (pixel size 160 nm) of a CMOS camera.
6. STORM images are analyzed with the STORM module of the NIS element Nikon software [176] as described below.

STORM analysis

Data acquisition and analysis play an important part in the STORM imaging process, and thus detailed protocols should be included in each experiment. As described in Figure 1., the centroid position of each detected fluorophore is statistically fitted to a Gaussian function, with the precision depending directly on the number of detected photons.

The specific localization of single emitters and the Gaussian fitting is performed using the STORM module in NIS Elements based on the minimum and maximum height parameters. The darkest bright point is selected as the molecule and its brightness minus the background intensity as the minimum height (minimum intensity, 150 in this case). The maximum height possible is 65000 for a sCMOS camera system, and the baseline 100. The PSF fit width is set to 300, minimum width 200, and maximum width 400. The first 500 frames are discarded due to incomplete photoswitching.

The number of photons per localization is quantified to ensure the reproducibility of the imaging resolution using a protocol elaborated elsewhere [542]. The resulting resolution is 20 nm, as expected.

A molecule list is rendered in binary format and the coordinates are translated into an image. This STORM image is either shown in cross or gaussian mode by the NIKON software. Using cross you can visualize directly all the localizations, whilst Gaussian is a Gaussian rendering of localizations considering lateral localization accuracy (average of 17.9 ± 4.6 nm) for each localization. In this instance Gaussian mode is used.

TEM staining

Following STORM acquisition, additional post-staining with uranyl acetate/methyl cellulose is required to create the contrast in TEM and protect the delicate structures. This is done according to the standard Tokuyasu method [536], summarized below.
1. The grid containing the sample ribbon is recovered from the microscopy slide, by placing a droplet of PBS next to the coverslip.
2. Using ultra fine tweezers, the coverslip is easily lifted to reveal the grid with the sample on top.
3. The grid is rinsed in ddH_2O and the backside of the grid is dried with compressed air, while holding the sample side of the grid against a droplet of ddH_2O.
4. The sample attached to the grid is washed 5 x 2 min on droplets of ddH_2O.
5. Droplets of uranyl acetate/methyl cellulose are placed on clean Parafilm, attached to a plate lid, placed on ice to keep the solution cold.
6. The grid is touched on a droplet, then transferred to another droplet and incubated for 5 min.
7. Using a metal loop, attached to a pipette tip, the grid is recovered from the droplet and the excess uranyl acetate/methyl cellulose is immediately removed by touching the loop sideways on a piece of filter paper, until only a thin film remains.
8. The grid is airdried for 20 min and can then be stored indefinitely at room temperature.

TEM imaging and stitching

Manual correlation of different image modalities should ideally be performed stepwise, as it greatly reduces the difficulty of finding the area of interest. An overview image of the TEM grid will provide a non-symmetrical reference for identifying the relevant grid window from which the fluorescence images were acquired. In the same way, an overview image of the grid window will provide a reference for identifying the area of interest from which the high-resolution STORM image was acquired. It is recommended to first correlate the STORM image to the low-resolution fluorescence image, then correlate the combined fluorescence images to a low-magnification (~200X) TEM image, and finally correlating the low-magnification TEM image to a high-magnification (~11,000X) TEM image. An intermediate correlation step with a medium-magnification (~2,000X) TEM image is optional but recommended, as it simplifies image registration. Since the field of view (FoV) of FM/STORM is larger than that of TEM at high magnification, it is useful to apply a stitching algorithm to obtain a larger FoV TEM image for correlation.

1. Using a stereoscope, orient the sample grid in the TEM sample holder in the correct way. The final orientation of the grid at the required magnification should correspond to the original orientation during FM/STORM acquisition and can be guided by the asymmetric central marking of the TEM grid. Note that the orientation inside the TEM can change upon increasing magnification, due to the different lenses.
2. At low magnification, identify the grid window that has been imaged by FM/STORM.
3. Acquire a reference TEM image at low magnification (~200X) and use this image to identify the FoV that has been imaged by low res FM. This reference image can be roughly correlated to the FM/STORM image, to assist in identifying the relevant FoV.
4. Acquire a second reference TEM image/stitch at ~2000X magnification and use this image to identify the FoV that has been imaged by STORM. This reference image can be roughly correlated to the FM/STORM image, to assist in identifying the relevant FoV.
5. Acquire the final TEM image/stitch at high magnification (~11,000X), corresponding approximately to the same FoV that has been imaged by STORM.

Correlation

All fluorescence images were pre-processed (brightness/contrast corrected) in ImageJ. The low-resolution fluorescence images were first imported into Photoshop as separate layers, rasterized and grouped.Next, the canvas size was increased (e.g. 10-fold) and the high-resolution STORM image was imported as a new top layer (overlay mode: Lighten). The STORM image was transformed (scaling [bicubic interpolation], rotation, translation) to match the low-resolution image, based on the available reference landmarks. All layers were grouped (group overlay mode: Color) and the canvas size was increased again (e.g. 10-fold). The TEM image (low magnification or

high magnification stitch) was loaded separately into Photoshop. The TEM image was then copied onto the fluorescence images and arranged to the background.

To facilitate correlation of fluorescence to EM, the contrast of the reference markers (nuclear staining and fiducial markers) was temporarily increased, and the grouped fluorescence layers were transformed (scaling [bicubic], rotation, translation) to approximately match the low-magnification (~200X) TEM image. All layers were linked, and the fluorescence layers were hidden, as EM-to-EM correlation is easier. The canvas size was again scaled if required and the next TEM image was imported in the same manner. Correlation of the low-magnification TEM image to the high-magnification TEM image was achieved by reducing the opacity of the top layer (low magnification) and applying transformations to match the high magnification TEM image. The layers were unlinked, and the low magnification TEM image hidden. Finally, the grouped fluorescence were unhidden and fine transformations (scaling, rotation, translation) were applied to match the reference landmarks (nuclei and fiducials). Image registration should be performed using the available landmarks, to avoid biased correlation of the objects of interest. However, the bacteria described here can be considered as intrinsic landmarks, due to their clear visibility in all image modalities. This means that minor transformations are allowed to match the STORM image to the TEM image more accurately but should be minimized. Ideally, STORM-compatible reference markers should be included to avoid user bias in the correlation (FluoSpheres in our case).
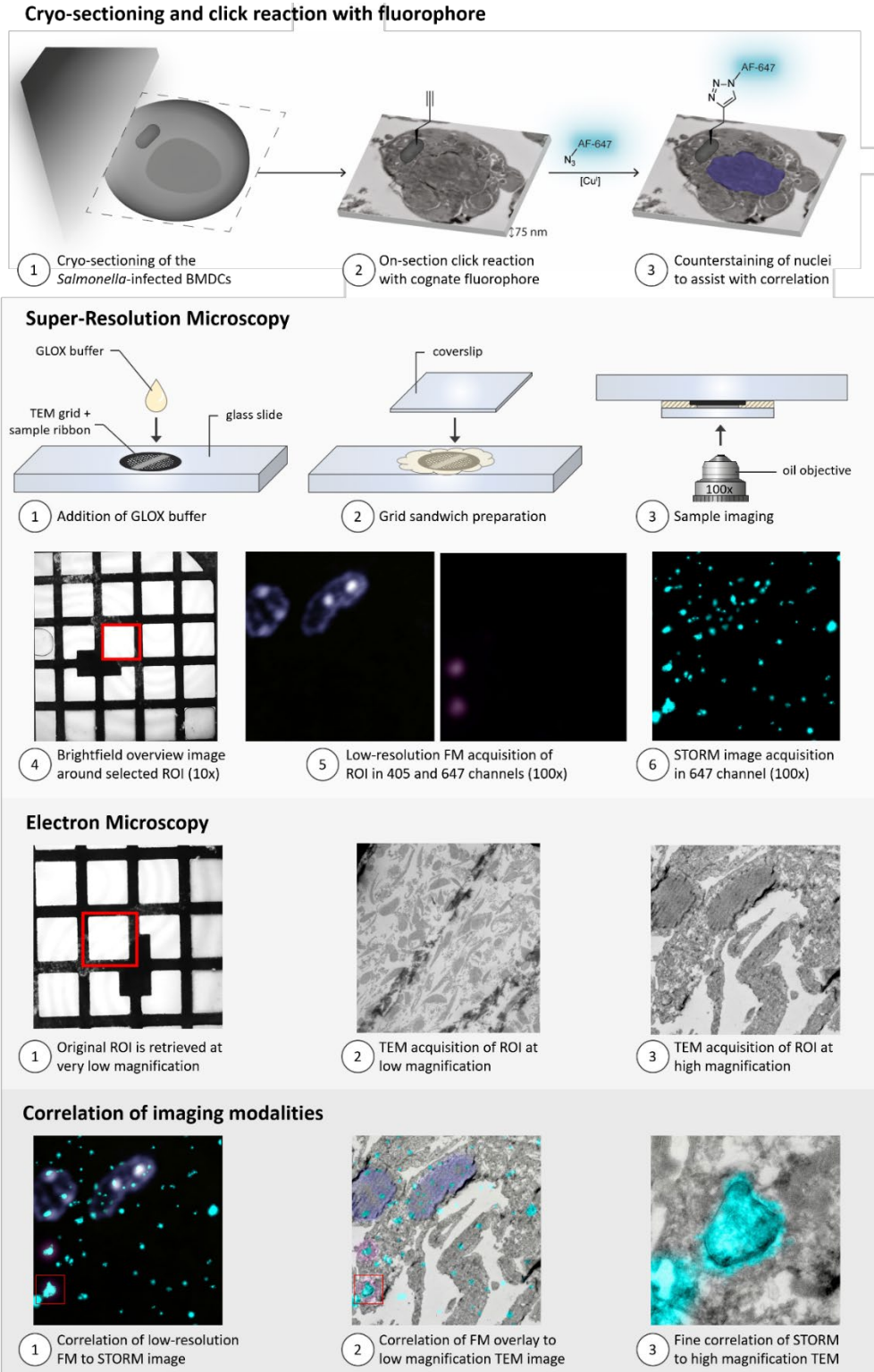
Figure 3. *Graphical summary of the bioorthogonal STORM-CLEM protocol.*
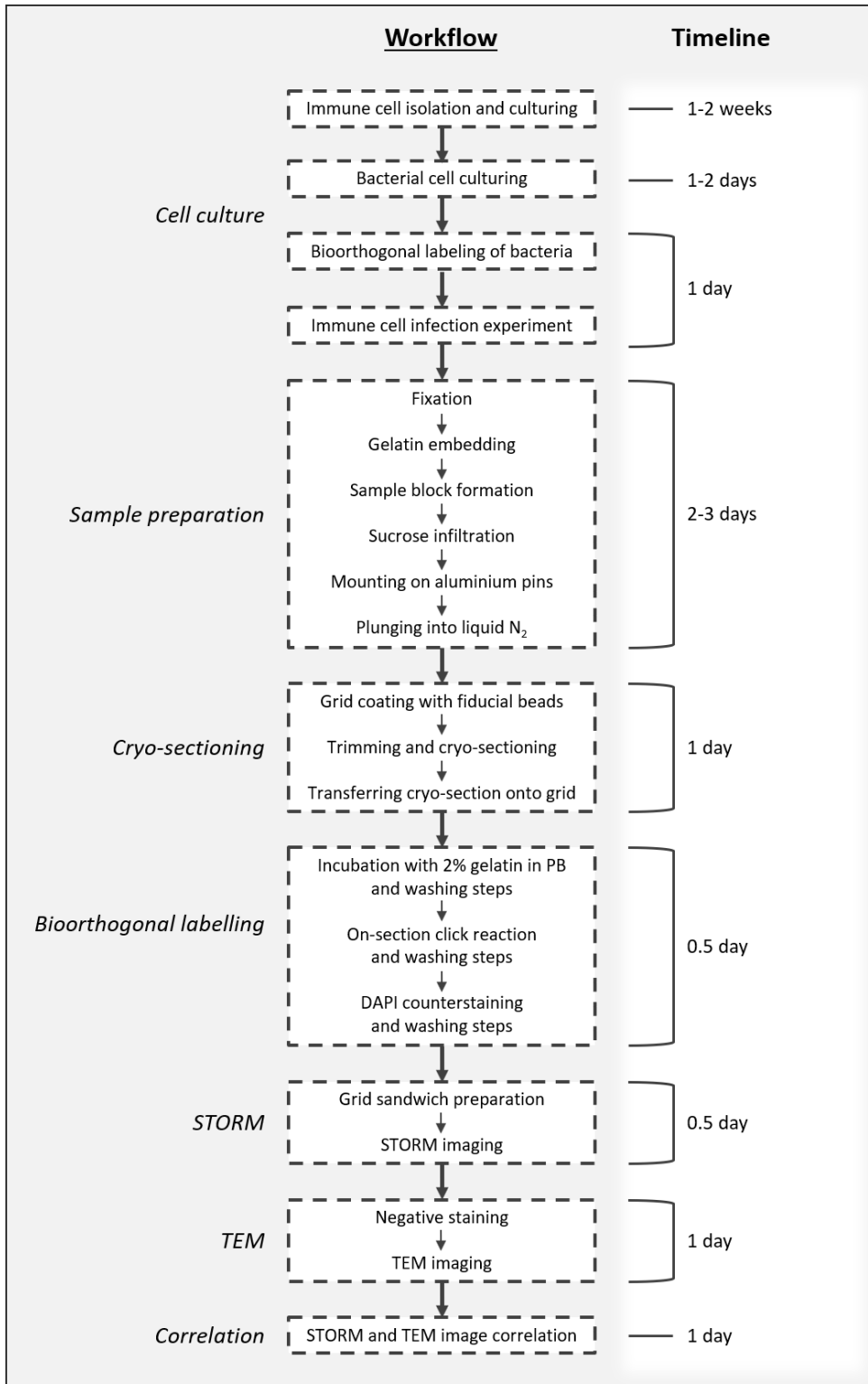
Figure 4. *Workflow and timeline of the bioorthogonal STORM-CLEM protocol.*

Instrumentation and materials

Bioorthogonal labeling and cell infection experiments:

Instrumentation: Bacterial culture facility, cell culture facility, laminar flood cabinet compatible with bacterial infection, OD_{600} spectrophotometer.

Bacteria and mammalian cells: Pathogenic bacteria of interest (*Salmonella enterica* serovar Typhimurium [*Salmonella*] strain SL1344), phagocytic immune cells of interest (murine bone marrow derived dendritic cells [BMDCs] generated from B57BL/6 mice bone marrow).

Materials: Culture flasks, 50 mL Falcon tubes, 10 cm cell culture dishes. *Reagents:* Lysogeny Broth (LB), ampicillin, SelenoMet medium (Molecular Dimensions), 400 mM L-methionine (Met), 400 mM L-homopropargylglycine (Hpg), mammalian cell growth medium (IMDM, FCS, GlutaMAX, penicillin, streptomycin, 2-mercaptoethanol, GM-CSF), sterile PBS.

Fixation and preparation of ultrathin cryo-sections:

Instrumentation: 37°C incubator, sonicator bath, stereoscope, Leica UC7 Ultramicrotome equipped with Leica EM FC7 Cryochamber and Leica EM Crion ionizer/charger, Diatome Micromanipulator, Diatome Trim 20° knife, Diatome Cryo Immuno 35° knife.

Materials: Cell scrapers, glass Pasteur pipettes and bulb, single edge and double edge razor blades, ultra-fine tip and regular tweezers, plastic vials with cap, metal support pins, filter paper, liquid nitrogen and Dewar, small container for plunge freezing, glass trimming knife, diamond sectioning knife, Formvar/carbon-coated TEM grids (titanium, 100 square mesh, 3.05 mm, center-marked), fiducials (carboxylate-modified blue [350/440] FluoSpheres), metal loop on a handle (with lift-up hinge), 200 µL PCR tubes, 35 mm Petri dishes.

Reagents: fixative (8% aqueous paraformaldehyde [EM-grade] and freshly prepared 0.2 M phosphate buffer pH 7.2 mixed in a ratio of 1:3), 15 mM glycine in PBS, 12% gelatin (type A, bloom 300) in PBS with 0.01% sodium azide, 2.3 M sucrose, 2% methyl cellulose (25 centipoise).

Click reaction and counterstaining of thawed cryo-sections:

Instrumentation: N.A.

Materials: Parafilm, plastic loop on a handle, 1.5 mL Eppendorf tubes.

Reagents: 0.1 M copper sulfate, 1 M sodium ascorbate, 0.1 M THPTA, 1 M aminoguanidine, 0.1 M HEPES pH 7.4, 2 mM Alexa Fluor 647-azide in DMSO, BSA, 2 mg/mL DAPI solution.

Super-resolution microscopy:

Instrumentation: Nikon N-STORM microscope (100x oil lens, N.A.=1.49), system configured for HILO imaging, with a quadband pass dichroic filter (97335 Nikon) and a Hamamatsu ORCA-Flash 4.0 camera. NIS-Elements Software.

Materials: Glass slides, Coverslip (24 mm x 24 mm, thickness 0.15 mm).

Reagents: GLOX buffer with 30% glycerol: 100 µL PBS, 20 µL 50% glucose, 20 µL MEA 1M (b-MercaptoEthylamine) and 2 µL GLOX (0.7 mg/mL glucose oxidase, 5 mg/mL catalase in PBS) plus 30% glycerol (60 µL).

Transmission Electron Microscopy:

Instrumentation: Tecnai 12 Biotwin transmission electron microscope (FEI).

Materials: one metal loop attached to a pipette tip for every grid.

R*eagents:* uranyl acetate/methyl cellulose (4% uranyl acetate and 2% methyl cellulose [25 centipoise] mixed in a ratio of 1:9), ddH$_2$O.

Software: TEM stitching algorithm developed in-house [543].

Correlation:

Software: FIJI, Adobe Photoshop CS6 (or higher).

Discussion

Flexibility offered by click-chemistry

As explained in the introduction, click-chemistry allows performing the click reaction on the thawed cryo-sections, thus avoiding reporter interference in the biological process studied. An additional benefit is the freedom to use any clickable fluorophore (or other reporter such as biotin) of choice. Since the number of STORM-compatible fluorophores is limited, this is of major importance. Generally, cyanine-based fluorophores are considered ideal for STORM, due to their high brightness, blinking rate and photon count [515]. When considering clickable fluorophores, an additional consideration should be made in terms of solubility, to minimize non-specific hydrophobic interactions with the sample. This generally steers the selection towards the water-soluble Alexa Fluors, with Alexa Fluor 647 giving the highest blinking rate/photon count [515]. Alternatively, photoactivatable fluorophores for PALM could hypothetically be used as well [544]. Other options for fluorescent labeling include the use of a clickable biotin, followed by a separate incubation step with fluorescently modified streptavidin, which may contain an additional gold particle for detection by EM as well [545,546].

Bioorthogonal metabolic labels have been developed for virtually all biomolecules and have so far shown compatibility with nearly all biological systems, including whole animals [547]. Various mutually-orthogonal bioorthogonal reactions have previously been

reported [548–550], providing an interesting approach to multiplex labeling and potential multi-color STORM-CLEM. The feasibility and limitations of this approach will depend on the number of mutually orthogonal reactions, as well as the number of STORM-compatible fluorophores and emission filters available.

Tokuyasu cryo-sections allow fluorophore or gold-modified antibodies as well, to allow multiplex labeling [507]. Although bioorthogonal labeling can be a good alternative for fluorescent proteins, the Tokuyasu method does allow most fluorescent proteins to retain their fluorescence, making them an attractive option to include [526,531,551]. Moreover, direct chemical modifications such as fluorescent probes are compatible as well, provided they are fixable [552]. However, these must be included in the biological workflow and therefore lack the flexibility of on-section fluorescent labeling. Activity-based probes containing a bioorthogonal group represent a useful alternative for fluorescent probes, maintaining the reporter flexibility after cryo-sectioning [526].

Choice of grids

An important aspect to consider in our STORM-CLEM protocol is the choice of grids. Two reasons limit the choice of grids. First, they need to be mounted between a coverslip and a glass slide for STORM imaging and later on they have to be retrieved from it, thus they need to be robust. Second, when performing STORM imaging GLOX buffer is used, so inert metals should be chosen to avoid corrosion. Similarly, copper grids will be affected by the reducing agent of the copper click reaction. For these reasons, we found Titanium grids were the ideal choice for our protocol.

Moreover, we used 100-mesh grids with a non-symmetrical center, as a guide for the correlation. The 100-mesh is just large enough to image one FoV in confocal/low resolution FM and supports the sample to keep it as flat as possible. The non-symmetrical center helps to orient the grid correctly in the TEM and to find the correct window to image.

How to correlate

The ease of correlation is largely dependent on available reference markers, structural landmarks and/or fiducials, that should be detectable in all imaging modalities (low-resolution FM, super-resolution FM and EM). The most effective markers for the initial coarse correlation are large structures such as nuclei, which can easily be labeled with a fluorescent dye (e.g. DAPI) and are identifiable from low magnification (~300x) TEM. For fine correlation, smaller fiducial markers are required that should be sufficiently spread, as to provide any small area of interest with ideally three fiducials. Various types of fiducials are available, from (multicolor) fluorescent beads [553,554] to fluorescent gold nanoparticles [555] and quantum dots (QDots) [556], each with specific strengths and limitations.

As mentioned before, more accurate correlation could be achieved by introducing SRM-compatible reference markers. The compatibility and accuracy of fiducials depends on their excitation/emission spectra, brightness, photostability and fluorescence lifetime for detection by SRM, and their size and electron density for detection by TEM. QDots have proven to be most broadly compatible with SRM

techniques and applicable for CLEM as well [557–559]. Fluorescent nanodiamonds (fNDs) have shown great promise for computational SRM or STED-based CLEM, due to their extremely high photostability [560–563] but have been used very effectively for multi-color dSTORM (madSTORM) as well [564].

Added value of STORM

In this protocol a bioorthogonal STORM-CLEM approach was used to visualize an intracellular pathogens (*Salmonella)* within the ultrastructural context of a host cell (BMDCs). We previously tested the BONCAT-CLEM method on 75 nm cryo-sections of *Salmonella* but found that due to the limited resolution of the confocal microscope, the method was not sensitive enough to allow proper imaging of the phagocyte-pathogen interaction [565]. STORM was chosen as it is able to circumvent the diffraction barrier and provide one of the best spatial resolutions and sensitivities in the SMLM group [165,494]. SRM is a fast-evolving addition to CLEM, and since its initial development [498], it is proving to be a true game-changer in overcoming the resolution gap between FM and EM. In our experiments, STORM left the sample relatively unaffected, resulting in a well-preserved ultrastructure in EM. Several small structures (10-20 nm) were observed surrounding the bacterium and even outside the bacterium-containing vesicle, that could not have been detected without the SRM addition to the CLEM technique [531]. Although further scrutiny is required to identify the origin of these structures, they may represent bacterial proteins that have been secreted by *Salmonella*, which is a well-known phenomenon [566–570]. The bioorthogonal labeling strategy hypothetically enables the visualization of these secreted proteins, while FP-fusion proteins were shown to be too large to fit through the *Salmonella* secretion system [571].

The SRM-CLEM technique described here in combination with Tokuyasu cryo-sectioning demonstrates improved sensitivity of detection of intracellular pathogens, good preservation of dye photoswitching properties and a better resolution alignment when used in correlation with TEM compared to confocal microscopy. Other SRM-CLEM techniques were achieved in literature *via* different approaches such as lowering the concentrations of OsO_4 during post-fixation and by optimizing the resin embedding step, leading to reduced fluorescence quenching, as reported with PALM [498] and STED with TEM [497] or SEM [216].

STORM uses highly inclined and laminated optical sheet (HILO) as the standard mode of imaging, an approach that is not limited to imaging the surface of samples as in total internal reflection fluorescence (TIRF). This means that using HILO mode we can achieve an imaging depth of up to 10 µm, with a signal-to-noise ratio only slightly lower than in TIRF. Nevertheless, sample thickness is not an issue for Tokuyasu cryo-sections that are only 75 nm thick, thus serve as excellent biological samples in STORM in either modes.

One of the most remarkable traits of fluorescence microscopy is multi-color imaging, as it enables the determination of colocalization and interaction between different proteins or structures of interest. Through the use of spectrally distinct photoswitchable fluorophores, dSTORM enables multi-color imaging with reduced cross-talk [172–174]. Still, although two-color dSTORM has been achieved by imaging different structures using spectrally separated dyes [175,176], the limited availability of spectrally different

photoswitchable fluorophores hinders the use of more colors. Most organic fluorescent dyes display photoswitching properties, but not all of them meet the criteria required for dSTORM imaging. Generally red fluorophores such as Alexa Fluor 647 and Cy5 perform significantly better than the best-performing dyes in other spectral regions. Therefore, even if one chooses four spectrally different dyes, those in the blue (480-540 nm), yellow (545-600 nm) and NIR (740-805 nm) will be considerably dimmer than those in the red (640-700 nm) spectrum, which may negatively affect the image resolution. It is important to note that in order to improve multi-color imaging, the longer wavelength color (i.e. 647 nm) should be imaged first to reduce the photobleaching caused by the shorter wavelength laser (i.e. 561 nm) due to the overlapping spectra of the two dyes [177].

Moreover, STORM requires aqueous imaging buffers, that typically contain a reducing agent (e.g. β-MercaptoEthylamine/ β-mercaptoethanol) and an oxygen scavenger system [572]. In this protocol we use a mixture of catalase, glucose, and glucose oxidase (GLOX) in combination with a reducing agent (β-MercaptoEthylamine, MEA), in which our chosen fluorophore Alexa Fluor 647 performs best. Unfortunately, different dyes blink optimally in different imaging buffers, hence the multi-color acquisition with STORM is challenging [170], but possible in 2-3 colors through the use of specific buffers such as Oxyrase/MEA (OxEA) [161]. Alternatives to these limitations include sequential labeling and imaging using a single fluorophore [171] or spectral demixing dSTORM (SD-dSTORM), that combines the benefits of red-emitting carbocyanine dyes with spectral demixing [172].

It is important to note that the need for longer image acquisition times in combination with issues arising from the use of imaging buffers – such as acidification of buffer over time affecting the cell integrity [494] – can make the study of dynamic processes or live-cell imaging difficult. However, whilst live-cell imaging is a setback for *in vivo* experiments, it presents no problem as an imaging tool for fixed-cell applications as seen in this SRM-CLEM protocol [531,573,574].

Furthermore, optimizing the labeling density is a crucial parameter in any STORM protocol. A lower-than-optimal labeling density can have a negative consequence on the image resolution and can augment image artefacts. In this protocol we imaged our 75 nm cryo-sections of *Salmonella* after incubation with Hpg at increasing concentrations (0.04, 0.4 or 4 mM), and found that at 0.04 mM Hpg the signal was too low for the bacteria to be completely reconstructed with STORM.

As previously mentioned, the Tokuyasu cryo-sectioning method was chosen in this protocol as it provides a better structure preservation, molecular diffusivity, and ease of use than the conventional chemical fixation and resin embedding steps. Although originally intended for immunostaining protocols, the two-step nature of our biorthogonal ligations is convenient for Tokuyasu cryo-sectioning, as the click-fluorophore can be introduced after the biological time course and sample preparation, with good diffusivity through the 75 nm cryo-section. Furthermore, by using this technique the STORM imaging buffer can easily access the clicked fluorophores, ensuring optimal photoswitching properties of the dyes.

General applicability of the method

The presented STORM-CLEM method is applied to the case study of intracellular trafficking of pathogens, but it could potentially be applied to different types of biological samples and could be extended to other types of samples, like synthetic materials, as long they can be fixed and thin-sectioned. As explained, it is a very versatile workflow that could accept many variations: we have described it with clickable dyes, but other types of labelling could also be applied, like immunolabelling, previously labelled structures or fluorescent proteins. When correlating with single-molecule microscopy, the right fluorophore/ fluorescent protein should be chosen. Other types of microscopies, like confocal microscopy, STED or SIM could also be implemented.
All in all, we have described a detailed workflow for correlating STORM with TEM on cryo-sections prepared using the Tokuyasu method. Correlating nanoscopic techniques allows access to more detailed information. In the case studied on intracellular pathogens, we could get insights into their intracellular mechanism of invasion. Lastly, click-chemistry labelling allows for freedom on the fluorophore of choice.

Appendix 6

Bibliography

(1)   Ventola, C. L. Progress in Nanomedicine: Approved and Investigational Nanodrugs. **2017**, *42* (12), 742–755.

(2)   Puolamaa, M. The Appropriateness of Existing Methodologies to Assess the Potential Risks Associated with Engineered and Adventitious Produc. 79.

(3)   Bobo, D.; Robinson, K. J.; Islam, J.; Thurecht, K. J.; Corrie, S. R. Nanoparticle-Based Medicines: A Review of FDA-Approved Materials and Clinical Trials to Date. *Pharm Res* **2016**, *33* (10), 2373–2387. https://doi.org/10.1007/s11095-016-1958-5.

(4)   Sainz, V.; Conniot, J.; Matos, A. I.; Peres, C.; Zupanǒiǒ, E.; Moura, L.; Silva, L. C.; Florindo, H. F.; Gaspar, R. S. Regulatory Aspects on Nanomedicines. *Biochemical and Biophysical Research Communications* **2015**, *468* (3), 504–510. https://doi.org/10.1016/j.bbrc.2015.08.023.

(5)   The Nanomedicine Revolution, Part 1: Emerging Concepts. 7.

(6)   Havel, H.; Finch, G.; Strode, P.; Wolfgang, M.; Zale, S.; Bobe, I.; Youssoufian, H.; Peterson, M.; Liu, M. Nanomedicines: From Bench to Bedside and Beyond. *AAPS J* **2016**, *18* (6), 1373–1378. https://doi.org/10.1208/s12248-016-9961-7.

(7)   Kumar, S.; Dilbaghi, N.; Saharan, R.; Bhanjana, G. Nanotechnology as Emerging Tool for Enhancing Solubility of Poorly Water-Soluble Drugs. *BioNanoSci.* **2012**, *2* (4), 227–250. https://doi.org/10.1007/s12668-012-0060-7.

(8)   Kalepu, S.; Nekkanti, V. Improved Delivery of Poorly Soluble Compounds Using Nanoparticle Technology: A Review. 14.

(9)   Wolfram, J.; Zhu, M.; Yang, Y.; Shen, J.; Gentile, E.; Paolino, D.; Fresta, M.; Nie, G.; Chen, C.; Shen, H.; Ferrari, M.; Zhao, Y. Safety of Nanoparticles in Medicine. **2016**, 25.

(10)   Xiaoming He, H. W.; Jianhua Yu; Xiongbin Lu. Nanoparticle Systems Reduce Systemic Toxicity in Cancer Treatment. *Nanomedicine (Lond.) 11* (2), 103–106. https://doi.org/10.2217/nnm.15.166.

(11)   Theresa M. Allen. LIGAND-TARGETED THERAPEUTICS IN ANTICANCER THERAPY. *Nat. Rev. 2*, 750–763. https://doi.org/10.1038/nrc903.

(12)   Yao, Y.; Zhou, Y.; Liu, L.; Xu, Y.; Chen, Q.; Wang, Y.; Wu, S.; Deng, Y.; Zhang, J.; Shao, A. Nanoparticle-Based Drug Delivery in Cancer Therapy and Its Role in Overcoming Drug Resistance. *Front. Mol. Biosci.* **2020**, *7*, 193. https://doi.org/10.3389/fmolb.2020.00193.

(13)   Mitchell, M. J.; Billingsley, M. M.; Haley, R. M.; Wechsler, M. E.; Peppas, N. A.; Langer, R. Engineering Precision Nanoparticles for Drug Delivery. *Nat Rev Drug Discov* **2021**, *20* (2), 101–124. https://doi.org/10.1038/s41573-020-0090-8.

(14)   Chen, Z. (Georgia). Small-Molecule Delivery by Nanoparticles for Anticancer Therapy. *Trends in Molecular Medicine* **2010**, *16* (12), 594–602. https://doi.org/10.1016/j.molmed.2010.08.001.

(15)   Pudlarz, A.; Szemraj, J. Nanoparticles as Carriers of Proteins, Peptides and Other Therapeutic Molecules. *Open Life Sciences* **2018**, *13* (1), 285–298. https://doi.org/10.1515/biol-2018-0035.

(16)   Mukalel, A. J.; Riley, R. S.; Zhang, R.; Mitchell, M. J. Nanoparticles for Nucleic Acid Delivery: Applications in Cancer Immunotherapy. *Cancer Letters* **2019**, *458*, 102–112. https://doi.org/10.1016/j.canlet.2019.04.040.

(17)   Deng, Y.; Zhang, X.; Shen, H.; He, Q.; Wu, Z.; Liao, W.; Yuan, M. Application of the Nano-Drug Delivery System in Treatment of Cardiovascular Diseases. *Front. Bioeng. Biotechnol.* **2020**, *7*, 489. https://doi.org/10.3389/fbioe.2019.00489.

(18)   Fries, C. N.; Curvino, E. J.; Chen, J.-L.; Permar, S. R.; Fouda, G. G.; Collier, J. H. Advances in Nanomaterial Vaccine Strategies to Address Infectious Diseases Impacting

Global Health. *Nat. Nanotechnol.* **2021**, *16* (4), 1–14. https://doi.org/10.1038/s41565-020-0739-9.

(19)   James, N. D.; Coker, R. J.; Tomlinson, D.; Harris, J. R. W.; Gompels, M.; Pinching, A. J.; Stewart, J. S. W. Liposomal Doxorubicin (Doxil): An Effective New Treatment for Kaposi's Sarcoma in AIDS. *Clinical Oncology* **1994**, *6* (5), 294–296. https://doi.org/10.1016/S0936-6555(05)80269-9.

(20)   Figueiró Longo, J. P.; Muehlmann, L. A. How Has Nanomedical Innovation Contributed to the COVID-19 Vaccine Development? *Nanomedicine* **2021**, *16* (14), 1179–1181. https://doi.org/10.2217/nnm-2021-0035.

(21)   Caster, J. M.; Patel, A. N.; Zhang, T.; Wang, A. Investigational Nanomedicines in 2016: A Review of Nanotherapeutics Currently Undergoing Clinical Trials: Investigational Nanomedicines in 2016. *WIREs Nanomed Nanobiotechnol* **2017**, *9* (1), e1416. https://doi.org/10.1002/wnan.1416.

(22)   Akinc, A.; Maier, M. A.; Manoharan, M.; Fitzgerald, K.; Jayaraman, M.; Barros, S.; Ansell, S.; Du, X.; Hope, M. J.; Madden, T. D.; Mui, B. L.; Semple, S. C.; Tam, Y. K.; Ciufolini, M.; Witzigmann, D.; Kulkarni, J. A.; van der Meel, R.; Cullis, P. R. The Onpattro Story and the Clinical Translation of Nanomedicines Containing Nucleic Acid-Based Drugs. *Nat. Nanotechnol.* **2019**, *14* (12), 1084–1087. https://doi.org/10.1038/s41565-019-0591-y.

(23)   Al-Ahmady, Z. S.; Ali-Boucetta, H. Nanomedicine & Nanotoxicology Future Could Be Reshaped Post-COVID-19 Pandemic. *Front. Nanotechnol.* **2020**, *2*, 610465. https://doi.org/10.3389/fnano.2020.610465.

(24)   Anselmo, A. C.; Mitragotri, S. Nanoparticles in the Clinic: An Update. *Bioeng Transl Med* **2019**, *4* (3). https://doi.org/10.1002/btm2.10143.

(25)   Bozzuto, G.; Molinari, A. Liposomes as Nanomedical Devices. *IJN* **2015**, 975. https://doi.org/10.2147/IJN.S68861.

(26)   Fenton, O. S.; Olafson, K. N.; Pillai, P. S.; Mitchell, M. J.; Langer, R. Advances in Biomaterials for Drug Delivery. *Adv. Mater.* **2018**, *30* (29), 1705328. https://doi.org/10.1002/adma.201705328.

(27)   Gulati, M.; Grover, M.; Singh, S.; Singh, M. Lipophilic Drug Derivatives in Liposomes. *International Journal of Pharmaceutics* **1998**, *165* (2), 129–168. https://doi.org/10.1016/S0378-5173(98)00006-4.

(28)   Markman, M. Pegylated Liposomal Doxorubicin in the Treatment of Cancers of the Breast and Ovary. *Expert Opinion on Pharmacotherapy* **2006**, *7* (11), 1469–1474. https://doi.org/10.1517/14656566.7.11.1469.

(29)   Petersen, G. H.; Alzghari, S. K.; Chee, W.; Sankari, S. S.; La-Beck, N. M. Meta-Analysis of Clinical and Preclinical Studies Comparing the Anticancer Efficacy of Liposomal versus Conventional Non-Liposomal Doxorubicin. *Journal of Controlled Release* **2016**, *232*, 255–264. https://doi.org/10.1016/j.jconrel.2016.04.028.

(30)   Luan, X.; Yuan, H.; Song, Y.; Hu, H.; Wen, B.; He, M.; Zhang, H.; Li, Y.; Li, F.; Shu, P.; Burnett, J. P.; Truchan, N.; Palmisano, M.; Pai, M. P.; Zhou, S.; Gao, W.; Sun, D. Reappraisal of Anticancer Nanomedicine Design Criteria in Three Types of Preclinical Cancer Models for Better Clinical Translation. *Biomaterials* **2021**, *275*, 120910. https://doi.org/10.1016/j.biomaterials.2021.120910.

(31)   Birrer, M. J.; Moore, K. N.; Betella, I.; Bates, R. C. Antibody-Drug Conjugate-Based Therapeutics: State of the Science. *JNCI: Journal of the National Cancer Institute* **2019**, *111* (6), 538–549. https://doi.org/10.1093/jnci/djz035.

(32)   Ricart, A. D. Antibody-Drug Conjugates of Calicheamicin Derivative: Gemtuzumab Ozogamicin and Inotuzumab Ozogamicin. *Clin Cancer Res* **2011**, *17* (20), 6417–6427. https://doi.org/10.1158/1078-0432.CCR-11-0486.

(33)   Yildiz, I.; Shukla, S.; Steinmetz, N. F. Applications of Viral Nanoparticles in Medicine. *Current Opinion in Biotechnology* **2011**, *22* (6), 901–908. https://doi.org/10.1016/j.copbio.2011.04.020.

(34)   Lawler, S. E.; Speranza, M.-C.; Cho, C.-F.; Chiocca, E. A. Oncolytic Viruses in Cancer Treatment: A Review. *JAMA Oncol* **2017**, *3* (6), 841. https://doi.org/10.1001/jamaoncol.2016.2064.

(35)   Conry, R. M.; Westbrook, B.; McKee, S.; Norwood, T. G. Talimogene Laherparepvec: First in Class Oncolytic Virotherapy. *Human Vaccines & Immunotherapeutics* **2018**, *14* (4), 839–846. https://doi.org/10.1080/21645515.2017.1412896.

(36)   Wicki, A.; Witzigmann, D.; Balasubramanian, V.; Huwyler, J. Nanomedicine in Cancer Therapy: Challenges, Opportunities, and Clinical Applications. *Journal of Controlled Release* **2015**, *200*, 138–157. https://doi.org/10.1016/j.jconrel.2014.12.030.

(37)   Vile, R.; Ando, D.; Kirn, D. The Oncolytic Virotherapy Treatment Platform for Cancer: Unique Biological and Biosafety Points to Consider. *Cancer Gene Ther* **2002**, *9* (12), 1062–1067. https://doi.org/10.1038/sj.cgt.7700548.

(38)   Huang, H.; Feng, W.; Chen, Y.; Shi, J. Inorganic Nanoparticles in Clinical Trials and Translations. *Nano Today* **2020**, *35*, 100972. https://doi.org/10.1016/j.nantod.2020.100972.

(39)   Na, H. B.; Song, I. C.; Hyeon, T. Inorganic Nanoparticles for MRI Contrast Agents. *Adv. Mater.* **2009**, *21* (21), 2133–2148. https://doi.org/10.1002/adma.200802366.

(40)   Thiesen, B.; Jordan, A. Clinical Applications of Magnetic Nanoparticles for Hyperthermia. *International Journal of Hyperthermia* **2008**, *24* (6), 467–474. https://doi.org/10.1080/02656730802104757.

(41)   Singh, P.; Pandit, S.; Mokkapati, V. R. S. S.; Garg, A.; Ravikumar, V.; Mijakovic, I. Gold Nanoparticles in Diagnostics and Therapeutics for Human Cancer. *IJMS* **2018**, *19* (7), 1979. https://doi.org/10.3390/ijms19071979.

(42)   Libutti, S. K.; Paciotti, G. F.; Byrnes, A. A.; Alexander, H. R.; Gannon, W. E.; Walker, M.; Seidel, G. D.; Yuldasheva, N.; Tamarkin, L. Phase I and Pharmacokinetic Studies of CYT-6091, a Novel PEGylated Colloidal Gold-RhTNF Nanomedicine. *Clin Cancer Res* **2010**, *16* (24), 6139–6149. https://doi.org/10.1158/1078-0432.CCR-10-0978.

(43)   Boisselier, E.; Astruc, D. Gold Nanoparticles in Nanomedicine: Preparations, Imaging, Diagnostics, Therapies and Toxicity. *Chem. Soc. Rev.* **2009**, *38* (6), 1759. https://doi.org/10.1039/b806051g.

(44)   Rastinehad, A. R.; Anastos, H.; Wajswol, E.; Winoker, J. S.; Sfakianos, J. P.; Doppalapudi, S. K.; Carrick, M. R.; Knauer, C. J.; Taouli, B.; Lewis, S. C.; Tewari, A. K.; Schwartz, J. A.; Canfield, S. E.; George, A. K.; West, J. L.; Halas, N. J. Gold Nanoshell-Localized Photothermal Ablation of Prostate Tumors in a Clinical Pilot Device Study. *Proc Natl Acad Sci USA* **2019**, *116* (37), 18590–18596. https://doi.org/10.1073/pnas.1906929116.

(45)   Valcourt, D. M.; Dang, M. N.; Scully, M. A.; Day, E. S. Nanoparticle-Mediated Co-Delivery of Notch-1 Antibodies and ABT-737 as a Potent Treatment Strategy for Triple-Negative Breast Cancer. *ACS Nano* **2020**, *14* (3), 3378–3388. https://doi.org/10.1021/acsnano.9b09263.

(46)   Gradishar, W. J. Albumin-Bound Paclitaxel: A next-Generation Taxane. *Expert Opinion on Pharmacotherapy* **2006**, *7* (8), 1041–1053. https://doi.org/10.1517/14656566.7.8.1041.

(47)   Park, J.; Fong, P. M.; Lu, J.; Russell, K. S.; Booth, C. J.; Saltzman, W. M.; Fahmy, T. M. PEGylated PLGA Nanoparticles for the Improved Delivery of Doxorubicin. *Nanomedicine: Nanotechnology, Biology and Medicine* **2009**, *5* (4), 410–418. https://doi.org/10.1016/j.nano.2009.02.002.

(48)   Ahn, H. K.; Jung, M.; Sym, S. J.; Shin, D. B.; Kang, S. M.; Kyung, S. Y.; Park, J.-W.; Jeong, S. H.; Cho, E. K. A Phase II Trial of Cremorphor EL-Free Paclitaxel (Genexol-

PM) and Gemcitabine in Patients with Advanced Non-Small Cell Lung Cancer. *Cancer Chemother Pharmacol* **2014**, *74* (2), 277–282. https://doi.org/10.1007/s00280-014-2498-5.

(49)   Lee, K. S.; Chung, H. C.; Im, S. A.; Park, Y. H.; Kim, C. S.; Kim, S.-B.; Rha, S. Y.; Lee, M. Y.; Ro, J. Multicenter Phase II Trial of Genexol-PM, a Cremophor-Free, Polymeric Micelle Formulation of Paclitaxel, in Patients with Metastatic Breast Cancer. *Breast Cancer Res Treat* **2008**, *108* (2), 241–250. https://doi.org/10.1007/s10549-007-9591-y.

(50)   Li, Z.; Tan, S.; Li, S.; Shen, Q.; Wang, K. Cancer Drug Delivery in the Nano Era: An Overview and Perspectives. *Oncology Reports* **2017**, *38* (2), 611–624. https://doi.org/10.3892/or.2017.5718.

(51)   Pérez-Herrero, E.; Fernández-Medarde, A. Advanced Targeted Therapies in Cancer: Drug Nanocarriers, the Future of Chemotherapy. *European Journal of Pharmaceutics and Biopharmaceutics* **2015**, *93*, 52–79. https://doi.org/10.1016/j.ejpb.2015.03.018.

(52)   Li, B.; Li, Q.; Mo, J.; Dai, H. Drug-Loaded Polymeric Nanoparticles for Cancer Stem Cell Targeting. *Front. Pharmacol.* **2017**, *8*. https://doi.org/10.3389/fphar.2017.00051.

(53)   Niza, E.; Ocaña, A.; Castro-Osma, J. A.; Bravo, I.; Alonso-Moreno, C. Polyester Polymeric Nanoparticles as Platforms in the Development of Novel Nanomedicines for Cancer Treatment. *Cancers* **2021**, *13* (14), 3387. https://doi.org/10.3390/cancers13143387.

(54)   Autio, K. A.; Dreicer, R.; Anderson, J.; Garcia, J. A.; Alva, A.; Hart, L. L.; Milowsky, M. I.; Posadas, E. M.; Ryan, C. J.; Graf, R. P.; Dittamore, R.; Schreiber, N. A.; Summa, J. M.; Youssoufian, H.; Morris, M. J.; Scher, H. I. Safety and Efficacy of BIND-014, a Docetaxel Nanoparticle Targeting Prostate-Specific Membrane Antigen for Patients With Metastatic Castration-Resistant Prostate Cancer: A Phase 2 Clinical Trial. *JAMA Oncol* **2018**, *4* (10), 1344. https://doi.org/10.1001/jamaoncol.2018.2168.

(55)   Jain, M. M.; Gupte, S. U.; Patil, S. G.; Pathak, A. B.; Deshmukh, C. D.; Bhatt, N.; Haritha, C.; Govind Babu, K.; Bondarde, S. A.; Digumarti, R.; Bajpai, J.; Kumar, R.; Bakshi, A. V.; Bhattacharya, G. S.; Patil, P.; Subramanian, S.; Vaid, A. K.; Desai, C. J.; Khopade, A.; Chimote, G.; Bapsy, P. P.; Bhowmik, S. Paclitaxel Injection Concentrate for Nanodispersion versus Nab-Paclitaxel in Women with Metastatic Breast Cancer: A Multicenter, Randomized, Comparative Phase II/III Study. *Breast Cancer Res Treat* **2016**, *156* (1), 125–134. https://doi.org/10.1007/s10549-016-3736-9.

(56)   Ita, K. Polyplexes for Gene and Nucleic Acid Delivery: Progress and Bottlenecks. *European Journal of Pharmaceutical Sciences* **2020**, *150*, 105358. https://doi.org/10.1016/j.ejps.2020.105358.

(57)   Laconi, E.; Marongiu, F.; DeGregori, J. Cancer as a Disease of Old Age: Changing Mutational and Microenvironmental Landscapes. *Br J Cancer* **2020**, *122* (7), 943–952. https://doi.org/10.1038/s41416-019-0721-1.

(58)   *Global Status Report on Noncommunicable Diseases 2014: Attaining the Nine Global Noncommunicable Diseases Targets, a Shared Responsibility*; Organisation mondiale de la santé, Ed.; World health organization: Geneva, 2014.

(59)   Chabner, B. A.; Roberts, T. G. Chemotherapy and the War on Cancer. *Nat Rev Cancer* **2005**, *5* (1), 65–72. https://doi.org/10.1038/nrc1529.

(60)   Nurgali, K.; Jagoe, R. T.; Abalo, R. Editorial: Adverse Effects of Cancer Chemotherapy: Anything New to Improve Tolerance and Reduce Sequelae? *Front. Pharmacol.* **2018**, *9*, 245. https://doi.org/10.3389/fphar.2018.00245.

(61)   Northfelt, D. W.; Martin, F. J.; Working, P.; Volberding, P. A.; Russell, J.; Newman, M.; Amantea, M. A.; Kaplan, L. D. Doxorubicin Encapsulated in Liposomes Containing Surface-Bound Polyethylene Glycol: Pharmacokinetics, Tumor Localization, and Safety in Patients with AIDS-Related Kaposi's Sarcoma. *The Journal of Clinical Pharmacology* **1996**, *36* (1), 55–63. https://doi.org/10.1002/j.1552-4604.1996.tb04152.x.

(62)   Kumari, P.; Ghosh, B.; Biswas, S. Nanocarriers for Cancer-Targeted Drug Delivery. *Journal of Drug Targeting* **2016**, *24* (3), 179–191. https://doi.org/10.3109/1061186X.2015.1051049.

(63)   He, H.; Liu, L.; Morin, E. E.; Liu, M.; Schwendeman, A. Survey of Clinical Translation of Cancer Nanomedicines—Lessons Learned from Successes and Failures. *Acc. Chem. Res.* **2019**, *52* (9), 2445–2461. https://doi.org/10.1021/acs.accounts.9b00228.

(64)   Danhier, F.; Feron, O.; Préat, V. To Exploit the Tumor Microenvironment: Passive and Active Tumor Targeting of Nanocarriers for Anti-Cancer Drug Delivery. *Journal of Controlled Release* **2010**, *148* (2), 135–146. https://doi.org/10.1016/j.jconrel.2010.08.027.

(65)   Peer, D. Harnessing RNAi Nanomedicine for Precision Therapy. *Mol and Cell Ther* **2014**, *2* (1), 5. https://doi.org/10.1186/2052-8426-2-5.

(66)   Golombek, S. K.; May, J.-N.; Theek, B.; Appold, L.; Drude, N.; Kiessling, F.; Lammers, T. Tumor Targeting via EPR: Strategies to Enhance Patient Responses. *Advanced Drug Delivery Reviews* **2018**, *130*, 17–38. https://doi.org/10.1016/j.addr.2018.07.007.

(67)   Hashizume, H.; Baluk, P.; Morikawa, S.; McLean, J. W.; Thurston, G.; Roberge, S.; Jain, R. K.; McDonald, D. M. Openings between Defective Endothelial Cells Explain Tumor Vessel Leakiness. *The American Journal of Pathology* **2000**, *156* (4), 1363–1380. https://doi.org/10.1016/S0002-9440(10)65006-7.

(68)   Hansen, A. E.; Petersen, A. L.; Henriksen, J. R.; Boerresen, B.; Rasmussen, P.; Elema, D. R.; Rosenschöld, P. M. af; Kristensen, A. T.; Kjær, A.; Andresen, T. L. Positron Emission Tomography Based Elucidation of the Enhanced Permeability and Retention Effect in Dogs with Cancer Using Copper-64 Liposomes. *ACS Nano* **2015**, *9* (7), 6985–6995. https://doi.org/10.1021/acsnano.5b01324.

(69)   Lee, H.; Shields, A. F.; Siegel, B. A.; Miller, K. D.; Krop, I.; Ma, C. X.; LoRusso, P. M.; Munster, P. N.; Campbell, K.; Gaddy, D. F.; Leonard, S. C.; Geretti, E.; Blocker, S. J.; Kirpotin, D. B.; Moyo, V.; Wickham, T. J.; Hendriks, B. S. ^{64}Cu-MM-302 Positron Emission Tomography Quantifies Variability of Enhanced Permeability and Retention of Nanoparticles in Relation to Treatment Response in Patients with Metastatic Breast Cancer. *Clin Cancer Res* **2017**, *23* (15), 4190–4202. https://doi.org/10.1158/1078-0432.CCR-16-3193.

(70)   Challenging Paradigms in Tumour Drug Delivery. *Nat. Mater.* **2020**, *19* (5), 477–477. https://doi.org/10.1038/s41563-020-0676-x.

(71)   Sindhwani, S.; Syed, A. M.; Ngai, J.; Kingston, B. R.; Maiorino, L.; Rothschild, J.; MacMillan, P.; Zhang, Y.; Rajesh, N. U.; Hoang, T.; Wu, J. L. Y.; Wilhelm, S.; Zilman, A.; Gadde, S.; Sulaiman, A.; Ouyang, B.; Lin, Z.; Wang, L.; Egeblad, M.; Chan, W. C. W. The Entry of Nanoparticles into Solid Tumours. *Nat. Mater.* **2020**, *19* (5), 566–575. https://doi.org/10.1038/s41563-019-0566-2.

(72)   Liu, X.; Lin, P.; Perrett, I.; Lin, J.; Liao, Y.-P.; Chang, C. H.; Jiang, J.; Wu, N.; Donahue, T.; Wainberg, Z.; Nel, A. E.; Meng, H. Tumor-Penetrating Peptide Enhances Transcytosis of Silicasome-Based Chemotherapy for Pancreatic Cancer. *Journal of Clinical Investigation* **2017**, *127* (5), 2007–2018. https://doi.org/10.1172/JCI92284.

(73)   Salahpour Anarjan, F. Active Targeting Drug Delivery Nanocarriers: Ligands. *Nano-Structures & Nano-Objects* **2019**, *19*, 100370. https://doi.org/10.1016/j.nanoso.2019.100370.

(74)   Juliano, R. L. The Delivery of Therapeutic Oligonucleotides. *Nucleic Acids Res* **2016**, *44* (14), 6518–6548. https://doi.org/10.1093/nar/gkw236.

(75)   Srinivasarao, M.; Galliford, C. V.; Low, P. S. Principles in the Design of Ligand-Targeted Cancer Therapeutics and Imaging Agents. *Nat Rev Drug Discov* **2015**, *14* (3), 203–219. https://doi.org/10.1038/nrd4519.

(76)   Wang, Y.; Cheetham, A. G.; Angacian, G.; Su, H.; Xie, L.; Cui, H. Peptide–Drug Conjugates as Effective Prodrug Strategies for Targeted Delivery. *Advanced Drug Delivery Reviews* **2017**, *110–111*, 112–126. https://doi.org/10.1016/j.addr.2016.06.015.

(77)   Jo, H.; Ban, C. Aptamer–Nanoparticle Complexes as Powerful Diagnostic and Therapeutic Tools. *Exp Mol Med* **2016**, *48* (5), e230–e230. https://doi.org/10.1038/emm.2016.44.

(78)   Friedman, A.; Claypool, S.; Liu, R. The Smart Targeting of Nanoparticles. *CPD* **2013**, *19* (35), 6315–6329. https://doi.org/10.2174/13816128113199990375.

(79)   Phua, K. K. L. Towards Targeted Delivery Systems: Ligand Conjugation Strategies for MRNA Nanoparticle Tumor Vaccines. *Journal of Immunology Research* **2015**, *2015*, 1–8. https://doi.org/10.1155/2015/680620.

(80)   Pearce, A. K.; O'Reilly, R. K. Insights into Active Targeting of Nanoparticles in Drug Delivery: Advances in Clinical Studies and Design Considerations for Cancer Nanomedicine. *Bioconjugate Chem.* **2019**, *30* (9), 2300–2311. https://doi.org/10.1021/acs.bioconjchem.9b00456.

(81)   Espelin, C. W.; Leonard, S. C.; Geretti, E.; Wickham, T. J.; Hendriks, B. S. Dual HER2 Targeting with Trastuzumab and Liposomal-Encapsulated Doxorubicin (MM-302) Demonstrates Synergistic Antitumor Activity in Breast and Gastric Cancer. *Cancer Res* **2016**, *76* (6), 1517–1527. https://doi.org/10.1158/0008-5472.CAN-15-1518.

(82)   Munster, P.; Krop, I. E.; LoRusso, P.; Ma, C.; Siegel, B. A.; Shields, A. F.; Molnár, I.; Wickham, T. J.; Reynolds, J.; Campbell, K.; Hendriks, B. S.; Adiwijaya, B. S.; Geretti, E.; Moyo, V.; Miller, K. D. Safety and Pharmacokinetics of MM-302, a HER2-Targeted Antibody–Liposomal Doxorubicin Conjugate, in Patients with Advanced HER2-Positive Breast Cancer: A Phase 1 Dose-Escalation Study. *Br J Cancer* **2018**, *119* (9), 1086–1093. https://doi.org/10.1038/s41416-018-0235-2.

(83)   Sechi, M.; Sanna, V.; Pala, N. Targeted Therapy Using Nanotechnology: Focus on Cancer. *IJN* **2014**, 467. https://doi.org/10.2147/IJN.S36654.

(84)   Miller, K.; Cortes, J.; Hurvitz, S. A.; Krop, I. E.; Tripathy, D.; Verma, S.; Riahi, K.; Reynolds, J. G.; Wickham, T. J.; Molnar, I.; Yardley, D. A. HERMIONE: A Randomized Phase 2 Trial of MM-302 plus Trastuzumab versus Chemotherapy of Physician's Choice plus Trastuzumab in Patients with Previously Treated, Anthracycline-Naïve, HER2-Positive, Locally Advanced/Metastatic Breast Cancer. *BMC Cancer* **2016**, *16* (1), 352. https://doi.org/10.1186/s12885-016-2385-z.

(85)   Heath, T.; Fraley, R.; Papahdjopoulos, D. Antibody Targeting of Liposomes: Cell Specificity Obtained by Conjugation of F(Ab')2 to Vesicle Surface. *Science* **1980**, *210* (4469), 539–541. https://doi.org/10.1126/science.7423203.

(86)   Albanese, A.; Tang, P. S.; Chan, W. C. W. The Effect of Nanoparticle Size, Shape, and Surface Chemistry on Biological Systems. *Annu. Rev. Biomed. Eng.* **2012**, *14* (1), 1–16. https://doi.org/10.1146/annurev-bioeng-071811-150124.

(87)   Blanco, E.; Shen, H.; Ferrari, M. Principles of Nanoparticle Design for Overcoming Biological Barriers to Drug Delivery. *Nat Biotechnol* **2015**, *33* (9), 941–951. https://doi.org/10.1038/nbt.3330.

(88)   Shi, J.; Kantoff, P. W.; Wooster, R.; Farokhzad, O. C. Cancer Nanomedicine: Progress, Challenges and Opportunities. *Nat Rev Cancer* **2017**, *17* (1), 20–37. https://doi.org/10.1038/nrc.2016.108.

(89)   Walkey, C. D.; Olsen, J. B.; Guo, H.; Emili, A.; Chan, W. C. W. Nanoparticle Size and Surface Chemistry Determine Serum Protein Adsorption and Macrophage Uptake. *J. Am. Chem. Soc.* **2012**, *134* (4), 2139–2147. https://doi.org/10.1021/ja2084338.

(90)   Elias, D. R.; Poloukhtine, A.; Popik, V.; Tsourkas, A. Effect of Ligand Density, Receptor Density, and Nanoparticle Size on Cell Targeting. *Nanomedicine: Nanotechnology, Biology and Medicine* **2013**, *9* (2), 194–201. https://doi.org/10.1016/j.nano.2012.05.015.

(91)   Hoshyar, N.; Gray, S.; Han, H.; Bao, G. The Effect of Nanoparticle Size on *in Vivo* Pharmacokinetics and Cellular Interaction. *Nanomedicine* **2016**, *11* (6), 673–692. https://doi.org/10.2217/nnm.16.5.

(92)   Ma, N.; Ma, C.; Li, C.; Wang, T.; Tang, Y.; Wang, H.; Mou, X.; Chen, Z.; He, N. Influence of Nanoparticle Shape, Size, and Surface Functionalization on Cellular Uptake. *j. nanosci. nanotech.* **2013**, *13* (10), 6485–6498. https://doi.org/10.1166/jnn.2013.7525.

(93)   Dreaden, E. C.; Austin, L. A.; Mackey, M. A.; El-Sayed, M. A. Size Matters: Gold Nanoparticles in Targeted Cancer Drug Delivery. **2013**, 36.

(94)   Almeida, J. P. M.; Chen, A. L.; Foster, A.; Drezek, R. *In Vivo* Biodistribution of Nanoparticles. *Nanomedicine* **2011**, *6* (5), 815–835. https://doi.org/10.2217/nnm.11.79.

(95)   Moghimi, S. M.; Hunter, A. C.; Andresen, T. L. Factors Controlling Nanoparticle Pharmacokinetics: An Integrated Analysis and Perspective. *Annu. Rev. Pharmacol. Toxicol.* **2012**, *52* (1), 481–503. https://doi.org/10.1146/annurev-pharmtox-010611-134623.

(96)   Kulkarni, S. A.; Feng, S.-S. Effects of Particle Size and Surface Modification on Cellular Uptake and Biodistribution of Polymeric Nanoparticles for Drug Delivery. *Pharm Res* **2013**, *30* (10), 2512–2522. https://doi.org/10.1007/s11095-012-0958-3.

(97)   Jain, R. K.; Stylianopoulos, T. Delivering Nanomedicine to Solid Tumors. *Nat Rev Clin Oncol* **2010**, *7* (11), 653–664. https://doi.org/10.1038/nrclinonc.2010.139.

(98)   Liu, Y.; Hardie, J.; Zhang, X.; Rotello, V. M. Effects of Engineered Nanoparticles on the Innate Immune System. *Seminars in Immunology* **2017**, *34*, 25–32. https://doi.org/10.1016/j.smim.2017.09.011.

(99)   Soo Choi, H.; Liu, W.; Misra, P.; Tanaka, E.; Zimmer, J. P.; Itty Ipe, B.; Bawendi, M. G.; Frangioni, J. V. Renal Clearance of Quantum Dots. *Nat Biotechnol* **2007**, *25* (10), 1165–1170. https://doi.org/10.1038/nbt1340.

(100)   Moghimi, S. M. Mechanisms of Splenic Clearance of Blood Cells and Particles: Towards Development of New Splenotropic Agents. *Advanced Drug Delivery Reviews* **1995**, *17* (1), 103–115. https://doi.org/10.1016/0169-409X(95)00043-7.

(101)   Gaumet, M.; Vargas, A.; Gurny, R.; Delie, F. Nanoparticles for Drug Delivery: The Need for Precision in Reporting Particle Size Parameters. *European Journal of Pharmaceutics and Biopharmaceutics* **2008**, *69* (1), 1–9. https://doi.org/10.1016/j.ejpb.2007.08.001.

(102)   Bertrand, N.; Grenier, P.; Mahmoudi, M.; Lima, E. M.; Appel, E. A.; Dormont, F.; Lim, J.-M.; Karnik, R.; Langer, R.; Farokhzad, O. C. Mechanistic Understanding of in Vivo Protein Corona Formation on Polymeric Nanoparticles and Impact on Pharmacokinetics. *Nat Commun* **2017**, *8* (1), 777. https://doi.org/10.1038/s41467-017-00600-w.

(103)   Fang, C.; Shi, B.; Pei, Y.-Y.; Hong, M.-H.; Wu, J.; Chen, H.-Z. In Vivo Tumor Targeting of Tumor Necrosis Factor-α-Loaded Stealth Nanoparticles: Effect of MePEG Molecular Weight and Particle Size. *European Journal of Pharmaceutical Sciences* **2006**, *27* (1), 27–36. https://doi.org/10.1016/j.ejps.2005.08.002.

(104)   Pettitt, M. E.; Lead, J. R. Minimum Physicochemical Characterisation Requirements for Nanomaterial Regulation. *Environment International* **2013**, *52*, 41–50. https://doi.org/10.1016/j.envint.2012.11.009.

(105)   Sperling, R. A.; Liedl, T.; Duhr, S.; Kudera, S.; Zanella, M.; Lin, C.-A. J.; Chang, W. H.; Braun, D.; Parak, W. J. Size Determination of (Bio)Conjugated Water-Soluble Colloidal Nanoparticles: A Comparison of Different Techniques. *J. Phys. Chem. C* **2007**, *111* (31), 11552–11559. https://doi.org/10.1021/jp070999d.

(106)   Mares, A. G.; Pacassoni, G.; Marti, J. S.; Pujals, S.; Albertazzi, L. Formulation of Tunable Size PLGA-PEG Nanoparticles for Drug Delivery Using Microfluidic Technology. *PLoS ONE* **2021**, *16* (6), e0251821. https://doi.org/10.1371/journal.pone.0251821.

(107)   Gao, Y.; Nai, J.; Yang, Z.; Zhang, J.; Ma, S.; Zhao, Y.; Li, H.; Li, J.; Yang, Y.; Yang, M.; Wang, Y.; Gong, W.; Yu, F.; Gao, C.; Li, Z.; Mei, X. A Novel Preparative Method for Nanoparticle Albumin-Bound Paclitaxel with High Drug Loading and Its Evaluation Both in Vitro and in Vivo. *PLoS ONE* **2021**, *16* (4), e0250670. https://doi.org/10.1371/journal.pone.0250670.

(108)   Tinkle, S.; McNeil, S. E.; Mühlebach, S.; Bawa, R.; Borchard, G.; Barenholz, Y. C.; Tamarkin, L.; Desai, N. Nanomedicines: Addressing the Scientific and Regulatory Gap: Nanomedicines. *Ann. N.Y. Acad. Sci.* **2014**, *1313* (1), 35–56. https://doi.org/10.1111/nyas.12403.

(109)   Zhao, Y.; Wang, Y.; Ran, F.; Cui, Y.; Liu, C.; Zhao, Q.; Gao, Y.; Wang, D.; Wang, S. A Comparison between Sphere and Rod Nanoparticles Regarding Their in Vivo Biological Behavior and Pharmacokinetics. *Sci Rep* **2017**, *7* (1), 4131. https://doi.org/10.1038/s41598-017-03834-2.

(110)   Li, D.; Tang, Z.; Gao, Y.; Sun, H.; Zhou, S. A Bio-Inspired Rod-Shaped Nanoplatform for Strongly Infecting Tumor Cells and Enhancing the Delivery Efficiency of Anticancer Drugs. *Adv. Funct. Mater.* **2016**, *26* (1), 66–79. https://doi.org/10.1002/adfm.201503664.

(111)   Geng, Y.; Dalhaimer, P.; Cai, S.; Tsai, R.; Tewari, M.; Minko, T.; Discher, D. E. Shape Effects of Filaments versus Spherical Particles in Flow and Drug Delivery. *Nature Nanotech* **2007**, *2* (4), 249–255. https://doi.org/10.1038/nnano.2007.70.

(112)   Chithrani, B. D.; Ghazani, A. A.; Chan, W. C. W. Determining the Size and Shape Dependence of Gold Nanoparticle Uptake into Mammalian Cells. *Nano Lett.* **2006**, *6* (4), 662–668. https://doi.org/10.1021/nl052396o.

(113)   Rasmussen, M. K.; Pedersen, J. N.; Marie, R. Size and Surface Charge Characterization of Nanoparticles with a Salt Gradient. *Nat Commun* **2020**, *11* (1), 2337. https://doi.org/10.1038/s41467-020-15889-3.

(114)   Alexis, F.; Pridgen, E.; Molnar, L. K.; Farokhzad, O. C. Factors Affecting the Clearance and Biodistribution of Polymeric Nanoparticles. *Mol. Pharmaceutics* **2008**, *5* (4), 505–515. https://doi.org/10.1021/mp800051m.

(115)   Yamamoto, Y.; Nagasaki, Y.; Kato, Y.; Sugiyama, Y.; Kataoka, K. Long-Circulating Poly(Ethylene Glycol)–Poly(d,l-Lactide) Block Copolymer Micelles with Modulated Surface Charge. *Journal of Controlled Release* **2001**, *77* (1–2), 27–38. https://doi.org/10.1016/S0168-3659(01)00451-5.

(116)   He, C.; Hu, Y.; Yin, L.; Tang, C.; Yin, C. Effects of Particle Size and Surface Charge on Cellular Uptake and Biodistribution of Polymeric Nanoparticles. *Biomaterials* **2010**, *31* (13), 3657–3666. https://doi.org/10.1016/j.biomaterials.2010.01.065.

(117)   Yue, Z.-G.; Wei, W.; Lv, P.-P.; Yue, H.; Wang, L.-Y.; Su, Z.-G.; Ma, G.-H. Surface Charge Affects Cellular Uptake and Intracellular Trafficking of Chitosan-Based Nanoparticles. *Biomacromolecules* **2011**, *12* (7), 2440–2446. https://doi.org/10.1021/bm101482r.

(118)   Fröhlich, E. The Role of Surface Charge in Cellular Uptake and Cytotoxicity of Medical Nanoparticles. *IJN* **2012**, 5577. https://doi.org/10.2147/IJN.S36111.

(119)   Thurston, G.; McLean, J. W.; Rizen, M.; Baluk, P.; Haskell, A.; Murphy, T. J.; Hanahan, D.; McDonald, D. M. Cationic Liposomes Target Angiogenic Endothelial Cells in Tumors and Chronic Inflammation in Mice. *J. Clin. Invest.* **1998**, *101* (7), 1401–1413. https://doi.org/10.1172/JCI965.

(120)   Krasnici, S.; Werner, A.; Eichhorn, M. E.; Schmitt-Sody, M.; Pahernik, S. A.; Sauer, B.; Schulze, B.; Teifel, M.; Michaelis, U.; Naujoks, K.; Dellian, M. Effect of the Surface Charge of Liposomes on Their Uptake by Angiogenic Tumor Vessels. *Int. J. Cancer* **2003**, *105* (4), 561–567. https://doi.org/10.1002/ijc.11108.

(121)   Nel, A. E.; Mädler, L.; Velegol, D.; Xia, T.; Hoek, E. M. V.; Somasundaran, P.; Klaessig, F.; Castranova, V.; Thompson, M. Understanding Biophysicochemical

Interactions at the Nano–Bio Interface. *Nature Mater* **2009**, *8* (7), 543–557. https://doi.org/10.1038/nmat2442.

(122)   Bus, T.; Traeger, A.; Schubert, U. S. The Great Escape: How Cationic Polyplexes Overcome the Endosomal Barrier. *J. Mater. Chem. B* **2018**, *6* (43), 6904–6918. https://doi.org/10.1039/C8TB00967H.

(123)   Yuan, Y.-Y.; Mao, C.-Q.; Du, X.-J.; Du, J.-Z.; Wang, F.; Wang, J. Surface Charge Switchable Nanoparticles Based on Zwitterionic Polymer for Enhanced Drug Delivery to Tumor. *Adv. Mater.* **2012**, *24* (40), 5476–5480. https://doi.org/10.1002/adma.201202296.

(124)   Samimi, S.; Maghsoudnia, N.; Eftekhari, R. B.; Dorkoosh, F. Lipid-Based Nanoparticles for Drug Delivery Systems. In *Characterization and Biology of Nanomaterials for Drug Delivery*; Elsevier, 2019; pp 47–76. https://doi.org/10.1016/B978-0-12-814031-4.00003-9.

(125)   Herzberg, M.; Dobberschütz, S.; Okhrimenko, D.; Bovet, N. E.; Andersson, M. P.; Stipp, S. L. S.; Hassenkam, T. Comparison of Atomic Force Microscopy and Zeta Potential Derived Surface Charge Density. *EPL* **2020**, *130* (3), 36001. https://doi.org/10.1209/0295-5075/130/36001.

(126)   Alkilany, A. M.; Zhu, L.; Weller, H.; Mews, A.; Parak, W. J.; Barz, M.; Feliu, N. Ligand Density on Nanoparticles: A Parameter with Critical Impact on Nanomedicine. *Advanced Drug Delivery Reviews* **2019**, *143*, 22–36. https://doi.org/10.1016/j.addr.2019.05.010.

(127)   Kawano, K.; Maitani, Y. Effects of Polyethylene Glycol Spacer Length and Ligand Density on Folate Receptor Targeting of Liposomal Doxorubicin In Vitro. *Journal of Drug Delivery* **2011**, *2011*, 1–6. https://doi.org/10.1155/2011/160967.

(128)   Herda, L. M.; Hristov, D. R.; Lo Giudice, M. C.; Polo, E.; Dawson, K. A. Mapping of Molecular Structure of the Nanoscale Surface in Bionanoparticles. *J. Am. Chem. Soc.* **2017**, *139* (1), 111–114. https://doi.org/10.1021/jacs.6b12297.

(129)   Rabanel, J.-M.; Adibnia, V.; Tehrani, S. F.; Sanche, S.; Hildgen, P.; Banquy, X.; Ramassamy, C. Nanoparticle Heterogeneity: An Emerging Structural Parameter Influencing Particle Fate in Biological Media? *Nanoscale* **2019**, *11* (2), 383–406. https://doi.org/10.1039/C8NR04916E.

(130)   Mullen, D. G.; Banaszak Holl, M. M. Heterogeneous Ligand–Nanoparticle Distributions: A Major Obstacle to Scientific Understanding and Commercial Translation. *Acc. Chem. Res.* **2011**, *44* (11), 1135–1145. https://doi.org/10.1021/ar1001389.

(131)   Mullen, D. G.; Fang, M.; Desai, A.; Baker, J. R.; Orr, B. G.; Banaszak Holl, M. M. A Quantitative Assessment of Nanoparticle−Ligand Distributions: Implications for Targeted Drug and Imaging Delivery in Dendrimer Conjugates. *ACS Nano* **2010**, *4* (2), 657–670. https://doi.org/10.1021/nn900999c.

(132)   Belfiore, L.; Spenkelink, L. M.; Ranson, M.; van Oijen, A. M.; Vine, K. L. Quantification of Ligand Density and Stoichiometry on the Surface of Liposomes Using Single-Molecule Fluorescence Imaging. *Journal of Controlled Release* **2018**, *278*, 80–86. https://doi.org/10.1016/j.jconrel.2018.03.022.

(133)   Woythe, L.; Tito, N. B.; Albertazzi, L. A Quantitative View on Multivalent Nanomedicine Targeting. *Advanced Drug Delivery Reviews* **2020**, S0169409X20302234. https://doi.org/10.1016/j.addr.2020.11.010.

(134)   Faria, M. Minimum Information Reporting in Bio–Nano Experimental Literature. *Nature Nanotechnology* **2018**, *13*, 9.

(135)   Reuter, K. G.; Perry, J. L.; Kim, D.; Luft, J. C.; Liu, R.; DeSimone, J. M. Targeted PRINT Hydrogels: The Role of Nanoparticle Size and Ligand Density on Cell Association, Biodistribution, and Tumor Accumulation. *Nano Lett.* **2015**, *15* (10), 6371–6378. https://doi.org/10.1021/acs.nanolett.5b01362.

(136)   Yue, J.; Feliciano, T. J.; Li, W.; Lee, A.; Odom, T. W. Gold Nanoparticle Size and Shape Effects on Cellular Uptake and Intracellular Distribution of SiRNA Nanoconstructs. *Bioconjugate Chem.* **2017**, *28* (6), 1791–1800. https://doi.org/10.1021/acs.bioconjchem.7b00252.

(137)   Park, J. H.; Oh, N. Endocytosis and Exocytosis of Nanoparticles in Mammalian Cells. *IJN* **2014**, 51. https://doi.org/10.2147/IJN.S26592.

(138)   Durymanov, M.; Reineke, J. Non-Viral Delivery of Nucleic Acids: Insight Into Mechanisms of Overcoming Intracellular Barriers. *Front. Pharmacol.* **2018**, *9*, 971. https://doi.org/10.3389/fphar.2018.00971.

(139)   Kanasty, R.; Dorkin, J. R.; Vegas, A.; Anderson, D. Delivery Materials for SiRNA Therapeutics. *Nature Mater* **2013**, *12* (11), 967–977. https://doi.org/10.1038/nmat3765.

(140)   Yang, Y.; Wang, Z.; Peng, Y.; Ding, J.; Zhou, W. A Smart PH-Sensitive Delivery System for Enhanced Anticancer Efficacy via Paclitaxel Endosomal Escape. *Front. Pharmacol.* **2019**, *10*, 10. https://doi.org/10.3389/fphar.2019.00010.

(141)   Lee, Y.-W.; Luther, D. C.; Kretzmann, J. A.; Burden, A.; Jeon, T.; Zhai, S.; Rotello, V. M. Protein Delivery into the Cell Cytosol Using Non-Viral Nanocarriers. *Theranostics* **2019**, *9* (11), 3280–3292. https://doi.org/10.7150/thno.34412.

(142)   Battistella, C.; Klok, H.-A. Controlling and Monitoring Intracellular Delivery of Anticancer Polymer Nanomedicines. *Macromol. Biosci.* **2017**, *17* (10), 1700022. https://doi.org/10.1002/mabi.201700022.

(143)   Rosenblum, D.; Joshi, N.; Tao, W.; Karp, J. M.; Peer, D. Progress and Challenges towards Targeted Delivery of Cancer Therapeutics. *Nat Commun* **2018**, *9* (1), 1410. https://doi.org/10.1038/s41467-018-03705-y.

(144)   Wilhelm, S.; Tavares, A. J.; Dai, Q.; Ohta, S.; Audet, J.; Dvorak, H. F.; Chan, W. C. W. Analysis of Nanoparticle Delivery to Tumours. *Nat Rev Mater* **2016**, *1* (5), 16014. https://doi.org/10.1038/natrevmats.2016.14.

(145)   Selby, L. I.; Cortez-Jugo, C. M.; Such, G. K.; Johnston, A. P. R. Nanoescapology: Progress toward Understanding the Endosomal Escape of Polymeric Nanoparticles: Endosomal Escape of Polymeric Nanoparticles. *WIREs Nanomed Nanobiotechnol* **2017**, *9* (5), e1452. https://doi.org/10.1002/wnan.1452.

(146)   Andrian, T.; Riera, R.; Pujals, S.; Albertazzi, L. Nanoscopy for Endosomal Escape Quantification. *Nanoscale Adv.* **2021**, *3* (1), 10–23. https://doi.org/10.1039/D0NA00454E.

(147)   Smith, S. A.; Selby, L. I.; Johnston, A. P. R.; Such, G. K. The Endosomal Escape of Nanoparticles: Towards More Efficient Cellular Delivery. *Bioconjugate Chemistry* **2018**, 30. https://doi.org/10.1021/ acs.bioconjchem.8b00732.

(148)   Stewart, M. P.; Lorenz, A.; Dahlman, J.; Sahay, G. Challenges in Carrier-Mediated Intracellular Delivery: Moving beyond Endosomal Barriers: Challenges in Carrier-Mediated Intracellular Delivery. *WIREs Nanomed Nanobiotechnol* **2016**, *8* (3), 465–478. https://doi.org/10.1002/wnan.1377.

(149)   Ma, D. Enhancing Endosomal Escape for Nanoparticle Mediated SiRNA Delivery. *Nanoscale* **2014**, *6* (12), 6415. https://doi.org/10.1039/c4nr00018h.

(150)   Hou, K. K.; Pan, H.; Schlesinger, P. H.; Wickline, S. A. A Role for Peptides in Overcoming Endosomal Entrapment in SiRNA Delivery — A Focus on Melittin. *Biotechnology Advances* **2015**, *33* (6), 931–940. https://doi.org/10.1016/j.biotechadv.2015.05.005.

(151)   Vermeulen, L. M. P.; Brans, T.; De Smedt, S. C.; Remaut, K.; Braeckmans, K. Methodologies to Investigate Intracellular Barriers for Nucleic Acid Delivery in Non-Viral Gene Therapy. *Nano Today* **2018**, *21*, 74–90. https://doi.org/10.1016/j.nantod.2018.06.007.

(152)   Martens, T. F.; Remaut, K.; Demeester, J.; De Smedt, S. C.; Braeckmans, K. Intracellular Delivery of Nanomaterials: How to Catch Endosomal Escape in the Act. *Nano Today* **2014**, *9* (3), 344–364. https://doi.org/10.1016/j.nantod.2014.04.011.

(153)   Duncan, R.; Richardson, S. C. W. Endocytosis and Intracellular Trafficking as Gateways for Nanomedicine Delivery: Opportunities and Challenges. *Mol. Pharmaceutics* **2012**, *9* (9), 2380–2402. https://doi.org/10.1021/mp300293n.

(154)   Foroozandeh, P. Insight into Cellular Uptake and Intracellular Trafficking of Nanoparticles. **2018**, 12.

(155)   Méndez-Ardoy, A.; Lostalé-Seijo, I.; Montenegro, J. Where in the Cell Is Our Cargo? Methods Currently Used To Study Intracellular Cytosolic Localisation. *ChemBioChem* **2019**, *20* (4), 488–498. https://doi.org/10.1002/cbic.201800390.

(156)   Thorley, J. A.; Pike, J.; Rappoport, J. Z. Super-Resolution Microscopy. In *Fluorescence Microscopy*; Elsevier, 2014; pp 199–212. https://doi.org/10.1016/B978-0-12-409513-7.00014-2.

(157)   Huang, B.; Bates, M.; Zhuang, X. Super-Resolution Fluorescence Microscopy. *Annu. Rev. Biochem.* **2009**, *78* (1), 993–1016. https://doi.org/10.1146/annurev.biochem.77.061906.092014.

(158)   Schermelleh, L.; Heintzmann, R.; Leonhardt, H. A Guide to Super-Resolution Fluorescence Microscopy. *The Journal of Cell Biology* **2010**, *190* (2), 165–175. https://doi.org/10.1083/jcb.201002018.

(159)   Gustafsson, M. G. L. Surpassing the Lateral Resolution Limit by a Factor of Two Using Structured Illumination Microscopy. SHORT COMMUNICATION. *J Microsc* **2000**, *198* (2), 82–87. https://doi.org/10.1046/j.1365-2818.2000.00710.x.

(160)   Hell, S. W.; Wichmann, J. Breaking the Diffraction Resolution Limit by Stimulated Emission: Stimulated-Emission-Depletion Fluorescence Microscopy. *Opt. Lett.* **1994**, *19* (11), 780. https://doi.org/10.1364/OL.19.000780.

(161)   Nahidiazar, L.; Agronskaia, A. V.; Broertjes, J.; van den Broek, B.; Jalink, K. Optimizing Imaging Conditions for Demanding Multi-Color Super Resolution Localization Microscopy. *PLoS ONE* **2016**, *11* (7), e0158884. https://doi.org/10.1371/journal.pone.0158884.

(162)   Coltharp, C.; Yang, X.; Xiao, J. Quantitative Analysis of Single-Molecule Superresolution Images. *Curr Opin Struct Biol* **2014**, *0*, 112–121. https://doi.org/10.1016/j.sbi.2014.08.008.

(163)   Jungmann, R.; Avendaño, M. S.; Dai, M.; Woehrstein, J. B.; Agasti, S. S.; Feiger, Z.; Rodal, A.; Yin, P. Quantitative Super-Resolution Imaging with QPAINT. *Nat Methods* **2016**, *13* (5), 439–442. https://doi.org/10.1038/nmeth.3804.

(164)   Hess, S. T.; Girirajan, T. P. K.; Mason, M. D. Ultra-High Resolution Imaging by Fluorescence Photoactivation Localization Microscopy. *Biophysical Journal* **2006**, *91* (11), 4258–4272. https://doi.org/10.1529/biophysj.106.091116.

(165)   Rust, M. J.; Bates, M.; Zhuang, X. Sub-Diffraction-Limit Imaging by Stochastic Optical Reconstruction Microscopy (STORM). *Nat Methods* **2006**, *3* (10), 793–796. https://doi.org/10.1038/nmeth929.

(166)   Jungmann, R.; Steinhauer, C.; Scheible, M.; Kuzyk, A.; Tinnefeld, P.; Simmel, F. C. Single-Molecule Kinetics and Super-Resolution Microscopy by Fluorescence Imaging of Transient Binding on DNA Origami. *Nano Lett.* **2010**, *10* (11), 4756–4761. https://doi.org/10.1021/nl103427w.

(167)   Schnitzbauer, J.; Strauss, M. T.; Schlichthaerle, T.; Schueder, F.; Jungmann, R. Super-Resolution Microscopy with DNA-PAINT. *Nat Protoc* **2017**, *12* (6), 1198–1228. https://doi.org/10.1038/nprot.2017.024.

(168)   Andrian, T.; Bakkum, T.; van Elsland, D. M.; Bos, E.; Koster, A. J.; Albertazzi, L.; van Kasteren, S. I.; Pujals, S. Super-Resolution Correlative Light-Electron Microscopy Using a Click-Chemistry Approach for Studying Intracellular Trafficking. In *Methods in Cell Biology*; Elsevier, 2021; Vol. 162, pp 303–331. https://doi.org/10.1016/bs.mcb.2020.09.001.

(169)   Weisenburger, S.; Sandoghdar, V. Light Microscopy: An Ongoing Contemporary Revolution. *Contemporary Physics* **2015**, *56* (2), 123–143. https://doi.org/10.1080/00107514.2015.1026557.

(170)   van de Linde, S.; Löschberger, A.; Klein, T.; Heidbreder, M.; Wolter, S.; Heilemann, M.; Sauer, M. Direct Stochastic Optical Reconstruction Microscopy with Standard Fluorescent Probes. *Nat Protoc* **2011**, *6* (7), 991–1009. https://doi.org/10.1038/nprot.2011.336.

(171)   Tam, J.; Cordier, G. A.; Borbely, J. S.; Sandoval Álvarez, Á.; Lakadamyali, M. Cross-Talk-Free Multi-Color STORM Imaging Using a Single Fluorophore. *PLoS ONE* **2014**, *9* (7), e101772. https://doi.org/10.1371/journal.pone.0101772.

(172)   Lampe, A.; Haucke, V.; Sigrist, S. J.; Heilemann, M.; Schmoranzer, J. Multi-Colour Direct STORM with Red Emitting Carbocyanines. *Biology of the Cell* **2012**, *104* (4), 229–237. https://doi.org/10.1111/boc.201100011.

(173)   Bates, M.; Dempsey, G. T.; Chen, K. H.; Zhuang, X. Multicolor Super-Resolution Fluorescence Imaging via Multi-Parameter Fluorophore Detection. *ChemPhysChem* **2012**, *13* (1), 99–107. https://doi.org/10.1002/cphc.201100735.

(174)   Endesfelder, U.; Malkusch, S.; Flottmann, B.; Mondry, J.; Liguzinski, P.; Verveer, P. J.; Heilemann, M. Chemically Induced Photoswitching of Fluorescent Probes—A General Concept for Super-Resolution Microscopy. *Molecules* **2011**, *16* (4), 3106–3118. https://doi.org/10.3390/molecules16043106.

(175)   Feiner-Gracia, N.; Olea, R. A.; Fitzner, R.; El Boujnouni, N.; van Asbeck, A. H.; Brock, R.; Albertazzi, L. Super-Resolution Imaging of Structure, Molecular Composition, and Stability of Single Oligonucleotide Polyplexes. *Nano Lett.* **2019**, *19* (5), 2784–2792. https://doi.org/10.1021/acs.nanolett.8b04407.

(176)   van der Zwaag, D.; Vanparijs, N.; Wijnands, S.; De Rycke, R.; De Geest, B. G.; Albertazzi, L. Super Resolution Imaging of Nanoparticles Cellular Uptake and Trafficking. *ACS Appl. Mater. Interfaces* **2016**, *8* (10), 6391–6399. https://doi.org/10.1021/acsami.6b00811.

(177)   Xu, J.; Ma, H.; Liu, Y. Stochastic Optical Reconstruction Microscopy (STORM). *Current Protocols in Cytometry* **2017**, *81* (1). https://doi.org/10.1002/cpcy.23.

(178)   Sahl, S. J.; Hell, S. W.; Jakobs, S. Fluorescence Nanoscopy in Cell Biology. *Nat Rev Mol Cell Biol* **2017**, *18* (11), 685–701. https://doi.org/10.1038/nrm.2017.71.

(179)   Pujals, S.; Feiner-Gracia, N.; Delcanale, P.; Voets, I.; Albertazzi, L. Super-Resolution Microscopy as a Powerful Tool to Study Complex Synthetic Materials. *Nat Rev Chem* **2019**, *3* (2), 68–84. https://doi.org/10.1038/s41570-018-0070-2.

(180)   Baker, M. B.; Albertazzi, L.; Voets, I. K.; Leenders, C. M. A.; Palmans, A. R. A.; Pavan, G. M.; Meijer, E. W. Consequences of Chirality on the Dynamics of a Water-Soluble Supramolecular Polymer. *Nat Commun* **2015**, *6* (1), 6234. https://doi.org/10.1038/ncomms7234.

(181)   Baker, M. B.; Gosens, R. P. J.; Albertazzi, L.; Matsumoto, N. M.; Palmans, A. R. A.; Meijer, E. W. Exposing Differences in Monomer Exchange Rates of Multicomponent Supramolecular Polymers in Water. *ChemBioChem* **2016**, *17* (3), 207–213. https://doi.org/10.1002/cbic.201500606.

(182)   Gramlich, M. W.; Bae, J.; Hayward, R. C.; Ross, J. L. Fluorescence Imaging of Nanoscale Domains in Polymer Blends Using Stochastic Optical Reconstruction Microscopy (STORM). *Opt. Express* **2014**, *22* (7), 8438. https://doi.org/10.1364/OE.22.008438.

(183)   Feiner-Gracia, N.; Beck, M.; Pujals, S.; Tosi, S.; Mandal, T.; Buske, C.; Linden, M.; Albertazzi, L. Super-Resolution Microscopy Unveils Dynamic Heterogeneities in Nanoparticle Protein Corona. *Small* **2017**, *13* (41), 1701631. https://doi.org/10.1002/smll.201701631.

(184)   Sharonov, A.; Hochstrasser, R. M. Wide-Field Subdiffraction Imaging by Accumulated Binding of Diffusing Probes. *PNAS* **2006**, *103* (50), 18911–18916. https://doi.org/10.1073/pnas.0609643104.

(185)   Wade, O. K.; Woehrstein, J. B.; Nickels, P. C.; Strauss, S.; Stehr, F.; Stein, J.; Schueder, F.; Strauss, M. T.; Ganji, M.; Schnitzbauer, J.; Grabmayr, H.; Yin, P.; Schwille, P.; Jungmann, R. 124-Color Super-Resolution Imaging by Engineering DNA-PAINT Blinking Kinetics. *Nano Lett.* **2019**, *19* (4), 2641–2646. https://doi.org/10.1021/acs.nanolett.9b00508.

(186)   Agasti, S. S.; Wang, Y.; Schueder, F.; Sukumar, A.; Jungmann, R.; Yin, P. DNA-Barcoded Labeling Probes for Highly Multiplexed Exchange-PAINT Imaging. *Chem. Sci.* **2017**, *8* (4), 3080–3091. https://doi.org/10.1039/C6SC05420J.

(187)   Dai, M.; Jungmann, R.; Yin, P. Optical Imaging of Individual Biomolecules in Densely Packed Clusters. *Nature Nanotech* **2016**, *11* (9), 798–807. https://doi.org/10.1038/nnano.2016.95.

(188)   Delcanale, P.; Miret-Ontiveros, B.; Arista-Romero, M.; Pujals, S.; Albertazzi, L. Nanoscale Mapping Functional Sites on Nanoparticles by Points Accumulation for Imaging in Nanoscale Topography (PAINT). *ACS Nano* **2018**, *12* (8), 7629–7637. https://doi.org/10.1021/acsnano.7b09063.

(189)   Delcanale, P.; Albertazzi, L. DNA-PAINT Super-Resolution Imaging Data of Surface Exposed Active Sites on Particles. *Data in Brief* **2020**, *30*, 105468. https://doi.org/10.1016/j.dib.2020.105468.

(190)   Horáček, M.; Engels, D. J.; Zijlstra, P. Dynamic Single-Molecule Counting for the Quantification and Optimization of Nanoparticle Functionalization Protocols. *Nanoscale* **2020**, *12* (6), 4128–4136. https://doi.org/10.1039/C9NR10218C.

(191)   Hughes, L. D.; Rawle, R. J.; Boxer, S. G. Choose Your Label Wisely: Water-Soluble Fluorophores Often Interact with Lipid Bilayers. *PLoS ONE* **2014**, *9* (2), e87649. https://doi.org/10.1371/journal.pone.0087649.

(192)   Malatesta, M. Transmission Electron Microscopy for Nanomedicine: Novel Applications for Long-Established Techniques. *Eur J Histochem* **2016**, *60* (4). https://doi.org/10.4081/ejh.2016.2751.

(193)   Gilleron, J.; Querbes, W.; Zeigerer, A.; Borodovsky, A.; Marsico, G.; Schubert, U.; Manygoats, K.; Seifert, S.; Andree, C.; Stöter, M.; Epstein-Barash, H.; Zhang, L.; Kotelianksy, V.; Fitzgerald, K.; Fava, E.; Bickle, M.; Kalaidzidis, Y.; Akinc, A.; Maier, M.; Zerial, M. Image-Based Analysis of Lipid Nanoparticle–Mediated SiRNA Delivery, Intracellular Trafficking and Endosomal Escape. *Nat Biotechnol* **2013**, *31* (7), 638–646. https://doi.org/10.1038/nbt.2612.

(194)   Plaza-GA, I.; Manzaneda-González, V.; Kisovec, M.; Almendro-Vedia, V.; Muñoz-Úbeda, M.; Anderluh, G.; Guerrero-Martínez, A.; Natale, P.; López Montero, I. PH-Triggered Endosomal Escape of Pore-Forming Listeriolysin O Toxin-Coated Gold Nanoparticles. *J Nanobiotechnol* **2019**, *17* (1), 108. https://doi.org/10.1186/s12951-019-0543-6.

(195)   Hondow, N.; Brown, M. R.; Starborg, T.; Monteith, A. G.; Brydson, R.; Summers, H. D.; Rees, P.; Brown, A. Quantifying the Cellular Uptake of Semiconductor Quantum Dot Nanoparticles by Analytical Electron Microscopy: QUANTIFYING THE CELLULAR UPTAKE OF SEMICONDUCTOR QUANTUM DOT NANOPARTICLES. *Journal of Microscopy* **2016**, *261* (2), 167–176. https://doi.org/10.1111/jmi.12239.

(196)   Smith, D. J. Ultimate Resolution in the Electron Microscope? *Materials Today* **2008**, *11*, 30–38. https://doi.org/10.1016/S1369-7021(09)70005-7.

(197)   Vladár, A. E.; Hodoroaba, V.-D. Characterization of Nanoparticles by Scanning Electron Microscopy. In *Characterization of Nanoparticles*; Elsevier, 2020; pp 7–27. https://doi.org/10.1016/B978-0-12-814182-3.00002-X.

(198) Kler, S.; Wang, J. C.-Y.; Dhason, M.; Oppenheim, A.; Zlotnick, A. Scaffold Properties Are a Key Determinant of the Size and Shape of Self-Assembled Virus-Derived Particles. *ACS Chem. Biol.* **2013**, *8* (12), 2753–2761. https://doi.org/10.1021/cb4005518.

(199) Barauskas, J.; Johnsson, M.; Tiberg, F. Self-Assembled Lipid Superstructures: Beyond Vesicles and Liposomes. *Nano Lett.* **2005**, *5* (8), 1615–1619. https://doi.org/10.1021/nl050678i.

(200) Johnson, S.; Brorson, K. A.; Frey, D. D.; Dhar, A. K.; Cetlin, D. A. Characterization of Non-Infectious Virus-Like Particle Surrogates for Viral Clearance Applications. *Appl Biochem Biotechnol* **2017**, *183* (1), 318–331. https://doi.org/10.1007/s12010-017-2447-y.

(201) Costanzo, M.; Malatesta, M. Embedding Cell Monolayers to Investigate Nanoparticle-Plasmalemma Interactions at Transmission Electron Microscopy. *Eur J Histochem* **2019**, *63* (1). https://doi.org/10.4081/ejh.2019.3026.

(202) Malatesta, M.; Giagnacovo, M.; Costanzo, M.; Conti, B.; Genta, I.; Dorati, R.; Galimberti, V.; Biggiogera, M.; Zancanaro, C. Diaminobenzidine Photoconversion Is a Suitable Tool for Tracking the Intracellular Location of Fluorescently Labelled Nanoparticles at Transmission Electron Microscopy. *Eur J Histochem* **2012**, *56* (2), e20. https://doi.org/10.4081/ejh.2012.e20.

(203) Costanzo, M.; Carton, F.; Marengo, A.; Berlier, G.; Stella, B.; Arpicco, S.; Malatesta, M. Fluorescence and Electron Microscopy to Visualize the Intracellular Fate of Nanoparticles for Drug Delivery. *Eur J Histochem* **2016**, *60* (2). https://doi.org/10.4081/ejh.2016.2640.

(204) Rothen-Rutishauser, B.; Kuhn, D. A.; Ali, Z.; Gasser, M.; Amin, F.; Parak, W. J.; Vanhecke, D.; Fink, A.; Gehr, P.; Brandenberger, C. Quantification of Gold Nanoparticle Cell Uptake under Controlled Biological Conditions and Adequate Resolution. *Nanomedicine* **2014**, *9* (5), 607–621. https://doi.org/10.2217/nnm.13.24.

(205) Malatesta, M. Transmission Electron Microscopy as a Powerful Tool to Investigate the Interaction of Nanoparticles with Subcellular Structures. *Int. J. Mol. Sci.* **2021**, 17.

(206) Wu, X. A.; Choi, C. H. J.; Zhang, C.; Hao, L.; Mirkin, C. A. Intracellular Fate of Spherical Nucleic Acid Nanoparticle Conjugates. *J. Am. Chem. Soc.* **2014**, *136* (21), 7726–7733. https://doi.org/10.1021/ja503010a.

(207) Wu, M.; Guo, H.; Liu, L.; Liu, Y.; Xie, L. Size-Dependent Cellular Uptake and Localization Profiles of Silver Nanoparticles. *IJN* **2019**, *Volume 14*, 4247–4259. https://doi.org/10.2147/IJN.S201107.

(208) Cortadellas, N.; Garcia, A.; Fernández, E. Transmission Electron Microscopy in Cell Biology: Sample Preparation Techniques. 12.

(209) de Boer, P.; Hoogenboom, J. P.; Giepmans, B. N. G. Correlated Light and Electron Microscopy: Ultrastructure Lights Up! *Nat Methods* **2015**, *12* (6), 503–513. https://doi.org/10.1038/nmeth.3400.

(210) Bykov, Y. S.; Cortese, M.; Briggs, J. A. G.; Bartenschlager, R. Correlative Light and Electron Microscopy Methods for the Study of Virus-Cell Interactions. *FEBS Lett* **2016**, *590* (13), 1877–1895. https://doi.org/10.1002/1873-3468.12153.

(211) Ando, T.; Bhamidimarri, S. P.; Brending, N.; Colin-York, H.; Collinson, L.; De Jonge, N.; de Pablo, P. J.; Debroye, E.; Eggeling, C.; Franck, C.; Fritzsche, M.; Gerritsen, H.; Giepmans, B. N. G.; Grunewald, K.; Hofkens, J.; Hoogenboom, J. P.; Janssen, K. P. F.; Kaufmann, R.; Klumperman, J.; Kurniawan, N.; Kusch, J.; Liv, N.; Parekh, V.; Peckys, D. B.; Rehfeldt, F.; Reutens, D. C.; Roeffaers, M. B. J.; Salditt, T.; Schaap, I. A. T.; Schwarz, U. S.; Verkade, P.; Vogel, M. W.; Wagner, R.; Winterhalter, M.; Yuan, H.; Zifarelli, G. The 2018 Correlative Microscopy Techniques Roadmap. *J. Phys. D: Appl. Phys.* **2018**, *51* (44), 443001. https://doi.org/10.1088/1361-6463/aad055.

(212) Sikirzhytski, V.; Renda, F.; Tikhonenko, I.; Magidson, V.; McEwen, B. F.; Khodjakov, A. Microtubules Assemble near Most Kinetochores during Early Prometaphase

in Human Cells. *Journal of Cell Biology* **2018**, *217* (8), 2647–2659. https://doi.org/10.1083/jcb.201710094.

(213)   Fermie, J.; Liv, N.; ten Brink, C.; van Donselaar, E. G.; Müller, W. H.; Schieber, N. L.; Schwab, Y.; Gerritsen, H. C.; Klumperman, J. Single Organelle Dynamics Linked to 3D Structure by Correlative Live-Cell Imaging and 3D Electron Microscopy. *Traffic* **2018**, *19* (5), 354–369. https://doi.org/10.1111/tra.12557.

(214)   Sommi, P.; Necchi, V.; Vitali, A.; Montagna, D.; De Luigi, A.; Salmona, M.; Ricci, V.; Solcia, E. PaCS Is a Novel Cytoplasmic Structure Containing Functional Proteasome and Inducible by Cytokines/Trophic Factors. *PLoS ONE* **2013**, *8* (12), e82560. https://doi.org/10.1371/journal.pone.0082560.

(215)   Betzig, E.; Patterson, G. H.; Sougrat, R.; Lindwasser, O. W.; Olenych, S.; Bonifacino, J. S.; Davidson, M. W.; Lippincott-Schwartz, J.; Hess, H. F. Imaging Intracellular Fluorescent Proteins at Nanometer Resolution. *Science* **2006**, *313* (5793), 1642–1645. https://doi.org/10.1126/science.1127344.

(216)   Kopek, B. G.; Shtengel, G.; Xu, C. S.; Clayton, D. A.; Hess, H. F. Correlative 3D Superresolution Fluorescence and Electron Microscopy Reveal the Relationship of Mitochondrial Nucleoids to Membranes. *Proceedings of the National Academy of Sciences* **2012**, *109* (16), 6136–6141. https://doi.org/10.1073/pnas.1121558109.

(217)   van Elsland, D. M.; Pujals, S.; Bakkum, T.; Bos, E.; Oikonomeas-Koppasis, N.; Berlin, I.; Neefjes, J.; Meijer, A. H.; Koster, A. J.; Albertazzi, L.; van Kasteren, S. I. Ultrastructural Imaging of *Salmonella* -Host Interactions Using Super-Resolution Correlative Light-Electron Microscopy of Bioorthogonal Pathogens. *ChemBioChem* **2018**, *19* (16), 1766–1770. https://doi.org/10.1002/cbic.201800230.

(218)   Kim, D.; Deerinck, T. J.; Sigal, Y. M.; Babcock, H. P.; Ellisman, M. H.; Zhuang, X. Correlative Stochastic Optical Reconstruction Microscopy and Electron Microscopy. *PLoS ONE* **2015**, *10* (4), e0124581. https://doi.org/10.1371/journal.pone.0124581.

(219)   Le Trequesser, Q.; Devès, G.; Saez, G.; Daudin, L.; Barberet, P.; Michelet, C.; Delville, M.-H.; Seznec, H. Single Cell *In Situ* Detection and Quantification of Metal Oxide Nanoparticles Using Multimodal Correlative Microscopy. *Anal. Chem.* **2014**, *86* (15), 7311–7319. https://doi.org/10.1021/ac501318c.

(220)   Frey, M.; Han, S.; Halim, H.; Kaltbeitzel, A.; Riedinger, A.; Landfester, K.; Lieberwirth, I. Nanocarriers Made of Proteins: Intracellular Visualization of a Smart Biodegradable Drug Delivery System. *Small* **2022**, 2106094. https://doi.org/10.1002/smll.202106094.

(221)   Han, S.; Raabe, M.; Hodgson, L.; Mantell, J.; Verkade, P.; Lasser, T.; Landfester, K.; Weil, T.; Lieberwirth, I. High-Contrast Imaging of Nanodiamonds in Cells by Energy Filtered and Correlative Light-Electron Microscopy: Toward a Quantitative Nanoparticle-Cell Analysis. *Nano Lett.* **2019**, *19* (3), 2178–2185. https://doi.org/10.1021/acs.nanolett.9b00752.

(222)   Allen, T. M. Drug Delivery Systems: Entering the Mainstream. *Science* **2004**, *303* (5665), 1818–1822. https://doi.org/10.1126/science.1095833.

(223)   Byrne, J. D.; Betancourt, T.; Brannon-Peppas, L. Active Targeting Schemes for Nanoparticle Systems in Cancer Therapeutics. *Advanced Drug Delivery Reviews* **2008**, 12.

(224)   Suk, J. S.; Xu, Q.; Kim, N.; Hanes, J.; Ensign, L. M. PEGylation as a Strategy for Improving Nanoparticle-Based Drug and Gene Delivery. *Advanced Drug Delivery Reviews* **2016**, *99*, 28–51. https://doi.org/10.1016/j.addr.2015.09.012.

(225)   Gref, R.; Lück, M.; Quellec, P.; Marchand, M.; Dellacherie, E.; Harnisch, S.; Blunk, T.; Müller, R. H. 'Stealth' Corona-Core Nanoparticles Surface Modified by Polyethylene Glycol (PEG): Influences of the Corona (PEG Chain Length and Surface Density) and of the Core Composition on Phagocytic Uptake and Plasma Protein Adsorption. *Colloids and*

Surfaces B: Biointerfaces **2000**, *18* (3–4), 301–313. https://doi.org/10.1016/S0927-7765(99)00156-3.

(226)   Klibanov, A. L.; Maruyama, K.; Torchilin, V. P.; Huang, L. Amphipathic Polyethyleneglycols Effectively Prolong the Circulation Time of Liposomes. *FEBS Letters* **1990**, *268* (1), 235–237. https://doi.org/10.1016/0014-5793(90)81016-H.

(227)   Ishii, T.; Miyata, K.; Anraku, Y.; Naito, M.; Yi, Y.; Jinbo, T.; Takae, S.; Fukusato, Y.; Hori, M.; Osada, K.; Kataoka, K. Enhanced Target Recognition of Nanoparticles by Cocktail PEGylation with Chains of Varying Lengths. *Chem. Commun.* **2016**, *52* (7), 1517–1519. https://doi.org/10.1039/C5CC06661A.

(228)   Miyata, K. Smart Polymeric Nanocarriers for Small Nucleic Acid Delivery. 12.

(229)   Pereira Gomes, C.; Leiro, V.; Ferreira Lopes, C. D.; Spencer, A. P.; Pêgo, A. P. Fine Tuning Neuronal Targeting of Nanoparticles by Adjusting the Ligand Grafting Density and Combining PEG Spacers of Different Length. *Acta Biomaterialia* **2018**, *78*, 247–259. https://doi.org/10.1016/j.actbio.2018.08.005.

(230)   Maslanka Figueroa, S.; Fleischmann, D.; Beck, S.; Goepferich, A. The Effect of Ligand Mobility on the Cellular Interaction of Multivalent Nanoparticles. *Macromol. Biosci.* **2020**, *20* (4), 1900427. https://doi.org/10.1002/mabi.201900427.

(231)   Post, R. A. J.; van der Zwaag, D.; Bet, G.; Wijnands, S. P. W.; Albertazzi, L.; Meijer, E. W.; van der Hofstad, R. W. A Stochastic View on Surface Inhomogeneity of Nanoparticles. *Nat Commun* **2019**, *10* (1), 1663. https://doi.org/10.1038/s41467-019-09595-y.

(232)   Barichello, J. M.; Morishita, M.; Takayama, K.; Nagai, T. Encapsulation of Hydrophilic and Lipophilic Drugs in PLGA Nanoparticles by the Nanoprecipitation Method. *Drug Development and Industrial Pharmacy* **1999**, *25* (4), 471–476. https://doi.org/10.1081/DDC-100102197.

(233)   Demetrios Papahadjopoulos, Francis J. Martin. Irreversible Coupling of Immunoglobulin Fragments to Preformed Vesicles. *JBC* **1982**, *257* (1), 286–288.

(234)   Gholizadeh, S.; Kamps, Jan. A. A. M.; Hennink, W. E.; Kok, R. J. PLGA-PEG Nanoparticles for Targeted Delivery of the MTOR/PI3kinase Inhibitor Dactolisib to Inflamed Endothelium. *International Journal of Pharmaceutics* **2018**, *548* (2), 747–758. https://doi.org/10.1016/j.ijpharm.2017.10.032.

(235)   Mohan, L. J.; McDonald, L.; Daly, J. S.; Ramtoola, Z. Optimising PLGA-PEG Nanoparticle Size and Distribution for Enhanced Drug Targeting to the Inflamed Intestinal Barrier. *Pharmaceutics* **2020**, *12* (11), 1114. https://doi.org/10.3390/pharmaceutics12111114.

(236)   Pochapski, D. J.; Carvalho dos Santos, C.; Leite, G. W.; Pulcinelli, S. H.; Santilli, C. V. Zeta Potential and Colloidal Stability Predictions for Inorganic Nanoparticle Dispersions: Effects of Experimental Conditions and Electrokinetic Models on the Interpretation of Results. *Langmuir* **2021**, *37* (45), 13379–13389. https://doi.org/10.1021/acs.langmuir.1c02056.

(237)   Saha, B.; Evers, T. H.; Prins, M. W. J. How Antibody Surface Coverage on Nanoparticles Determines the Activity and Kinetics of Antigen Capturing for Biosensing. *Anal. Chem.* **2014**, *86* (16), 8158–8166. https://doi.org/10.1021/ac501536z.

(238)   Saha, B.; Songe, P.; Evers, T. H.; Prins, M. W. J. The Influence of Covalent Immobilization Conditions on Antibody Accessibility on Nanoparticles. *Analyst* **2017**, *142* (22), 4247–4256. https://doi.org/10.1039/C7AN01424D.

(239)   Parolo, C.; de la Escosura-Muñiz, A.; Polo, E.; Grazú, V.; de la Fuente, J. M.; Merkoçi, A. Design, Preparation, and Evaluation of a Fixed-Orientation Antibody/Gold-Nanoparticle Conjugate as an Immunosensing Label. *ACS Appl. Mater. Interfaces* **2013**, *5* (21), 10753–10759. https://doi.org/10.1021/am4029153.

(240)   Andrian, T.; Delcanale, P.; Pujals, S.; Albertazzi, L. Correlating Super-Resolution Microscopy and Transmission Electron Microscopy Reveals Multiparametric Heterogeneity in Nanoparticles. *Nano Letters* 9.

(241)   Martínez-Jothar, L.; Doulkeridou, S.; Schiffelers, R. M.; Sastre Torano, J.; Oliveira, S.; van Nostrum, C. F.; Hennink, W. E. Insights into Maleimide-Thiol Conjugation Chemistry: Conditions for Efficient Surface Functionalization of Nanoparticles for Receptor Targeting. *Journal of Controlled Release* **2018**, *282*, 101–109. https://doi.org/10.1016/j.jconrel.2018.03.002.

(242)   Vega, E.; Egea; Calpena; Espina; García. Role of Hydroxypropyl-β-Cyclodextrin on Freeze-Dried and Gamma-Irradiated PLGA and PLGA–PEG Diblock Copolymer Nanospheres for Ophthalmic Flurbiprofen Delivery. *IJN* **2012**, 1357. https://doi.org/10.2147/IJN.S28481.

(243)   Abe, K.; Higashi, K.; Watabe, K.; Kobayashi, A.; Limwikrant, W.; Yamamoto, K.; Moribe, K. Effects of the PEG Molecular Weight of a PEG-Lipid and Cholesterol on PEG Chain Flexibility on Liposome Surfaces. *Colloids and Surfaces A: Physicochemical and Engineering Aspects* **2015**, *474*, 63–70. https://doi.org/10.1016/j.colsurfa.2015.03.006.

(244)   Hennig, R.; Pollinger, K.; Veser, A.; Breunig, M.; Goepferich, A. Nanoparticle Multivalency Counterbalances the Ligand Affinity Loss upon PEGylation. *Journal of Controlled Release* **2014**, *194*, 20–27. https://doi.org/10.1016/j.jconrel.2014.07.062.

(245)   Amoozgar, Z.; Yeo, Y. Recent Advances in Stealth Coating of Nanoparticle Drug Delivery Systems: Stealth Coating of Nanoparticle Drug Delivery Systems. *WIREs Nanomed Nanobiotechnol* **2012**, *4* (2), 219–233. https://doi.org/10.1002/wnan.1157.

(246)   Abstiens, K.; Gregoritza, M.; Goepferich, A. M. Ligand Density and Linker Length Are Critical Factors for Multivalent Nanoparticle–Receptor Interactions. *ACS Appl. Mater. Interfaces* **2019**, *11* (1), 1311–1320. https://doi.org/10.1021/acsami.8b18843.

(247)   Pozzi, D.; Colapicchioni, V.; Caracciolo, G.; Piovesana, S.; Capriotti, A. L.; Palchetti, S.; De Grossi, S.; Riccioli, A.; Amenitsch, H.; Laganà, A. Effect of Polyethyleneglycol (PEG) Chain Length on the Bio–Nano-Interactions between PEGylated Lipid Nanoparticles and Biological Fluids: From Nanostructure to Uptake in Cancer Cells. *Nanoscale* **2014**, *6* (5), 2782. https://doi.org/10.1039/c3nr05559k.

(248)   Invitrogen Molecular Probes. Thiol-Reactive Probes, 2006.

(249)   Spherotech Inc. *Particle characteristics*. https://www.spherotech.com/particle.html (accessed 2020-07-20).

(250)   *Ellman's Reagent Instructions*. ThermoFisher Scientific. https://assets.thermofisher.com/TFS-Assets/LSG/manuals/MAN0011216_Ellmans_Reag_UG.pdf (accessed 2020-10-05).

(251)   Jain, K. Future of Nanomedicine: Impact on Healthcare & Society. *Nanomedicine* **2015**, *10* (21), 3199–3202. https://doi.org/10.2217/nnm.15.153.

(252)   Martinelli, C.; Pucci, C.; Ciofani, G. Nanostructured Carriers as Innovative Tools for Cancer Diagnosis and Therapy. *APL Bioengineering* **2019**, *3* (1), 011502. https://doi.org/10.1063/1.5079943.

(253)   Loo, C.; Lowery, A.; Halas, N.; West, J.; Drezek, R. Immunotargeted Nanoshells for Integrated Cancer Imaging and Therapy. *Nano Lett.* **2005**, *5* (4), 709–711. https://doi.org/10.1021/nl050127s.

(254)   Karra, N.; Benita, S. The Ligand Nanoparticle Conjugation Approach for Targeted Cancer Therapy. *CDM* **2012**, *13* (1), 22–41. https://doi.org/10.2174/138920012798356899.

(255)   Karagoz, B.; Esser, L.; Duong, H. T.; Basuki, J. S.; Boyer, C.; Davis, T. P. Polymerization-Induced Self-Assembly (PISA) – Control over the Morphology of Nanoparticles for Drug Delivery Applications. *Polym. Chem.* **2014**, *5* (2), 350–355. https://doi.org/10.1039/C3PY01306E.

(256)   Niikura, K.; Matsunaga, T.; Suzuki, T.; Kobayashi, S.; Yamaguchi, H.; Orba, Y.; Kawaguchi, A.; Hasegawa, H.; Kajino, K.; Ninomiya, T.; Ijiro, K.; Sawa, H. Gold Nanoparticles as a Vaccine Platform: Influence of Size and Shape on Immunological Responses *in Vitro* and *in Vivo*. *ACS Nano* **2013**, *7* (5), 3926–3938. https://doi.org/10.1021/nn3057005.

(257)   Choi, C. H. J.; Zuckerman, J. E.; Webster, P.; Davis, M. E. Targeting Kidney Mesangium by Nanoparticles of Defined Size. *Proceedings of the National Academy of Sciences* **2011**, *108* (16), 6656–6661. https://doi.org/10.1073/pnas.1103573108.

(258)   Gao, H.; Yang, Z.; Zhang, S.; Cao, S.; Shen, S.; Pang, Z.; Jiang, X. Ligand Modified Nanoparticles Increases Cell Uptake, Alters Endocytosis and Elevates Glioma Distribution and Internalization. *Sci Rep* **2013**, *3* (1), 2534. https://doi.org/10.1038/srep02534.

(259)   Yao, V. J.; D'Angelo, S.; Butler, K. S.; Theron, C.; Smith, T. L.; Marchiò, S.; Gelovani, J. G.; Sidman, R. L.; Dobroff, A. S.; Brinker, C. J.; Bradbury, A. R. M.; Arap, W.; Pasqualini, R. Ligand-Targeted Theranostic Nanomedicines against Cancer. *Journal of Controlled Release* **2016**, *240*, 267–286. https://doi.org/10.1016/j.jconrel.2016.01.002.

(260)   Boyd, R. D. New Approach to Inter-Technique Comparisons for Nanoparticle Size Measurements; Using Atomic Force Microscopy, Nanoparticle Tracking Analysis and Dynamic Light Scattering. **2011**, 8.

(261)   Jee, A.-Y.; Lee, M. Surface Functionalization and Physicochemical Characterization of Diamond Nanoparticles. *Current Applied Physics* **2009**, *9* (2), e144–e147. https://doi.org/10.1016/j.cap.2008.12.045.

(262)   Clemments, A. M.; Botella, P.; Landry, C. C. Spatial Mapping of Protein Adsorption on Mesoporous Silica Nanoparticles by Stochastic Optical Reconstruction Microscopy. *J. Am. Chem. Soc.* **2017**, *139* (11), 3978–3981. https://doi.org/10.1021/jacs.7b01118.

(263)   Albertazzi, L.; van der Zwaag, D.; Leenders, C. M. A.; Fitzner, R.; van der Hofstad, R. W.; Meijer, E. W. Probing Exchange Pathways in One-Dimensional Aggregates with Super-Resolution Microscopy. *Science* **2014**, *344* (6183), 491–495. https://doi.org/10.1126/science.1250945.

(264)   Chen, X.; Cui, J.; Ping, Y.; Suma, T.; Cavalieri, F.; Besford, Q. A.; Chen, G.; Braunger, J. A.; Caruso, F. Probing Cell Internalisation Mechanics with Polymer Capsules. *Nanoscale* **2016**, *8* (39), 17096–17101. https://doi.org/10.1039/C6NR06657G.

(265)   Agasti, S. S.; Wang, Y.; Schueder, F.; Sukumar, A.; Jungmann, R.; Yin, P. DNA-Barcoded Labeling Probes for Highly Multiplexed Exchange-PAINT Imaging. *Chem. Sci.* **2017**, *8* (4), 3080–3091. https://doi.org/10.1039/C6SC05420J.

(266)   Andrian, T.; Pujals, S.; Albertazzi, L. Quantifying the Effect of PEG Architecture on Nanoparticle Ligand Availability Using DNA-PAINT. *Nanoscale Adv.* **2021**, *3* (24), 6876–6881. https://doi.org/10.1039/D1NA00696G.

(267)   Xu, M.; Soliman, M. G.; Sun, X.; Pelaz, B.; Feliu, N.; Parak, W. J.; Liu, S. How Entanglement of Different Physicochemical Properties Complicates the Prediction of in Vitro and in Vivo Interactions of Gold Nanoparticles. *ACS Nano* **2018**, 10.

(268)   Jiang, Y.; Huo, S.; Mizuhara, T.; Das, R.; Lee, Y.-W.; Hou, S.; Moyano, D. F.; Duncan, B.; Liang, X.-J.; Rotello, V. M. The Interplay of Size and Surface Functionality on the Cellular Uptake of Sub-10 Nm Gold Nanoparticles. *ACS Nano* **2015**, *9* (10), 9986–9993. https://doi.org/10.1021/acsnano.5b03521.

(269)   Watanabe, S.; Punge, A.; Hollopeter, G.; Willig, K. I.; Hobson, R. J.; Davis, M. W.; Hell, S. W.; Jorgensen, E. M. Protein Localization in Electron Micrographs Using Fluorescence Nanoscopy. *Nat Methods* **2011**, *8* (1), 80–84. https://doi.org/10.1038/nmeth.1537.

(270)   Tuijtel, M. W.; Koster, A. J.; Jakobs, S.; Faas, F. G. A.; Sharp, T. H. Correlative Cryo Super-Resolution Light and Electron Microscopy on Mammalian Cells Using Fluorescent Proteins. *Sci Rep* **2019**, *9* (1), 1369. https://doi.org/10.1038/s41598-018-37728-8.

(271)   Rezvantalab, S.; Drude, N. I.; Moraveji, M. K.; Güvener, N.; Koons, E. K.; Shi, Y.; Lammers, T.; Kiessling, F. PLGA-Based Nanoparticles in Cancer Treatment. *Front. Pharmacol.* **2018**, *9*, 1260. https://doi.org/10.3389/fphar.2018.01260.

(272)   Danhier, F.; Ansorena, E.; Silva, J. M.; Coco, R.; Le Breton, A.; Préat, V. PLGA-Based Nanoparticles: An Overview of Biomedical Applications. *Journal of Controlled Release* **2012**, *161* (2), 505–522. https://doi.org/10.1016/j.jconrel.2012.01.043.

(273)   Makadia, H. K.; Siegel, S. J. Poly Lactic-Co-Glycolic Acid (PLGA) as Biodegradable Controlled Drug Delivery Carrier. *Polymers* **2011**, *3* (3), 1377–1397. https://doi.org/10.3390/polym3031377.

(274)   Jokerst, J. V.; Lobovkina, T.; Zare, R. N.; Gambhir, S. S. Nanoparticle PEGylation for Imaging and Therapy. **2011**, *6* (4), 715–728. https://doi.org/10.2217/nnm.11.19.

(275)   Turecek, P. L.; Bossard, M. J.; Schoetens, F.; Ivens, I. A. PEGylation of Biopharmaceuticals: A Review of Chemistry and Nonclinical Safety Information of Approved Drugs. *Journal of Pharmaceutical Sciences* **2016**, *105* (2), 460–475. https://doi.org/10.1016/j.xphs.2015.11.015.

(276)   Vllasaliu, D.; Fowler, R.; Stolnik, S. PEGylated Nanomedicines: Recent Progress and Remaining Concerns. *Expert Opinion on Drug Delivery* **2014**, *11* (1), 139–154. https://doi.org/10.1517/17425247.2014.866651.

(277)   Nobs, L.; Buchegger, F.; Gurny, R.; Allémann, E. Current Methods for Attaching Targeting Ligands to Liposomes and Nanoparticles. *Journal of Pharmaceutical Sciences* **2004**, *93* (8), 1980–1992. https://doi.org/10.1002/jps.20098.

(278)   Yu, M. K.; Park, J.; Jon, S. Targeting Strategies for Multifunctional Nanoparticles in Cancer Imaging and Therapy. *Theranostics* **2012**, *2* (1), 3–44. https://doi.org/10.7150/thno.3463.

(279)   Delcanale, P.; Porciani, D.; Pujals, S.; Jurkevich, A.; Chetrusca, A.; Tawiah, K. D.; Burke, D. H.; Albertazzi, L. Aptamers with Tunable Affinity Enable Single-Molecule Tracking and Localization of Membrane Receptors on Living Cancer Cells. *Angew. Chem. Int. Ed.* **2020**, *59* (42), 18546–18555. https://doi.org/10.1002/anie.202004764.

(280)   Kiuchi, T.; Higuchi, M.; Takamura, A.; Maruoka, M.; Watanabe, N. Multitarget Super-Resolution Microscopy with High-Density Labeling by Exchangeable Probes. *Nat Methods* **2015**, *12* (8), 743–746. https://doi.org/10.1038/nmeth.3466.

(281)   Perry, J. L.; Herlihy, K. P.; Napier, M. E.; DeSimone, J. M. PRINT: A Novel Platform Toward Shape and Size Specific Nanoparticle Theranostics. *Acc. Chem. Res.* **2011**, *44* (10), 990–998. https://doi.org/10.1021/ar2000315.

(282)   Zhang, J.; Pei, Y.; Zhang, H.; Wang, L.; Arrington, L.; Zhang, Y.; Glass, A.; Leone, A. M. Assessing the Heterogeneity Level in Lipid Nanoparticles for SiRNA Delivery: Size-Based Separation, Compositional Heterogeneity, and Impact on Bioperformance. *Mol. Pharmaceutics* **2013**, *10* (1), 397–405. https://doi.org/10.1021/mp3005337.

(283)   Dutta, D.; Salifu, M.; Sirianni, R. W.; Stabenfeldt, S. E. Tailoring Sub-Micron PLGA Particle Release Profiles via Centrifugal Fractioning: TAILORING SUB-MICRON PLGA PARTICLE. *J. Biomed. Mater. Res.* **2016**, *104* (3), 688–696. https://doi.org/10.1002/jbm.a.35608.

(284)   Mullen, D. G.; Borgmeier, E. L.; Desai, A. M.; van Dongen, M. A.; Barash, M.; Cheng, X.; Baker, J. R.; Banaszak Holl, M. M. Isolation and Characterization of Dendrimers with Precise Numbers of Functional Groups. *Chem. Eur. J.* **2010**, *16* (35), 10675–10678. https://doi.org/10.1002/chem.201001175.

(285)   Javiya, C.; Jonnalagadda, S. Physicochemical Characterization of Spray-Dried PLGA/PEG Microspheres, and Preliminary Assessment of Biological Response. *Drug Development and Industrial Pharmacy* **2016**, *42* (9), 1504–1514. https://doi.org/10.3109/03639045.2016.1151030.

(286)   Hennig, R.; Pollinger, K.; Veser, A.; Breunig, M.; Goepferich, A. Nanoparticle Multivalency Counterbalances the Ligand Affinity Loss upon PEGylation. *Journal of Controlled Release* **2014**, *194*, 20–27. https://doi.org/10.1016/j.jconrel.2014.07.062.

(287)   Halperin-Sternfeld, M.; Ghosh, M.; Adler-Abramovich, L. Advantages of Self-Assembled Supramolecular Polymers Toward Biological Applications. In *Supramolecular Chemistry of Biomimetic Systems*; Li, J., Ed.; Springer Singapore: Singapore, 2017; pp 9–35. https://doi.org/10.1007/978-981-10-6059-5_2.

(288)   Fuentes, E.; Gerth, M.; Berrocal, J. A.; Matera, C.; Gorostiza, P.; Voets, I. K.; Pujals, S.; Albertazzi, L. An Azobenzene-Based Single-Component Supramolecular Polymer Responsive to Multiple Stimuli in Water. *J. Am. Chem. Soc.* **2020**, *142* (22), 10069–10078. https://doi.org/10.1021/jacs.0c02067.

(289)   Zhang, S. Emerging Biological Materials through Molecular Self-Assembly. *Biotechnology Advances* **2002**, *20* (5–6), 321–339. https://doi.org/10.1016/S0734-9750(02)00026-5.

(290)   Albertazzi, L.; van der Zwaag, D.; Leenders, C. M. A.; Fitzner, R.; van der Hofstad, R. W.; Meijer, E. W. Probing Exchange Pathways in One-Dimensional Aggregates with Super-Resolution Microscopy. *Science* **2014**, *344* (6183), 491–495. https://doi.org/10.1126/science.1250945.

(291)   Bahrami, B. Nanoparticles and Targeted Drug Delivery in Cancer Therapy. 47.

(292)   Jahan, S. T.; Sadat, S. M. A.; Walliser, M.; Haddadi, A. Targeted Therapeutic Nanoparticles: An Immense Promise to Fight against Cancer. *Journal of Drug Delivery* 25.

(293)   Wu, J. The Enhanced Permeability and Retention (EPR) Effect: The Significance of the Concept and Methods to Enhance Its Application. **2021**, 8.

(294)   Patel, S.; Kim, J.; Herrera, M.; Mukherjee, A.; Kabanov, A. V.; Sahay, G. Brief Update on Endocytosis of Nanomedicines. *Advanced Drug Delivery Reviews* **2019**, *144*, 90–111. https://doi.org/10.1016/j.addr.2019.08.004.

(295)   Degors, I. M. S.; Wang, C.; Rehman, Z. U.; Zuhorn, I. S. Carriers Break Barriers in Drug Delivery: Endocytosis and Endosomal Escape of Gene Delivery Vectors. *Acc. Chem. Res.* **2019**, *52* (7), 1750–1760. https://doi.org/10.1021/acs.accounts.9b00177.

(296)   Iversen, T.-G. Endocytosis and Intracellular Transport of Nanoparticles: Present Knowledge and Need for Future Studies. 10.

(297)   Chou, L. Y. T.; Ming, K.; Chan, W. C. W. Strategies for the Intracellular Delivery of Nanoparticles. **2011**, 13.

(298)   Chakkarapani, S. K. Quantifying Intracellular Trafficking of Silica-Coated Magnetic Nanoparticles in Live Single Cells by Site-Specific Direct Stochastic Optical Reconstruction Microscopy. **2021**, 15.

(299)   Wojnilowicz, M.; Glab, A.; Bertucci, A.; Caruso, F.; Cavalieri, F. Super-Resolution Imaging of Proton Sponge-Triggered Rupture of Endosomes and Cytosolic Release of Small Interfering RNA. *ACS Nano* **2019**, *13* (1), 187–202. https://doi.org/10.1021/acsnano.8b05151.

(300)   Riera, R.; Feiner-Gracia, N.; Fornaguera, C.; Cascante, A.; Borrós, S.; Albertazzi, L. Tracking the DNA Complexation State of PBAE Polyplexes in Cells with Super Resolution Microscopy. **2019**, 9.

(301)   Riera, R.; Tauler, J.; Feiner-Gracia, N.; Borrós, S.; Fornaguera, C.; Albertazzi, L. Complex PBAE Nanoparticle Cell Trafficking: Tracking Both Position and Composition Using Super Resolution Microscopy. **2022**, 9.

(302)   Woythe, L.; Madhikar, P.; Feiner-Gracia, N.; Storm, C.; Albertazzi, L. A Single-Molecule View at Nanoparticle Targeting Selectivity: Correlating Ligand Functionality and Cell Receptor Density. *ACS Nano* **2022**, *16* (3), 3785–3796. https://doi.org/10.1021/acsnano.1c08277.

(303)   Jiang, W.; Kim, B. Y. S.; Rutka, J. T.; Chan, W. C. W. Nanoparticle-Mediated Cellular Response Is Size-Dependent. *nature nanotechnology* **2008**, *3*, 6.

(304)   Dobbie, I. M. Bridging the Resolution Gap: Correlative Super-Resolution Imaging. *Nat Rev Microbiol* **2019**, *17* (6), 337–337. https://doi.org/10.1038/s41579-019-0203-8.

(305)   *Correlative Light and Electron Microscopy IV*, First edition.; Müller-Reichert, T., Verkade, P., Eds.; Methods in cell biology; Academic Press, an imprint of Elsevier: Cambridge San Diego Oxford London, 2021.

(306)   Müller-Reichert, T.; Verkade, P. *Correlative Light and Electron Microscopy II*, 1st. edition.; Methods in cell biology; Elsevier/Academic Press: Amsterdam, 2014.

(307)   *Correlative Light and Electron Microscopy III*, First edition.; Müller-Reichert, T., Verkade, P., Eds.; Methods in cell biology; Elsevier/Academic Press: Cambridge, MA, 2017.

(308)   Tuijtel, M. W.; Koster, A. J.; Jakobs, S.; Faas, F. G. A.; Sharp, T. H. Correlative Cryo Super-Resolution Light and Electron Microscopy on Mammalian Cells Using Fluorescent Proteins. *Sci Rep* **2019**, *9* (1), 1369. https://doi.org/10.1038/s41598-018-37728-8.

(309)   Monaghan; Perusinghe; Muller. High-Pressure Freezing for Immunocytochemistry. *J Microsc* **1998**, *192* (3), 248–258. https://doi.org/10.1046/j.1365-2818.1998.00387.x.

(310)   Tokuyasu, K. T. A TECHNIQUE FOR ULTRACRYOTOMY OF CELL SUSPENSIONS AND TISSUES. *Journal of Cell Biology* **1973**, *57* (2), 551–565. https://doi.org/10.1083/jcb.57.2.551.

(311)   Paez-Segala, M. G.; Sun, M. G.; Shtengel, G.; Viswanathan, S.; Baird, M. A.; Macklin, J. J.; Patel, R.; Allen, J. R.; Howe, E. S.; Piszczek, G.; Hess, H. F.; Davidson, M. W.; Wang, Y.; Looger, L. L. Fixation-Resistant Photoactivatable Fluorescent Proteins for CLEM. *Nat Methods* **2015**, *12* (3), 215–218. https://doi.org/10.1038/nmeth.3225.

(312)   Masich, S.; Östberg, T.; Norlén, L.; Shupliakov, O.; Daneholt, B. A Procedure to Deposit Fiducial Markers on Vitreous Cryo-Sections for Cellular Tomography. *Journal of Structural Biology* **2006**, *156* (3), 461–468. https://doi.org/10.1016/j.jsb.2006.05.010.

(313)   Kukulski, W.; Schorb, M.; Welsch, S.; Picco, A.; Kaksonen, M.; Briggs, J. A. G. Precise, Correlated Fluorescence Microscopy and Electron Tomography of Lowicryl Sections Using Fluorescent Fiducial Markers. In *Methods in Cell Biology*; Elsevier, 2012; Vol. 111, pp 235–257. https://doi.org/10.1016/B978-0-12-416026-2.00013-3.

(314)   Paul-Gilloteaux, P.; Heiligenstein, X.; Belle, M.; Domart, M.-C.; Larijani, B.; Collinson, L.; Raposo, G.; Salamero, J. EC-CLEM: Flexible Multidimensional Registration Software for Correlative Microscopies. *Nat Methods* **2017**, *14* (2), 102–103. https://doi.org/10.1038/nmeth.4170.

(315)   Agronskaia, A. V.; Valentijn, J. A.; van Driel, L. F.; Schneijdenberg, C. T. W. M.; Humbel, B. M.; van Bergen en Henegouwen, P. M. P.; Verkleij, A. J.; Koster, A. J.; Gerritsen, H. C. Integrated Fluorescence and Transmission Electron Microscopy. *Journal of Structural Biology* **2008**, *164* (2), 183–189. https://doi.org/10.1016/j.jsb.2008.07.003.

(316)   Solomonov, I.; Talmi-Frank, D.; Milstein, Y.; Addadi, S.; Aloshin, A.; Sagi, I. Introduction of Correlative Light and AirSEMTM Microscopy Imaging for Tissue Research under Ambient Conditions. *Sci Rep* **2014**, *4*, 5987. https://doi.org/10.1038/srep05987.

(317)   LR White Embedding Medium Technical Data Sheet.

(318)   Wild, P.; Schraner, E. M.; Adler, H.; Humbel, B. M. Enhanced Resolution of Membranes in Cultured Cells by Cryoimmobilization and Freeze-Substitution. *Microsc. Res. Tech.* **2001**, *53* (4), 313–321. https://doi.org/10.1002/jemt.1098.

(319)   Katheder, N. S.; Khezri, R.; O'Farrell, F.; Schultz, S. W.; Jain, A.; Rahman, M. M.; Schink, K. O.; Theodossiou, T. A.; Johansen, T.; Juhász, G.; Bilder, D.; Brech, A.; Stenmark, H.; Rusten, T. E. Microenvironmental Autophagy Promotes Tumour Growth. *Nature* **2017**, *541* (7637), 417–420. https://doi.org/10.1038/nature20815.

(320)   Nixon, S. J.; Webb, R. I.; Floetenmeyer, M.; Schieber, N.; Lo, H. P.; Parton, R. G. A Single Method for Cryofixation and Correlative Light, Electron Microscopy and

Tomography of Zebrafish Embryos. *Traffic* **2009**, *10* (2), 131–136. https://doi.org/10.1111/j.1600-0854.2008.00859.x.

(321)   Kukulski, W.; Schorb, M.; Welsch, S.; Picco, A.; Kaksonen, M.; Briggs, J. A. G. Correlated Fluorescence and 3D Electron Microscopy with High Sensitivity and Spatial Precision. *Journal of Cell Biology* **2011**, *192* (1), 111–119. https://doi.org/10.1083/jcb.201009037.

(322)   Fu, Z.; Peng, D.; Zhang, M.; Xue, F.; Zhang, R.; He, W.; Xu, T.; Xu, P. MEosEM Withstands Osmium Staining and Epon Embedding for Super-Resolution CLEM. *Nat Methods* **2020**, *17* (1), 55–58. https://doi.org/10.1038/s41592-019-0613-6.

(323)   Sims, L. B.; Curtis, L. T.; Frieboes, H. B.; Steinbach-Rankins, J. M. Enhanced Uptake and Transport of PLGA-Modified Nanoparticles in Cervical Cancer. *J Nanobiotechnol* **2016**, *14* (1), 33. https://doi.org/10.1186/s12951-016-0185-x.

(324)   Chu, C.-H.; Wang, Y.-C.; Huang, H.-Y.; Wu, L.-C.; Yang, C.-S. Ultrafine PEG-Coated Poly(Lactic- *Co* -Glycolic Acid) Nanoparticles Formulated by Hydrophobic Surfactant-Assisted One-Pot Synthesis for Biomedical Applications. *Nanotechnology* **2011**, *22* (18), 185601. https://doi.org/10.1088/0957-4484/22/18/185601.

(325)   Danhier, F.; Lecouturier, N.; Vroman, B.; Jérôme, C.; Marchand-Brynaert, J.; Feron, O.; Préat, V. Paclitaxel-Loaded PEGylated PLGA-Based Nanoparticles: In Vitro and in Vivo Evaluation. *Journal of Controlled Release* **2009**, *133* (1), 11–17. https://doi.org/10.1016/j.jconrel.2008.09.086.

(326)   Fornaguera, C.; Castells-Sala, C.; Borrós, S. Unraveling Polymeric Nanoparticles Cell Uptake Pathways: Two Decades Working to Understand Nanoparticles Journey to Improve Gene Therapy. In *Cell Biology and Translational Medicine, Volume 9*; Turksen, K., Ed.; Advances in Experimental Medicine and Biology; Springer International Publishing: Cham, 2019; Vol. 1288, pp 117–138. https://doi.org/10.1007/5584_2019_467.

(327)   Sandin, P.; Fitzpatrick, L. W.; Simpson, J. C.; Dawson, K. A. High-Speed Imaging of Rab Family Small GTPases Reveals Rare Events in Nanoparticle Trafficking in Living Cells. *ACS Nano* **2012**, *6* (2), 1513–1521. https://doi.org/10.1021/nn204448x.

(328)   Huotari, J.; Helenius, A. Endosome Maturation: Endosome Maturation. *The EMBO Journal* **2011**, *30* (17), 3481–3500. https://doi.org/10.1038/emboj.2011.286.

(329)   Zhang, J.; Chang, D.; Yang, Y.; Zhang, X.; Tao, W.; Jiang, L.; Liang, X.; Tsai, H.; Huang, L.; Mei, L. Systematic Investigation on the Intracellular Trafficking Network of Polymeric Nanoparticles. *Nanoscale* **2017**, *9* (9), 3269–3282. https://doi.org/10.1039/C7NR00532F.

(330)   Vinod Labhasetwar, J. P. Dynamics of Endocytosis and Exocytosis of Poly(D,L-Lactide-Co-Glycolide) Nanoparticles in Vascular Smooth Muscle Cells. *Pharm. Res.* **2003**, *20* (2), 212–220.

(331)   Chu, Z.; Huang, Y.; Tao, Q.; Li, Q. Cellular Uptake, Evolution, and Excretion of Silica Nanoparticles in Human Cells. *Nanoscale* **2011**, *3* (8), 3291. https://doi.org/10.1039/c1nr10499c.

(332)   Sakhtianchi, R.; Minchin, R. F.; Lee, K.-B.; Alkilany, A. M.; Serpooshan, V.; Mahmoudi, M. Exocytosis of Nanoparticles from Cells: Role in Cellular Retention and Toxicity. *Advances in Colloid and Interface Science* **2013**, *201–202*, 18–29. https://doi.org/10.1016/j.cis.2013.10.013.

(333)   Behzadi, S.; Serpooshan, V.; Tao, W.; Hamaly, M. A.; Alkawareek, M. Y.; Dreaden, E. C.; Brown, D.; Alkilany, A. M.; Farokhzad, O. C.; Mahmoudi, M. Cellular Uptake of Nanoparticles: Journey inside the Cell. *Chem. Soc. Rev.* **2017**, *46* (14), 4218–4244. https://doi.org/10.1039/C6CS00636A.

(334)   Chithrani, B. D.; Chan, W. C. W. Elucidating the Mechanism of Cellular Uptake and Removal of Protein-Coated Gold Nanoparticles of Different Sizes and Shapes. *Nano Lett.* **2007**, *7* (6), 1542–1550. https://doi.org/10.1021/nl070363y.

(335)   Sato, S.; Rancourt, A.; Sato, Y.; Satoh, M. S. Single-Cell Lineage Tracking Analysis Reveals That an Established Cell Line Comprises Putative Cancer Stem Cells and Their Heterogeneous Progeny. *Sci Rep* **2016**, *6* (1), 23328. https://doi.org/10.1038/srep23328.

(336)   Kim, J. A.; Åberg, C.; Salvati, A.; Dawson, K. A. Role of Cell Cycle on the Cellular Uptake and Dilution of Nanoparticles in a Cell Population. *Nature Nanotech* **2012**, *7* (1), 62–68. https://doi.org/10.1038/nnano.2011.191.

(337)   Lönn, P.; Kacsinta, A. D.; Cui, X.-S.; Hamil, A. S.; Kaulich, M.; Gogoi, K.; Dowdy, S. F. Enhancing Endosomal Escape for Intracellular Delivery of Macromolecular Biologic Therapeutics. *Sci Rep* **2016**, *6* (1), 32301. https://doi.org/10.1038/srep32301.

(338)   Varkouhi, A. K.; Scholte, M.; Storm, G.; Haisma, H. J. Endosomal Escape Pathways for Delivery of Biologicals. *Journal of Controlled Release* **2011**, *151* (3), 220–228. https://doi.org/10.1016/j.jconrel.2010.11.004.

(339)   Ginn, S. L.; Amaya, A. K.; Alexander, I. E.; Edelstein, M.; Abedi, M. R. Gene Therapy Clinical Trials Worldwide to 2017: An Update. *J Gene Med* **2018**, *20* (5), e3015. https://doi.org/10.1002/jgm.3015.

(340)   Pack, D. W.; Hoffman, A. S.; Pun, S.; Stayton, P. S. Design and Development of Polymers for Gene Delivery. *Nat Rev Drug Discov* **2005**, *4* (7), 581–593. https://doi.org/10.1038/nrd1775.

(341)   Lächelt, U.; Wagner, E. Nucleic Acid Therapeutics Using Polyplexes: A Journey of 50 Years (and Beyond). *Chem. Rev.* **2015**, *115* (19), 11043–11078. https://doi.org/10.1021/cr5006793.

(342)   van Asbeck, A. H.; Beyerle, A.; McNeill, H.; Bovee-Geurts, P. H. M.; Lindberg, S.; Verdurmen, W. P. R.; Hällbrink, M.; Langel, Ü.; Heidenreich, O.; Brock, R. Molecular Parameters of SiRNA–Cell Penetrating Peptide Nanocomplexes for Efficient Cellular Delivery. *ACS Nano* **2013**, *7* (5), 3797–3807. https://doi.org/10.1021/nn305754c.

(343)   Andrian, T. Nanoscopy for Endosomal Escape Quantification. **2021**, 14.

(344)   Segovia, N.; Dosta, P.; Cascante, A.; Ramos, V.; Borrós, S. Oligopeptide-Terminated Poly(β-Amino Ester)s for Highly Efficient Gene Delivery and Intracellular Localization. *Acta Biomaterialia* **2014**, *10* (5), 2147–2158. https://doi.org/10.1016/j.actbio.2013.12.054.

(345)   Lai, W.-F.; Wong, W.-T. Design of Polymeric Gene Carriers for Effective Intracellular Delivery. *Trends in Biotechnology* **2018**, *36* (7), 713–728. https://doi.org/10.1016/j.tibtech.2018.02.006.

(346)   Vaidyanathan, S.; Chen, J.; Orr, B. G.; Banaszak Holl, M. M. Cationic Polymer Intercalation into the Lipid Membrane Enables Intact Polyplex DNA Escape from Endosomes for Gene Delivery. *Mol. Pharmaceutics* **2016**, *13* (6), 1967–1978. https://doi.org/10.1021/acs.molpharmaceut.6b00139.

(347)   Funhoff, A. M.; van Nostrum, C. F.; Koning, G. A.; Schuurmans-Nieuwenbroek, N. M. E.; Crommelin, D. J. A.; Hennink, W. E. Endosomal Escape of Polymeric Gene Delivery Complexes Is Not Always Enhanced by Polymers Buffering at Low PH. 8.

(348)   Benjaminsen, R. V.; Mattebjerg, M. A.; Henriksen, J. R.; Moghimi, S. M.; Andresen, T. L. The Possible "Proton Sponge" Effect of Polyethylenimine (PEI) Does Not Include Change in Lysosomal PH. *Molecular Therapy* **2013**, *21* (1), 149–157. https://doi.org/10.1038/mt.2012.185.

(349)   Ingle, N. P.; Xue, L.; Reineke, T. M. Spatiotemporal Cellular Imaging of Polymer–PDNA Nanocomplexes Affords in Situ Morphology and Trafficking Trends. *Mol. Pharmaceutics* **2013**, *10* (11), 4120–4135. https://doi.org/10.1021/mp400115y.

(350)   Fichter, K. M.; Ingle, N. P.; McLendon, P. M.; Reineke, T. M. Polymeric Nucleic Acid Vehicles Exploit Active Interorganelle Trafficking Mechanisms. *ACS Nano* **2013**, *7* (1), 347–364. https://doi.org/10.1021/nn304218q.

(351)   Reilly, M. J.; Larsen, J. D.; Sullivan, M. O. Polyplexes Traffic through Caveolae to the Golgi and Endoplasmic Reticulum En Route to the Nucleus. *Mol. Pharmaceutics* **2012**, *9* (5), 1280–1290. https://doi.org/10.1021/mp200583d.

(352)   Rehman, Z. ur; Hoekstra, D.; Zuhorn, I. S. Mechanism of Polyplex- and Lipoplex-Mediated Delivery of Nucleic Acids: Real-Time Visualization of Transient Membrane Destabilization without Endosomal Lysis. *ACS Nano* **2013**, *7* (5), 3767–3777. https://doi.org/10.1021/nn3049494.

(353)   Desai, A. S.; Hunter, M. R.; Kapustin, A. N. Using Macropinocytosis for Intracellular Delivery of Therapeutic Nucleic Acids to Tumour Cells. *Phil. Trans. R. Soc. B* **2019**, *374* (1765), 20180156. https://doi.org/10.1098/rstb.2018.0156.

(354)   Rennick, J. J.; Johnston, A. P. R.; Parton, R. G. Key Principles and Methods for Studying the Endocytosis of Biological and Nanoparticle Therapeutics. *Nat. Nanotechnol.* **2021**, *16* (3), 266–276. https://doi.org/10.1038/s41565-021-00858-8.

(355)   Riera, R.; Tauler, J.; Feiner-Gracia, N.; Borrós, S.; Fornaguera, C.; Albertazzi, L. Complex PBAE Nanoparticle Cell Trafficking: Tracking Both Position and Composition Using Super Resolution Microscopy. *ChemMedChem* **2022**. https://doi.org/10.1002/cmdc.202100633.

(356)   Green, J. J.; Shi, J.; Chiu, E.; Leshchiner, E. S.; Langer, R.; Anderson, D. G. Biodegradable Polymeric Vectors for Gene Delivery to Human Endothelial Cells. *Bioconjugate Chem.* **2006**, *17* (5), 1162–1169. https://doi.org/10.1021/bc0600968.

(357)   Green, J. J.; Langer, R.; Anderson, D. G. A Combinatorial Polymer Library Approach Yields Insight into Nonviral Gene Delivery. *Acc. Chem. Res.* **2008**, *41* (6), 749–759. https://doi.org/10.1021/ar7002336.

(358)   Fornaguera, C.; Guerra-Rebollo, M.; Ángel Lázaro, M.; Castells-Sala, C.; Meca-Cortés, O.; Ramos-Pérez, V.; Cascante, A.; Rubio, N.; Blanco, J.; Borrós, S. MRNA Delivery System for Targeting Antigen-Presenting Cells In Vivo. *Adv. Healthcare Mater.* **2018**, *7* (17), 1800335. https://doi.org/10.1002/adhm.201800335.

(359)   Dosta, P.; Ramos, V.; Borrós, S. Stable and Efficient Generation of Poly(β-Amino Ester)s for RNAi Delivery. *Mol. Syst. Des. Eng.* **2018**, *3* (4), 677–689. https://doi.org/10.1039/C8ME00006A.

(360)   Pere Lopez Gutierrez Silvia Pujals, S. P. R. Development of an Analysis Tool for Quantification of Cellular Strctures by Single Molecule Localization Microscopy, 2020.

(361)   Tanja Bus Ulrich S. Schubert. 3rd Generation Poly(Ethylene Imine)s for Gene Delivery. *J. Mater. Chem. B 5*, 1258–1274.

(362)   Gonçalves, C.; Mennesson, E.; Fuchs, R.; Gorvel, J.-P.; Midoux, P.; Pichon, C. Macropinocytosis of Polyplexes and Recycling of Plasmid via the Clathrin-Dependent Pathway Impair the Transfection Efficiency of Human Hepatocarcinoma Cells. *Molecular Therapy* **2004**, *10* (2), 373–385. https://doi.org/10.1016/j.ymthe.2004.05.023.

(363)   Walsh, M.; Tangney, M.; O'Neill, M. J.; Larkin, J. O.; Soden, D. M.; McKenna, S. L.; Darcy, R.; O'Sullivan, G. C.; O'Driscoll, C. M. Evaluation of Cellular Uptake and Gene Transfer Efficiency of Pegylated Poly- L -Lysine Compacted DNA: Implications for Cancer Gene Therapy. *Mol. Pharmaceutics* **2006**, *3* (6), 644–653. https://doi.org/10.1021/mp0600034.

(364)   Rejman, J.; Bragonzi, A.; Conese, M. Role of Clathrin- and Caveolae-Mediated Endocytosis in Gene Transfer Mediated by Lipo- and Polyplexes. *Molecular Therapy* **2005**, *12* (3), 468–474. https://doi.org/10.1016/j.ymthe.2005.03.038.

(365)   Gabrielson, N. P.; Pack, D. W. Efficient Polyethylenimine-Mediated Gene Delivery Proceeds via a Caveolar Pathway in HeLa Cells. *Journal of Controlled Release* **2009**, *136* (1), 54–61. https://doi.org/10.1016/j.jconrel.2009.02.003.

(366)   Moore, T. L.; Rodriguez-Lorenzo, L.; Hirsch, V.; Balog, S.; Urban, D.; Jud, C.; Rothen-Rutishauser, B.; Lattuada, M.; Petri-Fink, A. Nanoparticle Colloidal Stability in Cell

Culture Media and Impact on Cellular Interactions. *Chem. Soc. Rev.* **2015**, *44* (17), 6287–6305. https://doi.org/10.1039/C4CS00487F.

(367)   Kuhn, D. A.; Vanhecke, D.; Michen, B.; Blank, F.; Gehr, P.; Petri-Fink, A.; Rothen-Rutishauser, B. Different Endocytotic Uptake Mechanisms for Nanoparticles in Epithelial Cells and Macrophages. *Beilstein J. Nanotechnol.* **2014**, *5*, 1625–1636. https://doi.org/10.3762/bjnano.5.174.

(368)   Lin, X. P.; Mintern, J. D.; Gleeson, P. A. Macropinocytosis in Different Cell Types: Similarities and Differences. *Membranes* **2020**, *10* (8), 177. https://doi.org/10.3390/membranes10080177.

(369)   Dosta, P.; Segovia, N.; Cascante, A.; Ramos, V.; Borrós, S. Surface Charge Tunability as a Powerful Strategy to Control Electrostatic Interaction for High Efficiency Silencing, Using Tailored Oligopeptide-Modified Poly(Beta-Amino Ester)s (PBAEs). *Acta Biomaterialia* **2015**, *20*, 82–93. https://doi.org/10.1016/j.actbio.2015.03.029.

(370)   Taylor, A.; Verhoef, R.; Beuwer, M.; Wang, Y.; Zijlstra, P. All-Optical Imaging of Gold Nanoparticle Geometry Using Super-Resolution Microscopy. *J. Phys. Chem. C* **2018**, *122* (4), 2336–2342. https://doi.org/10.1021/acs.jpcc.7b12473.

(371)   Post, R. A. J.; van der Zwaag, D.; Bet, G.; Wijnands, S. P. W.; Albertazzi, L.; Meijer, E. W.; van der Hofstad, R. W. A Stochastic View on Surface Inhomogeneity of Nanoparticles. *Nat Commun* **2019**, *10* (1), 1663. https://doi.org/10.1038/s41467-019-09595-y.

(372)   Dai, Q.; Wilhelm, S.; Ding, D.; Syed, A. M.; Sindhwani, S.; Zhang, Y.; Chen, Y. Y.; MacMillan, P.; Chan, W. C. W. Quantifying the Ligand-Coated Nanoparticle Delivery to Cancer Cells in Solid Tumors. *ACS Nano* **2018**, *12* (8), 8423–8435. https://doi.org/10.1021/acsnano.8b03900.

(373)   Tran, S.; DeGiovanni, P.-J.; Piel, B.; Rai, P. Cancer Nanomedicine: A Review of Recent Success in Drug Delivery. *Clin Trans Med* **2017**, *6* (1), 44. https://doi.org/10.1186/s40169-017-0175-0.

(374)   Sonawane, A. Nanoparticle Vaccines Against Infectious Diseases. *Frontiers in Immunology* **2018**, *9*, 16.

(375)   Iafisco, M.; Alogna, A.; Miragoli, M.; Catalucci, D. Cardiovascular Nanomedicine: The Route Ahead. *Nanomedicine* **2019**, *14* (18), 2391–2394. https://doi.org/10.2217/nnm-2019-0228.

(376)   Martín Giménez, V. M.; Kassuha, D. E.; Manucha, W. Nanomedicine Applied to Cardiovascular Diseases: Latest Developments. *Therapeutic Advances in Cardiovascular Disease* **2017**, *11* (4), 133–142. https://doi.org/10.1177/1753944717692293.

(377)   Smerkova, K.; Dolezelikova, K.; Bozdechova, L.; Heger, Z.; Zurek, L.; Adam, V. Nanomaterials with Active Targeting as Advanced Antimicrobials. *WIREs Nanomed Nanobiotechnol* **2020**. https://doi.org/10.1002/wnan.1636.

(378)   El-Readi, M. Z.; Althubiti, M. A. Cancer Nanomedicine: A New Era of Successful Targeted Therapy. *Journal of Nanomaterials* **2019**, *2019*, 1–13. https://doi.org/10.1155/2019/4927312.

(379)   Wang, Y.; Yang, P.; Zhao, X.; Gao, D.; Sun, N.; Tian, Z.; Ma, T.; Yang, Z. Multifunctional Cargo-Free Nanomedicine for Cancer Therapy. *IJMS* **2018**, *19* (10), 2963. https://doi.org/10.3390/ijms19102963.

(380)   Katsuki, S.; Matoba, T.; Koga, J.; Nakano, K.; Egashira, K. Anti-Inflammatory Nanomedicine for Cardiovascular Disease. *Front. Cardiovasc. Med.* **2017**, *4*, 87. https://doi.org/10.3389/fcvm.2017.00087.

(381)   Patra, J. K.; Das, G.; Fraceto, L. F.; Campos, E. V. R.; Rodriguez-Torres, M. del P.; Acosta-Torres, L. S.; Diaz-Torres, L. A.; Grillo, R.; Swamy, M. K.; Sharma, S.; Habtemariam, S.; Shin, H.-S. Nano Based Drug Delivery Systems: Recent Developments

and Future Prospects. *J Nanobiotechnol* **2018**, *16* (1), 71. https://doi.org/10.1186/s12951-018-0392-8.

(382)   Karimi, M.; Mirshekari, H.; Aliakbari, M.; Sahandi-Zangabad, P.; Hamblin, M. R. Smart Mesoporous Silica Nanoparticles for Controlled-Release Drug Delivery. *Nanotechnology Reviews* **2016**, *5* (2). https://doi.org/10.1515/ntrev-2015-0057.

(383)   Eskandari, Z.; Bahadori, F.; Celik, B.; Onyuksel, H. Targeted Nanomedicines for Cancer Therapy, From Basics to Clinical Trials. *J Pharm Pharm Sci* **2020**, *23*, 132–157. https://doi.org/10.18433/jpps30583.

(384)   Garbayo, E.; Pascual-Gil, S.; Rodríguez-Nogales, C.; Saludas, L.; Estella-Hermoso de Mendoza, A.; Blanco-Prieto, M. J. Nanomedicine and Drug Delivery Systems in Cancer and Regenerative Medicine. *WIREs Nanomed Nanobiotechnol* **2020**. https://doi.org/10.1002/wnan.1637.

(385)   Farjadian, F.; Ghasemi, A.; Gohari, O.; Roointan, A.; Karimi, M.; Hamblin, M. R. Nanopharmaceuticals and Nanomedicines Currently on the Market: Challenges and Opportunities. *Nanomedicine* **2019**, *14* (1), 93–126. https://doi.org/10.2217/nnm-2018-0120.

(386)   Sabnis, S.; Kumarasinghe, E. S.; Salerno, T.; Mihai, C.; Ketova, T.; Senn, J. J.; Lynn, A.; Bulychev, A.; McFadyen, I.; Chan, J.; Almarsson, Ö.; Stanton, M. G.; Benenato, K. E. A Novel Amino Lipid Series for MRNA Delivery: Improved Endosomal Escape and Sustained Pharmacology and Safety in Non-Human Primates. *Molecular Therapy* **2018**, *26* (6), 1509–1519. https://doi.org/10.1016/j.ymthe.2018.03.010.

(387)   Stewart, M. P.; Lorenz, A.; Dahlman, J.; Sahay, G. Challenges in Carrier-Mediated Intracellular Delivery: Moving beyond Endosomal Barriers: Challenges in Carrier-Mediated Intracellular Delivery. *WIREs Nanomed Nanobiotechnol* **2016**, *8* (3), 465–478. https://doi.org/10.1002/wnan.1377.

(388)   Ahmad, A.; Khan, J. M.; Haque, S. Strategies in the Design of Endosomolytic Agents for Facilitating Endosomal Escape in Nanoparticles. *Biochimie* **2019**, *160*, 61–75. https://doi.org/10.1016/j.biochi.2019.02.012.

(389)   Pei, D.; Buyanova, M. Overcoming Endosomal Entrapment in Drug Delivery. *Bioconjugate Chem.* **2019**, *30* (2), 273–283. https://doi.org/10.1021/acs.bioconjchem.8b00778.

(390)   Shete, H. K.; Prabhu, R. H.; Patravale, V. B. Endosomal Escape: A Bottleneck in Intracellular Delivery. *j. nanosci. nanotech.* **2014**, *14* (1), 460–474. https://doi.org/10.1166/jnn.2014.9082.

(391)   Gilleron, J.; Querbes, W.; Zeigerer, A.; Borodovsky, A.; Marsico, G.; Schubert, U.; Manygoats, K.; Seifert, S.; Andree, C.; Stöter, M.; Epstein-Barash, H.; Zhang, L.; Koteliansky, V.; Fitzgerald, K.; Fava, E.; Bickle, M.; Kalaidzidis, Y.; Akinc, A.; Maier, M.; Zerial, M. Image-Based Analysis of Lipid Nanoparticle–Mediated SiRNA Delivery, Intracellular Trafficking and Endosomal Escape. *Nat Biotechnol* **2013**, *31* (7), 638–646. https://doi.org/10.1038/nbt.2612.

(392)   Cheng, X.; Lee, R. J. The Role of Helper Lipids in Lipid Nanoparticles (LNPs) Designed for Oligonucleotide Delivery. *Advanced Drug Delivery Reviews* **2016**, *99*, 129–137. https://doi.org/10.1016/j.addr.2016.01.022.

(393)   Tai, W.; Gao, X. Functional Peptides for SiRNA Delivery. *Advanced Drug Delivery Reviews* **2017**, *110–111*, 157–168. https://doi.org/10.1016/j.addr.2016.08.004.

(394)   Wang, H.; Tam, Y. Y. C.; Chen, S.; Zaifman, J.; van der Meel, R.; Ciufolini, M. A.; Cullis, P. R. The Niemann-Pick C1 Inhibitor NP3.47 Enhances Gene Silencing Potency of Lipid Nanoparticles Containing SiRNA. *Molecular Therapy* **2016**, *24* (12), 2100–2108. https://doi.org/10.1038/mt.2016.179.

(395)   Ben Djemaa, S.; David, S.; Hervé-Aubert, K.; Falanga, A.; Galdiero, S.; Allard-Vannier, E.; Chourpa, I.; Munnier, E. Formulation and in Vitro Evaluation of a SiRNA Delivery Nanosystem Decorated with GH625 Peptide for Triple Negative Breast Cancer

Theranosis. *European Journal of Pharmaceutics and Biopharmaceutics* **2018**, *131*, 99–108. https://doi.org/10.1016/j.ejpb.2018.07.024.

(396)   dos Santos Rodrigues, B.; Banerjee, A.; Kanekiyo, T.; Singh, J. Functionalized Liposomal Nanoparticles for Efficient Gene Delivery System to Neuronal Cell Transfection. *International Journal of Pharmaceutics* **2019**, *566*, 717–730. https://doi.org/10.1016/j.ijpharm.2019.06.026.

(397)   Shae, D.; Becker, K. W.; Christov, P.; Yun, D. S.; Lytton-Jean, A. K. R.; Sevimli, S.; Ascano, M.; Kelley, M.; Johnson, D. B.; Balko, J. M.; Wilson, J. T. Endosomolytic Polymersomes Increase the Activity of Cyclic Dinucleotide STING Agonists to Enhance Cancer Immunotherapy. *Nat. Nanotechnol.* **2019**, *14* (3), 269–278. https://doi.org/10.1038/s41565-018-0342-5.

(398)   Pang, Y. T.; Ge, Z.; Zhang, B.; Xiu, P.; Li, Q.; Wang, Y. Pore Formation Induced by Nanoparticles Binding to a Lipid Membrane. *Nanoscale* **2020**, *12* (14), 7902–7913. https://doi.org/10.1039/C9NR10534D.

(399)   Ohtsuki, T.; Miki, S.; Kobayashi, S.; Haraguchi, T.; Nakata, E.; Hirakawa, K.; Sumita, K.; Watanabe, K.; Okazaki, S. The Molecular Mechanism of Photochemical Internalization of Cell Penetrating Peptide-Cargo-Photosensitizer Conjugates. *Sci Rep* **2016**, *5* (1), 18577. https://doi.org/10.1038/srep18577.

(400)   Martínez-Jothar, L.; Beztsinna, N.; van Nostrum, C. F.; Hennink, W. E.; Oliveira, S. Selective Cytotoxicity to HER2 Positive Breast Cancer Cells by Saporin-Loaded Nanobody-Targeted Polymeric Nanoparticles in Combination with Photochemical Internalization. *Mol. Pharmaceutics* **2019**, *16* (4), 1633–1647. https://doi.org/10.1021/acs.molpharmaceut.8b01318.

(401)   Rehman, Z. ur; Hoekstra, D.; Zuhorn, I. S. Mechanism of Polyplex- and Lipoplex-Mediated Delivery of Nucleic Acids: Real-Time Visualization of Transient Membrane Destabilization without Endosomal Lysis. *ACS Nano* **2013**, *7* (5), 3767–3777. https://doi.org/10.1021/nn3049494.

(402)   Ngwa, V. M.; Axford, D. S.; Healey, A. N.; Nowak, S. J.; Chrestensen, C. A.; McMurry, J. L. A Versatile Cell-Penetrating Peptide-Adaptor System for Efficient Delivery of Molecular Cargos to Subcellular Destinations. *PLoS ONE* **2017**, *12* (5), e0178648. https://doi.org/10.1371/journal.pone.0178648.

(403)   White, J. M.; Whittaker, G. R. Fusion of Enveloped Viruses in Endosomes: Virus Fusion in Endosomes. *Traffic* **2016**, *17* (6), 593–614. https://doi.org/10.1111/tra.12389.

(404)   Wang, C.; Wang, Y.; Li, Y.; Bodemann, B.; Zhao, T.; Ma, X.; Huang, G.; Hu, Z.; DeBerardinis, R. J.; White, M. A.; Gao, J. A Nanobuffer Reporter Library for Fine-Scale Imaging and Perturbation of Endocytic Organelles. *Nat Commun* **2015**, *6* (1), 8524. https://doi.org/10.1038/ncomms9524.

(405)   Vermeulen, L. M. P.; De Smedt, S. C.; Remaut, K.; Braeckmans, K. The Proton Sponge Hypothesis: Fable or Fact? *European Journal of Pharmaceutics and Biopharmaceutics* **2018**, *129*, 184–190. https://doi.org/10.1016/j.ejpb.2018.05.034.

(406)   Elsaesser, A.; Barnes, C. A.; McKerr, G.; Salvati, A.; Lynch, I.; Dawson, K. A.; Howard, C. V. Quantification of Nanoparticle Uptake by Cells Using an Unbiased Sampling Method and Electron Microscopy. *Nanomedicine* **2011**, *6* (7), 1189–1198. https://doi.org/10.2217/nnm.11.70.

(407)   Erni, R.; Rossell, M. D.; Kisielowski, C.; Dahmen, U. Atomic-Resolution Imaging with a Sub-50-Pm Electron Probe. *Phys. Rev. Lett.* **2009**, *102* (9), 096101. https://doi.org/10.1103/PhysRevLett.102.096101.

(408)   Guglielmi, V.; Carton, F.; Vattemi, G.; Arpicco, S.; Stella, B.; Berlier, G.; Marengo, A.; Boschi, F.; Malatesta, M. Uptake and Intracellular Distribution of Different Types of Nanoparticles in Primary Human Myoblasts and Myotubes. *International Journal of Pharmaceutics* **2019**, *560*, 347–356. https://doi.org/10.1016/j.ijpharm.2019.02.017.

(409)	Chu, Z.; Miu, K.; Lung, P.; Zhang, S.; Zhao, S.; Chang, H.-C.; Lin, G.; Li, Q. Rapid Endosomal Escape of Prickly Nanodiamonds: Implications for Gene Delivery. *Sci Rep* **2015**, *5* (1), 11661. https://doi.org/10.1038/srep11661.

(410)	Cabezón, I.; Manich, G.; Martín-Venegas, R.; Camins, A.; Pelegrí, C.; Vilaplana, J. Trafficking of Gold Nanoparticles Coated with the 8D3 Anti-Transferrin Receptor Antibody at the Mouse Blood–Brain Barrier. *Mol. Pharmaceutics* **2015**, *12* (11), 4137–4145. https://doi.org/10.1021/acs.molpharmaceut.5b00597.

(411)	Iacovita, C.; Florea, A.; Dudric, R.; Pall, E.; Moldovan, A.; Tetean, R.; Stiufiuc, R.; Lucaciu, C. Small versus Large Iron Oxide Magnetic Nanoparticles: Hyperthermia and Cell Uptake Properties. *Molecules* **2016**, *21* (10), 1357. https://doi.org/10.3390/molecules21101357.

(412)	Feng, N.; Liu, Y.; He, M.; Niu, M.; Zhao, Y.; Zhu, Y.; Li, Z. Delivery of Vincristine Sulfate-Conjugated Gold Nanoparticles Using Liposomes: A Light-Responsive Nanocarrier with Enhanced Antitumor Efficiency. *IJN* **2015**, 3081. https://doi.org/10.2147/IJN.S79550.

(413)	Kilchrist, K. V.; Evans, B. C.; Brophy, C. M.; Duvall, C. L. Mechanism of Enhanced Cellular Uptake and Cytosolic Retention of MK2 Inhibitory Peptide Nano-Polyplexes. *Cel. Mol. Bioeng.* **2016**, *9* (3), 368–381. https://doi.org/10.1007/s12195-016-0446-7.

(414)	Fraire, J. C.; Houthaeve, G.; Liu, J.; Raes, L.; Vermeulen, L.; Stremersch, S.; Brans, T.; García-Díaz Barriga, G.; De Keulenaer, S.; Van Nieuwerburgh, F.; De Rycke, R.; Vandesompele, J.; Mestdagh, P.; Raemdonck, K.; De Vos, W. H.; De Smedt, S.; Braeckmans, K. Vapor Nanobubble Is the More Reliable Photothermal Mechanism for Inducing Endosomal Escape of SiRNA without Disturbing Cell Homeostasis. *Journal of Controlled Release* **2020**, *319*, 262–275. https://doi.org/10.1016/j.jconrel.2019.12.050.

(415)	Patel, S.; Ashwanikumar, N.; Robinson, E.; Xia, Y.; Mihai, C.; Griffith, J. P.; Hou, S.; Esposito, A. A.; Ketova, T.; Welsher, K.; Joyal, J. L.; Almarsson, Ö.; Sahay, G. Naturally-Occurring Cholesterol Analogues in Lipid Nanoparticles Induce Polymorphic Shape and Enhance Intracellular Delivery of MRNA. *Nat Commun* **2020**, *11* (1), 983. https://doi.org/10.1038/s41467-020-14527-2.

(416)	Azubel, M.; Carter, S. D.; Weiszmann, J.; Zhang, J.; Jensen, G. J.; Li, Y.; Kornberg, R. D. FGF21 Trafficking in Intact Human Cells Revealed by Cryo-Electron Tomography with Gold Nanoparticles. *eLife* **2019**, *8*, e43146. https://doi.org/10.7554/eLife.43146.

(417)	Saarinen, J.; Gütter, F.; Lindman, M.; Agopov, M.; Fraser-Miller, S. J.; Scherließ, R.; Jokitalo, E.; Santos, H. A.; Peltonen, L.; Isomäki, A.; Strachan, C. J. Cell-Nanoparticle Interactions at (Sub)–Nanometer Resolution Analyzed by Electron Microscopy and Correlative Coherent Anti-Stokes Raman Scattering. *Biotechnol. J.* **2019**, *14* (4), 1800413. https://doi.org/10.1002/biot.201800413.

(418)	Cristofolini, T.; Dalmina, M.; Sierra, J. A.; Silva, A. H.; Pasa, A. A.; Pittella, F.; Creczynski-Pasa, T. B. Multifunctional Hybrid Nanoparticles as Magnetic Delivery Systems for SiRNA Targeting the HER2 Gene in Breast Cancer Cells. *Materials Science and Engineering: C* **2020**, *109*, 110555. https://doi.org/10.1016/j.msec.2019.110555.

(419)	Deshayes, S.; Konate, K.; Dussot, M.; Chavey, B.; Vaissière, A.; Van, T. N. N.; Aldrian, G.; Padari, K.; Pooga, M.; Vivès, E.; Boisguérin, P. Deciphering the Internalization Mechanism of WRAP:SiRNA Nanoparticles. *Biochimica et Biophysica Acta (BBA) - Biomembranes* **2020**, *1862* (6), 183252. https://doi.org/10.1016/j.bbamem.2020.183252.

(420)	Han, S.; Raabe, M.; Hodgson, L.; Mantell, J.; Verkade, P.; Lasser, T.; Landfester, K.; Weil, T.; Lieberwirth, I. High-Contrast Imaging of Nanodiamonds in Cells by Energy Filtered and Correlative Light-Electron Microscopy: Toward a Quantitative Nanoparticle-Cell Analysis. *Nano Lett.* **2019**, *19* (3), 2178–2185. https://doi.org/10.1021/acs.nanolett.9b00752.

(421)	Grecchi, S.; Malatesta, M. Visualizing Endocytotic Pathways at Transmission Electron Microscopy via Diaminobenzidine Photo-Oxidation by a Fluorescent Cell-Membrane Dye. *Eur J Histochem* **2014**, *58* (4). https://doi.org/10.4081/ejh.2014.2449.

(422)   Pellicciari, C.; Biggiogera, M.; Malatesta, M. DAB Photo-Oxidation as a Tool for Detecting Low Amounts of Free and Membrane-Bounded Fluorescent Molecules at Transmission Electron Microscopy. **2015**, 9.

(423)   Ben Djemaa, S.; Hervé-Aubert, K.; Lajoie, L.; Falanga, A.; Galdiero, S.; Nedellec, S.; Soucé, M.; Munnier, E.; Chourpa, I.; David, S.; Allard-Vannier, E. GH625 Cell-Penetrating Peptide Promotes the Endosomal Escape of Nanovectorized SiRNA in a Triple-Negative Breast Cancer Cell Line. *Biomacromolecules* **2019**, *20* (8), 3076–3086. https://doi.org/10.1021/acs.biomac.9b00637.

(424)   Stewart, P. L. Cryo-Electron Microscopy and Cryo-Electron Tomography of Nanoparticles: Cryo-Electron Microscopy and Cryo-Electron Tomography of Nanoparticles. *WIREs Nanomed Nanobiotechnol* **2017**, *9* (2), e1417. https://doi.org/10.1002/wnan.1417.

(425)   Cheng, Y. Single-Particle Cryo-EM at Crystallographic Resolution. *Cell* **2015**, *161* (3), 450–457. https://doi.org/10.1016/j.cell.2015.03.049.

(426)   Remaut, K.; Oorschot, V.; Braeckmans, K.; Klumperman, J.; De Smedt, S. C. Lysosomal Capturing of Cytoplasmic Injected Nanoparticles by Autophagy: An Additional Barrier to Non Viral Gene Delivery. *Journal of Controlled Release* **2014**, *195*, 29–36. https://doi.org/10.1016/j.jconrel.2014.08.002.

(427)   *Basic Confocal Microscopy*; Jerome, W. G., Price, R. L., Eds.; Springer International Publishing: Cham, 2018. https://doi.org/10.1007/978-3-319-97454-5.

(428)   Abbe, E. Beiträge zur Theorie des Mikroskops und der mikroskopischen Wahrnehmung. *Archiv f. mikrosk. Anatomie* **1873**, *9* (1), 413–468. https://doi.org/10.1007/BF02956173.

(429)   *The Nobel Prize in Chemistry 2014*. NobelPrize.org. https://www.nobelprize.org/prizes/chemistry/2014/advanced-information/ (accessed 2020-05-31).

(430)   Bretschneider, S.; Eggeling, C.; Hell, S. W. Breaking the Diffraction Barrier in Fluorescence Microscopy by Optical Shelving. *Phys. Rev. Lett.* **2007**, *98* (21), 218103. https://doi.org/10.1103/PhysRevLett.98.218103.

(431)   Betzig, E.; Patterson, G. H.; Sougrat, R.; Lindwasser, O. W.; Olenych, S.; Bonifacino, J. S.; Davidson, M. W.; Lippincott-Schwartz, J.; Hess, H. F. Imaging Intracellular Fluorescent Proteins at Nanometer Resolution. *Science* **2006**, *313* (5793), 1642–1645. https://doi.org/10.1126/science.1127344.

(432)   Rust, M. J.; Bates, M.; Zhuang, X. Sub-Diffraction-Limit Imaging by Stochastic Optical Reconstruction Microscopy (STORM). *Nature Methods* **2006**, *3* (10), 793–796. https://doi.org/10.1038/nmeth929.

(433)   Hess, S. T.; Girirajan, T. P. K.; Mason, M. D. Ultra-High Resolution Imaging by Fluorescence Photoactivation Localization Microscopy. *Biophysical Journal* **2006**, *91* (11), 4258–4272. https://doi.org/10.1529/biophysj.106.091116.

(434)   Heilemann, M.; van de Linde, S.; Schüttpelz, M.; Kasper, R.; Seefeldt, B.; Mukherjee, A.; Tinnefeld, P.; Sauer, M. Subdiffraction-Resolution Fluorescence Imaging with Conventional Fluorescent Probes. *Angewandte Chemie International Edition* **2008**, *47* (33), 6172–6176. https://doi.org/10.1002/anie.200802376.

(435)   Giannone, G.; Hosy, E.; Levet, F.; Constals, A.; Schulze, K.; Sobolevsky, A. I.; Rosconi, M. P.; Gouaux, E.; Tampé, R.; Choquet, D.; Cognet, L. Dynamic Superresolution Imaging of Endogenous Proteins on Living Cells at Ultra-High Density. *Biophysical Journal* **2010**, *99* (4), 1303–1310. https://doi.org/10.1016/j.bpj.2010.06.005.

(436)   Jungmann, R.; Avendaño, M. S.; Woehrstein, J. B.; Dai, M.; Shih, W. M.; Yin, P. Multiplexed 3D Cellular Super-Resolution Imaging with DNA-PAINT and Exchange-PAINT. *Nature Methods* **2014**, *11* (3), 313–318. https://doi.org/10.1038/nmeth.2835.

(437)   Lew, M. D.; Lee, S. F.; Ptacin, J. L.; Lee, M. K.; Twieg, R. J.; Shapiro, L.; Moerner, W. E. Three-Dimensional Superresolution Colocalization of Intracellular Protein

Superstructures and the Cell Surface in Live Caulobacter Crescentus. *PNAS* **2011**, *108* (46), E1102–E1110. https://doi.org/10.1073/pnas.1114444108.

(438)   Nicovich, P. R.; Owen, D. M.; Gaus, K. Turning Single-Molecule Localization Microscopy into a Quantitative Bioanalytical Tool. *Nature Protocols* **2017**, *12* (3), 453–460. https://doi.org/10.1038/nprot.2016.166.

(439)   S. Agasti, S.; Wang, Y.; Schueder, F.; Sukumar, A.; Jungmann, R.; Yin, P. DNA-Barcoded Labeling Probes for Highly Multiplexed Exchange-PAINT Imaging. *Chemical Science* **2017**, *8* (4), 3080–3091. https://doi.org/10.1039/C6SC05420J.

(440)   Wade, O. K.; Woehrstein, J. B.; Nickels, P. C.; Strauss, S.; Stehr, F.; Stein, J.; Schueder, F.; Strauss, M. T.; Ganji, M.; Schnitzbauer, J.; Grabmayr, H.; Yin, P.; Schwille, P.; Jungmann, R. 124-Color Super-Resolution Imaging by Engineering DNA-PAINT Blinking Kinetics. *Nano Lett* **2019**, *19* (4), 2641–2646. https://doi.org/10.1021/acs.nanolett.9b00508.

(441)   Wojnilowicz, M.; Glab, A.; Bertucci, A.; Caruso, F.; Cavalieri, F. Super-Resolution Imaging of Proton Sponge-Triggered Rupture of Endosomes and Cytosolic Release of Small Interfering RNA. *ACS Nano* **2019**, *13* (1), 187–202. https://doi.org/10.1021/acsnano.8b05151.

(442)   van der Zwaag, D.; Vanparijs, N.; Wijnands, S.; De Rycke, R.; De Geest, B. G.; Albertazzi, L. Super Resolution Imaging of Nanoparticles Cellular Uptake and Trafficking. *ACS Appl. Mater. Interfaces* **2016**, *8* (10), 6391–6399. https://doi.org/10.1021/acsami.6b00811.

(443)   Feiner-Gracia, N.; Olea, R. A.; Fitzner, R.; El Boujnouni, N.; van Asbeck, A. H.; Brock, R.; Albertazzi, L. Super-Resolution Imaging of Structure, Molecular Composition, and Stability of Single Oligonucleotide Polyplexes. *Nano Lett.* **2019**, *19* (5), 2784–2792. https://doi.org/10.1021/acs.nanolett.8b04407.

(444)   Riera, R.; Feiner-Gracia, N.; Fornaguera, C.; Cascante, A.; Borrós, S.; Albertazzi, L. Tracking the DNA Complexation State of PBAE Polyplexes in Cells with Super Resolution Microscopy. *Nanoscale* **2019**, *11* (38), 17869–17877. https://doi.org/10.1039/C9NR02858G.

(445)   Kiuchi, T.; Higuchi, M.; Takamura, A.; Maruoka, M.; Watanabe, N. Multitarget Super-Resolution Microscopy with High-Density Labeling by Exchangeable Probes. *Nat. Methods* **2015**, *12* (8), 743–746. https://doi.org/10.1038/nmeth.3466.

(446)   Hell, S. W.; Wichmann, J. Breaking the Diffraction Resolution Limit by Stimulated Emission: Stimulated-Emission-Depletion Fluorescence Microscopy. *Opt. Lett., OL* **1994**, *19* (11), 780–782. https://doi.org/10.1364/OL.19.000780.

(447)   Klar, T. A.; Jakobs, S.; Dyba, M.; Egner, A.; Hell, S. W. Fluorescence Microscopy with Diffraction Resolution Barrier Broken by Stimulated Emission. *Proceedings of the National Academy of Sciences* **2000**, *97* (15), 8206–8210. https://doi.org/10.1073/pnas.97.15.8206.

(448)   Foresti, R.; Rossi, S.; Pinelli, S.; Alinovi, R.; Sciancalepore, C.; Delmonte, N.; Selleri, S.; Caffarra, C.; Raposio, E.; Macaluso, G.; Macaluso, C.; Freyrie, A.; Miragoli, M.; Perini, P. In-Vivo Vascular Application via Ultra-Fast Bioprinting for Future 5D Personalised Nanomedicine. *Scientific Reports* **2020**, *10* (1), 3205. https://doi.org/10.1038/s41598-020-60196-y.

(449)   May, J.-N.; Golombek, S. K.; Baues, M.; Dasgupta, A.; Drude, N.; Rix, A.; Rommel, D.; von Stillfried, S.; Appold, L.; Pola, R.; Pechar, M.; van Bloois, L.; Storm, G.; Kuehne, A. J. C.; Gremse, F.; Theek, B.; Kiessling, F.; Lammers, T. Multimodal and Multiscale Optical Imaging of Nanomedicine Delivery across the Blood-Brain Barrier upon Sonopermeation. *Theranostics* **2020**, *10* (4), 1948–1959. https://doi.org/10.7150/thno.41161.

(450)   Wäldchen, S.; Lehmann, J.; Klein, T.; van de Linde, S.; Sauer, M. Light-Induced Cell Damage in Live-Cell Super-Resolution Microscopy. *Scientific Reports* **2015**, *5* (1), 15348. https://doi.org/10.1038/srep15348.

(451) Kilian, N.; Goryaynov, A.; Lessard, M. D.; Hooker, G.; Toomre, D.; Rothman, J. E.; Bewersdorf, J. Assessing Photodamage in Live-Cell STED Microscopy. *Nature Methods* **2018**, *15* (10), 755–756. https://doi.org/10.1038/s41592-018-0145-5.

(452) Peuschel, H.; Ruckelshausen, T.; Cavelius, C.; Kraegeloh, A. *Quantification of Internalized Silica Nanoparticles via STED Microscopy*. BioMed Research International. https://www.hindawi.com/journals/bmri/2015/961208/ (accessed 2020-05-17). https://doi.org/10.1155/2015/961208.

(453) Hanne, J.; Falk, H. J.; Görlitz, F.; Hoyer, P.; Engelhardt, J.; Sahl, S. J.; Hell, S. W. STED Nanoscopy with Fluorescent Quantum Dots. *Nature Communications* **2015**, *6* (1), 7127. https://doi.org/10.1038/ncomms8127.

(454) Shang, L.; Gao, P.; Wang, H.; Popescu, R.; Gerthsen, D.; Nienhaus, G. U. Protein-Based Fluorescent Nanoparticles for Super-Resolution STED Imaging of Live Cells. *Chem. Sci.* **2017**, *8* (3), 2396–2400. https://doi.org/10.1039/C6SC04664A.

(455) Gustafsson, M. G. L. Surpassing the Lateral Resolution Limit by a Factor of Two Using Structured Illumination Microscopy. *Journal of Microscopy* **2000**, *198* (2), 82–87. https://doi.org/10.1046/j.1365-2818.2000.00710.x.

(456) Chen, X.; Cui, J.; Ping, Y.; Suma, T.; Cavalieri, F.; Besford, Q. A.; Chen, G.; Braunger, J. A.; Caruso, F. Probing Cell Internalisation Mechanics with Polymer Capsules. *Nanoscale* **2016**, *8* (39), 17096–17101. https://doi.org/10.1039/C6NR06657G.

(457) Teplensky, M. H.; Fantham, M.; Li, P.; Wang, T. C.; Mehta, J. P.; Young, L. J.; Moghadam, P. Z.; Hupp, J. T.; Farha, O. K.; Kaminski, C. F.; Fairen-Jimenez, D. Temperature Treatment of Highly Porous Zirconium-Containing Metal–Organic Frameworks Extends Drug Delivery Release. *J. Am. Chem. Soc.* **2017**, *139* (22), 7522–7532. https://doi.org/10.1021/jacs.7b01451.

(458) Chen, X.; Cui, J.; Sun, H.; Müllner, M.; Yan, Y.; Fung Noi, K.; Ping, Y.; Caruso, F. Analysing Intracellular Deformation of Polymer Capsules Using Structured Illumination Microscopy. *Nanoscale* **2016**, *8* (23), 11924–11931. https://doi.org/10.1039/C6NR02151D.

(459) Tolstik, E.; Osminkina, L. A.; Matthäus, C.; Burkhardt, M.; Tsurikov, K. E.; Natashina, U. A.; Timoshenko, V. Y.; Heintzmann, R.; Popp, J.; Sivakov, V. Studies of Silicon Nanoparticles Uptake and Biodegradation in Cancer Cells by Raman Spectroscopy. *Nanomedicine: Nanotechnology, Biology and Medicine* **2016**, *12* (7), 1931–1940. https://doi.org/10.1016/j.nano.2016.04.004.

(460) Li, D.; Shao, L.; Chen, B.-C.; Zhang, X.; Zhang, M.; Moses, B.; Milkie, D. E.; Beach, J. R.; Hammer, J. A.; Pasham, M.; Kirchhausen, T.; Baird, M. A.; Davidson, M. W.; Xu, P.; Betzig, E. Extended-Resolution Structured Illumination Imaging of Endocytic and Cytoskeletal Dynamics. *Science* **2015**, *349* (6251). https://doi.org/10.1126/science.aab3500.

(461) Guo, Y.; Li, D.; Zhang, S.; Yang, Y.; Liu, J.-J.; Wang, X.; Liu, C.; Milkie, D. E.; Moore, R. P.; Tulu, U. S.; Kiehart, D. P.; Hu, J.; Lippincott-Schwartz, J.; Betzig, E.; Li, D. Visualizing Intracellular Organelle and Cytoskeletal Interactions at Nanoscale Resolution on Millisecond Timescales. *Cell* **2018**, *175* (5), 1430-1442.e17. https://doi.org/10.1016/j.cell.2018.09.057.

(462) Bus, T.; Englert, C.; Reifarth, M.; Borchers, P.; Hartlieb, M.; Vollrath, A.; Hoeppener, S.; Traeger, A.; S. Schubert, U. 3rd Generation Poly(Ethylene Imine)s for Gene Delivery. *Journal of Materials Chemistry B* **2017**, *5* (6), 1258–1274. https://doi.org/10.1039/C6TB02592G.

(463) Huff, J. The Airyscan Detector from ZEISS: Confocal Imaging with Improved Signal-to-Noise Ratio and Super-Resolution. *Nature Methods* **2015**, *12* (12), i–ii. https://doi.org/10.1038/nmeth.f.388.

(464)   Hofmann, M.; Eggeling, C.; Jakobs, S.; Hell, S. W. Breaking the Diffraction Barrier in Fluorescence Microscopy at Low Light Intensities by Using Reversibly Photoswitchable Proteins. *PNAS* **2005**, *102* (49), 17565–17569. https://doi.org/10.1073/pnas.0506010102.

(465)   Balzarotti, F.; Eilers, Y.; Gwosch, K. C.; Gynnå, A. H.; Westphal, V.; Stefani, F. D.; Elf, J.; Hell, S. W. Nanometer Resolution Imaging and Tracking of Fluorescent Molecules with Minimal Photon Fluxes. *Science* **2017**, *355* (6325), 606–612. https://doi.org/10.1126/science.aak9913.

(466)   Gwosch, K. C.; Pape, J. K.; Balzarotti, F.; Hoess, P.; Ellenberg, J.; Ries, J.; Hell, S. W. MINFLUX Nanoscopy Delivers 3D Multicolor Nanometer Resolution in Cells. *Nature Methods* **2020**, *17* (2), 217–224. https://doi.org/10.1038/s41592-019-0688-0.

(467)   Wang, Z.; Luo, M.; Mao, C.; Wei, Q.; Zhao, T.; Li, Y.; Huang, G.; Gao, J. A Redox-Activatable Fluorescent Sensor for the High-Throughput Quantification of Cytosolic Delivery of Macromolecules. *Angewandte Chemie* **2017**, *129* (5), 1339–1343. https://doi.org/10.1002/ange.201610302.

(468)   Guo, X.; Wang, L.; Duval, K.; Fan, J.; Zhou, S.; Chen, Z. Dimeric Drug Polymeric Micelles with Acid-Active Tumor Targeting and FRET-Traceable Drug Release. *Advanced Materials* **2018**, *30* (3), 1705436. https://doi.org/10.1002/adma.201705436.

(469)   Rayamajhi, S.; Marchitto, J.; Nguyen, T. D. T.; Marasini, R.; Celia, C.; Aryal, S. PH-Responsive Cationic Liposome for Endosomal Escape Mediated Drug Delivery. *Colloids and Surfaces B: Biointerfaces* **2020**, *188*, 110804. https://doi.org/10.1016/j.colsurfb.2020.110804.

(470)   Lanzanò, L.; Scipioni, L.; Di Bona, M.; Bianchini, P.; Bizzarri, R.; Cardarelli, F.; Diaspro, A.; Vicidomini, G. Measurement of Nanoscale Three-Dimensional Diffusion in the Interior of Living Cells by STED-FCS. *Nature Communications* **2017**, *8* (1), 65. https://doi.org/10.1038/s41467-017-00117-2.

(471)   Sezgin, E.; Schneider, F.; Galiani, S.; Urbančič, I.; Waithe, D.; Lagerholm, B. C.; Eggeling, C. Measuring Nanoscale Diffusion Dynamics in Cellular Membranes with Super-Resolution STED–FCS. *Nature Protocols* **2019**, *14* (4), 1054–1083. https://doi.org/10.1038/s41596-019-0127-9.

(472)   Shin, K.; Song, Y.; Goh, Y.; Lee, K. Two-Dimensional and Three-Dimensional Single Particle Tracking of Upconverting Nanoparticles in Living Cells. *IJMS* **2019**, *20* (6), 1424. https://doi.org/10.3390/ijms20061424.

(473)   Jin, D.; Xi, P.; Wang, B.; Zhang, L.; Enderlein, J.; van Oijen, A. M. Nanoparticles for Super-Resolution Microscopy and Single-Molecule Tracking. *Nat Methods* **2018**, *15* (6), 415–423. https://doi.org/10.1038/s41592-018-0012-4.

(474)   Gabriel, M.; Moya-Díaz, J.; Gallo, L. I.; Marengo, F. D.; Estrada, L. C. Single Particle Tracking of Internalized Metallic Nanoparticles Reveals Heterogeneous Directed Motion after Clathrin Dependent Endocytosis in Mouse Chromaffin Cells. *Methods Appl. Fluoresc.* **2017**, *6* (1), 014003. https://doi.org/10.1088/2050-6120/aa8c64.

(475)   Hou, S.; Lang, X.; Welsher, K. Robust Real-Time 3D Single-Particle Tracking Using a Dynamically Moving Laser Spot. *Opt. Lett.* **2017**, *42* (12), 2390. https://doi.org/10.1364/OL.42.002390.

(476)   Zagato, E.; Forier, K.; Martens, T.; Neyts, K.; Demeester, J.; Smedt, S. D.; Remaut, K.; Braeckmans, K. Single-Particle Tracking for Studying Nanomaterial Dynamics: Applications and Fundamentals in Drug Delivery. *Nanomedicine* **2014**, *9* (6), 913–927. https://doi.org/10.2217/nnm.14.43.

(477)   Zahid, M. U.; Ma, L.; Lim, S. J.; Smith, A. M. Single Quantum Dot Tracking Reveals the Impact of Nanoparticle Surface on Intracellular State. *Nat Commun* **2018**, *9* (1), 1830. https://doi.org/10.1038/s41467-018-04185-w.

(478)   Liu, M.; Li, Q.; Liang, L.; Li, J.; Wang, K.; Li, J.; Lv, M.; Chen, N.; Song, H.; Lee, J.; Shi, J.; Wang, L.; Lal, R.; Fan, C. Real-Time Visualization of Clustering and Intracellular

Transport of Gold Nanoparticles by Correlative Imaging. *Nat Commun* **2017**, *8* (1), 15646. https://doi.org/10.1038/ncomms15646.

(479)   Li, Q.; Li, W.; Yin, W.; Guo, J.; Zhang, Z.-P.; Zeng, D.; Zhang, X.; Wu, Y.; Zhang, X.-E.; Cui, Z. Single-Particle Tracking of Human Immunodeficiency Virus Type 1 Productive Entry into Human Primary Macrophages. *ACS Nano* **2017**, *11* (4), 3890–3903. https://doi.org/10.1021/acsnano.7b00275.

(480)   Bhatia, D.; Arumugam, S.; Nasilowski, M.; Joshi, H.; Wunder, C.; Chambon, V.; Prakash, V.; Grazon, C.; Nadal, B.; Maiti, P. K.; Johannes, L.; Dubertret, B.; Krishnan, Y. Quantum Dot-Loaded Monofunctionalized DNA Icosahedra for Single-Particle Tracking of Endocytic Pathways. *Nature Nanotech* **2016**, *11* (12), 1112–1119. https://doi.org/10.1038/nnano.2016.150.

(481)   Tiffany, M.; Szoka, F. C. Co-Localization of Fluorescent Labeled Lipid Nanoparticles with Specifically Tagged Subcellular Compartments by Single Particle Tracking at Low Nanoparticle to Cell Ratios. *Journal of Drug Targeting* **2016**, *24* (9), 857–864. https://doi.org/10.1080/1061186X.2016.1233976.

(482)   Deville, S.; Penjweini, R.; Smisdom, N.; Notelaers, K.; Nelissen, I.; Hooyberghs, J.; Ameloot, M. Intracellular Dynamics and Fate of Polystyrene Nanoparticles in A549 Lung Epithelial Cells Monitored by Image (Cross-) Correlation Spectroscopy and Single Particle Tracking. *Biochimica et Biophysica Acta (BBA) - Molecular Cell Research* **2015**, *1853* (10), 2411–2419. https://doi.org/10.1016/j.bbamcr.2015.07.004.

(483)   Deschout, H.; Martens, T.; Vercauteren, D.; Remaut, K.; Demeester, J.; De Smedt, S.; Neyts, K.; Braeckmans, K. Correlation of Dual Colour Single Particle Trajectories for Improved Detection and Analysis of Interactions in Living Cells. *IJMS* **2013**, *14* (8), 16485–16514. https://doi.org/10.3390/ijms140816485.

(484)   Krawinkel, J.; Richter, U.; Torres-Mapa, M. L.; Westermann, M.; Gamrad, L.; Rehbock, C.; Barcikowski, S.; Heisterkamp, A. Optical and Electron Microscopy Study of Laser-Based Intracellular Molecule Delivery Using Peptide-Conjugated Photodispersible Gold Nanoparticle Agglomerates. *J Nanobiotechnol* **2016**, *14* (1), 2. https://doi.org/10.1186/s12951-015-0155-8.

(485)   Liu, W.; Naydenov, B.; Chakrabortty, S.; Wuensch, B.; Hübner, K.; Ritz, S.; Cölfen, H.; Barth, H.; Koynov, K.; Qi, H.; Leiter, R.; Reuter, R.; Wrachtrup, J.; Boldt, F.; Scheuer, J.; Kaiser, U.; Sison, M.; Lasser, T.; Tinnefeld, P.; Jelezko, F.; Walther, P.; Wu, Y.; Weil, T. Fluorescent Nanodiamond–Gold Hybrid Particles for Multimodal Optical and Electron Microscopy Cellular Imaging. *Nano Lett.* **2016**, *16* (10), 6236–6244. https://doi.org/10.1021/acs.nanolett.6b02456.

(486)   Anderson, K.; Nilsson, T.; Fernandez-Rodriguez, J. Challenges for CLEM from a Light Microscopy Perspective. In *Correlative Imaging*; Verkade, P., Collinson, L., Eds.; Wiley, 2019; pp 23–35. https://doi.org/10.1002/9781119086420.ch2.

(487)   Haruta, T.; Hasumi, K.; Ikeda, Y.; Konyuba, Y.; Fukuda, T.; Nishioka, H. Local Surface Plasmon Resonance of Gold Nanoparticles as a Correlative Light and Electron Microscopy (CLEM) Tag for Biological Samples. *Microscopy* **2019**, dfz031. https://doi.org/10.1093/jmicro/dfz031.

(488)   Prabhakar, N.; Peurla, M.; Koho, S.; Deguchi, T.; Näreoja, T.; Chang, H.-C.; Rosenholm, J. M.; Hänninen, P. E. STED-TEM Correlative Microscopy Leveraging Nanodiamonds as Intracellular Dual-Contrast Markers. *Small* **2018**, *14* (5), 1701807. https://doi.org/10.1002/smll.201701807.

(489)   Hemelaar, S. R.; de Boer, P.; Chipaux, M.; Zuidema, W.; Hamoh, T.; Martinez, F. P.; Nagl, A.; Hoogenboom, J. P.; Giepmans, B. N. G.; Schirhagl, R. Nanodiamonds as Multi-Purpose Labels for Microscopy. *Sci Rep* **2017**, *7* (1), 720. https://doi.org/10.1038/s41598-017-00797-2.

(490)   Nicovich, P. R.; Owen, D. M.; Gaus, K. Turning Single-Molecule Localization Microscopy into a Quantitative Bioanalytical Tool. *Nat Protoc* **2017**, *12* (3), 453–460. https://doi.org/10.1038/nprot.2016.166.

(491)   Heilemann, M.; van de Linde, S.; Schüttpelz, M.; Kasper, R.; Seefeldt, B.; Mukherjee, A.; Tinnefeld, P.; Sauer, M. Subdiffraction-Resolution Fluorescence Imaging with Conventional Fluorescent Probes. *Angew. Chem. Int. Ed.* **2008**, *47* (33), 6172–6176. https://doi.org/10.1002/anie.200802376.

(492)   Xu, K.; Babcock, H. P.; Zhuang, X. Dual-Objective STORM Reveals Three-Dimensional Filament Organization in the Actin Cytoskeleton. *Nat Methods* **2012**, *9* (2), 185–188. https://doi.org/10.1038/nmeth.1841.

(493)   Hauser, M.; Wojcik, M.; Kim, D.; Mahmoudi, M.; Li, W.; Xu, K. Correlative Super-Resolution Microscopy: New Dimensions and New Opportunities. *Chem. Rev.* **2017**, *117* (11), 7428–7456. https://doi.org/10.1021/acs.chemrev.6b00604.

(494)   Jones, S. A.; Shim, S.-H.; He, J.; Zhuang, X. Fast, Three-Dimensional Super-Resolution Imaging of Live Cells. *Nat Methods* **2011**, *8* (6), 499–505. https://doi.org/10.1038/nmeth.1605.

(495)   Mateos-Gil, P.; Letschert, S.; Doose, S.; Sauer, M. Super-Resolution Imaging of Plasma Membrane Proteins with Click Chemistry. *Frontiers in Cell and Developmental Biology* **2016**, *4* (SEP), 1–16. https://doi.org/10.3389/fcell.2016.00098.

(496)   Clancy, B.; Cauller, L. J. Reduction of Background Autofluorescence in Brain Sections Following Immersion in Sodium Borohydride. *Journal of Neuroscience Methods* **1998**, *83* (2), 97–102. https://doi.org/10.1016/S0165-0270(98)00066-1.

(497)   Watanabe, S.; Punge, A.; Hollopeter, G.; Willig, K. I.; Hobson, R. J.; Davis, M. W.; Hell, S. W.; Jorgensen, E. M. Protein Localization in Electron Micrographs Using Fluorescence Nanoscopy. *Nat Methods* **2011**, *8* (1), 80–84. https://doi.org/10.1038/nmeth.1537.

(498)   Betzig, E.; Patterson, G. H.; Sougrat, R.; Lindwasser, O. W.; Olenych, S.; Bonifacino, J. S.; Davidson, M. W.; Lippincott-Schwartz, J.; Hess, H. F. Imaging Intracellular Fluorescent Proteins at Nanometer Resolution. *Science* **2006**, *313* (5793), 1642–1645. https://doi.org/10.1126/science.1127344.

(499)   Tokuyasu, K. T. Application of Cryoultramicrotomy to Immunocytochemistry. *Journal of Microscopy* **1986**, *143* (2), 139–149. https://doi.org/10.1111/j.1365-2818.1986.tb02772.x.

(500)   Cortese, K.; Diaspro, A.; Tacchetti, C. Advanced Correlative Light/Electron Microscopy: Current Methods and New Developments Using Tokuyasu Cryosections. *J Histochem Cytochem.* **2009**, *57* (12), 1103–1112. https://doi.org/10.1369/jhc.2009.954214.

(501)   Oorschot, V. M. J.; Sztal, T. E.; Bryson-Richardson, R. J.; Ramm, G. Immuno Correlative Light and Electron Microscopy on Tokuyasu Cryosections. In *Methods in Cell Biology*; Elsevier, 2014; Vol. 124, pp 241–258. https://doi.org/10.1016/B978-0-12-801075-4.00011-2.

(502)   van Rijnsoever, C.; Oorschot, V.; Klumperman, J. Correlative Light-Electron Microscopy (CLEM) Combining Live-Cell Imaging and Immunolabeling of Ultrathin Cryosections. *Nat Methods* **2008**, *5* (11), 973–980. https://doi.org/10.1038/nmeth.1263.

(503)   McDonald, K. L. Rapid Embedding Methods into Epoxy and LR White Resins for Morphological and Immunological Analysis of Cryofixed Biological Specimens. *Microsc Microanal* **2014**, *20* (1), 152–163. https://doi.org/10.1017/S1431927613013846.

(504)   Ando, T.; Bhamidimarri, S. P.; Brending, N.; Colin-York, H.; Collinson, L.; De Jonge, N.; de Pablo, P. J.; Debroye, E.; Eggeling, C.; Franck, C.; Fritzsche, M.; Gerritsen, H.; Giepmans, B. N. G.; Grunewald, K.; Hofkens, J.; Hoogenboom, J. P.; Janssen, K. P. F.; Kaufmann, R.; Klumperman, J.; Kurniawan, N.; Kusch, J.; Liv, N.; Parekh, V.; Peckys, D. B.; Rehfeldt, F.; Reutens, D. C.; Roeffaers, M. B. J.; Salditt, T.; Schaap, I. A. T.; Schwarz, U. S.; Verkade, P.; Vogel, M. W.; Wagner, R.; Winterhalter, M.; Yuan, H.; Zifarelli, G. The

2018 Correlative Microscopy Techniques Roadmap. *J. Phys. D: Appl. Phys.* **2018**, *51* (44), 443001. https://doi.org/10.1088/1361-6463/aad055.

(505) Schnell, U.; Dijk, F.; Sjollema, K. A.; Giepmans, B. N. G. Immunolabeling Artifacts and the Need for Live-Cell Imaging. *Nat Methods* **2012**, *9* (2), 152–158. https://doi.org/10.1038/nmeth.1855.

(506) Griffiths, G.; Lucocq, J. M. Antibodies for Immunolabeling by Light and Electron Microscopy: Not for the Faint Hearted. *Histochemistry and Cell Biology* **2014**, *142* (4), 347–360. https://doi.org/10.1007/s00418-014-1263-5.

(507) Möbius, W.; Posthuma, G. Sugar and Ice: Immunoelectron Microscopy Using Cryosections According to the Tokuyasu Method. *Tissue and Cell* **2018**, No. July, 1–13. https://doi.org/10.1016/j.tice.2018.08.010.

(508) Shu, X.; Lev-Ram, V.; Deerinck, T. J.; Qi, Y.; Ramko, E. B.; Davidson, M. W.; Jin, Y.; Ellisman, M. H.; Tsien, R. Y. A Genetically Encoded Tag for Correlated Light and Electron Microscopy of Intact Cells, Tissues, and Organisms. *PLoS Biol* **2011**, *9* (4), e1001041. https://doi.org/10.1371/journal.pbio.1001041.

(509) Jensen, E. C. Use of Fluorescent Probes: Their Effect on Cell Biology and Limitations. *Anatomical Record* **2012**, *295* (12), 2031–2036. https://doi.org/10.1002/ar.22602.

(510) Chan, C. E. Z.; Lim, A. P. C.; MacAry, P. A.; Hanson, B. J. The Role of Phage Display in Therapeutic Antibody Discovery. *International immunology* **2014**, *26* (12), 649–657. https://doi.org/10.1093/intimm/dxu082.

(511) Prescher, J. a; Bertozzi, C. R. Chemistry in Living Systems. *Nature chemical biology* **2005**, *1* (1), 13–21. https://doi.org/10.1038/nchembio0605-13.

(512) Toseland, C. P. Fluorescent Labeling and Modification of Proteins. *Journal of Chemical Biology* **2013**, *6* (3), 85–95. https://doi.org/10.1007/s12154-013-0094-5.

(513) Patterson, D. M.; Nazarova, L. A.; Prescher, J. A. Finding the Right (Bioorthogonal) Chemistry. *ACS Chemical Biology* **2014**, *9* (3), 592–605. https://doi.org/10.1021/cb400828a.

(514) Sahoo, H. Fluorescent Labeling Techniques in Biomolecules: A Flashback. *RSC Advances* **2012**, *2* (18), 7017–7029. https://doi.org/10.1039/c2ra20389h.

(515) Dempsey, G. T.; Vaughan, J. C.; Chen, K. H.; Bates, M.; Zhuang, X. Evaluation of Fluorophores for Optimal Performance in Localization-Based Super-Resolution Imaging. *Nature Methods* **2011**, *8* (12), 1027–1040. https://doi.org/10.1038/nmeth.1768.

(516) Araman, C.; Pieper-Pournara, L.; van Leeuwen, T.; Kampstra, A. S. B.; Bakkum, T.; Marqvorsen, M. H. S.; Nascimento, C. R.; Mirjam Groenewold, G. J.; van der Wulp, W.; Camps, M. G. M.; Overkleeft, H. S.; Ossendorp, F. A.; Toes, R. E. M.; van Kasteren, S. I. *Bioorthogonal Antigens Allow the Unbiased Study of Antigen Processing and Presentation*; preprint; Immunology, 2018. https://doi.org/10.1101/439323.

(517) Hos, B. J.; Tondini, E.; van Kasteren, S. I.; Ossendorp, F. Approaches to Improve Chemically Defined Synthetic Peptide Vaccines. *Front. Immunol.* **2018**, *9*, 884. https://doi.org/10.3389/fimmu.2018.00884.

(518) Szabó, Á.; Szendi-Szatmári, T.; Ujlaky-Nagy, L.; Rádi, I.; Vereb, G.; Szöllősi, J.; Nagy, P. The Effect of Fluorophore Conjugation on Antibody Affinity and the Photophysical Properties of Dyes. *Biophysical Journal* **2018**, *114* (3), 688–700. https://doi.org/10.1016/j.bpj.2017.12.011.

(519) McKay, C. S.; Finn, M. G. Click Chemistry in Complex Mixtures: Bioorthogonal Bioconjugation. *Chemistry & Biology* **2014**, *21* (9), 1075–1101. https://doi.org/10.1016/j.chembiol.2014.09.002.

(520) Devaraj, N. K. The Future of Bioorthogonal Chemistry. *ACS Central Science* **2018**, *4*, 952–959. https://doi.org/10.1021/acscentsci.8b00251.

(521)   Row, R. D.; Prescher, J. A. Constructing New Bioorthogonal Reagents and Reactions. *Acc. Chem. Res.* **2015**, *51* (5), 1073–1081. https://doi.org/10.1016/j.physbeh.2017.03.040.

(522)   Rostovtsev, V. V.; Green, L. G.; Fokin, V. V.; Sharpless, K. B. A Stepwise Huisgen Cycloaddition Process: Copper(I)-Catalyzed Regioselective "Ligation" of Azides and Terminal Alkynes. *Angewandte Chemie - International Edition* **2002**, *41* (14), 2596–2599. https://doi.org/10.1002/1521-3773(20020715)41:14<2596::AID-ANIE2596>3.0.CO;2-4.

(523)   Bakkum, T.; van Leeuwen, T.; Sarris, A. J. C.; van Elsland, D. M.; Poulcharidis, D.; Overkleeft, H. S.; van Kasteren, S. I. Quantification of Bioorthogonal Stability in Immune Phagocytes Using Flow Cytometry Reveals Rapid Degradation of Strained Alkynes. *ACS Chemical Biology* **2018**, *13* (5), 1173–1179. https://doi.org/10.1021/acschembio.8b00355.

(524)   Sletten, E. M.; Bertozzi, C. R. From Mechanism to Mouse; A Tale of Two Bioorthogonal Reactions. *Acc. Chem. Res.* **2011**, *44* (9), 666–676. https://doi.org/10.1021/ar200148z.

(525)   Neef, A. B.; Luedtke, N. W. An Azide-Modified Nucleoside for Metabolic Labeling of DNA. *ChemBioChem* **2014**, *15* (6), 789–793. https://doi.org/10.1002/cbic.201400037.

(526)   van Elsland, D. M.; Bos, E.; de Boer, W.; Overkleeft, H. S.; Koster, A. J.; van Kasteren, S. I. Detection of Bioorthogonal Groups by Correlative Light and Electron Microscopy Allows Imaging of Degraded Bacteria in Phagocytes. *Chem. Sci.* **2016**, *7* (1), 752–758. https://doi.org/10.1039/C5SC02905H.

(527)   Murphy, K. (Kenneth M.); Weaver, C. *Janeway's Immunobiology*.

(528)   McCarville, J.; Ayres, J. Disease Tolerance: Concept and Mechanisms. *Current Opinion in Immunology* **2018**, *50*, 88–93. https://doi.org/10.1016/j.physbeh.2017.03.040.

(529)   Kinchen, J. M.; Ravichandran, K. S. Phagosome Maturation: Going through the Acid Test. *Nature Reviews Molecular Cell Biology* **2008**, *9* (10), 781–795. https://doi.org/10.1038/nrm2515.

(530)   Fields, K. A.; Heinzen, R. A.; Carabeo, R. The Obligate Intracellular Lifestyle. *Frontiers in Microbiology* **2011**, *2* (MAY), 1–2. https://doi.org/10.3389/fmicb.2011.00099.

(531)   van Elsland, D. M.; Pujals, S.; Bakkum, T.; Bos, E.; Oikonomeas-Koppasis, N.; Berlin, I.; Neefjes, J.; Meijer, A. H.; Koster, A. J.; Albertazzi, L.; van Kasteren, S. I. Ultrastructural Imaging of Salmonella–Host Interactions Using Super-Resolution Correlative Light-Electron Microscopy of Bioorthogonal Pathogens. *ChemBioChem* **2018**, *19* (16), 1766–1770. https://doi.org/10.1002/cbic.201800230.

(532)   Dieterich, D. C.; Link, A. J.; Graumann, J.; Tirrell, D. A.; Schuman, E. M. Selective Identification of Newly Synthesized Proteins in Mammalian Cells Using Bioorthogonal Noncanonical Amino Acid Tagging (BONCAT). *Proceedings of the National Academy of Sciences* **2006**, *103* (25), 9482–9487. https://doi.org/10.1073/pnas.0601637103.

(533)   Landgraf, P.; Antileo, E. R.; Schuman, E. M.; Dieterich, D. C. BONCAT: Metabolic Labeling, Click Chemistry, and Affinity Purification of Newly Synthesized Proteomes. *Methods in Molecular Biology* **2015**, *1266*, 199–215. https://doi.org/10.1007/978-1-4939-2272-7_14.

(534)   Vicidomini, G.; Gagliani, M. C.; Canfora, M.; Cortese, K.; Frosi, F.; Santangelo, C.; Di Fiore, P. P.; Boccacci, P.; Diaspro, A.; Tacchetti, C. High Data Output and Automated 3D Correlative Light-Electron Microscopy Method. *Traffic* **2008**, *9* (11), 1828–1838. https://doi.org/10.1111/j.1600-0854.2008.00815.x.

(535)   Vicidomini, G.; Gagliani, M. C.; Cortese, K.; Krieger, J.; Buescher, P.; Bianchini, P.; Boccacci, P.; Tacchetti, C.; Diaspro, A. A Novel Approach for Correlative Light Electron Microscopy Analysis. *Microscopy Research and Technique* **2010**, *73* (3), 215–224. https://doi.org/10.1002/jemt.20777.

(536)   Peters, P. J.; Bos, E.; Griekspoor, A. Cryo-Immunogold Electron Microscopy. *Current Protocols in Cell Biology* **2006**, *30* (1), 4.7.1-4.7.19. https://doi.org/10.1002/0471143030.cb0407s30.

(537)   LeicaMicrosystems. *Double Micromanipulator for Cryo-Ultramicrotomy - YouTube*. https://www.youtube.com/watch?v=wy1F0oEsckk (accessed 2020-05-04).

(538)   Bos, E.; Sań Anna, C.; Gnaegi, H.; Pinto, R. F.; Ravelli, R. B. G.; Koster, A. J.; Souza, W. de; Peters, P. J. A New Approach to Improve the Quality of Ultrathin Cryo-Sections; Its Use for Immunogold EM and Correlative Electron Cryo-Tomography. *Journal of Structural Biology* **2011**, *175* (1), 62–72. https://doi.org/10.1016/j.jsb.2011.03.022.

(539)   Hong, V.; Presolski, S. I.; Ma, C.; Finn, M. G. Analysis and Optimization of Copper-Catalyzed Azide-Alkyne Cycloaddition for Bioconjugation. *Angewandte Chemie - International Edition* **2009**, *48* (52), 9879–9883. https://doi.org/10.1002/anie.200905087.

(540)   Hong, V.; Steinmetz, N. F.; Manchester, M.; Finn, M. G. Labeling Live Cells by Copper-Catalyzed Alkyne - Azide Click Chemistry. *Bioconjugate chem.* **2010**, *21* (10), 1912–1916. https://doi.org/10.1021/bc100272z.

(541)   Presolski, S. L.; Hong, V. P.; Finn, M. G. Copper-Catalyzed Azide–Alkyne Click Chemistry for Bioconjugation. *Current Protocols in Chemical Biology* **2011**, *3* (4), 153–162. https://doi.org/10.1002/9780470559277.ch110148.Copper-Catalyzed.

(542)   Deschout, H.; Zanacchi, F. C.; Mlodzianoski, M.; Diaspro, A.; Bewersdorf, J.; Hess, S. T.; Braeckmans, K. Precisely and Accurately Localizing Single Emitters in Fluorescence Microscopy. *Nat Methods* **2014**, *11* (3), 253–266. https://doi.org/10.1038/nmeth.2843.

(543)   Faas, F. G. A.; Cristina Avramut, M.; van den Berg, B. M.; Mieke Mommaas, A.; Koster, A. J.; Ravelli, R. B. G. Virtual Nanoscopy: Generation of Ultra-Large High Resolution Electron Microscopy Maps. *Journal of Cell Biology* **2012**, *198* (3), 457–469. https://doi.org/10.1083/jcb.201201140.

(544)   Betzig, E.; Patterson, G. H.; Sougrat, R.; Lindwasser, O. W.; Olenych, S.; Bonifacino, J. S.; Davidson, M. W.; Lippincott-Schwartz, J.; Hess, H. F. Imaging Intracellular Fluorescent Proteins at Nanometer Resolution. *Science* **2006**, *313* (5793), 1642–1645. https://doi.org/10.1126/science.1127344.

(545)   Cheutin, T.; Sauvage, C.; Tchélidzé, P.; O'Donohue, M. F.; Kaplan, H.; Beorchia, A.; Ploton, D. Visualizing Macromolecules with Fluoronanogold: From Photon Microscopy to Electron Tomography. *Methods in Cell Biology* **2007**, *79* (79), 559–574. https://doi.org/10.1016/S0091-679X(06)79022-7.

(546)   Kurdekar, A. D.; Chunduri, L. A. A.; Manohar, C. S.; Haleyurgirisetty, M. K.; Hewlett, I. K.; Venkataramaniah, K. Streptavidin-Conjugated Gold Nanoclusters as Ultrasensitive Fluorescent Sensors for Early Diagnosis of HIV Infection. *Science Advances* **2018**, *4* (11), 1–11. https://doi.org/10.1126/sciadv.aar6280.

(547)   Grammel, M.; Hang, H. C. Chemical Reporters for Biological Discovery. *Nature chemical biology* **2013**, *9* (8), 475–484. https://doi.org/10.1038/nchembio.1296.

(548)   Patterson, D. M.; Prescher, J. A. Orthogonal Bioorthogonal Chemistries. *Current Opinion in Chemical Biology* **2015**, *28*, 141–149. https://doi.org/10.1016/j.cbpa.2015.07.006.

(549)   Willems, L. I.; Li, N.; Florea, B. I.; Ruben, M.; Van Der Marel, G. A.; Overkleeft, H. S. Triple Bioorthogonal Ligation Strategy for Simultaneous Labeling of Multiple Enzymatic Activities. *Angewandte Chemie - International Edition* **2012**, *51* (18), 4431–4434. https://doi.org/10.1002/anie.201200923.

(550)   Liang, Y.; Mackey, J. L.; Lopez, S. A.; Liu, F.; Houk, K. N. Control and Design of Mutual Orthogonality in Bioorthogonal Cycloadditions. *Journal of the American Chemical Society* **2012**, *134* (43), 17904–17907. https://doi.org/10.1021/ja309241e.

(551)   ten Brink, C.; Oorschot, V.; Klumperman, J. Correlative Light and Electron Microscopy (CLEM) on Biological Samples Using Immuno Electron Microscopy. *Microsc Microanal* **2015**, *21* (S3), 1379–1380. https://doi.org/10.1017/S1431927615007680.

(552)   van Meel, E.; Bos, E.; van der Lienden, M. J. C.; Overkleeft, H. S.; van Kasteren, S. I.; Koster, A. J.; Aerts, J. M. F. G. Localization of Active Endogenous and Exogenous β-

Glucocerebrosidase by Correlative Light-Electron Microscopy in Human Fibroblasts. *Traffic* **2019**, *20* (5), 346–356. https://doi.org/10.1111/tra.12641.

(553)   Fu, X.; Ning, J.; Zhong, Z.; Ambrose, Z.; Charles Watkins, S.; Zhang, P. AutoCLEM: An Automated Workflow for Correlative Live-Cell Fluorescence Microscopy and Cryo-Electron Tomography. *Scientific Reports* **2019**, *9* (1), 1–10. https://doi.org/10.1038/s41598-019-55766-8.

(554)   Tuijtel, M. W.; Koster, A. J.; Jakobs, S.; Faas, F. G. A.; Sharp, T. H. Correlative Cryo Super-Resolution Light and Electron Microscopy on Mammalian Cells Using Fluorescent Proteins. *Scientific Reports* **2019**, *9* (1), 1369. https://doi.org/10.1038/s41598-018-37728-8.

(555)   Fokkema, J.; Fermie, J.; Liv, N.; van den Heuvel, D. J.; Konings, T. O. M.; Blab, G. A.; Meijerink, A.; Klumperman, J.; Gerritsen, H. C. Fluorescently Labelled Silica Coated Gold Nanoparticles as Fiducial Markers for Correlative Light and Electron Microscopy. *Scientific Reports* **2018**, *8* (1), 13625. https://doi.org/10.1038/s41598-018-31836-1.

(556)   VAN HEST, J. J. H. A.; AGRONSKAIA, A. V.; FOKKEMA, J.; MONTANARELLA, F.; GREGORIO PUIG, A.; DE MELLO DONEGA, C.; MEIJERINK, A.; BLAB, G. A.; GERRITSEN, H. C. Towards Robust and Versatile Single Nanoparticle Fiducial Markers for Correlative Light and Electron Microscopy. *Journal of Microscopy* **2019**, *00* (0), 1–10. https://doi.org/10.1111/jmi.12778.

(557)   Jin, D.; Xi, P.; Wang, B.; Zhang, L.; Enderlein, J.; Oijen, A. M. Van. Nanoparticles for Super-Resolution Microscopy and Single-Molecule Tracking. *Nature Methods* **2018**, *15* (June), 1–10. https://doi.org/10.1038/s41592-018-0012-4.

(558)   Vu, T. Q.; Lam, W. Y.; Hatch, E. W.; Lidke, D. S. Quantum Dots for Quantitative Imaging: From Single Molecules to Tissue. *Cell and Tissue Research* **2015**, *360* (1), 71–86. https://doi.org/10.1007/s00441-014-2087-2.

(559)   Killingsworth, M. C.; Lai, K.; Wu, X.; Yong, J. L. C.; Lee, C. S. Quantum Dot Immunocytochemical Localization of Somatostatin in Somatostatinoma by Widefield Epifluorescence, Superresolution Light, and Immunoelectron Microscopy. *Journal of Histochemistry and Cytochemistry* **2012**, *60* (11), 832–843. https://doi.org/10.1369/0022155412459856.

(560)   Han, S.; Raabe, M.; Hodgson, L.; Mantell, J.; Verkade, P.; Lasser, T.; Landfester, K.; Weil, T.; Lieberwirth, I. High-Contrast Imaging of Nanodiamonds in Cells by Energy Filtered and Correlative Light-Electron Microscopy: Toward a Quantitative Nanoparticle-Cell Analysis. *Nano Letters* **2019**, *19* (3), 2178–2185. https://doi.org/10.1021/acs.nanolett.9b00752.

(561)   Hsiao, W. W. W.; Hui, Y. Y.; Tsai, P. C.; Chang, H. C. Fluorescent Nanodiamond: A Versatile Tool for Long-Term Cell Tracking, Super-Resolution Imaging, and Nanoscale Temperature Sensing. *Accounts of Chemical Research* **2016**, *49* (3), 400–407. https://doi.org/10.1021/acs.accounts.5b00484.

(562)   Chen, E. H.; Gaathon, O.; Trusheim, M. E.; Englund, D. Wide-Field Multispectral Super-Resolution Imaging Using Spin-Dependent Fluorescence in Nanodiamonds. *Nano Letters* **2013**, *13* (5), 2073–2077. https://doi.org/10.1021/nl400346k.

(563)   Johnstone, G. E.; Cairns, G. S.; Patton, B. R. Nanodiamonds Enable Adaptive-Optics Enhanced, Super-Resolution, Twophoton Excitation Microscopy. *Royal Society Open Science* **2019**, *6* (7). https://doi.org/10.1098/rsos.190589.

(564)   Yi, J.; Manna, A.; Barr, V. A.; Hong, J.; Neuman, K. C.; Samelson, L. E. MadSTORM: A Superresolution Technique for Large-Scale Multiplexing at Single-Molecule Accuracy. *Molecular Biology of the Cell* **2016**, *27* (22), 3591–3600. https://doi.org/10.1091/mbc.E16-05-0330.

(565)   van Elsland, D. M.; Bos, E.; de Boer, W.; Overkleeft, H. S.; Koster, A. J.; van Kasteren, S. I. Detection of Bioorthogonal Groups by Correlative Light and Electron

Microscopy Allows Imaging of Degraded Bacteria in Phagocytes. *Chem. Sci.* **2016**, *7* (1), 752–758. https://doi.org/10.1039/C5SC02905H.

(566)   Ramos-Morales, F. Impact of *Salmonella Enterica* Type III Secretion System Effectors on the Eukaryotic Host Cell. *ISRN Cell Biology* **2012**, *2012*, 1–36. https://doi.org/10.5402/2012/787934.

(567)   Park, D.; Lara-Tejero, M.; Waxham, M. N.; Li, W.; Hu, B.; Galán, J. E.; Liu, J. Visualization of the Type III Secretion Mediated Salmonella-Host Cell Interface Using Cryo-Electron Tomography. *eLIFE* **2018**, 1–15. https://doi.org/10.1101/359166.

(568)   Steele-Mortimer, O.; Brumell, J. H.; Knodler, L. A.; Méresse, S.; Lopez, A.; Finlay, B. B. The Invasion-Associated Type III Secretion System of Salmonella Enterica Serovar Typhimurium Is Necessary for Intracellular Proliferation and Vacuole Biogenesis in Epithelial Cells. *Cellular Microbiology* **2002**, *4* (1), 43–54. https://doi.org/10.1046/j.1462-5822.2002.00170.x.

(569)   Anderson, C. J.; Kendall, M. M. Salmonella Enterica Serovar Typhimurium Strategies for Host Adaptation. *Frontiers in Microbiology* **2017**, *8* (OCT), 1–16. https://doi.org/10.3389/fmicb.2017.01983.

(570)   Uchiya, K.; Barbieri, M. A.; Funato, K.; Shah, A. H.; Stahl, P. D.; Groisman, E. A. A Salmonella Virulence Protein That Inhibits Cellular Trafficking. *The EMBO Journal* **1999**, *18* (14), 3924–3933.

(571)   Van Engelenburg, S. B.; Palmer, A. E. Imaging Type-III Secretion Reveals Dynamics and Spatial Segregation of Salmonella Effectors. *Nature Methods* **2010**, *7* (4), 325–330. https://doi.org/10.1038/nmeth.1437.

(572)   Dempsey, G. T.; Vaughan, J. C.; Chen, K. H.; Bates, M.; Zhuang, X. Evaluation of Fluorophores for Optimal Performance in Localization-Based Super-Resolution Imaging. *Nat Methods* **2011**, *8* (12), 1027–1036. https://doi.org/10.1038/nmeth.1768.

(573)   Dani, A.; Huang, B.; Bergan, J.; Dulac, C.; Zhuang, X. Superresolution Imaging of Chemical Synapses in the Brain. *Neuron* **2010**, *68* (5), 843–856. https://doi.org/10.1016/j.neuron.2010.11.021.

(574)   Loschberger, A.; van de Linde, S.; Dabauvalle, M.-C.; Rieger, B.; Heilemann, M.; Krohne, G.; Sauer, M. Super-Resolution Imaging Visualizes the Eightfold Symmetry of Gp210 Proteins around the Nuclear Pore Complex and Resolves the Central Channel with Nanometer Resolution. *Journal of Cell Science* **2012**, *125* (3), 570–575. https://doi.org/10.1242/jcs.098822.

Bibliography

Glossary

AFM - Atomic Force Microscopy

BTA - Benzene-1,3,5-tricarboxamide

CE - Conjugation Efficiency

CLEM - Correlative Light and Electron Microscopy

CLSM - Confocal Laser Scanning Microscopy

CQ - Chloroquine

CV - Coefficient of Variation

DLS - Dynamic Light Scattering

DMEM - Duldecco's Modified Eage Medium

DiI - 1,1′-dioctadecyl-3,3,3′,3′-tetramethylindocarbocyanine perchlorate

DNA-PAINT - DNA Points Accumulation for Imaging Nanoscale Topography

dSTORM - Direct STochastic Optical Reconstruction Microscopy

EE - Early Endosome

EFTEM - Energy Filtered Transmission Electron Microscopy

EM - Electron Microscopy

ER - Endoplasmic Reticulum

FBS - Fetal Bovine Serum

FDA - Food and Drug Administration

FM - Fluorescence Microscopy

FOV - Field Of View

FS - Freeze Substitution

GA - Glutaraldehyde

H - Hisitidine (amino acid)

HILO - Highly Inclined Laminated Optical Sheet

HPF – High-Pressure Freezing

LE - Late Endosome

MEA - Mercaptoethylamine

MIRIBEL - Minimum Information Reporting in Bio-nano Experimental Literature

NP - Nanoparticle

OsO$_4$ - Osmium Tetroxide

PdI - Polydispersity Index

pBAE - Poly(β-aminoesters)

pDNA - Plasmid DNA

PEG - Polyethylene glycol

PFA - Paraformaldehyde

pGFP - Plasmid Green Fluorescent Protein

PLGA - Poly(lactic-co-glycolic) acid

qPAINT - Quantitative Points Accumulation for Imaging Nanoscale Topography

R - Arginine (amino acid)

ROI - Region Of Interest

SEM - Scanning Electron Microscopy

SMLM - Single Molecule Localization Microscopy

SRM - Super-Resolution Microscopy

STORM - Stochastic Optical Reconstruction Microscopy

Super-resCLEM - Super-resolution Correlative Light and Electron Microscopy

TCEP - (tris(2-carboxyethyl)phosphine)

TEM - Transmission electron microscopy

TIRF - Total Internal Reflection Fluorescence

UA - Uranyl Acetate

ZP - Zeta Potential

Acknowledgements

Completing a 3-year PhD during a global pandemic and in a foreign country has been a bit of a rollercoaster ride. Luckily, I have always liked rollercoaster rides.

Prior to my PhD I had worked as a hospital pharmacist for a couple of years, so at the start of this journey I was worried of not having the most typical scientific background, and never ever having worked with an electron microscope or super-resolution microscope! But I think this made my voyage even more exciting, since every day there was something new to learn. Also, the environment helped massively. Barcelona is such a phenomenal city to live in, with its beautiful bohemian sights, an endless blue coastline, and extremely wonderful and kind residents. In my humble opinion, there is no better place to live in. But when the pandemic hit, I was in the middle of my PhD journey and far away from home, and I must admit as the months went by and the situation worsened, I could not see the light at the end of the tunnel. Thankfully, I had the support of my Nanoscopy for Nanomedicine (N4N) group, my family and friends and together we managed to overcome the obstacles set in front of us. These are the people I would like to thank for making my PhD experience a truly unforgettable one.

First, I would like to thank my supervisors Silvia and Lorenzo, who have offered me their advice and support from day 1. Silvia, thank you for being such a good listener, for all your unconditional advice, and for being a great example of a woman in science. Before the pandemic, we had the opportunity to travel together several times, and I will always cherish the fun moments spent together as very colorful highlights from my PhD. I wish you all the best in your new career and I know our friendship will not end here. Lorenzo, thank you for welcoming me in your group, being patient and offering me great scientific and life advice, despite the distance between Barcelona and Eindhoven. I hope we keep in touch in the future! I would also like to express how much I appreciate the extra months I received to finish my PhD project, that have greatly improved my life-work balance and without which I would have not been able to conclude many of the experiments and ideas we had in mind.

To my scientific family, N4N, I am so grateful I landed in this group, and I had the chance to get to know each one of you and to make such wonderful memories together. Madhura, you are a ray of sunshine and you have been my closest ally during these challenging years. Thank you for always putting a smile on my face, for your unconditional advice, for your dedication to try and teach me Zumba, for being my gym buddy and for all the fun moments travelling, they will not be the last. Edgar, you are my favourite Catalan. You have made me laugh continuously during my PhD, you have given me amazing lunch-time lessons from how the tax system works to the universal laws of physics, you are the person I go to with any questions. Please come back from Eindhoven, you are truly missed. Adrianna, you were the first person I met out of the group, and I will always relish your professionalism, sweet nature, and sense of humour, you are one of a kind! Maria, you have been the most helpful person, without exaggeration. Every time I was lost in the lab, in the microscope, in life, you have been there. Academia needs more people like you, and I am extremely happy I was able to share this journey with you. Pietro, although we only had the chance to work for a year or two together, I really don't know what I would have done without you in my PhD. Thank you for teaching me DNA-PAINT inside out, for having the patience to show me

how MATLAB works, and for all the lovely moments in the office. Alis, creativitatea ta m-a lăsat fără cuvinte, ești o persoană extrem de talentată in toate aspectele, și iți multumesc pentru toate momentele petrecute impreuna. Iți doresc un viitor minunat și per să ne revedem! And of course, I would like to thank you for your beautiful design of my PhD thesis cover!!

For the N4N members in Eindhoven, I really wish we spent more time together because you are all such wonderful people. Laura, thank you for always so kindly accepting to check my drafts and for the virtual coffee breaks, I am so excited to see what the future brings for you! Cristina, you were the best student I have had, you are so so smart, I still don't understand half of the MATLAB you did in your project with me. I am so proud to see you are now a PhD student in such a great university. Believe in yourself because you will do great! Roger, thank you for your help during these years, you were always someone I could count on. Larry, although we haven't met (yet) I would like to thank you for offering to look at my article and thesis, and for providing such insightful comments, I really wish we worked more closely together! Manos, although we only met briefly, your lovely Greek nature has always stood out, and I honestly wish you'd have worked in Barcelona instead! Natalia, I wish I started my PhD earlier, so I would have had opportunity to work with you, because you are such a brilliant scientist. Ana, Marrit and Miao, thank you for the fruitful meetings, I have learnt a lot from all of you, and I really hope we have the chance to meet. Yuyang, Joppe and Steijn, I also wish you all the best in the future, I am looking forward to seeing your work in the group!

Having been awarded the INPhINIT fellowship was a proud moment in my life. However, the best part of this fellowship were the fellows, such an exceptional group of people from all around the world, with whom I have shared some truly wonderful memories. La Caixitos, you have made this experience exciting, fun and generally so very memorable and I will always be grateful for the moment spent together. No matter what, we will always have karaoke night. Max, Maximilian, you are the person who told me to apply to this fellowship, and in a way, you have probably changed the path of my career and life forever (no pressure). You are such an amazing human being; I thank you for having been part of my life these past 4 years and I hope you continue to be because you always brighten up my days.

I would also like to thank all the collaborators I have had the pleasure to work with throughout these 3 years. First, I would like to thank the TEM department at PCB including Yolanda, Lidia, and Gemma. Yolanda, thank you for your patience and advice during all the long CLEM protocols and TEM imaging, without you and this department I would have probably not been able to carry out half of my PhD. I would also like to thank Thomas from Leiden University who has taught me all the little tricks on the Nikon microscope and who has been exceptionally professional and dedicated during our experimental and written collaboration. Marta, I always found your research at Hospital St Pau to be so impactful, and I thank you for letting me have a small part in it; the long microscopy sessions were so much more enjoyable when chatting to you about life and science. Maria and Cristina, you are both such talented and hardworking scientists, I look up to both of you and to the amazing work you do at IQS, thank you for teaching me patiently all about polyplexes and I hope to see more CLEM-polyplex data in the future! To my other two students, Guillem and Stan, I learnt a lot about myself supervising you, and saw the flaws in my knowledge when you curiously asked me questions, I thank you for this and your patience. Dr Anna Bassols, thank you for

kindly accepting me in your department at UAB and for guiding me through all the bureaucratic documents and processes, you have been extremely kind and helpful. Everything has run smoothly because of you!

To my close friends, all scattered around the world, from London to Dubai, to Romania and Sweden, I thank you for your unconditional support during these years, despite the distance. Thank you for celebrating my successes with me and helping me see the bright side when things didn't go so well. I hope I can always give you the same in return. I miss you all so very much.

To Harm, thank you for sharing this experience with me and for being supportive every mile of the way. Gracias por tu paciencia infinita y por estar ahí en los buenos, los malos, y los entremedios. Tu cariño y humor, tu falta de egoísmo y el apoyo incondicional que me das me hace una mejor persona. To my family, thank you for always supporting me in my life decisions and career choices, and for being proud of me when things went well but also when they didn't. Mum and dad, your life-long struggles and perseverance for a brighter future shaped me to be the ambitious person I am today, and I can only hope to carry on with the same energy you both show every day. All my achievements are yours.

I am so lucky to have you all in my life, thank you!

Teodora

Funding Acknowledgements

Scientific activity

<u>Publications</u>

- **Andrian, T.;** Bakkum, T.; van Elsland, D. M.; Bos, E.; Koster, A. J.; Albertazzi, L.; van Kasteren, S. I.; Pujals, S. Super-Resolution Correlative Light-Electron Microscopy Using a Click-Chemistry Approach for Studying Intracellular Trafficking. *Methods Cell Biol.*; *Elsevier*, 2021;162, 303–331. https://doi.org/10.1016/bs.mcb.2020.09.001.
- **Andrian, T.;** Riera, R.; Pujals, S.; Albertazzi, L. Nanoscopy for Endosomal Escape Quantification. *Nanoscale Adv.*, 2021,3, 10-23. https://doi.org/10.1039/D0NA00454E.
- **Andrian, T.;** Delcanale, P.; Pujals, S.; Albertazzi, L. Correlating Super-Resolution Microscopy and Transmission Electron Microscopy Reveals Multiparametric Heterogeneity in Nanoparticles. *Nano Lett.,* 2021, 21, 12, 5360–5368. https://doi.org/10.1021/acs.nanolett.1c01666.
- **Andrian, T.;** Pujals, S.; Albertazzi, L. Quantifying the effect of PEG architecture on nanoparticle ligand availability using DNA-PAINT. Nanoscale Adv., 2021, 3, 6876-6881. https://doi.org/10.1039/D1NA00696G.
- Dhiman, S.; **Andrian, T.;** Gonzalez, G.S.; Tholen, M.M.E; Wang, Y.; Albertazzi, L. Can super-resolution microscopy become a standard characterization technique for materials chemistry?. Chem. Sci., 2022, 13, 2152-2166. https://doi.org/10.1039/D1SC05506B.
- **Andrian T**, Pujals S, Albertazzi L. A super-resolution and transmission electron microscopy correlative approach to studying intracellular trafficking of nanoparticles. Under publication.

<u>Student supervision</u>

- Jul. 2019-Jan. 2020 (6 months) - <u>Double bachelor's degree</u> (Biotechnology and Computer Engineering) project supervision from Universitat Rovira I Virgili, on the characterization of nanomaterials using different techniques (DLS, TEM, *d*STORM) and the development of a *d*STORM quantification protocol of encapsulation efficiency of fluorescent dye.
- May 2020-Nov.2020 (6 months) - <u>Double bachelor's degree</u> (Biotechnology and Computer Engineering) project supervision from Universitat Rovira I Virgili on the development of a MATLAB script to correlate *d*STORM and TEM imaging.
- Sept. 2020-Jun.2021 (9 months) – <u>Master's degree</u> (Biomedical engineering) project supervision from Universitat de Barcelona on the formulation of supramolecular polymers and the development of a *d*STORM-TEM correlative protocol to characterize them.
- Nov. 2021-Feb. 2022 – <u>Master's degree </u>external internship from Eindhoven University of Technology (TU/e) on correlating low-resolution FM and TEM to study how diameter dispersity influences the concentration of encapsulated material.

<u>Attendance to conferences with a poster or oral presentations</u>

- 27/10/2020-**Poster presentation** at the 13th IBEC Annual Symposium.

- 19/11/2020-**Poster and flash talk presentation** at the Annual Congress of Nanoscience and Nanotechnology, where I was awarded the best poster award.
- 27/11/2020-**Oral presentation** at the Spanish and Portuguese Advanced Optical Microscopy Meeting.
- 17/06/2021-**Oral presentation** at the XVII Science Congress at the Department of Biochemistry of UAB.
- 30/04/2021-**Oral presentation** at the IBEC PhD Discussion.
- 7/04/2022-**Oral presentation** at the TU/e Institute for Complex Molecular Systems (ICMS) advanced analysis lectures.

<u>Other collaborations</u>

- Leiden University-collaboration with the group of Dr Sander I. van Kasteren on studying intracellular trafficking pathogens using a DNA-PAINT-TEM correlative approach.
- St Pau Hospital-collaboration with the group of Dr Alberto Lleo Bisa on the study of neuropathological disorders using a *d*STORM array tomography approach.

Curriculum Vitae

Teodora Andrian was born on December 10th in 1993 in Romania. She attended secondary school and college in London, England. In 2016 she qualified with a First-Class Honors Degree in Masters of Pharmacy (MPharm) from King's College London. During this time, she was selected to carry out an industry internship with AstraZeneca on validation of predictive tools for oral compounds, and she completed her MPharm research project at Utrecht University (Netherlands) as part of the ERASMUS scheme on 'thermosensitive liposomes as carriers for cytotoxic proteins'. In 2017 she completed her pharmacy hospital pre-registration training at the Royal Free London NHS Foundation trust and qualified as a pharmacist. Until 2018 she worked as a hospital pharmacist in the same trust and carried out part-time volunteering as a research assistant at King's College London on 'deriving proteases for enzymatic degradation of albumin nanoparticles in lung models'. In 2018 she was awarded the Marie Skłodowska–Curie and La Caixa Foundation INPhINIT COFUND fellowship to carry out her PhD at the Institute for Bioengineering of Catalonia (IBEC) on correlating light and electron microscopy to study nanomaterials. This thesis presents her most significant results. After the completion of her PhD, Teodora will be starting a position as a Global Regulatory Affairs Associate in oncology at Eli Lilly.